Study and characterisation of surface integrity modification after ultrasonic vibration-assisted ball burnishing

Ramon Jerez Mesa

Ramon Jerez Mesa. Study and characterisation of surface integrity modification after ultrasonic vibration-assisted ball burnishing. Mechanics of materials [physics.class-ph]. Université Paul Sabatier - Toulouse III, 2018. English. NNT : 2018TOU30024 . tel-02061706

HAL Id: tel-02061706

https://theses.hal.science/tel-02061706

Submitted on 8 Mar 2019

THÈSE

En vue de l'obtention du

DOCTORAT DE L'UNIVERSITÉ DE TOULOUSE

Délivré par:
Université Toulouse III Paul Sabatier (UT3 Paul Sabatier)
Cotutelle internationale avec Universitat Politècnica de Catalunya

---

Présentée et soutenue par :
Ramón JEREZ MESA

le 2 Mars 2018

Titre :
Study and characterisation of surface integrity modification after ultrasonic vibration-assisted ball burnishing

---

École doctorale et discipline ou spécialité :
ED MEGEP : Génie mécanique, mécanique des matériaux

Unité de recherche :
Institut Clément Ader, CNRS UMR 5312

Directeurs de Thèse :

Yann LANDON	Université Toulouse III Paul Sabatier	Directeur
José Antonio TRAVIESO	Universitat Politècnica de Catalunya	Directeur
Gilles DESSEIN	École Nationale d'Ingénieurs de Tarbes	Co-Directeur

Jury :

Mehdi CHÉRIF	ENSAM de Bordeaux	Rapporteur
Guillermo REYES	IQS, Universitat Ramon Llull	Rapporteur
Philippe DARNIS	IUT de Bordeaux	Examinateur
Irene BUJ CORRAL	Universitat Politècnica de Catalunya	Examinatrice
Giovanni GÓMEZ GRAS	IQS, Universitat Ramon Llull	Examinateur

Title: Study and characterisation of surface integrity modification after ultrasonic vibration-assisted ball burnishing

Author: Ramón JEREZ MESA

Advisors:
J. Antonio TRAVIESO-RODRÍGUEZ
Yann LANDON
Jordi LLUMÀ-FUENTES
Gilles DESSEIN

Date: February 2018

Abstract: This dissertation is an experimental research project into the mechanical effects of the ultrasonic vibration-assisted ball burnishing process on the surface integrity of surfaces machined through ball-end milling.

First, a prototype able to perform the process is designed and characterised. Then, it is tested on AISI 1038 and Ti-6Al-4V surfaces, following an experimental campaign based on a Taguchi orthogonal array. The preload, number of passes, feed velocity, strategy and initial surface texture are included as factors. Results are analysed in terms of topological characteristics, residual stress and hardness. The original texture proves to be the most influential parameter on all outcomes. Texture results show that the vibrations can enhance the roughness and texture results, as long as they have sufficient low initial amplitude.

The main conclusion arising from the study are different parameter sets that can deliver the best results from the performance of the vibration-assisted ball burnishing process, accoding to a specific desired optimisation target.

Keywords: vibration-assisted ball burnishing; surface integrity; surface texture; residual stress; hardness; steel; titanium

This thesis was written in LaTeX.
Figures were drawn using Inkscape.

Dissertation presented by Ramón Jerez Mesa in partial fulfillment of the
requirements for the degrees of
Doctor per la Universitat Politècnica de Catalunya
and
Doctorat de l'Université de Toulouse

Für Harald

Acknowledgements

Fist of all, I would like to sincerely thank all professors that honour me by participating of the evaluation of this dissertation: Irene Buj, Medi Chérif, Philippe Darnis, Giovanni Gomez and Guillermo Reyes.

Por supuesto, me gustaría dar las gracias a mis directores españoles, José Antonio Travieso y Jordi Llumà, tanto por vuestra implicación para con esta tesis, como por la amistad compartida, forjada en el día a día. Juntos, siempre llegamos.

Je voudrais bien aussi remercier mes directeurs français Yann Landon et Gilles Dessein, ainsi comme mon encadrant Vincent Wagner. Vos aportations a cette thèse ont été plus qu'enrichissant. Mais, surtout, je remercie sincèrement de m'avoir ouvert les portes de chez vous pendant mes séjours en France. Je me rejouis de ces amitiés imprévues de l'autre côté des Pyrénées.

Esta tesis es la culminación de un camino que tomé hace mucho tiempo, luego aparqué, pensando que de forma permanente, y al que volví hace pocos aos sin haberlo esperado. Todo este proceso tiene diversos nombres propios asociados a él. En primer lugar, debo agradecer a los profesores de mi *alma mater*, la Universidad Politécnica de Cartagena, que, seguramente sin saberlo, atizaron la llama de mi vocación académica: José Ramón Navarro, con sus vectores deslizantes, y María Dolores Bermúdez y Ana Eva Jiménez con sus líquidos iónicos. Por último, ya en la Universitat Politcnica de Catalunya, debo agradecer a Toni Travieso, quién me regaló la oportunidad de vivir esta maravillosa aventura.

I would not like to forget my colleagues in UPC, ENIT and UPS, who have been in different ways a support in this fascinating, however sometimes arid, trip of developing a dissertation, and who have accompanied me when I was far from home. Giovanni, David, Eva, Joan, Silvia, Francesc Pozo, Marta, los Maneles y los Orioles, Quentin-Tarantino, Marcos and Landry. I would like to make special reference to Ismael Fernández, for his inestimable help during the acoustic emission measurements, and Cyrus Amini for his support for the finite element model. My gratitude also for Serge Tovar, Anis Hor, Abdallah Bouzid, and Mehdi Salem for their technical and operational support during my working days in Toulouse.

Por supuesto, quiero dedicar unas palabras a mis padres Juana y Ramón, porque de pequeño nunca me dejaron conformarme, y me enseñaron el valor de esfuerzo para conseguir las metas. Sin este aprendizaje tan valioso, esta tesis no podría haberse culminado. También a mi hermana Patricia, cuya confianza ciega en mi no tiene límites.

Und schließlich, danke, Hari für deine ewige Geduld und unbedingte Großzügigkeit. Weil du immer für mich da warst, und weil du mich immer wieder auf den Boden der Wirklichkeit zurückgeholt hast.

Summary

This dissertation is an experimental research project into the mechanical effects of the ultrasonic vibration-assisted ball burnishing process on the surface integrity of surfaces machined through ball-end milling. Due to the lack of commercial tools able to perform this process, the study includes firstly the design and characterisation of a prototype to that effect. An experimental analysis is then undertaken, applying the process to AISI 1038 and Ti-6Al-4V surfaces of high industrial and aeronautical value. The experimental campaign is designed based on a Taguchi orthogonal array that includes five factors, namely: preload, number of passes, feed velocity, strategy and initial surface texture. Results are analysed in terms of topological characteristics, residual stress and hardness, in order to identify and understand the impact of process parameters on surface integrity, to define the best parameters for performing the process and to assess the positive effects caused by the introduction of vibrations as a means of assistance.

Results reveal that the initial texture is the most influential parameter on all outcomes. Texture results show that the vibrations can enhance the roughness and texture results, as long as they have sufficient low initial amplitude. Furthermore, only the preload and number of passes influence the results, with a pair of values being found in all cases that serve a threshold from which further plastic strain is detrimental for the final surface topology. In terms of residual stress, all parameters are influential in the results, especially the burnishing strategy, through which a certain component of the residual stress tensor can be adequately reinforced. Finally, the burnishing operation proves to modify the hardness of deep layers down to 0.5 mm, applying the vibration-assisted process. The main conclusion is that the optimal parameters for performing the process are different with regards to the optimisation objective. Some useful combinations are proposed for performing the process depending on the desired target.

Résumé

Cette thèse étudie les effets du processus de brunissage à bille assisté par vibrations ultrasoniques sur l'intégrité surface des surfaces usinées par fraisage hémisphérique. Compte tenu de l'inexistence d'outils commerciaux capables de réaliser ce processus, l'étude débute par la conception et la caractérisation d'un prototype capable de l'exécuter. Par la suite, une analyse expérimentale est menée, en utilisant le procédé sur les surfaces de deux alliages d'intérêt industriel et aéronautique, AISI 1038 et Ti-6Al-4V. Pour cela, un plan d'expériences est elaboré à base d'une matrice orthogonale Taguchi. Cinq facteurs sont inclus dans le modèle : la précharge, le nombre de passes, la vitesse d'avance, la stratégie de brunissage et la texture initiale de la surface préalablement usinée. Les résultats sont évalués en termes de texture finale, de contrainte résiduelle et de dureté, pour identifier et comprendre l'impact de ce procédé et des paramètres opératoires sur l'intégrité de surface, pour définir les meilleurs paramètres à appliquer pour chaque matériau, et pour évaluer les effets positifs provoqués par l'introduction de vibrations comme moyen d'assistance. Pour cela, la notion d'intégrité de surface est rappelée, voire redéfinie dans le cas de la texture de surface. En effet, les critères classiquement utilisés se révèlent inaptes à caractériser les surfaces obtenues, et une nouvelle méthodologie d'analyse des topologies de surface est proposée.

Les résultats obtenus suite à la réalisation du plan d'expériences révèlent que la texture initiale est le paramètre prépondérant. Les résultats de la topologie de surface montrent que les vibrations peuvent améliorer la rugosité et la texture des surfaces dans la mesure où létat de surface initial est suffisamment fin. Ensuite, seule la précharge et le nombre de passes influencent le résultat, avec, dans tous les cas, un couple de valeurs limites à partir desquelles les surfaces sont endommagées. Les résultats des contraintes résiduelles montrent que tous les paramètres influent sur le résultat final, en particulier la stratégie de brunissage, avec laquelle la direction préférentielle du tenseur de la contrainte superficielle peut être modifiée. Enfin, le brunissage montre une modification positive de la dureté à des couches d'environ 0,5 mm en appliquant le processus assisté avec vibrations. Nous concluons que les paramètres de processus optimaux sont différents en fonction de l'objectif d'optimisation, et que certaines combinaisons peuvent être utiles en fonction de ces objectifs.

Resumen

Esta tesis es un estudio experimental que versa sobre los efectos del proceso de bruñido con bola asistido por vibraciones ultrasónicas sobre la integridad superficial de superficies mecanizadas mediante fresa hemisférica. Dada la indisponibilidad de herramientas comerciales capaces de efectúar este proceso, el estudio incluye en primer lugar el diseño y caracterización de un prototipo a tal efecto. Posteriormente, se realiza un análisis experimental aplicando el proceso sobre superficies de dos aleaciones de interés industrial y aeronáutico, AISI 1038 y Ti-6Al-4V, siguiendo un diseño de experimentos parcial basado en una matriz ortogonal de Taguchi. Para ello, cinco factores son incluidos en el modelo, a saber: la precarga, el número de pasadas, la velocidad de avance, la estrategia de bruñido, y la amplitud de textura inicial. Los resultados se evalúan en términos de textura, tensiones residuales y dureza, para definir los mejores parámetros a aplicar para cada material, y con el fin de evaluar los efectos positivos provocados por la introducción de las vibraciones como medio de asistencia. Los resultados revelan que la textura inicial es el parámetro que define en mayor medida el estado de las superficies finales. Los resultados de textura evidencian que las vibraciones pueden mejorar en mayor medida la textura de las superficies objetivo, siempre que éstas sean suficientemente finas. Además, sólo la precarga y el número de pasadas influyen en el resultado, encontrando en todo caso un par de valores limítrofe a partir del cual las superficies se ven dañadas. Los resultados de tensiones residuales muestran que todos los parámetros son influyentes en el resultado final, especialmente la estrategia de bruñido, con la que puede modificarse la dirección preferencial del tensor de tensiones superficial. Finalmente, el bruñido demuestra modificar la dureza positivamente hasta capas de aproximadamente 0,5 mm, aplicando el proceso asistido con vibraciones. Se concluye que los parámetros óptimos de proceso son diferentes en función del objetivo de optimización, y deben definirse en base a dos variables de partida: el material objetivo y la textura que éste presenta antes del proceso.

Resumen

Aquesta tesi és un estudi experimental que tracta sobre els efectes del procés de brunyit amb bola assistit per vibracions ultrasòniques sobre la integritat superficial de superfícies mecanitzades amb fresa hemisfèrica. Degut a la indisponiblitat d'eines comercials capaces d'aplicar aquest procés, l'estudi inclou en primer lloc el disseny i la caracterització d'un prototip capa d'executar-lo. Posteriorment, es realitza una anàlisi experimental aplicant el procés sobre superfícies de dues aliatges d'interès industrial i aeronàutic, AISI 1038 i Ti-6Al-4V, seguint un disseny d'experiments basat en una matriu ortogonal Taguchi. Per això, cinc factors són inclous en el model: la precàrrega, el nombre d passades, la velocitat d'aven, l'estratègia de brunyit i la textura de la superfície inicial. Els resultats s'avaluen en termes de textura final, tensions residuals i duresa, per identificar i comprendre l'impacte d'aquest procés i dels seus paràmetres d'operació sobre la integritat superficial, definir els millors paràmetres a aplicar per a cada material, i amb l'objectiu d'avaluar els efectes positius provocats per la introducció de les vibracions com a mitjà d'assistència.

Els resultats evidencien que la textura inicial és el paràmetre que defineix en major mesura l'estat de les superfícies finals. Els resultats de textura indiquen que les vibracions poden millorar en major mesura la rugositat i textura de les superfícies, sempre que aquestes siguin suficientment fines. A més, només la precàrrega i el nombre de passades influeixen sobre el resultat, trobant en tot cas un parell de valors límit a partir del qual les superfícies són empitjorades. Els resultats de tensions residuals mostren que tots els paràmetres són influents sobre el resultat final, especialment l'estratègia, amb la què es pot millorar la direcció preferencial del tensor de tensions superficial. Finalment, el brunyit demostra modificar la duresa positivament fins a capes d'aproximadament 0.5 mm de profunditat, aplicant el procés assistit amb vibracions. Es conclou que els paràmetres òptims de procés són diferents en funció de l'objectiu d'optimització, i es proposen algunes combinacions que poden ser útils en funció del mateix.

Contents

List of Figures

List of Tables

List of Symbols

General parameters

A	Piezoelectric amplitude	
A_0	Fundamental frequency amplitude	58
$\varDelta F_v$	Half-cycle amplitude of the vibratory component	61
$\varDelta z$	Spring compression length	46
E	Young's module	51
f_0	Fundamental frequency transmitted by VABB prototype	58
F_0	Spring precompression force	46
F_b	Burnishing force	44
F_p	Burnishing preload	44
F_v	Vibratory component of burnishing force	44
ϕ_0	Sine phase of fitted ultrasonic signal	61
h_p	Depth of penetration	16
η	Low-frequency burnishing force variation	45
k	Spring elastic constant	48
ω	Sine angular frequency of fitted ultrasonic signal	61
ρ	Density	51

Piezoelectricity

$\mathbf{D}$	Electric displacement	50
d_{ij}	Piezoelectric strain constant along j due to electric field along i	50
I	Intensity	52
q	Number of piezoelectric disks in a stack	51
$\mathbf{S^E}$	Piezoelectric compliance coefficient matrix	50
σ	Piezoelectric stress vector	50
t	Piezoelectric thickness	50
V	Voltage	51

ξ^{σ}	Piezoelectric electric permittivity matrix	50
Z	Impedance	52

X-ray diffraction parameters

ψ	Tilt angle of the collimator with regards to surface	99
ϕ	Position of X-ray collimator goniometer	99
θ	Bragg's reflective angle	99

Texture and roughness parameters

λ_c	Cut-off length for roughness filtering	115
m_{min}	Least slope in AF curves	134
M_{min}	M_r value of point in least slope point of AF curves	134
M_r	AF curve material ratio	91
M_{r1}	Peak material ratio	91
M_{r2}	Valley material ratio	91
R_a	Average surface roughness	24
R_q	RMS roughness	26
S_a	Arithmetical mean surface height	87
S_{al}	Fastest decay autocorrelation length	87
S_{dq}	RMS gradient	87
S_{dr}	Developed interfacial area ratio	87
S_k	Abbot-Firestone core distance	91
S_{ku}	Surface texture kurtosis	87
S_{mq}	Abbot-Firestone relative material ratio	91
S_p	Surface maximum peak height	87
S_{pk}	Abbot-Firestone peak height	91
S_{pq}	Abbot-Firestone plateau RMS	91
S_q	Surface RMS height	87
Σ_s	Area under the AF curve slope function	130
S_{sk}	Surface texture skewness	87
S_{td}	Surface texture direction	87
S_{tr}	Surface texture aspect ratio	87
S_v	Surface maximum valley depth	87
S_{vk}	Abbot-Firestone valley depth	91
S_{vq}	Abbot-Firestone dale RMS	91
S_{xp}	Abbott-Firestone peak extreme height	91
S_{10z}	Surface ten-point height	87

V_{mc}	Abbott-Firestone core material volume	91
V_{mp}	Abbott-Firestone peak material volume	91
V_{vc}	Abbott-Firestone core void volume	91
V_{vv}	Abbott-Firestone valley void volume	91

Abbreviations

$ANOVA$	Analysis of Variance	84
$AACF$	Areal autocorrelation function of a surface	89
AF	Abbott-Firestone	90
FEM	Finite element model	161
FRU	Force regulation unit	46
FTU	Force transmission unit	53
$NVABB$	Non-vibration-assisted ball burnishing	33
$P\&V$	Peak & valley set	92
RS	Residual stress	98
SD	Standard deviation	64
S/N	Signal-to-noise ratio	82
$VABB$	Vibration-assisted ball burnishing	33
VTU	Vibrations transmission unit	48

Science is organised knowledge; wisdom is organised life.

Immanuel Kant

1

Introduction

1.1 Motivations and antecedents

The introduction of new materials has been one of the major historical facilitators for the enhancement of industrial products. For instance, a big leap forward in the aerospace manufacturing industry has been the expansion of composites in crucial components and parts such as the fuselage or major control surfaces. However, metallic components shall never be totally replaced, as they provide unique attributes difficult to be substituted by other materials.

Metallic parts are predominantly shaped from raw materials through machining routines. Although chip removal processes are nowadays highly reliable due to the expertise acquired during the last decades, innovation can always be achieved by developing alternative finishing methods to enhance the surface integrity of engineering parts. Indeed, today the term *enhancement* contemplates additional metrics other than adequate dimensioning or accurate material selection. In that respect, tailor-made surface integrity on workpieces is determinant to optimise product performance, and maximise the longevity and reliability of engineering parts. For instance, about 56% of catastrophic failure in turbine blades are caused by cracks initiated in positively stressed machined surfaces under high-frequency fatigue regimes, and can be prevented with adequate finishing treatments after machining, according to Prevéy *et al.* (2002) [113]. In this field, ball burnishing has proved to deliver better results in terms of surface roughness, residual stress and hardness of objective surfaces, when compared to other processes long integrated in the manufacturing industry such as laser shock peening (Altenberger *et al.*, 2012) [2], electropolishing or shot peening (Shepard *et al.*, 2004) [129]. Thus the necessity to increase the knowledge related to it.

Surface integrity management is remarkably important when special alloys are used to manufacture relevant parts. Advanced materials such as titanium or nickel alloys pose a high difficulty of surface integrity preservation after machining, as note numerous authors such as Ulutan *et al.* (2011) [155]. Consequently, thorough post-processing techniques are required to rectify the surface integrity. Manufacturing innovation through finishing processes development is not in contradiction with new material application. Much on the contrary, it can contribute to develop a mainstream of manufacturing technology enhancement.

One typical engineering surface that exemplifies the importance of surface integrity control are typically found in the transportation industry, formed by complex forms, conformed by juxtaposed curved surfaces. We can think about turbine blades or landing gears, but also moulds and dies for upsetting operations. This kind of parts are often manufactured through 3 or 5 axis machining with the aid of successive adjacent passes of hemispherical tools (Figure 1.1). Whereas this ball-end milling strategy allows to achieve complex surfaces by following the desired shape through NC interpolations generated by a CAM, it also has deep constraints. Guillemot (2010) [49] highlighted the importance of the tilt angle of the hemispherical tool during machining to guarantee a good surface integrity. However, these scientific recommendations are not taken into account by many manufacturers, who often use automatised CAM systems in which hemispherical milling is performed perpendicular to the surface, i.e. with tilt angle equal to zero. That type of machining execution is very often forced by the context defined by the only availability of 3-axis machines with no possibility of adjusting a specific tilt angle for the tool, thus generating a detrimental surface integrity.

In this context, ball burnishing can contribute to improve the described surfaces in industrial parts. The process is known for attaining a comprehensive surface im-

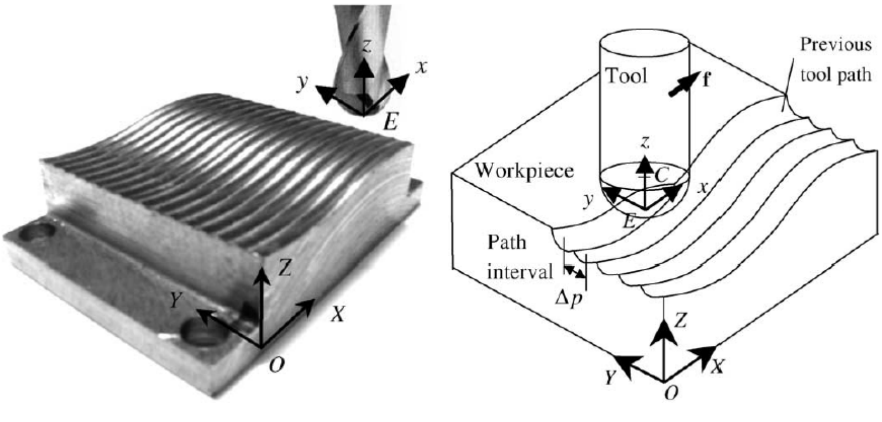

(a) (b)

Figure 1.1. Hemispherical milling of engineering surfaces. After Fontaine *et al.*, 2006 [38]. **a**. Overview of a ball-end milled surface. **b**. Ball-end milling kinematic parameters and scheme of the process.

provement in terms of texture, residual stress and hardness, as well as for being easily manoeuvrable from a procedural point of view. Spring-based ball burnishing tools are easily attachable to NC machines through custom commercial holders, simplifying the whole manufacturing system and equipment. That means that ball burnishing tools can be used at the same NC machines were previous machining has been performed, hence the reduction of handling and processing times, as well as an increase in the automation easiness. Burnishing tools, on the other hand, could be likely to be implemented on advanced automated systems such as robotic arms.

The presented pros attributed to ball burnishing makes it an interesting option to consider as an advanced finishing process for today's industry. On the other hand, the phenomenon of process assistance is today a highly extended strategy in manufacturing engineering innovation systems [14], since it allows to obtain emergent advantages from operations that are already totally integrated in manufacturing workshops. Taking this fact into account, it is worth questioning whether the ball burnishing operation can be enhanced by vibration-assistance, in search of emergent effects on industrial materials. In this thesis, the incorporation of ultrasonic vibrations is proposed to improve the ball burnishing process. The evidence that this combination can lead to interesting results is based on the physical phenomenon of acoustoplasticity, that is, the reduction of the quasi-static stress required to deform a material by the simultaneous propagation of waves inside it, while causing a residual hardening effect. Isolated results performed by other researchers have lead to think that this combination can be positive, as shall be presented in the state-of-the-art chapter [13]. As no comprehensive and consistent research has been developed previously, the following subsection presents the contributions expected to be delivered by this dissertation.

1.2 Research contributions

In this dissertation, a new finishing process resulting from modifying the ball burnishing process is executed on ball-end milled flat surfaces. At sight of the previously described surfaces, applying experimental design on flat surfaces means that we are dealing with surface states that are not necessarily realistic. However, they are obtained through a mastered machining strategy that allows to excerpt control on the surface topology by varying the peaks and amplitudes of the surface texture. On the other hand, they can be considered as preliminary results that shall eventually serve to characterise the process on curved more realistic surfaces.

The modification of the ball burnishing process is to be carried out by overlapping an oscillating force on the static burnishing preload, which allows to transmit an ultrasonic wave inside the material that makes it easier to deform plastically. The combination of ball burnishing with the acoustoplastic effect referred in this dissertation as vibration-assisted ball burnishing (VABB), in contrast to the non-vibration assisted process (NVABB), that is, conventional ball burnishing. The physical basis of the process enhancement is the acoustoplastic or Blaha effect [7]. This effect shows that acoustic and ultrasonic waves propagated inside a material while it is being deformed, reduce the quasi-static stress required to achieve a certain level of strain. This sort of metal softening has a transient effect, as is only present during the transmission of the wave inside the metal. In other words, when that irradiation stops, most materials show a residual hardening effect. As a process based on plastic deformation, ball burnishing is expected to be a recipient of enhancement through acoustoplasticity, which leads to enunciate the main hypothesis posed for this thesis:

The application of **acoustoplasticity** to enhance the **ball burnishing** operation leads to a technically feasible technology enabling the successful enhancement of the surface integrity of milled surfaces from topological, mechanical and metallurgical points of view.

To test that hypothesis, this dissertation must tackle with diverse scientific issues, that are due to be answered by a set of well-settled and properly formulated questions, as follows:

1. To what extent can the surface integrity of ball-end milled surfaces be enhanced by the introduction of the acoustoplastic effect in the ball burnishing operation?
2. Is surface texture essentially modified by the vibration-assisted ball burnishing process? Are R_a and R_t, as the classical surface roughness parameters, enough to describe that change?
3. What are the effects of the vibration-assisted ball burnishing process on the surface and sub-surface layers of the material from a mechanical and metallurgical perspective?
4. What is the impact of the original surface state on the results?

At sight of the described scientific issues, and due to the lack of comprehensive results of the VABB process on surface integrity, this dissertation adopts fundamentally an experimental scope that shall allow to provide comprehensive data about its results.

Furthermore, to fulfil the objectives of this dissertation, some technical issues can also be identified, and must be tackled to succeed in assessing the effects of the VABB process, and compare it to the non-vibration-assisted one. These technical issues can be described as follows:

1. No VABB tool is currently commercially available. For that reason, an innovative ultrasonic VABB prototype must be designed, protected by a patent, manufactured and characterised.
2. During the characterisation process, special instrumentation systems shall be required to sample and reconstruct the ultrasonic signals implicated in the process.

1.3 This dissertation in brief

The reader shall find in this text an extensive analysis of bibliographical studies and theoretical approaches that justify the application of VABB, along with extensive experimental results obtained from the application of the process on steel and titanium surfaces. The chapters of which it is composed are structured as follows.

Chapter 2 presents a review of bibliographical references that tackle with the issues at stake in this dissertation. Three main parts can be differentiated. The first one presents a definition of the ball burnishing process and different tooling configurations. Secondly, the effects of the ball burnishing process on the surface integrity of different materials is presented. The third section of this chapter focuses on explaining acoustoplasticity mechanisms as proposed by some authors, and the few references dealing with it to assist the ball burnishing process.

As no VABB prototype is available commercially, it must be designed, characterised and tested. **Chapter 3** shows all activities undertaken to this aim. Piezoelectricity is presented as the driver of vibration transmission on which the functioning of the prototype is based. A mechanical construction composed of three units is proposed in this chapter, and materialised in a prototype which is tested by applying acoustic emission, dynamometric measurements and motion track. These techniques ultimately deliver the characteristics of the vibratory force transmitted by the piezoelectric module installed inside the tool casing.

The prototype is then tested on Ti-6Al-4V and AISI 1038 surfaces. These materials have been chosen due to their industrial interest for applications on workpieces expected to function in highly demanding environments, such as fatigue regimes, thus requiring thorough finishing surface states. Specifically, the first one is known for its generalised presence in various aeronautical workpieces, whereas the AISI founds extended applications in gears, axes or power shovels. With that aim, an experimental design based on Taguchi orthogonal arrays is proposed, as explained in **Chapter 4**. That chapter also includes the set of techniques which are deployed to evaluate the surface integrity results on both materials. Specially interesting is the proposal of texture measurement through a comprehensive set of three-dimensional parameters, which has no precedents in the analysis of ball burnishing results.

Finally, the experimental results are compiled and explained in **chapter 5**. First, topological results are shown for both materials. The incorporation of surface parameters, in contrast to the two-dimensional parameters traditionally used to characterise burnished surface, is introduced. Then, the residual stress generated on the different VABB and NVABB patches is analysed. Finally, mechanical parameters describing the surface are presented to fulfil a comprehensive surface integrity characterisation of the VABB effects, including both metallography analysis and deep hardness measurement.

The knowledge developed along the referred chapters leads to formulate final conclusions and expected future works at the end of the text, which also includes appendices with relevant data not included in the report.

2

State of the art

This chapter includes the results emerging from an extensive bibliographical research which tackles with different burnishing references. Burnishing itself is a generic process that comprises innumerable versions defined by the contextual conditions that govern its execution, such as the geometry and construction of the burnishing tool. The first section of this chapter is a descriptive one, exposing the different burnishing versions by analysing different burnishing tools and the parameters governing the operation. The second section in this chapter establishes a definition of surface integrity, and includes the results found by ball burnishing on different materials. The first descriptive references found for the process were published in the 80's, and focus on steel, aluminium and copper alloys. The following years brought a breakthrough of the burnishing knowledge through the exploration of further similar alloys, and the incorporation of stainless steel to the system. Still today, the lack of results on the burnishing operation performed on titanium alloys or superalloys leaves a vast exploration territory for new research.

The VABB operation is defined and introduced in next section. The Blaha effect, which justifies its effectiveness, also known as acoustoplasticity, is presented along with a historical review of different explanations proposed by different authors. Last of all, the scarce references found related to the VABB process are presented.

2.1 General aspects of the burnishing operation

Burnishing is a general term that referes to a surface finishing operation based on local plastic deformation attained through the action of an indenter with a cylindrical or spherical geometry, which rolls over the objective surface while transmitting a preload [103]. Plastic deformation during the feed motion is successfully performed as a result of frictional engagement of the indenter and the surface irregularities.

The process is performed along successive adjacent passes with the aim of covering the whole target surface, as shown schematically in Figure 2.1. During the movement of the tool, the indenter makes contact with the peaks of the texture irregularities. At first, the peak material is deformed elastically, but the extended contact and deformation leads to the final plastification of the material, and its residual strain that is translated into a holistic modification of the surface. Indeed, this process modifies the surface integrity of the workpiece, as effects on surface topography, hardness, and residual stresses of subsurface layers are significant [64].

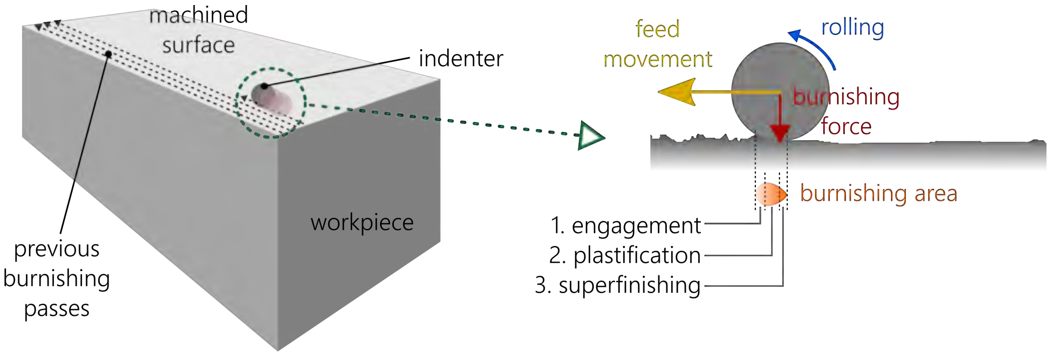

Figure 2.1. Schematic representation of the ball burnishing process.

Conceptually, the plastification process is gradual. The instantaneous contact area between the indenter and the surface can be described as a tear-shaped region, covering the wide range of strain states, starting from the elastic deformation in the engagement zone, until the superfinishing zone at the points with longer contact with the indenter. This mechanism provides the general roughness improvement along the burnishing direction [79]. Surface roughness is a fundamental feature of the surface integrity of the part, not solely for outer aspect matters, but also for its general performance. Poor surface finish disables geometric tolerances, and it affects wear resistance, fatigue life, and load-carrying capacity.

On the other hand, as the instantaneous application of the burnishing force is local, the topological changes are hardly larger than 10 $\mu\mathrm{m}$, so that general geometry of the part is not changed. Therefore, form errors and the general shape of the part are not significantly rectified through burnishing. This makes the process suitable for the finishing of parts manufactured until their final dimensions, and is especially interesting in manufacturing contexts where high precision results are required. It is the case, for instance, of mould manufacturing, filleted bearing components, or curved surfaces.

Burnishing can be found in the bibliography after diverse designations. Practically, the main difference among the different processes based on different tools is the objective that justifies the execution of the process. Deep Rolling (DR) is used to refer to the execution of ball or roller burnishing with the aim of inducing high compressive residual stresses and increasing cold work on the part surface. When the sought objective is decreasing the surface roughness of the objective part, the process is generally denoted as Low Plasticity Burnishing (LPB) [2].

From a systemic point of view, burnishing can be defined as a set of interrelated resources, whose function is to perform the finishing of an objective workpiece, and whose combination define a singular burnishing system. Under this perspective, Figure 2.2 shows a fishbone diagram of the different aspects which define burnishing systems. Items belonging to the tooling system categories allow to establish a certain classification of different burnishing operations. That is, by varying the shape of the indenter, the force regulation method, or the mechanical composition of a tool to be attached to different machines, diverse burnishing operations are feasible.

Burnishing tooling is therefore highly important when the implementation of a specific burnishing operation must be carried out. It plays a fundamental role in the definition of the burnishing system, as it enables the application of the process on one or several specific machines, and allows to regulate and control most of the burnishing parameters governing the process, and that determine the burnishing results. The next subsections present different burnishing tooling configurations, as a first step to decide the general features of the design of the VABB tool.

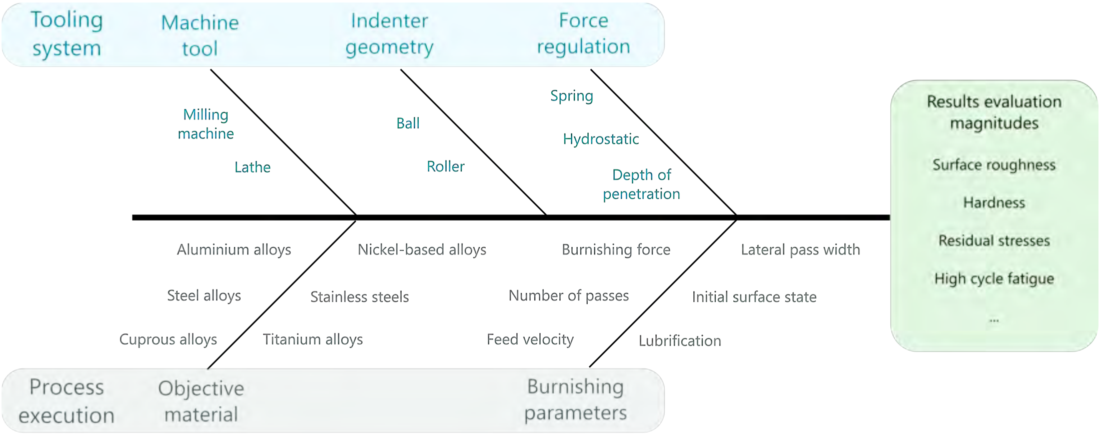

Figure 2.2. Items and descriptors comprising the burnishing manufacturing system.

2.1.1 An overview of burnishing tooling

The scientific bibliography shows a great variety of burnishing tool designs. In general, a burnishing tool must be conceived to fulfil the following requirements:

- It must be attachable to a specific machine tool where the process must be developed.
- It must guarantee mechanical engagement between the indenter and the material, allowing the free movement of the former while maintaining its mechanical integrity.
- It must bring into play the whole of the desired burnishing parameters, especially preload, while ensuring accessibility to the target surface.

Basic tools utilised originally in general applications of the burnishing technique were applied on simple geometries such as bores and shafts, hydraulic cylinders, pistons for hydraulic systems, or fillets. Classical burnishing tool–workpiece configurations can be consulted at Figure 2.3. The lack of automation and handling limitations presented by conventional machines made difficult to finish more complex parts. Later, the generalisation of NC machines in manufacturing workshops, and the emergence of more simple fixation systems, enabled new designs. The technique was subsequently embraced for more complex geometries such as the finishing of free-form parts (e.g. moulds), and contributed to its expansion [77, 132].

The geometry of the indenter is one of the main features defining a burnishing

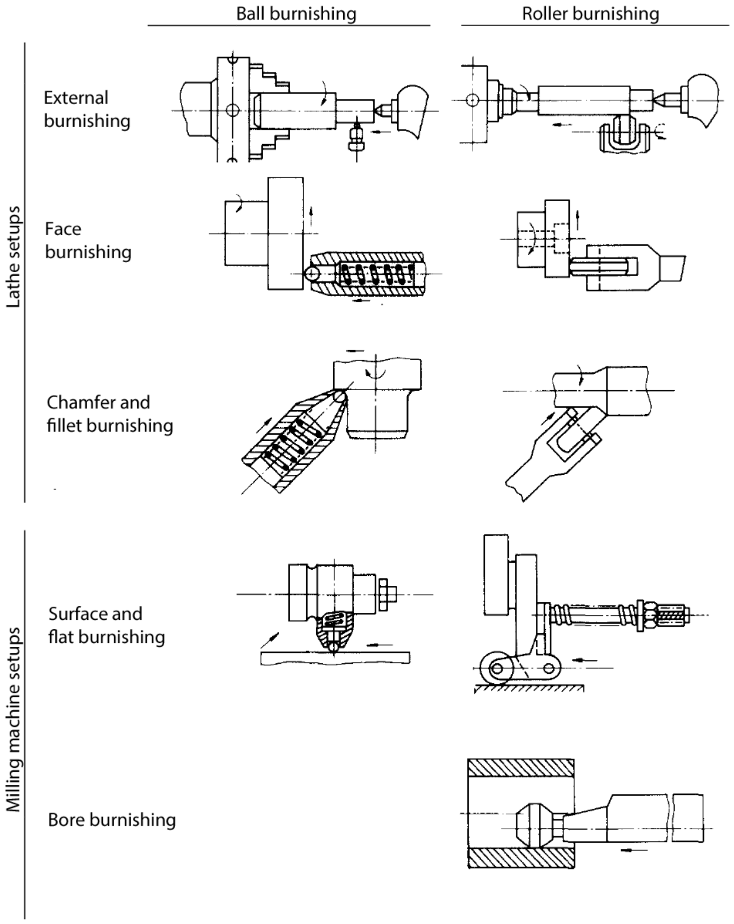

Figure 2.3. Classical burnishing tool configurations on lathe and milling machines. After Murthy, 1981 [103]

tool. Roller tools have been classically more widespread, for its higher simplicity in terms of preparatory activities and force adjustment [32, 33, 90, 92]. Regarding the roller geometry, dimensions and profiles are also diverse. Rollers with higher cylindrical land would allow the execution of the process by selecting higher feeds, as the contact surface between the tool and the part is higher. However, rollers lack of the versatility that balls offer to burnish, since they are inefficient to treat complex surfaces, extensively found in the advanced manufacturing industry.

However, roller burnishing tools are also known for their lower effectiveness in hardness improvement, and require higher forces to obtain the same improvements as with sphere shape indenters. Consequently, ball burnishing can be presented as a more advantageous process in terms of absolute results. Comparative research has proved that ball burnishing is able to achieve significantly lower surface roughness and higher hardness with lower forces in materials such as AISI 1335 steel [50], and non-ferrous alloys [53]. For that reason, the tool that shall be designed in this dissertation shall be based on a ball-burnishing configuration.

2.1.1.1 Special burnishing tool configurations

The development of tools with specific configurations is one of the innovative approaches to burnishing development (Figure 2.4). Multi-roller tools can be found at several bibliographical references. Thamizhmanii *et al.* (2009) [145] tested a frontal multiroller tool on TA6V speciments, and Tadic *et al.* (2013) [141] designed and successfully tested a multiroller tool on aluminium parts. Multi-ball tools can also be found at Gharbi *et al.* (2010) [41] and Tadic *et al.* (2016) [140]. In general, multi-indenter tools show a remarkable stability of the process due to higher surface contact of the burnishing indenters and the workpiece, although the range of objective geometries is not so wide.

More complex configurations have been also conceived and prototyped. El–Axir & Ibrahim (2005) [28] designed and mounted a multi-ball tool embedded in a centre rest, being able to burnish on a lathe through a steadier regime, and showing better results in terms on final roundness, compared to conventional burnishing. Okada *et al.* (2015) [107] designed a roller tool able to adapt at will the burnishing angle, and after testing it on ASTM 2017 aluminium and ASTM 1055 carbon steel specimens, concluded that burnishing at a 45 degrees angle is the optimum process in terms of surface roughness. Integrating cutting tools and finishing burnishing tools on one single piece has also been explored by Segawa *et al.* [127].

2.1.2 General description of ball burnishing parameters

In manufacturing engineering, controlling the parameters of any process is necessary to comply with design specifications, guarantee the repeatability of results, and their reproducibility from a small-scale research context to a real manufacturing workshop. Burnishing is no exception, as proves the preponderance of bibliographical references which focus on testing different levels of burnishing parameters on a great variety of objective materials. This subsection explains the different parameters that govern the

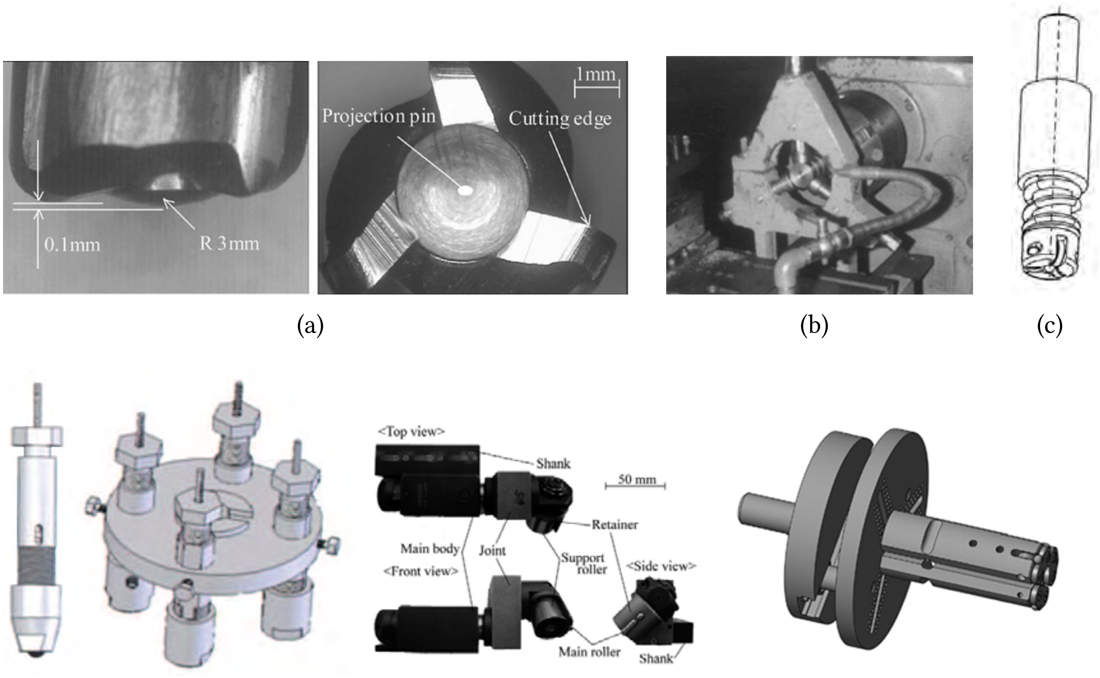

(a) (b) (c)

(d) (e) (f)

Figure 2.4. Special burnishing tool configurations. **a**. Milling & burnishing tool [127] **b**. Center rest multi-ball tool [28] **c**. Multi-roller tool [141] **d**. Multi-ball tool [41] **e**. Adjustable roller tool [107] **f**. Multi–ball tool [140]

operation.

2.1.2.1 Plastic strain parameters: burnishing force and number of passes

The most influential parameter on ball burnishing results is the burnishing force, that is, the normal force transmitted by the burnishing tool to the workpiece surface in order to deform plastically its microtopology. The specific pressure applied on the workpiece to achieve that plastic deformation is the direct result of this force, and must exceed the yield point of the material to succeed in achieving good results. It can be therefore considered as the essential physical driver of plastic strain.

The constructive configuration of the burnishing tool defines the way through which the force is controlled and transmitted to the workpiece. In other words, according to the technical solution adopted to apply the force on the surface through the ball on the surface, the force is controlled differently. From this point of view, mainly three kind of tool can be distinguished, as can be observed in Figure 2.5. These three solutions are explained below.

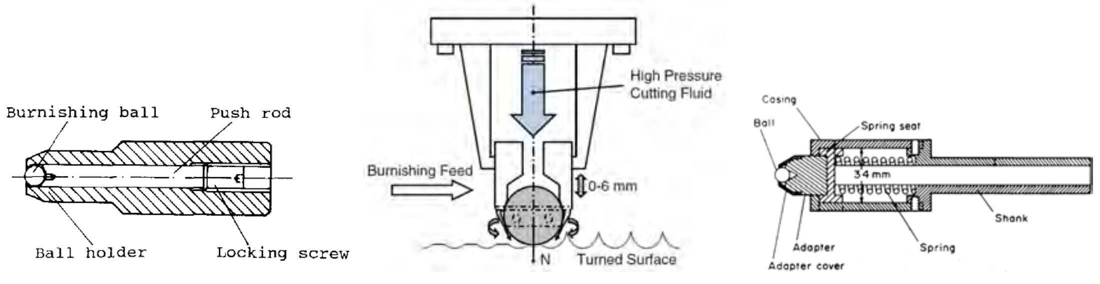

(a) (b) (c)

Figure 2.5. Force regulation systems in classical burnishing tools. **a**. Depth-of-penetration tool [80]. **b**. Hydrostatic tool [119]. **c**. Spring-regulated tool [52]

Depth of penetration This solution appears to be the original force regulation method, as is found in all the oldest references (Figure 2.5.a). The tools based on this force transmission principle are ended by a spherical shape in which the ball is housed, allowing its free rolling. In order to regulate the force, the tool tip is pressed onto the target surface. The force is exerted by screwing the supporting rod in which the burnishing ball is embedded. The linear length along which the screw is tightened along the supporting rod is called depth of penetration h_p . The burnishing force or preload, F_p, derived from this mechanism can be therefore deduced from the approximate solution of slipping of a rigid sphere over a plastic semi-plane, as shown in Eq. 2.1 [103].

$$F_p = \frac{\pi}{4} h_p \, HV \, R \tag{2.1}$$

where HV is the Vickers hardness of the material,and R is the indenter radius.

The fact that the preload is calculated through this indirect method does not allow its accurate regulation. Therefore, the actual values of the burnishing force applied during the burnishing process can only be known if the machine is equipped with a force measuring device. Consequently, this solution is advisable to burnish complicated geometries, which do not allow the application of other pressing systems [29].

Hydrostatic pressure These kind of tools often use a ceramic or chrome-steel ball embedded inside a support piece at the tip, which is connected to an inner channel which traverses the tool (Figure 2.5.b). The tool is fed by an auxiliary pump of the burnishing machine, which propels lubricant fluid through that channel. The fluid reaches the ball bed, and supports it due to the excerpted hydrostatic pressure. The lubricant acts therefore as a hydrostatic bearing, allowing the ball to roll freely. The burnishing pressure is regulated by adjusting the hydrostatic pressure of the lubricant, as a result of simple equilibrium of forces along the longitudinal axis of the tool. Due to the constructive solution, these tools cannot be applied on surfaces showing a degree higher than ±28°. Celaya *et al.* [16] estimated the burnishing force, P_b, by deducing it from the pressure delivered by the pump (Eq. 2.2), considering a 89% efficiency according to the results shown by a FEM.

$$P_b = 0.89 \frac{\pi}{4} D^2 \, p_h \tag{2.2}$$

where D is the ball diameter, and p_h is the hydrostatic pressure delivered by the pump.

Calibrated spring A linear spring is lodged inside this kind of tools, and accounts for the normal force regulation (Figure 2.5.c). After the ball contacts the target surface, the burnishing force increases as the spring is progressively compressed. The total axial force is ruled by Hooke's law (Eq. 2.3). The tool can be calibrated by knowing the stiffness of the spring, so that the burnishing force can be easily controlled by managing the z coordinate with the NC programme managing the burnishing operation, provided that the origin offset on the workpiece surface has been accurately determined. For that reason, the force regulated in this kind of tools can specifically be referred to as preload, F_p. Through these tools, the force regulation can be easily integrated in the process inside the NC code.

$$F_p = k \, \mathit{\Delta} z \tag{2.3}$$

where F_p is the axial preload transmitted by the spring, k is the elastic constant of the tool due to the spring, $\mathit{\Delta} z$ is the compressed length of the spring, being the result of the total compression executed by the NC and the microvariation due to the translation of the ball along the roughness profile.

Despite the capability of controlling the nominal force applied during the burnishing process, its actual value varies during its execution. This is mainly because of the friction present during the feed movement of the tool over the surface, as well as sufficiently prominent surface irregularities that oppose that movement. The consequence is that tangential components of the burnishing force appear during the execution of the process, diminishing the strain effect, as observed by Lye & Leong (1990) [91]. Figure 2.6 shows both tangential and normal burnishing forces, exemplifying the described effect.

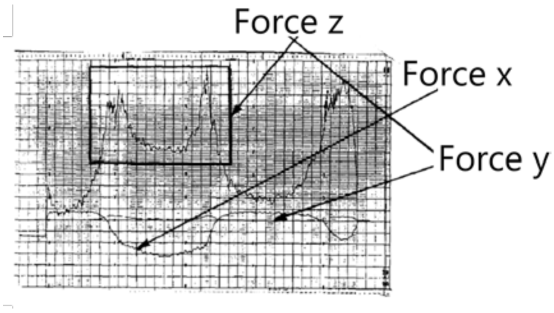

Figure 2.6. Experimental measure of force unevenness during a burnishing process. After Lye & Leong, 1990 [91].

The burnishing force is not the only parameter defining the degree of plastic strain after burnishing. It is also dependent on the number of passes, which quantifies the number of overlay passes performed over the burnished surface. This parameter is also a productivity parameter, as more passes require more processing time, but its higher relevance on the strain is undeniable.

Generally, the increase of the burnishing force and number of passes derive in a higher level of plastic deformation, so that both parameters are equivalent in terms of burnishing effectiveness. Both of them must be chosen correctly, as excessive cold hardening through plastic strain can also derive in detrimental results, as shall be further analysed in following sections of this chapter.

2.1.2.2 Productivity parameters: feed and lateral pass width

Productivity parameters affect the total time required to burnish a surface. References dealing with burnishing from a productivity point of view are scarce. It can be justified by the fact that these productivity parameters have not proved to positively affect the potential enhancement of burnishing as a finishing process.

The feed parameter refers to the linear speed at which the tool is displaced, which is usually programmed inside the NC code implemented on the machine tool where the process is applied. A study by Rodríguez *et al.* (2012) [119] proved that no influence is observed in terms of surface roughness, but the lack of further evidence leads to think that a certain influence could eventually be detected.

The second productivity parameter is the lateral pass width, that is, the offset length between two adjacent burnishing passes. Most authors do not pay attention to fix a specific value for this parameter, and take conservative values to guarantee the affectation of the whole surface. Obviously, although this is a compromise solution to achieve uniform results, the use of a too small lateral pass width increases the number of passes required to treat a surface, thus increasing burnishing time and harnessing the overall productivity.

In this regards, the works of Gómez-Gras *et al.* (2015) [44] concluded that to minimise burnishing time without harnessing the burnishing results, a standard lateral pass width could be established in function of the burnishing force, the type of burnishing which is applied (vibration-assisted or not), and the objective material. The latter is introduced in the model through its self-hardening coefficient. In effect, materials experiencing high strain hardening tend to form pile-ups at the limits of the plastically deformed area [59]. They conclude that the optimal lateral pass width should be included inside an interval $[0.5\,l, l]$, being l the width of a burnishing line performed by a certain set of parameters. The minimum limit of the interval was established by considering that smaller values would lead to redundant passes during the burnishing operation, with the consequent detrimental effect on productivity. On the other hand, the maximum boundary was established as a means of limiting the offset between passes, which would leave non-deformed material on the surface, diminishing the burnishing effects. Consequently, these values can be taken into account as a means of optimising the burnishing time without causing any harm on the surface finishing.

2.2 Experimental results on surface integrity after ball burnishing

The effect of ball burnishing affects exclusively surface and near-surface layers of a workpiece, as the bulk material is not modified by it. Consequently, burnishing results should be studied and quantified from a comprehensive scope by considering different surface parameters. In this regard, the concept of surface integrity can be presented as an adequate contextual reference to characterise the effects of the VABB process.

Surfaces confer unique properties to engineering parts besides their outward appearance. The realisation that minor and catastrophic failures of engineering parts cannot always be explained by detrimental properties of the bulk material, but they are the consequence of the inadequacy of the surface integrity of the part itself, was late embraced by engineers. Until this statement was acknowledged, numerous mechanical failures were being erroneously identified as uncontrollable, and consequently unmanaged. For instance, fatigue failure identified and characterised experimentally by Wöhler in the end of the 19th century, was not modelled until Irwin succeeded in the 50's to relate it to surface roughness by means of a stress concentration factor, K_I, as follows:

$$K_I = \sigma_{nom} Y \sqrt{\pi a} \tag{2.4}$$

where σ_{nom} is the maximum stress, Y is a geometrical factor, and a is the crack's length.

As Y can be linked to surface roughness, Irwin acknowledged in publishing this model the link between surface integrity and fatigue failure. The same as fatigue, today, we know that, other phenomena such as corrosion, contact mechanics or wear depend upon the surface state of the part, and not on the bulk material. Surface engineering was born as an extended branch of surface science, to characterise the relation between the design of surfaces and their functionality and cost effectiveness [20]. The ASTM Handbook defines it as the treatment of surface and near-surface regions of a material to provide unique properties that enable it to perform functions that are distinct from the ones delivered by the bulk material [36]. In this context, surface integrity can be described as the group of parameters that describe the comprehensive state of a finished surface. This definition exhibits that surface integrity can be described as an inherent consequence of materials processing techniques and parameters, as has been proved by numerous authors [35, 110, 155, 156].

Following the same principle, ball burnishing has been treated in the bibliography as an effective method to modify surface integrity. Historical ball burnishing references deal mainly with steel, aluminium and cuprous alloys. This is logical if one thinks of the kind of applications for which burnishing was originally applied –the finishing of shafts, moulds, dies and tubes. Table 2.1 summarises the most relevant references related to ball burnishing of these alloys.

Table 2.1. Ball burnishing references on steel, aluminium and cuprous alloys. *Light grey*: milling-machine tools. *White*: lathe tools.

Reference	Material	Force
Loh *et al.*, 1989,1990 [80, 82]	AISI 1045	d.o.p.
Loh *et al.*, 1989,1990,1991 [81, 83, 84]	AISI 1045	d.o.p.
Morimoto *et al.*, 1991 [102]	JIS–S38C	d.o.p.
Loh *et al.*, 1993 [85, 86]	ASSAB XW–5	d.o.p.
Hassan *et al.*, 1996 [54, 55]	pure Al & brass	spring
Lee & Loh, 1996 [77]	AISI P20	d.o.p.
Hassan, 1997 [53]	pure Al & AS 1573 brass	spring
Hassan, 1998 [52]	undefined brass	spring
Hassan, 1999 [56]	undefined brass	spring
Hassan *et al.*, 2000 [57]	brass & Al-Cu alloy	spring
Hassan *et al.*, 2000 [58]	pure Al & AS 1573 brass	spring
Némat & Lyons, 2000 [104]	ASTM A113 & AA6463-E	spring
Shiou & Chen, 2003 [132]	PDS5 mould steel	spring
Prevéy *et al.*, 2001 [112]	AA7075-T6	H
Bouzid *et al.*, 2004 [11]	AISI 1042	spring
El–Axir *et al.*, 2005 [28]	undefined steel	d.o.p.
Luca *et al.*, 2005 [89]	undefined steel	H
Basak *et al.*, 2007 [6]	AA7075-T6 & H62 brass	H
Hamadache *et al.*, 2006 [50]	Rb40 steel	spring
Rao *et al.*, 2008 [115]	undefined steel	d.o.p.
Seemikieri *et al.*, 2008 [126]	AISI 1045	H
Shiou & Cheng, 2008 [131]	NAK80 mould steel	d.o.p.
Gharbi *et al.*, 2008 [41]	AISI 1010	spring
El–Axir *et al.*, 2008 [29]	AW 2014	d.o.p.
El–Axir *et al.*, 2008 [30]	AW 2014	d.o.p.
Sagbas, 2008 [121]	AA 7178	spring
Majzoobi *et al.*, 2009 [92]	AA 7075-T6	spring
El–Taweel *et al.*, 2009	brass	spring
Shiou & Chuang, 2010 [133]	PDS5 mould steel	spring
Ugur, 2010 [154]	AA 7075	mill
L. de la Calle *et al.*, 2011 [88]	AISI 1045 & DIN 1.2379	H
Travieso-Rodriguez *et al.*, 2011 [149]	A92017 & G10380	H
Grzesik & Zak, 2012 [48]	EN 41Cr4	spring
Rodriguez *et al.*, 2012 [48]	41Cr4 steel	spring
Aviles *et al.*, 2015 [4]	AISI 1045	H
Kuznetsov *et al.*, 2015 [75]	EN 20Cr4 & EN X20Cr13	H
Tadic *et al.*, 2016 [140]	AW6082	d.o.p.
Amdouni *et al.*, 2017 [3]	AW2017-T4	d.o.p.

d.o.p.: depth of penetration; H: hydrostatic tool

The visual inspection of that table leads to the conclusion that the majority of ball burnishing references have focused on lathe burnishing. Although a certain correlation between lathe and milling burnishing can be found –for instance, lateral pass width in mill burnishing is the feed in lathe burnishing–, the kinematics of both processes are quite different, and should be treated as two independent processes. The tool to be designed in this thesis shall be used in a milling machine. Therefore, this state of the art shall focus mainly on this type of setup conditions, whereas lathe burnishing is referred only in specific cases where it is utterly necessary. Lathe references are also omitted if possible due to the limitations of lathe burnishing to treat complex surface geometries, such as warped surfaces, unfitted for the potential applications of the system which is being considered in this dissertation.

On the other hand, Table 2.2 gathers those references that focus on the study of ball burnishing on stainless steel, titanium and nickel-based alloys. These are conspicuously scarcer than the ones represented above, for two main reasons. Firstly, the need of developing special finishing processes for advanced materials in the industry is a relatively recent topic. Secondly, these materials are applied in the manufacturing of special parts, expected to function in highly demanding environments. Therefore, most of these studies tackle with the comparison of ball burnishing with other finishing processes that are already validated at an industrial level, such as shot peening, which exceeds the object of this dissertation.

At sight of the previous tables, it can be concluded that spring-based tools have been scarcely studied in the bibliography, and that there is an evident lack of information about ball burnishing of titanium alloys. Along the next subsections, results are classified in function of geometrical, mechanical and metallurgical parameters after ball burnishing. All materials are included in the analysis.

2.2.1 Geometrical parameters: surface roughness and texture

The presence of irregularities on a surface is the inherent result of the transformation process to which any material is subjected after a manufacturing operation. The DIN 4760 standard differentiates between macrogeometric –high scale deviations and waviness– and microgeometric deviations –cracks, grooves, texture or roughness profiles– on a surface. Engineering applications require the limitation of macrogeometric topological irregularities to guarantee, for example, the interchangeability of parts and the assembly of different components. On the other hand, many authors

Table 2.2. Ball burnishing references on stainless steel, titanium and nickel alloys. *Light grey*: milling-machine tools. *White*: lathe tools.

Reference	Material	Force
Stainless steel		
Lee *et al.*, 1993 [78]	316L	d.o.p.
Prevéy *et al.*, 2003 [114]	17-4PH	H
Jayaraman *et al.*, 2003 [65]	17-4PH	H
Zhang *et al.*, 2014 [161]	17-4PH	H
Chomienne *et al.*, 2016 [18]	15-5PH	H
Titanium alloys		
Schuh *et al.*, 2007 [125]	Ti-6Al-7Nb	H
Tsuji *et al.*, 2008 [152]	Ti-6Al-4V	H
Revankar *et al.*, 2014 [117, 118]	Ti-6Al-4V	H
Nickel-based alloys		
López de la Calle *et al.*, 2007 [87]	Inconel 718	H
Klocke *et al.*, 2009 [70]	Inconel 718	H
Sequera *et al.*, 2014 [128]	Inconel 718	H
Fu *et al.*, 2014 [39]	Nitinol	H

d.o.p.: depth of penetration; H: hydrostatic tool

have proved the impact of microgeometric deviations on the mechanical behaviour of parts [69]. This includes fatigue life [106] or tribological mechanisms [139].

Controlling surface geometry means, in practice, quantifying its features through different descriptors. Texture and roughness measurement methods are based on the idea of modelling the surface as a mathematical function formed by height points, and the calculation of parameters based on this function to make that data profitable for decision making. One of the original methods based on this idea was proposed by Abbott & Firestone (1933) [1]. They proposed transforming the heights of a surface into a bearing-area curve representing its as an accumulated function. On that representation, three parameters which described the bearing area and lubricant retention capabilities of the surface were calculated.

The evolution of height registration equipments to devices based on high-sensitivity diamond styli, supposed a considerable evolution in texture assessment. In the second half of the 20th century, profilometer diamond tips became actuated by a motor, through which they could automatically traverse the target surface along a line that shall represent the whole surface. This leap forward allowed the generalisation of an automatic surface characterisation method, and new standards defining two-dimensional descriptors of the surface were published. The profile method defined in ISO 4287 is the most generalised one. It establishes a methodology to filter and arranged the acquired height dataset with respect to a mean line obtained my least squares deviation. On that profile, different two-dimensional R parameters can be calculated to define the surface features based on the registered dataset [146]. These parameters can also be associated to specific processes [105], and are a good indicator to trace the manufacturing history of a surface [162]. The literature shows extensive work which interpret the roughness results through the R parameter set [130, 138], and the interrelation among some of their parameters as skewness or kurtosis [46,99].

Despite the diversity of parameters in that R set, the average surface roughness, R_a, is the most extended one to represent surface texture, as it offers an average indicator of the overall surface topological state. Originally, it could be easily calculated by primitive profilometer devices with low computing capacity. It is established in the ISO 1302 as the reference value to represent roughness in technical drawings. As it happens, R_a has been the most extensively chosen parameter to evaluate ball burnishing results, as show, for instance, the works of Shiou *et al.* on different mould steels [131–133]. They concluded that the force and the ball diameter had a high influence on burnishing results. Other researchers, such as Loh *et al.* (1989) [80], have evaluated the ball burnishing results on a AISI 1045 alloy in terms of R_t. In all cases, the inverse proportionality between burnishing force and roughness parameters is confirmed.

Adopting a different scope, the influence of the target surface shape on the topological effects of ball burnishing have also been studied. Travieso-Rodríguez *et al.* (2011) [149] compared the influence of different curvature radius on concave and convex parts made of AISI 1038 and EN AW 2017 aluminium. Both the R_a and R_t improvement along and perpendicular to the burnishing direction were higher as the radius of curvature increased. Curved surfaces have also been burnished by López de la Calle et al (2011) [88]. A 5-axis machine was used, by following two different strategies: continuous burnishing and patch strategy. Both of them lead to R_a decrease, although the continuous proved to be more effective while being less productive due to the limited feed of the rotary axes of the machine.

Studies have also proved that there is a threshold preload level for which roughness is actually harmed. Klocke *et al.* (2009) [70] studied the dependence of R_a as a function of the preload and the ball diameter, on Inconel 718 specimens (Figures 2.7.a and 2.7.b). In that case, increasing the burnishing pressure from 150 bar to 250 bar

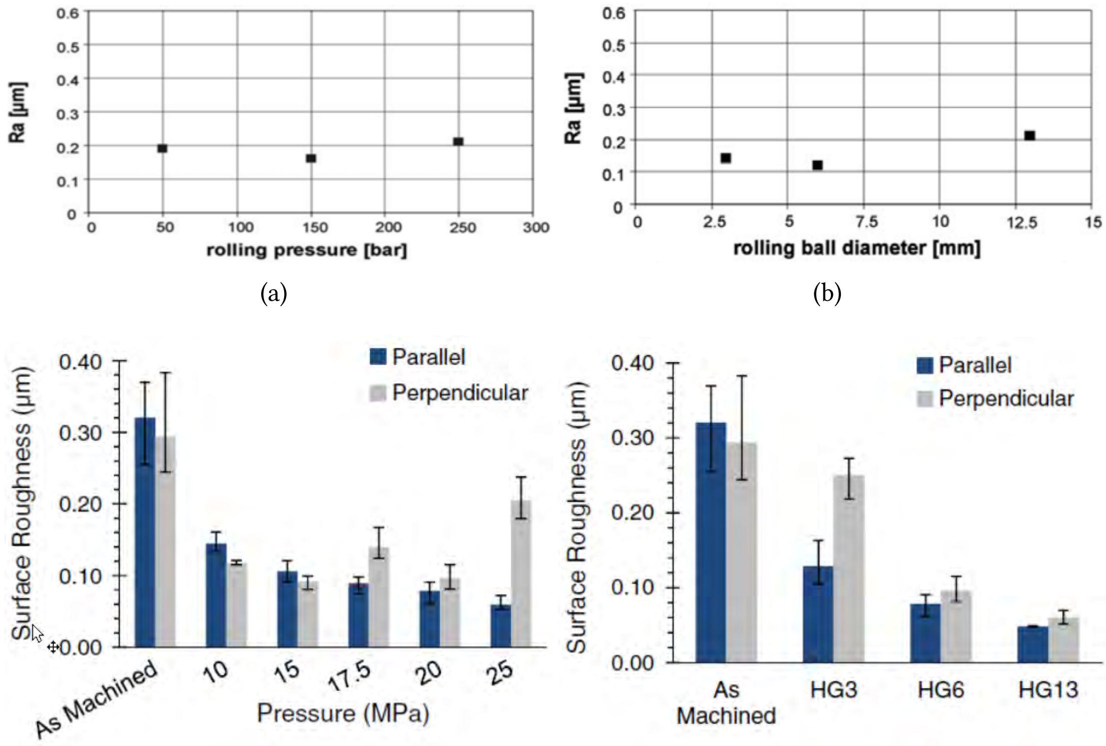

(a) (b)

(c) (d)

Figure 2.7. R_a results of burnished INCONEL 718 surfaces. **a**. Influence of burnishing pressure [70]. **b**. Influence of ball diameter [70]. **c**. Influence of burnishing pressure [128]. **d**. Influence of ball diameter [128]

.

proved to be detrimental to surface roughness. Furthermore, the surface exhibited roughness increase when the ball diameter was increased from 6 to 13 mm.

Therefore, the burnishing force and the diameter of the ball are limited by threshold values that should not be surpassed to prevent harmful effects on the surface. Sequera (2014) [128] ratified the same results for the burnishing pressure, although did not find a detrimental influence of the ball diameter (Figures 2.7.c and 2.7.d).

In all the evaluated cases, the topological assessment of ball burnishing is based on the evaluation of a limited number of parameters calculated on linear profiles, especially R_a and R_t. However, the limitation of these 2D parameters to represent a 3D surface must not be neglected, as surfaces actually interact in the three directions of the space [24]. Although nowadays the calculation potential of computers and equipment are highly advanced, the surface topology assessment methods are the heritage of old-fashioned two-dimensional height analysis marked by low computation capability which is no longer limiting factor in presently available systems. In fact, many authors have highlighted that the only reason why R_a parameter exists is because of the original computing limitations of roughness measurement devices [116], as it lacks of statistical meaning, and is insensitive to reflect changes in the shape of the profile [130]. As an alternative, Sherrington *et al.* (1987) proposed R_q as an alternative to R_a. While still being a two-dimensional parameter, its statistical meaning as the root mean square of the height profile, and its capability to describe any possible redistribution of material from one side of the mean line to the other. It is remarkable that no reference has been found considering other two-dimensional parameters, such as W or P, to analyse burnishing results. Nevertheless, could they provide further information about the effects of the process?

All these reasons lead to conclude that the parameters that have been traditionally used to describe surface topography can be upgraded to obtain further information about ball burnished surfaces. A new methodology shall be proposed to tackle with this objective in the following chapters.

2.2.2 Metallurgical parameters: hardness and metallography

The metallurgical state of a surface can be described by numerous factors, such as phase change after a surface treatment, or the presence of a phase gradient towards deeper layers. These parameters are of high importance to define surface integrity, as they are the result of the combination of mechanical or thermal mechanisms. As ball burnishing is not a thermal process, microstructure change is not due to occur. Consequently, other metallurgical factors must be more adequate to describe the process effects. That is the reason why the measurement of strain hardening is relevant to study the metallurgical state of the material, as it is the direct consequence of the plastic deformation caused by the ball.

Strain hardening is the phenomenon whereby ductile metals become harder and stronger as they are plastically deformed, whereas their ductility falls [15]. A practical way to define the degree of plastic deformation is by the calculation of the percent cold work experienced by the solid:

$$\%CW = \frac{A_0 - A_d}{A_0} \times 100 \tag{2.5}$$

where A_0 is the initial area of the cross section and A_d is the same section after deformation.

The direct consequences of strain hardening on a material is the increase of its yield and tensile strengths, caused by dislocation propagation due to stress. That multiplication of lattice defects results in an increase of resistance to further dislocation motion, which is subsequently revealed at a macro scale as an increase of hardness. Therefore, the quantification of the hardness can describe the microstructural surface integrity of burnished surfaces. For instance, López de la Calle *et al.* (2007) [87] determined the depth of affectation of burnishing in the order of 10 $\mu\mathrm{m}$, in both Inconel 718 and AISI P20 preheated steel alloys. The resulting hardness increased as more burnishing pressure was applied during the process. In all cases, the hardness obtained after machining was improved (Figure 2.8). The direct relationship between burnishing force and surface hardness had already been reported by Loh *et al.* [81,82], from experiments executed on AISI 1045 specimens.

Albeit the positive effect of the burnishing force on the metallurgical integrity of the burnished surface, if the force is too high, severe strain hardening may occur due to overplastification. This was reported by Kuznetsov *et al.* (2015) [75], who detected evident harm on the surface of a 20Cr4 steel alloy due to shear instability during burnishing as the burnishing force was increased (Figure 2.9). The extreme effect of this excessive force is the flaking of the surface material, which leads to a clear surface integrity degradation and unsuitability of the process.

Rao *et al.* (2008) [115] observed that this flaking phenomena due to excessive force has also detrimental effects on the surface hardness, and proposes the application of lubricants to decrease the shear stress that appears during burnishing due to friction dynamics.

Results also show that the maximum hardness improvement is not registered directly on the surface. Although their work is based on lathe burnishing, it is worth mentioning the results of Chomienne *et al.* (2016) [18] on 15-5PH stainless steel bars. Figure 2.10 shows not only a hardness improvement at the surface, but a substantial increase is conspicuous until a 0.3-mm depth. They also find that no recrystallisation

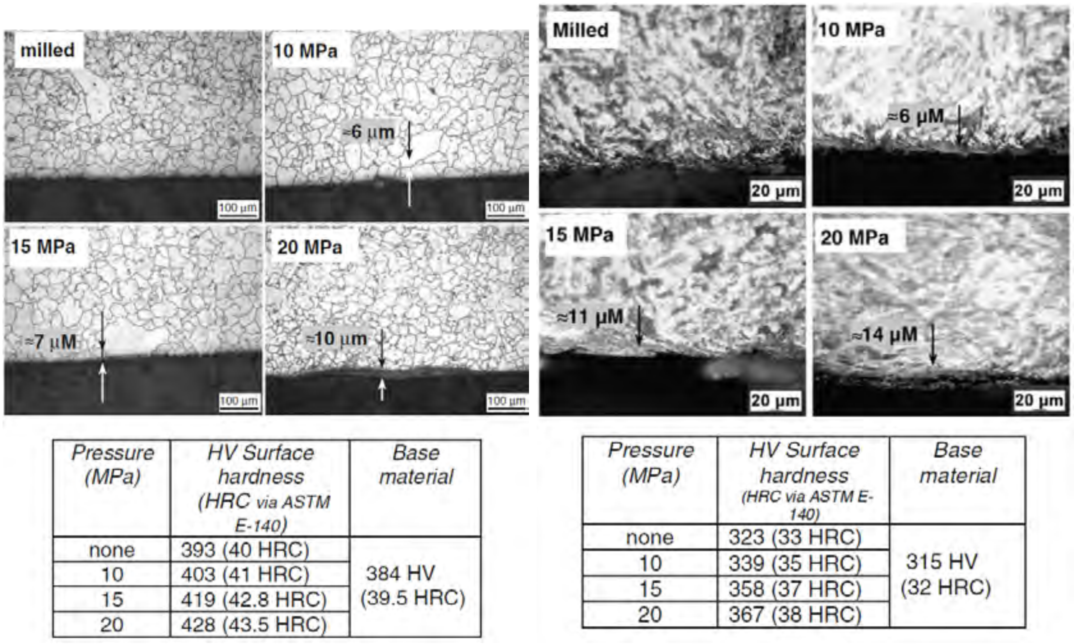

Pressure (MPa)	HV Surface hardness (HRC via ASTM E-140)	Base material
none	393 (40 HRC)	384 HV (39.5 HRC)
10	403 (41 HRC)	
15	419 (42.8 HRC)	
20	428 (43.5 HRC)	

(a)

Pressure (MPa)	HV Surface hardness (HRC via ASTM E-140)	Base material
none	323 (33 HRC)	315 HV (32 HRC)
10	339 (35 HRC)	
15	358 (37 HRC)	
20	367 (38 HRC)	

(b)

Figure 2.8. SEM images of the surface microstructure of burnished specimens at different pressure levels, and surface Vickers hardness. After López de la Calle *et al.*, 2007 [87]. **a**. Inconel 718. **b**. AISI P20 pre-heated steel

takes place at the surface, probably because not enough thermomechanical energy is added in the system by burnishing.

Ball burnishing has proved its positive effects for the improvement of corrosion resistance, not only on industrial parts [108], but also on biocompatible materials such as magnesium alloys used for implants, where it proves to be a very attractive alternative to coatings or chemical alloys [123, 153].

2.2.3 Mechanical parameters: residual stress

Residual stress is what remains in a material volume which is stationary and at equilibrium with its surroundings [158]. The reason why this internal stress state appears, is to balance the various misfits occurring between different regions of the body itself. They can have different physical origins, such as thermal gradients or mechanical disparities. The length or scale over which the equilibrium is achieved is usually taken

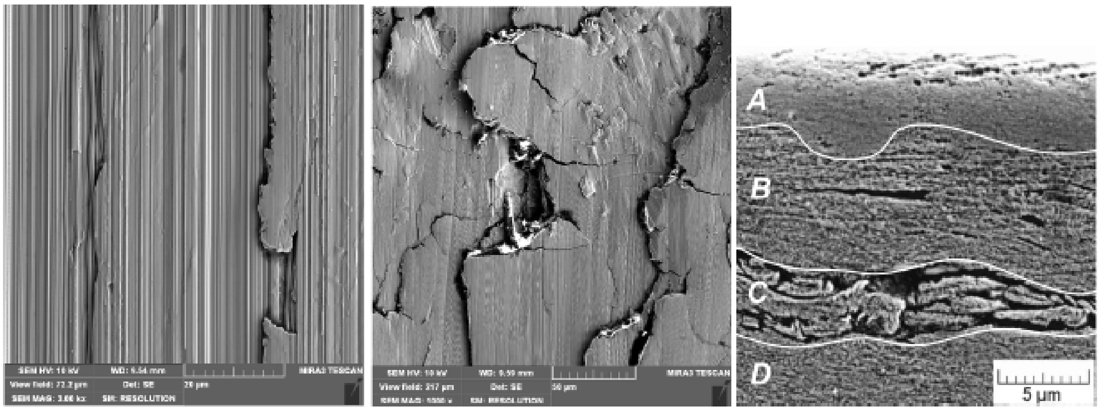

(a) (b) (c)

Figure 2.9. SEM images of 20Cr4 steel specimens. **a**. 200-N normal force. **b**. 400-N normal force. **c**. Subsurface shear instability caused by excessive plastic deformation. After Kuznetsov *et al.*, 2015 [75]

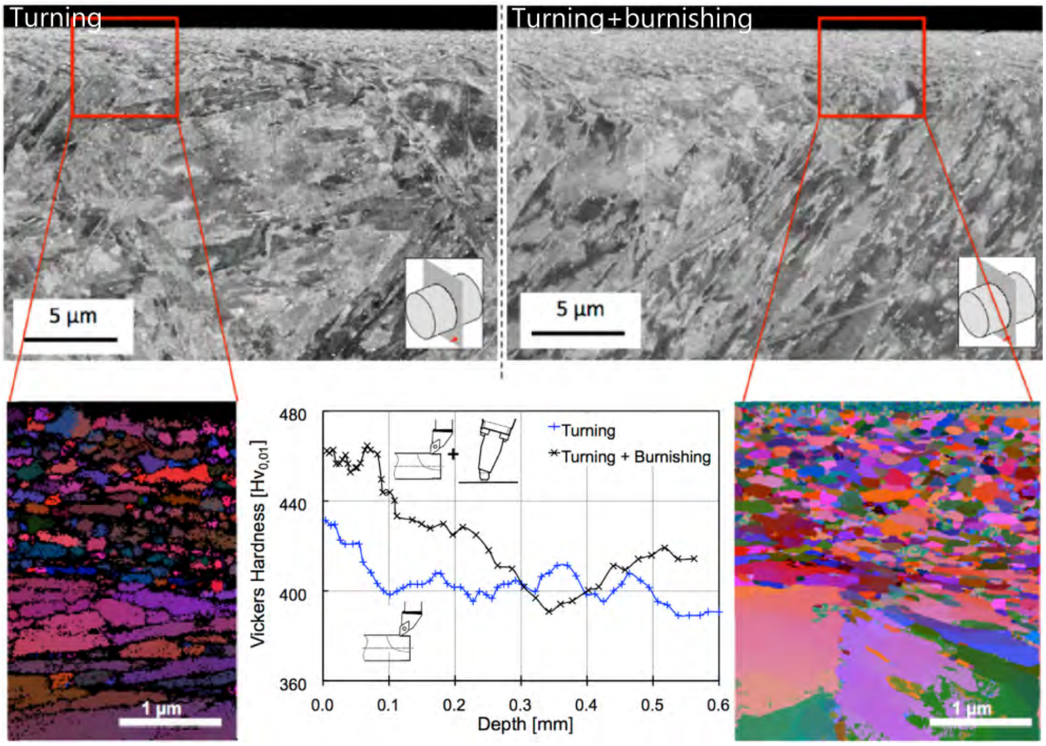

Figure 2.10. Microstructure and hardness of turned (v_c = 150 m/min, f = 0.18 mm/rev, a_p = 0.6 mm) and turned+burnished (250 N, n_b = 1 pass, 6-mm diameter ball) 15-5PH specimens. After Chomienne *et al.*, 2016 [18].

as a reference to classify the different types of residual stress (Figure 2.11). Based on that classification, residual stress can be typified as follows:

- **Type I** or macrostresses vary continuously over large distance range, $l_{0,I}$, originated by non-uniform plastic deformation, or the presence of bending moments which subject fibres at one side of the neutral plane to compression.
- **Type II** act in an intergranular domain, and are usually present in materials which are formed by adjacent grains with heterogeneous mechanical and thermal properties. Therefore, tend to be slightly higher in multiphase materials where that heterogeneity is much more abrupt. That is what origins an internal stress state to set the achieve the equilibrium of the volume.
- **Type III** have an atomic scale, $l_{0,III}$, typically due to lack of coherency at grain interface and dislocation stress fields.

From the perspective of manufacturing technology, all types are of interest, depending on the research focus. For instance, types II and III are interesting for composite materials designers, to learn how stress is transmitted from the matrix to the reinforcement. For this dissertation, only type I shall be measured, as are the ones related to fatigue performance. In this sense, the effect of residual stress on the mechanical behaviour of components is various depending on the stress distribution.Normally, compressive residual stress are associated to positive effects, as they prevent the initiation and propagation of cracks, as stated Novovic *et al.* (2004) [106]. This observation can be extended to different materials. For instance, Koster & Field (1973) [71] found that the fatigue life shown by Ti-6Al-4V specimens was dependent on the residual stress provoked by the applied finishing operation, and not its surface roughness. El-Helieby *et al.* (1980) [31] reached the same conclusion in AISI 52100 specimens.

The measuring technique used to quantify the residual stress of parts must usually be chosen according to the type which is desired to be measured. For instance, material removal techniques such as hole drilling tend to remove macroscopic layers of material, neglecting therefore types II and III, whereas other such as neutron strain gauges are sensitive enough to detect those residual stress types [157].

The assessment of residual stress is clearly oriented in the bibliography as a means of understanding its influence on the fatigue behaviour of materials with regards to other finishing processes. Furthermore, results focusing on the influence of burnishing parameters on the residual stress of materials are mainly focused on lathe bur-

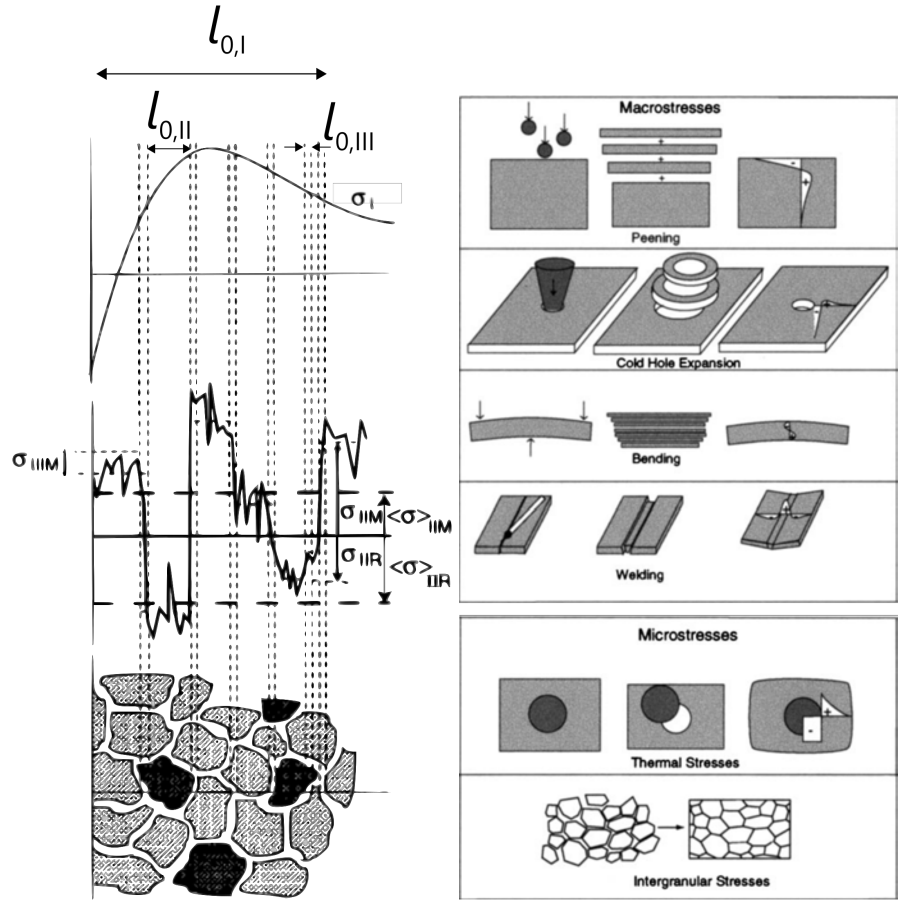

(a) (b)

Figure 2.11. **a**. Different residual stress scales $l_{0,I}$, $l_{0,II}$ and $l_{0,III}$. **b**. Examples of sources of macro and micro residual stress states. After Withers & Bhadeshia, 2001 [157]

nished surfaces, and do not tackle with the process exclusively. Below these lines, the residual stress results are partially presented, whereas the ones related to comparison with other finishing processes are included in the following subsection.

Avilés *et al.* (2013) [4] observed remarkable higher values of compressive residual stress on hourglass ASI 1045 specimens (Figure 2.12.a), in line with previous essays performed by Rodríguez *et al.* (2012) [119]. The same burnished specimens were then tested to rotative bending tests, concluding that ball burnishing increases high cycle fatigue lifespan to a maximum of 21.25%. On the contrary, fatigue improvement at low cycle fatigue is not remarkable (Figure 2.12.b). The authors also alert of the risk of crack nucleation at the boundaries caused between two burnished paths, as they behave as stress concentration points.

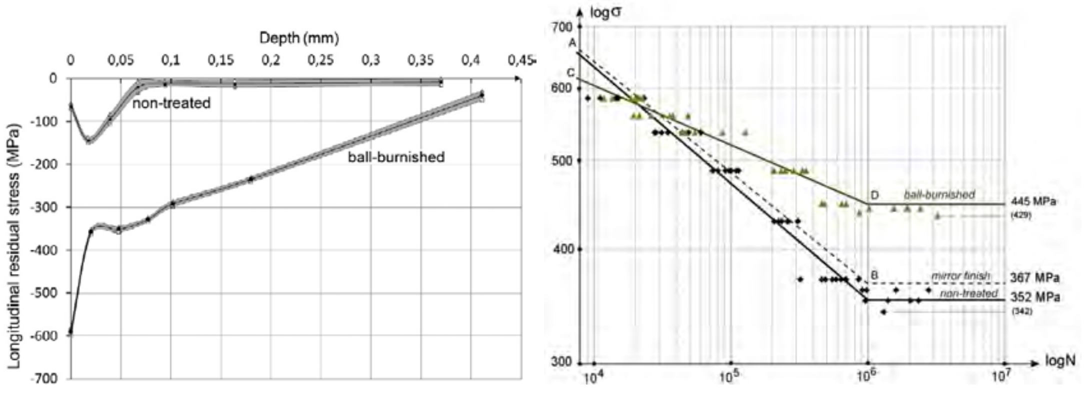

(a) (b)

Figure 2.12. Mechanical surface integrity results of ball burnished AISI 1045 specimens. After Avilés *et al.*, 2015 [4]. **a**. Depth dependence of residual stress. **b**. S-N fatigue diagram of burnished specimens.

The ball burnishing process executed via a milling machine by Klocke *et al.* (2009) [70] on Inconel 718 surfaces showed the positive effect of the burnishing force on the magnitude and maximum depth of residual stress. However, 150 bar is found as a critical value from which residual stress do not increase (Figure 2.13.a). The influence of the ball diameter can also be observed at Figure 2.13.b, where an increase of residual stress and depth are present at the surface as the ball diameter increases.

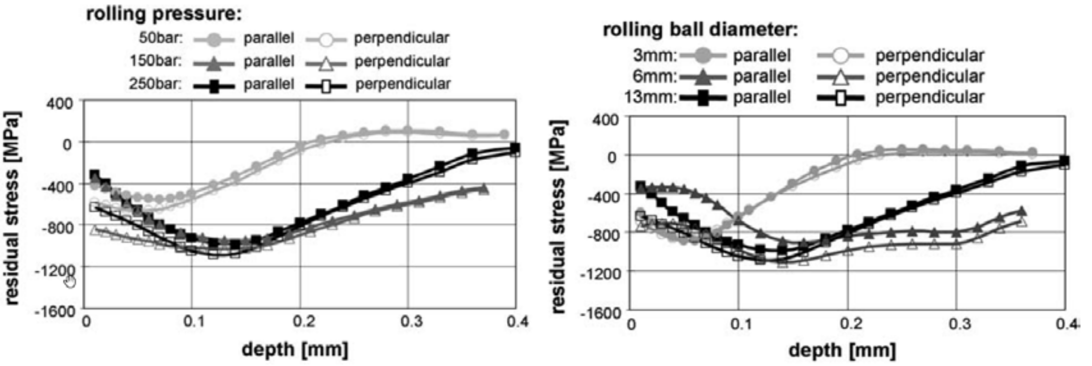

(a) (b)

Figure 2.13. Deep residual stress measured on Inconel 718. **a**. Influence of pressure. **b**. Influence of ball diameter. After Klocke *et al.*, 2009 [70]

Another relevant result found by Klocke *et al.* (2009) [70] is related to the comparison of two different measurement methods. The incremental hole drilling method and the X-Ray diffraction on a cut-off burnished material are performed, and show a very good correlation of both methods. The hole drilling method was also performed by García-Granada *et al.* (2017) [40] on ball burnished AA 2017-T4 and AISI 1038 surfaces. Results were compared to residual stress measured on the surface by X-ray diffraction. A satisfactory correlation of results between both methods was confirmed.

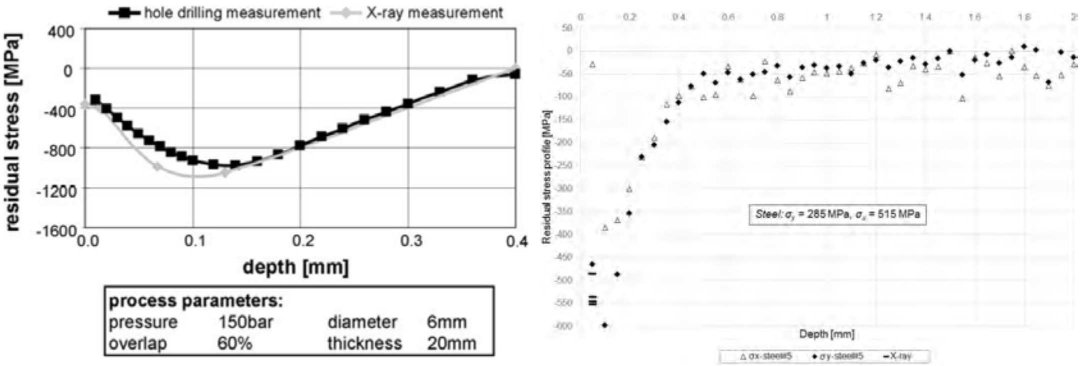

(a) (b)

Figure 2.14. Comparison of residual stress measurement of ball burnished surfaces through X-ray diffraction and incremental hole drilling. **a**. Results by Klocke *et al.* (2009) on Inconel 718 [70]. **b**. Results by García-Granada *et al.* (2017) [40].

2.3 Vibration-assisted ball burnishing

Innovation in the manufacturing industry often comes from improving already existing processes, instead of developing brand new operations based on radically different working principles. One possible way to undertake this innovative approach is based on the assistance of processes by combining a conventional operation with an external power source which triggers additional effects in the system, facilitating the cut or deformation of the objective material. This approach to manufacturing innovation is called process assistance.

The assistance source can be very varied, and includes laser beams [147], electric currents [72], current pulses [159] or magnetic fields [100]. This thesis is based on the assistance of the ball burnishing process by overlapping ultrasonic vibrations on a force preloaded on the target surface by controlled spring compression. The hypothesis of improvement is based on the acoustoplasticity principle, which is explained below in this section, along with successful case studies and some isolated applications on ball burnishing that have been found in the bibliography.

2.3.1 Description of the acoustoplastic effect

The hypothesis that the superposition of ultrasonic vibrations can improve the execution and results of the burnishing process is based on an physical phenomenon called acoustoplasticity, or Blaha effect, after the first researcher who observed it on an experimental basis. It consists on the overall reduction of the quasi-static stress required to deform a material as a result of the superimposition of vibrations on the deforming agent. As a process based on plastic deformation, the ball burnishing process can be susceptible of improvement by this principle.

Acoustoplasticity was first observed by Blaha & Langenecker in 1955 [7]. It was reported at sight of the results undertaken on pure zinc crystal specimens submerged in a carbon tetrachloride solution, and subjected to a 800 kHz ultrasonic wave. The tests were performed in two ways, as shows Figure 2.15. On one hand, the intermittent connection of the ultrasonic source proved to reduce the tensile stress by about 40%, whereas it returned to its value prior to insonation –curve A–. A second experimental development showed that continuous application of ultrasound from the beginning of the essay –curve B– lowered the stress to the same extent. Both strategies were declared equivalent, as they lead to the same approximate stress value at about 1.5% deformation with no significant increase of temperature of the liquid environment.

The acoustoplastic effect can be universally observed in metals, but its affectation depends on their physical characteristics. Izumi *et al.* (1966) [62] performed tests on annealed copper, brass, mild steel, Al-Al_2O_3 alloy and magnesium specimens. They observed a divergent behaviour according to the vibration amplitude, as shows Figure 2.16. Whereas mild steel showed a regular evolution of the stress as the amplitude increased, copper and aluminium alloy showed a higher sensitivity by the effect. Especially for high amplitudes, they showed a change in the behaviour, with an abrupt fall of stress as strain grew higher. This amplitude dependency has been confirmed by other authors [73, 74].

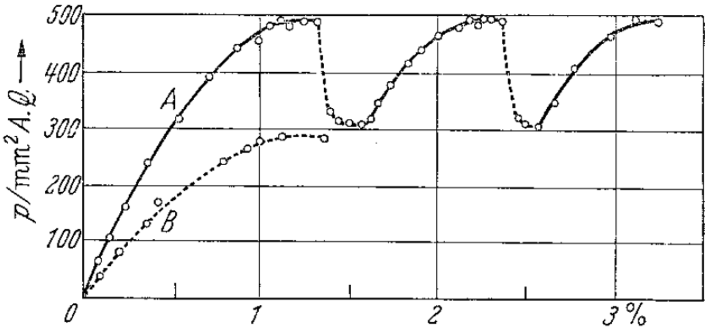

Figure 2.15. Effect of superimposed 800 kHz ultrasound on zinc crystal specimens deformation. ______ without, and - - - - with vibrations. After Blaha & Langenecker, 1955, [7]

The different reaction of materials to acoustoplastic strain can be quantified. Izumi et al. (1966) [63] defined the vibration sensitivity factor, k, that is, the material constant showing the decrease of flow stress per unit of the vibration amplitude, according to Eq. 2.6.

$$\sigma = \sigma_0 - k_s u_0 \tag{2.6}$$

where σ is the flow stress affected by the superimposed vibration, σ_0 is the flow stress with no vibration, k_s is the vibration sensitivity, and u_0 is the vibration amplitude.

Furthermore, they found a correlation with some of the main physical characteristics of the alloys, such as the acoustic impedance, Young's modulus, melting point, work-hardening and stacking-fault energy. Materials with higher acoustic impedance and higher elastic modulus showed a higher sensitivity to strain through vibration superposition, and therefore, softening by acoustoplasticity. A lower work-hardening coefficient also favours the process, as can be seen in Figure 2.17.

Acoustoplasticity is described in the literature to have dual effect on materials, as it causes softening during the application of the ultrasounds, but also residual hardening [76]. This result is actually the most interesting one to justify the assistance of ball burnishing by this effect, as it can eventually facilitate plastic deformation during the process, while causing a remnant hardness on the workpiece which can improve its wear during in-service functioning.

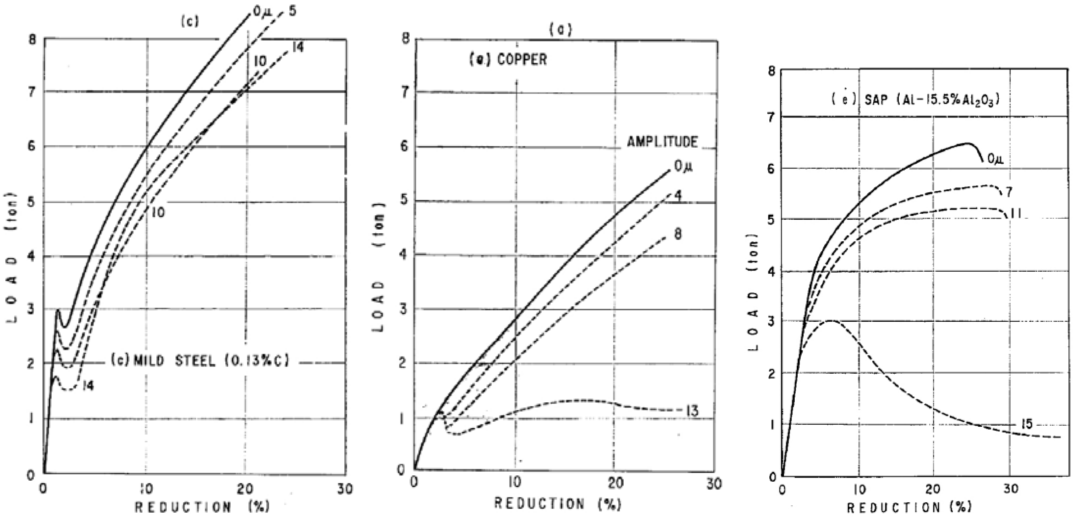

(a) (b) (c)

Figure 2.16. Stress reduction during compressive tests due to acoustoplasticity with different amplitudes. **a**. Mild steel. **b**. Copper. **c**. Al-Al_2O_3 alloy. After Izumi *et al.*, 1966 [62]

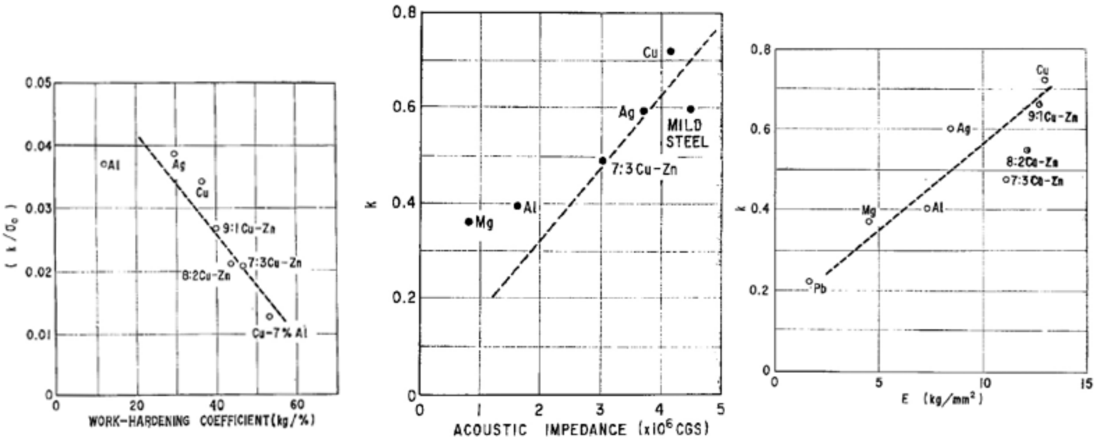

(a) (b) (c)

Figure 2.17. Linear correlation between the vibration sensitivity, k, and work-hardening coefficient, acoustic impedance and Young's module. After Izumi *et al.* 1966 [62]

2.3.1.1 Brief insight into acoustoplasticity causality

Albeit the observation of acoustoplasticity on different materials, its actual physical causality is still controversial, due to the lack of agreement about whether it has an extrinsic or intrinsic nature. That is, whether it is caused by the reaction of the material microstructure to the external source of ultrasonic energy, or by the increase –by the effect of ultrasounds– of the amount of input energy into the system, with no change in the intrinsic properties of the material.

In summary, it can be stated that the extrinsic approach based on an additive stress superposition, has been rejected by numerous authors due to the inconsistency of the proposed modes with experimental results [93, 143]. Another intrinsic approach, based on thermal causality, has already been rejected by Endo *et al.* (1979) [34]

On the contrary, the intrinsic approach based on preferential absorption of the ultrasonic wave by lattice defects has had more continuity in time and acceptation among researchers. It is based on the hypothesis that ultrasonic energy is preferentially absorbed by dislocations and defects in the metal lattice. As lattice defects define the plastic deformation mechanisms of a material, this approach can easily explain the facilitation of the process. This idea was suggested by Blaha & Langenecker [7, 8]. Mason (1955) [98] argued that the preferential absorption of ultrasonic energy by lattice defects derived in an increase in dislocation mobility which enabled the metal to deform at a lower load. This theory allowed Gindin *et al.* (1972) [42] to justify the observed residual hardening after acoustoplasticity, as a consequence of the newly formed stable vacancy accumulations and dislocation loops in the material lattice.

A steady discussion about the source of acoustoplasticity has been recently reactivated, enabled by the advances in technology for microstructure analysis. Siu *et al.* (2011) [137] used a vertical 30-kHz vibrating Vickers microindenter to perform hardness tests on pure aluminium. The softening-residual hardening dual effect of acoustoplasticity was observed on the resulting prints. SEM observations proved that indentation prints showed residual subgrain formation, an undetected effect on specimens which were quasi-statically indented. These effects were later confirmed experimentally on copper, molybdenum and aluminium specimens [135].

The explanation for acoustoplasticity resulting from the combined extrinsic and intrinsic theories, seems to be the most complete approach. Neither is acoustoplasticity a mere stress addition effect, nor a simple preferential absorption by lattice defects.

It also justifies the fact that no frequency dependence has been detected on the softening effect [136]. On the contrary, Cheng *et al.* (2015) found that softening during vibratory deformation and residual hardening depends on the amplitude, existing a threshold value which has to be surpassed to observe the effect [17]. Recent results established that subgrain formation is not always observed, and, therefore, cannot be considered as the ultimate acoustoplasticity explanation [27].

Regardless of the lack of definition of the actual source of the acoustoplastic effect, its experimental application has been long proved, and are to be incorporated to the ball burnishing operation to enhance its surface integrity results. The following subsection presents the results that have been already reported about the vibration-assisted process in the bibliography.

2.3.2 Experimental results of ultrasonic burnishing

The acoustoplasticity effect as the basis for the assistance of processes has been tested on some traditional operations such as polishing [134] or impact peening [101, 120]. The VABB process was first reported during the 70's under the designation of ultrasonic burnishing, assisted by vibrations characterised by 41.5 kHz frequency, and an amplitude ranging from 5 to 10 µm. Marakov (1973) [94] found a remarkable interaction between the amplitude of the oscillation and the surface roughness results, as the expected positive effect of higher forces on surface roughness was only detected if the amplitude of the vibration was higher than 2 µm (Figure 2.18.a), at mild steel specimens.

This result would be later contradicted by Pande & Patel (1984), as shows Figure 2.18.b. In this case, the process was assisted by vibrations with frequencies ranging from 10 to 70 Hz, and amplitudes from 0.2 to 2.5 µm. Accordingly, the process was called vibratory burnishing, in contrast to the high-frequency ultrasonic burnishing. Results revealed a reverted interaction between the force and the amplitudes, obtaining lower surface roughness for amplitudes lower than $0.5\,\mu\mathrm{m}$ [109].

Pande & Patel (1984) [109] also analysed the influence of the frequency on the results, through an experimental design with other three parameters, namely: burnishing force, feed and spindle speed. Both result variables, surface roughness and hardness, showed a positive direct relation with the vibration frequency. However, that positive effect was remarkable higher in terms hardness, as it can be enhanced

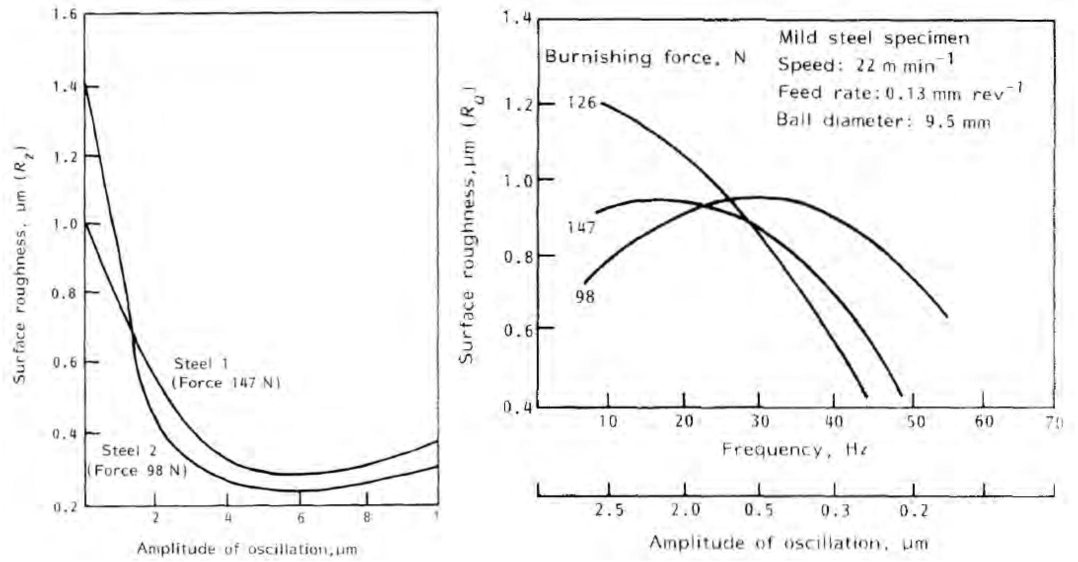

(a) (b)

Figure 2.18. Interaction of the burnishing force and the vibrations amplitude in **a**. ultrasonic burnishing (after Marakov, 1973 [94]) and **b**. vibratory burnishing (after Pande & Patel, 1984 [109]) on mild steel specimens.

by applying the lowest burnishing force assisted with the highest analysed frequency of 60 Hz.

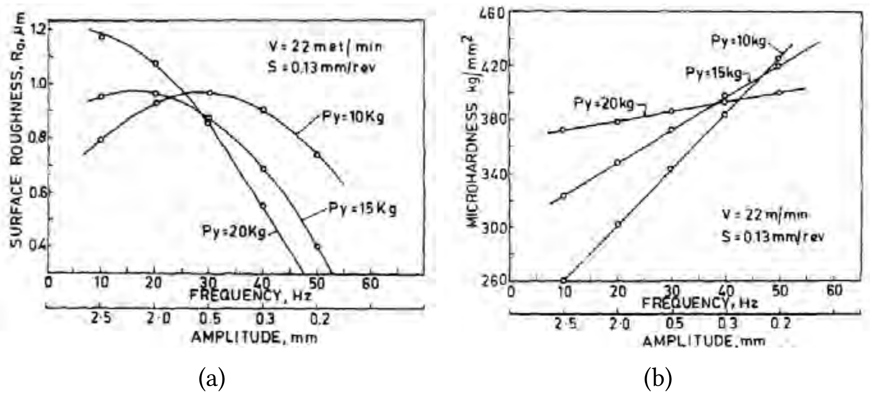

(a) (b)

Figure 2.19. Influence of burnishing force and frequency on **a**. surface roughness and **b**. surface hardness, after Pande & Patel, 1984 [109]).

The literature review undertaken for the composition of this state of the art has not evidenced any other research source about ultrasonic burnishing until the 2000, evidencing a long timespan since the results by Pande & Patel were published in 1984. Ti-6Al-4V specimens were subjected to ultrasonic burnishing by Bozdana *et al.* (2005,2008) [12, 13]. The experimental setup was composed of a hydrostatic tool attached to a milling machine. It was excited by a piezoelectric transducer that transmitted a 20 kHz and 6.75μm vibration.

According to the same author, surface roughness results are very modest and not especially promising for the ultrasonic burnishing process.The average surface roughness is improved to a higher extent through the non-assisted process, probably because *in situ* softening caused by acoustoplasticity may act as a harming phenomena in this material [12]. Results in terms of hardness and residual stress are much more encouraging. Figure 2.20 exemplifies that the ultrasonic process allows the result of higher surface hardness, whereas the deep residual stress profile shows the positive effects of ultrasonic burnishing, while applying half the force with respect to the conventional process.

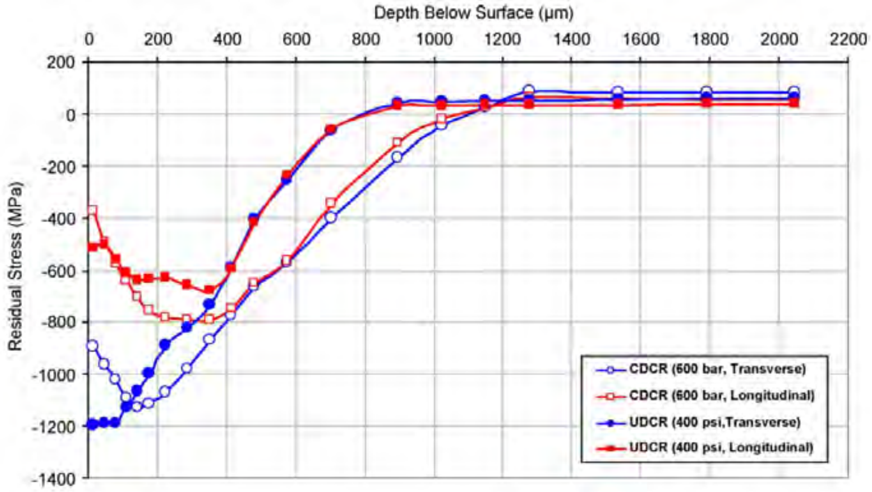

Figure 2.20. Deep residual stress profile comparison after conventional (CDCR) and ultrasonic burnishing (UDCR). After Bozdana, 2008 [12].

The major influence of ultrasonic burnishing on work hardening and superficial residual stress was confirmed by Huuki *et al.* (2014) [61] on AW 6082-T6 aluminium, 34CrNiMo6-M tempering steel and S355J2 structural steel. The materials were prepared as cylindrical specimens mounted on a lathe. The experimental setup was constituted by using a spring-regulated tool, 3-mm ball and assisting the process with 20 kHz vibrations, the maximum static force level was 195 N. Ultrasonic burnishing revealed to be a highly repeatable process, and results on surface roughness and out-of-roundness improved, regardless of the initial superficial state of the workpieces [60].

Within the framework of this thesis, the most relevant results about vibrations-assisted ball burnishing are those published by Gómez-Gras (2014) [43], since they represent the direct antecedent of the work to be developed throughout the next chapters. The results presented at that thesis are based on the application of the process through 2.4 kHz vibrations transmitted by a thin plate excited by a coil. When the coil was excited with a variable magnetic field, it caused an alternative deflection in those plates, which was transmitted to the burnishing ball [45].

This tool was tested on AISI 1038 and EN AW 7078, and results were compared to those derived from the conventional process. This characterisation was performed by analysing the surface roughness, hardness profile and compressive residual stress. In this case, the average surface roughness was substantially enhanced by the introduction of vibrations on both materials, and the authors concluded that one pass of the assisted process delivered a similar surface roughness as five passes of conventional burnishing. Nonetheless, although the improvement is also conspicuous in terms of residual stress and micro-hardness, results were not so determinant, especially in the steel specimens [150, 151]. The authors explain this fact because of an unsatisfactory frequency or amplitude transmission of the vibration, which scarcely reaches the minimum threshold to activate acoustoplasticity mechanisms, and propose further work to improve the process, which can be at last fulfilled with the development of this thesis.

2.4 Objectives arising from the state of the art

From the initial state of the art revision, the following conclusions can be drawn:

- There is enough evidence to think that the superposition of an ultrasonic vibration signal on a conventional ball burnishing process can deliver positive results on the surface integrity of the target material, due to a generalised residual hardening effect, and a lower quasi-static stress required to succeed in deforming metals plastically, on the basis of empirical works.
- There is no commercial tool able to apply the described process. In fact, although a few publications can be found by authors who claim to execute it,

references about the tooling and working principle are vague due to the lack of information shared with the scientific community. Consequently, a new tool should be design to apply the process successfully.

- The classical evaluation strategy followed by researchers with regards to the effects of traditional ball burnishing does not tackle the issue through a comprehensive approach. Specifically for the texture effects of ball burnishing, only the R_a, and eventually R_t, have been used to quantify the effects of the process. However, are these two-dimensional precise enough to characterise an operation that spans a whole surface?

At sight of those observations, the following specific objectives can be formulated. They shall drive the activities undertaken inside the framework of this dissertation:

1. To design, manufacture, and test a burnishing tool capable to execute the vibration-assisted ball burnishing process, that is, to deform plastically a surface through a preload force on which a vibratory component is overlapped.
2. To test the prototype on different engineering surfaces finished through ball-end milling.
3. To assess the effects of the VABB process on the surface integrity of two work-pieces made of AISI 1038 and Ti-6Al-4V alloys, including topological, metallurgical and mechanical parameters to describe it.
4. To propose an alternative set of parameters to describe the topological effects of the VABB process, considering three-dimensional parameters and descriptors other than amplitude ones.
5. To evaluate the improvement delivered by the vibration-assistance by comparing the results to those obtained by complementary tests using the non-assisted process.

3

Design and characterisation of the VABB tool

The implementation and validation of innovative tool design for manufacturing is the basis for the development of this thesis. With that aim, the conception of a prototype enabling the execution of the VABB process plays a decisive role in the quantification and characterisation of its effects on the surface integrity enhancement. This chapter presents the mechanical design of a VABB tool, structured in three different functional units which work together to execute the process. In this design, the role of piezoelectric transducers is fundamental to achieve the vibratory component of the burnishing force required for the VABB process.

A prototype manufactured based on the presented design is then validated through different techniques. However, the high frequency and low amplitude characteristic movement of the burnishing ball poses a remarkable technical challenge. Hence the need of deploying a set of different techniques to register and reconstruct the wave generated by the ultrasonic prototype. These tests include motion track with HD images, acoustic emission and dynamometric measurements with high sampling frequency to quantify the actual functioning of the tool when the piezoelectric are excited.

3.1 Mechanical construction

The tool presented hereafter is based on a design patented in Spain, and published on 2017 June 2 in the Spanish Official Bulletin of the Industrial Property with number 2615002 [66]. Obtaining the PCT extension is a work-in-progress due to be settled by mid 2018.

The prototype is based on spring compression to control the burnishing preload, and incorporates an innovative system of support of the burnishing ball. To successfully execute the burnishing process, the new prototype must comply with the following basic specifications:

- Guarantee the constant rolling of the burnishing ball during the process.
- Control with a certain reliability the burnishing preload magnitude through a calibrated spring.
- Enable the interchangeability of the tool on different machine tools.

Besides, to enable the tool to execute the VABB process, additional requirements must be demanded, as follows:

- Ensure that all electronic devices are separated from inside the humid machine tool environment.
- Transmit the vibratory movement originated at the piezoelectric thickness alternative change to the burnishing ball.

Beyond the cited practical aspects, the actual key feature that must be satisfied by the conceived tool is to deliver an oscillating burnishing force F_b, product of a superposition of two main components: a preload, F_p, applied during the preliminary phase of the burnishing operation by means of the controlled spring compression, and an oscillatory force, F_v, delivered by the vibration of a piezoelectric stack. During the process, the actual burnishing force shall be the result of a composition of both, modified by an uncontrolled variation due to the interaction of the ball with surface irregularities, as follows:

$$F_b = F_p + F_v + \eta \tag{3.1}$$

where F_b is the total burnishing force, F_p is the preload, F_v is the vibratory force originated from the piezoelectric vibration dynamics, and η is the low-frequency force variations due to the topological irregularities found during the feed motion of the tool.

The force perturbation, η, shall be neglected for the analysis undertaken in this dissertation, as shall be justified in the next subsection. All technical requirements considered, the final design consists of a tool composed of three different units (Figure 3.1). Conjointly, all three modules allow a feasible preload regulation, introduce the vibratory component in the system, and overlap and transmit both of them to the workpiece. Further explanation about them is presented along the subsequent subsections.

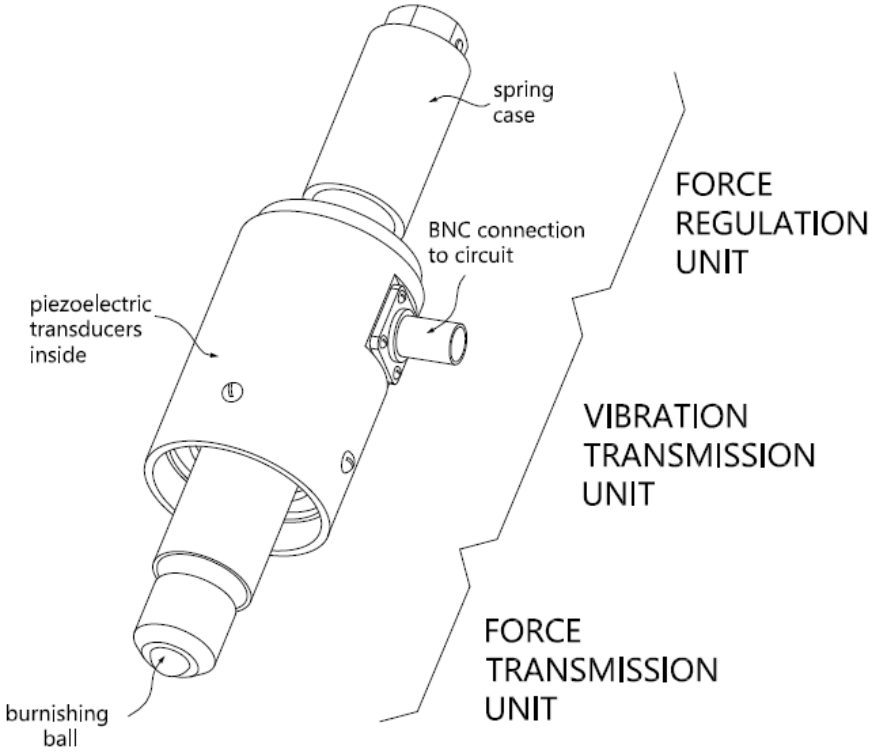

Figure 3.1. Structure of the ultrasonic vibration-assisted ball burnishing tool.

3.1.1 Force regulation unit

The force regulation unit is composed of the parts responsible for the selection and control of the preload, F_p, applied during a ball burnishing operation. This force is the main driver of plastic strain during both the NVABB and VABB processes. The calibrated spring responsible for force control is housed inside a ⌀25 AISI 1045 cylindrical case, which glides freely along a rod, in turn coaxial to the central axis of the tool (Figure 3.2). The steel case also serves to perform the fixation of the tool to the machine, by clamping it to the tool holder.

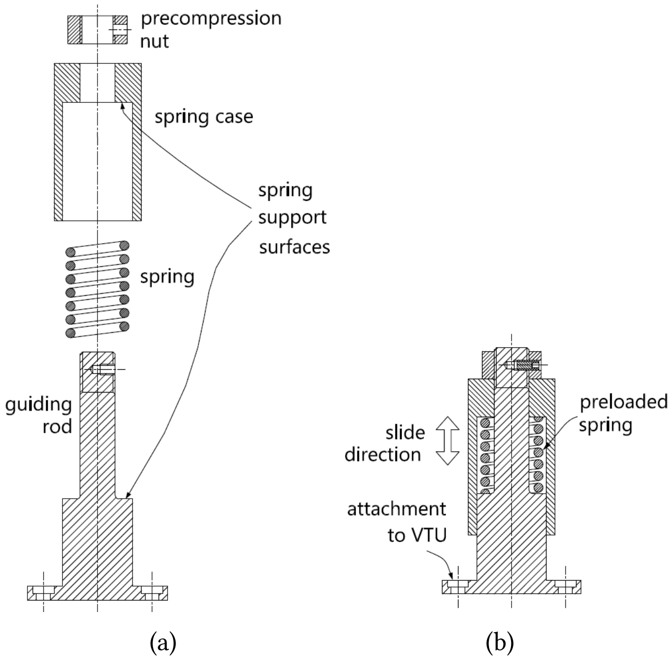

Figure 3.2. Diagram of the FTU. **a**. Exploded view. **b**. Assembled parts and spring compression.

The compression length experimented by the spring defines the burnishing preload, as it is the Hooke's law (Eq.3.2) that governs the elastic force exerted by the spring inside the unit. The compression of the spring is possible due to the described free axial movement of its case, which pushes on it so that preload can be regulated during the burnishing operation as follows. Once the tool is attached to the machine spindle, its head is approached to the workpiece until the ball makes contact with the surface. From that point on, further plunge of the tool head shall revert in compression of the spring. This force transmission is possible on account of the rigid connection between the rod base and the case of the central body of the tool (i.e. the vibration transmission unit).

$$F_p = F_0 + k\,\Delta z \tag{3.2}$$

where F_0 is the precompression force, k is the spring stiffness, Δz is the compression length of the spring.

For the realisation of the prototype, a drawn AISI 5160 die spring with rectangular section, according to ISO 10243, was mounted on the FRU. It has a nominal 100-N/mm stiffness. To accurately control the preload, a previous calibration phase was undertaken to define the actual stiffness and preload of the spring. The tool prototype used for the essays was tested through a universal testing machine equipped with a 2-kN load cell. The tool was supported on an auxiliary part which emulates the tool holder. The testing machine compressed then the spring at constant velocity, while the force was registered by a Spider8 data acquisition device, with a 60-Hz sampling rate (Figure 3.3.a).

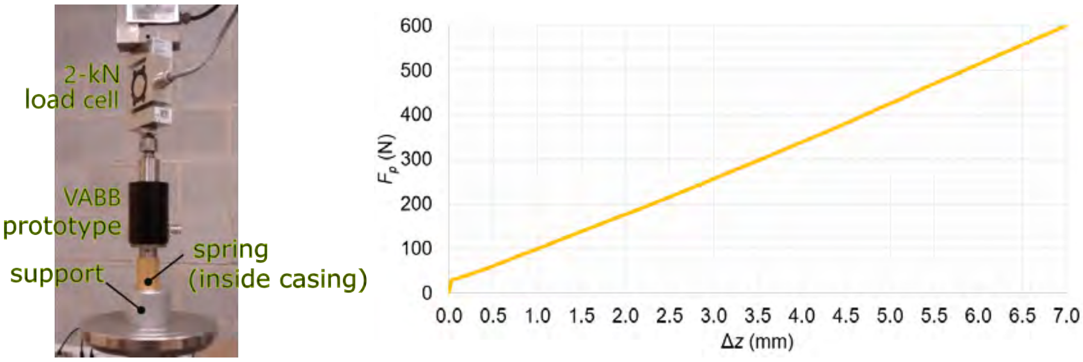

(a) (b)

Figure 3.3. Calibration of the VABB prototype. **a**. Overview of experimental setup. **b**. Curve obtained by compression at 100-mm/min velocity.

The recorded set of time data was translated into displacement, as the compression was performed at constant velocity. This calibration operation was performed at three different compression velocities: 1 mm/min, 10 mm/min and 100 mm/min. All dataset describe a rectilinear graph, as expected due to the nature of Hooke's Law. As an example, Figure 3.3.b shows the calibration curve for the 100 mm/min test.

The respective resulting calibration lines were calculated using a Microsoft Excel worksheet and the `INTERCEPT` and `SLOPE` native functions (Table 3.1). The y-intercept coordinate corresponds to the precompression force, due to the initial compression caused by the pressure exerted by the case as a result of a top nut screwed on the base support. Parameters are similar, although slightly different due to the variation in the sample size introduced taken by the software to perform the calculation.

Table 3.1. Spring calibration parameters calculated at different compression velocities.

v_{comp} (mm/min)	Calibration parameters F_0 (N)	 k (N/mm)	Pearson's R^2
1	30.33	83.12	0.9991
10	29.26	83.65	0.9999
100	28.31	84.34	0.9992

Results also show that the actual elastic constant of the spring, k , has an average value of 83.70 ± 0.61 N/m, inside the tolerance interval offered by the manufacturer in its catalogue. Only this physical spring is used for the experimental procedures included in this thesis. On the other hand, due to the variability of the precompression force depending on the thread length of the nut, a calibration operation was performed before every experimental test to verify its value. However, it will not be specified in this memoir, as it is considered a trivial preliminary operation.

At this point, it is easy to justify the omission of η in the quantification of the burnishing force, due to its negligible value with regards to the preload level. Indeed, the source of this variation is the absorption of the spring inside the tool of the surface topological features as the ball rolls over them during the process. Since they have units of $\mu\mathrm{m}$, considering the stiffness of the spring used for this tool, η shall have units of mN according to Hooke's law. Consequently, this perturbation can be ignored.

3.1.2 Vibration transmission unit

This module is composed of the elements necessary to generate the ultrasonic vibratory component of the burnishing force, F_v. The design specifications describing the force that this unit must be able to deliver are shown in Table 3.2.

Table 3.2. Dynamic specifications imposed for the VABB prototype.

item	value
Frequency	40 kHz
Amplitude (unloaded tool)	10 $\mu\mathrm{m}$

The principle on which the generation of F_v is based, is the change of the thickness of a polarized piezoelectric material when it is subjected to a difference of potential.

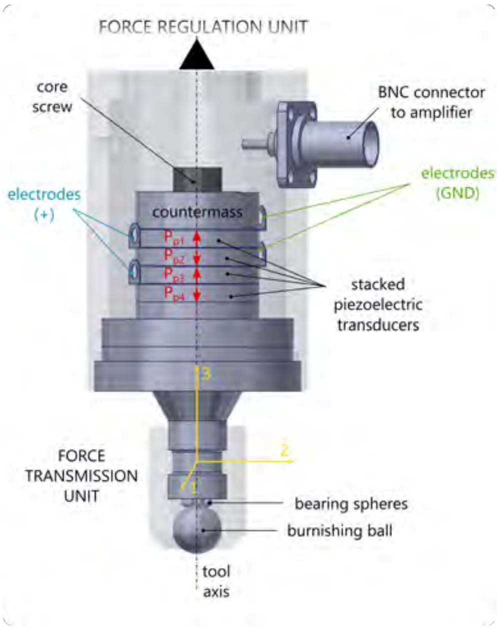

Figure 3.4. Stacked piezoelectric plates inside the VTU of the VABB prototype.

These piezoelectric transducers deform accordingly at the same frequency as the electrical field which excites it. This is the principle on which this VTU is based, and is based on previous successful applications on vibration-assisted machining tools [14].

The design contemplates the installation of a piezoelectric transducer stack inside an enclosed case along with the corresponding counterweight, and fixed on a thin surface extended at top of the sonotrode to ensure the connection with the FTU. Screwed at the top of that case is the spring support, and, therefore, the whole FRU described above. The electrical excitation of the vibration transmission unit is achieved by a BNC external plug that connects the electrodes among the piezoelectric disks and the electronic circuit (Figure 3.4).

The FRU explained above made reference to the static force supplied by the tool through spring compression. However, the differential feature of the prototype is the ability to overlay a vibratory movement on the burnishing ball by means of a set of piezoelectric ceramic parts attached conjointly to the burnishing ball. The principle of piezoelectricity justifies and explains the tool behaviour and its potential to implement the VABB process. Piezoelectricity describes the property of certain materials to transform mechanical energy in electrical energy –direct piezoelectric effect–, and vice versa –inverse effect–. This property can be artificially induced by polling in artificial materials such as lead zirconate titanate (PZT) for engineering applications.

The constitutive model of a piezoelectric transducer, comprising both the inverse and the direct effects, is composed of the electromechanical equations represented at Eq. 3.3. The second one models the inverse effect, and explains the utilisation of piezoelectric ceramics as actuators. It shows that the deformation experienced by a piezoelectric is the result of an external electric field forced on it and, eventually, the application of a stress on its surface.

$$\begin{bmatrix} \mathbf{D} \\ \varepsilon \end{bmatrix} = \begin{bmatrix} \xi^{\sigma} & \mathbf{d} \\ \mathbf{d} & \mathbf{S^E} \end{bmatrix} \begin{bmatrix} \mathbf{E} \\ \sigma \end{bmatrix} \tag{3.3}$$

where $\mathbf{D}$ is the vector of electric displacement , ε is the strain vector, $\mathbf{E}$ is the vector of applied electric field, σ is the stress vector, ξ^{σ} is the permittivity matrix measured at constant stress, $\mathbf{d}$ is the matrix of piezoelectric strain constants and $\mathbf{S^E}$ is the matrix of compliance coefficients measured at constant electric field.

This equation can be particularised for the case study. The vibratory displacement is desired along the longitudinal axis of the tool, that is, the direction 3 of the space, performed by an anisotropic piezoelectric polled along that same direction, with no external stress applied on it. Considering these requisites, Eq. 3.3 can be simplified to Eq. 3.4, which allows the calculation of the total elongation of the piezoelectric material.

$$\varDelta t = d_{33} V \tag{3.4}$$

where $\varDelta t$ is the piezoelectric thickness variation.

This equation calculates the displacement that any element attached to the piezoelectric volume is due to experience when the latter is excited, and does not depend on the original thickness.

The technical solution for the VTU was developed in collaboration with an industrial firm that manufactures and distributes piezoelectric sonotrodes. The resulting configuration inside the ball burnishing prototype consisted of four stacked hard PZT8 piezoelectric disks, whose properties are summarised in Table3.3. The disks are separated by metallic electrodes connected alternatively to an oscillating voltage source. This distribution allows an axial actuation of the system, as long as they are excited by an electric field aligned with the polarisation direction.

This configuration is a classical engineering solution which presents a high effi-

Table 3.3. Properties of hard PZT8 material used for the piezoelectric actuators in the VABB tool.

Property	value	units
ρ	7700	kg/m^3
E	63	MPa
d_{13}	$120 \cdot 10^{-12}$	m/V
d_{33}	$275 \cdot 10^{-12}$	m/V
d_{15}	$400 \cdot 10^{-12}$	m/V

ciency in transforming electrical to mechanical energy, and successfully delivers the vertical vibration of the burnishing ball. It also allows high magnitude resonant frequencies of the system, which is suited for the desired ultrasonic excitation of the prototype. The stack was fixed on the thin surface at the top of the sonotrode of the FTU, thus enabling the conjoint functioning of both units, as has been explained before. This VTU–FTU connection was already presented in Figure 3.4).

The behaviour of this stacked configuration can be explained by extending the constitutive equation represented by Eq. 3.4 for single piezoelectric layers to a sequence of q piezoelectric plates:

$$\Delta t = q\, d_{33} V \tag{3.5}$$

where q is the number of stacked ceramic modules , d_{33} is the longitudinal piezoelectric signal deformation coefficient along the axial direction, and V is the applied voltage .

The piezoelectric stack is excited through a BNC connection to an external generator which transforms the electrical signal into a 40 kHz and 1.3 kV mono-phase AC voltage. As the AC source excites the piezoelectric, it shall change its width in unison with the exciting current, as polarity reverses alternatively the strain sense of the piezoelectric material, i.e. negative potential shall make the piezoelectric thinner, and the negative potential thicker.

According to Eq.3.5, and the described characteristics, the nominal displacement of the whole stack can be estimated in 1.5 μm. A model property of the manufacturer of the whole sonotrode, resulted in a maximum displacement at the tip of the sonotrode, that is, the tool itself, of 8.9 μm, which is the value established at first at the design specifications.

3.1.2.1 External power circuit: resonance at maximum impedance

The external power circuit plays a fundamental role in making the tool function according to the described specifications, as it must be able to generate the correct electrical signal to make the piezoelectric vibrate at the desired frequency. For us, the generator is a black box whose composition is unknown for the purposes of this dissertation, and has been provided by the manufacturer of the piezoelectric actuator.

The electrical circuit has been tuned so that the actuator works always at resonant frequency, and at maximum impedance, Z . As the impedance is the measurement of the opposition that a circuit presents to a current when a voltage is applied, according to Ohm's Law, setting the mentioned condition as a design requirement has two main consequences. First of all, it is an electronic means of guaranteeing that the piezoelectric is always working at resonance frequency of 40 kHz. Secondly, the circuit always work at minimum intensity, I , and, therefore, with minimum power consumption.

To guarantee that this condition is invariable in time, the circuit of the external generator includes an electronic auto-tuning system which modifies the impedance automatically, through a feedback system reporting the value of the output signal to the input terminal of the amplifier. To check this condition, the prototype was connected to a Banry PV70A impedance analyser. This device enables the excitation the transducer of the prototype with a sequence of electrical signals of increasing frequency. Incremental steps of 100 Hz, from 30 kHz to 50 kHz, were taken to excite the transducer. Figure 3.5 represents the impedance value measured for each frequency. Maximum impedance can be found at around 42 kHz, as desired according to design specifications. A second measurement was taken while the piezoelectric was manually loaded on a free surface. The impedance presents a certain variability as a consequence of the circuit constant autotune, but the global maximum can be also seen at the same frequency level.

The electrical circuit is also equipped with a potentiometer which allows the variation of the vibration amplitude. The maximum amplitude is coded as a 100%, and is the reference value. This amplitude can be changed continuously just by interacting with the power circuit potentiometer switch. The quantification of this change and its consequence in the VABB process application shall be assessed in the following tool characterisation activities.

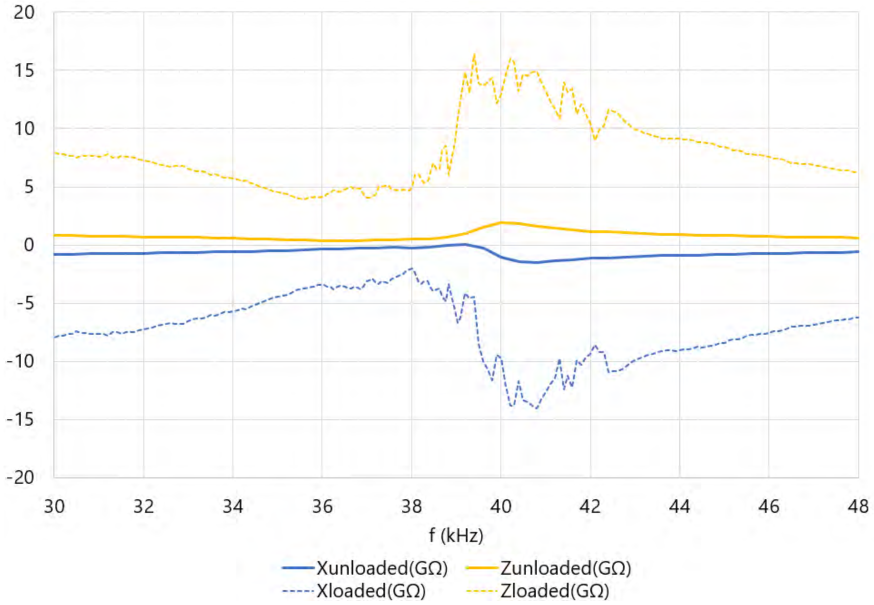

Figure 3.5. Frequency sweep and register of electrical impedance of the circuit which excites the tool.

3.1.3 Force transmission unit

The function assigned to this module is the execution of the burnishing force, F_b, by overlaying and transmitting both the preload controlled through the FRU, and the oscillating force, F_b, enabled by the VTU. The ultimate mechanical transmitter of that force is the burnishing ball, which is supported on a set of bearing spheres inside a hemispherical slot machined on the tool head (Figure 3.6). That head is actually the extension of the thin support surface on which the piezoelectric disks are fixed. Its second function is acting as a sonotrode amplifying the piezoelectric vibration amplitude from its top, on which the piezoelectric is fixed.

3.2 Frequency measurement through acoustic emission

An industrial firm holding the expertise in manufacturing and implementation of piezoelectric actuators executed the implementation of the design in a VABB prototype, which was used for the experiments described in this thesis. Before applying it

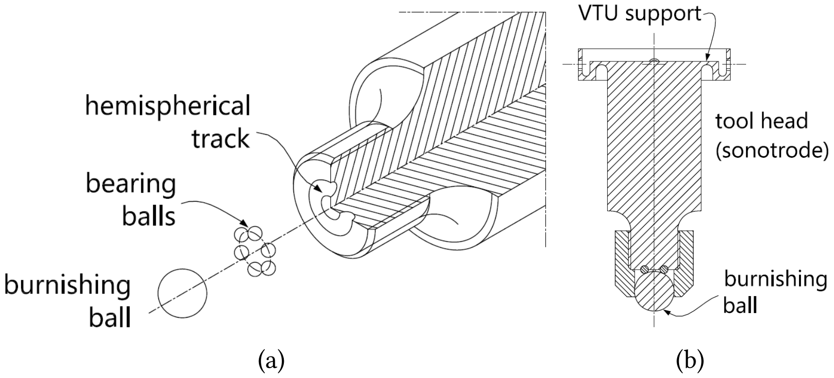

Figure 3.6. Schematic representation of the force transmission unit. **a.** Detail of bearing balls on hemispherical track machined on the sonotrode tip. **b.** Assembled section of FTU components.

on the materials of interest, a preliminary testing phase was performed to prove that vibrations were actually being transmitted to the objective material.

In this matter, the great technological challenge resided in the limitation of sensors to register ultrasonic frequency and micrometric displacements , in this case of the burnishing ball. For that reason, during this phase, the efforts were focused on the characterisation of the frequency of the signal transmitted from the tool to the part through alternative technologies.

A second handicap was found in the fact that conventional accelerometers and other equipments such as laser vibrometers cannot sample an ultrasonic signal. 20 kHz is usually considered as a the threshold value to define the adequacy of this kind of systems. Therefore, the reconstruction of the actual signal would not be representative of the actual one. As the Nyquist-Shannon sampling theorem states, the sampling frequency should be at least twice the expected measured frequency, so that the digitalised data is not aliased, and the real signal can be represented by the reconstructed signal. In this case, a frequency higher than 80 kHz would be necessary to succeed in the vibratory signal characterisation.

At sight of the described situation, an acoustic emission (AE) experimental setup was proposed as a first approach to the characterisation of the prototype dynamic behaviour. AE sensors are devices based on the inverse piezoelectric effect described above, as they transform a mechanical stimulus into a measurable difference of potential. The range of frequencies fully detected through AE goes from the acoustic to the ultrasonic frequency range, depending on the sensor and its resonant frequency, which fits the requirements for our needs.

However, an issue with this technique derives from the advantages it delivers in detecting high frequencies: it requires high sampling rates of a MHz magnitude, and, therefore, generates huge datasets difficult to postprocess [96]. Hence its usual application for non-continuous measurement, as a means to register transient high-frequency waves which do not require to be subjected to continuous sampling and acquisition. For instance, one of its applications is the detection and monitoring of elastic waves originated at subtle changes in materials lattice, such as underlayered breakdowns or microcrack nucleation [95, 97].

3.2.1 Acoustic emission experimental setup

In order to monitor the signal transmitted by the vibrating tool, these AE experiments took an AISI 1038 block as the solid to allow ultrasonic transmission. Table3.4 summarises the different testing conditions which where finally registered. Two preload levels where applied on the target surface, to perform both burnishing lines and points, that is, by imposing a feed movement to the prototype or not, respectively. This allows the evaluation of a possible influence of the feed motion on the measurements.

Table 3.4. Measuring conditions tested during the acoustic emission acquisitions.

Test	F_p (N)	A (%)
burnishing point	90	0
	90	25
	90	50
	270	0
	270	25
	270	50
burnishing line	90	0
	90	25
	90	50
	270	0
	270	25
	270	50

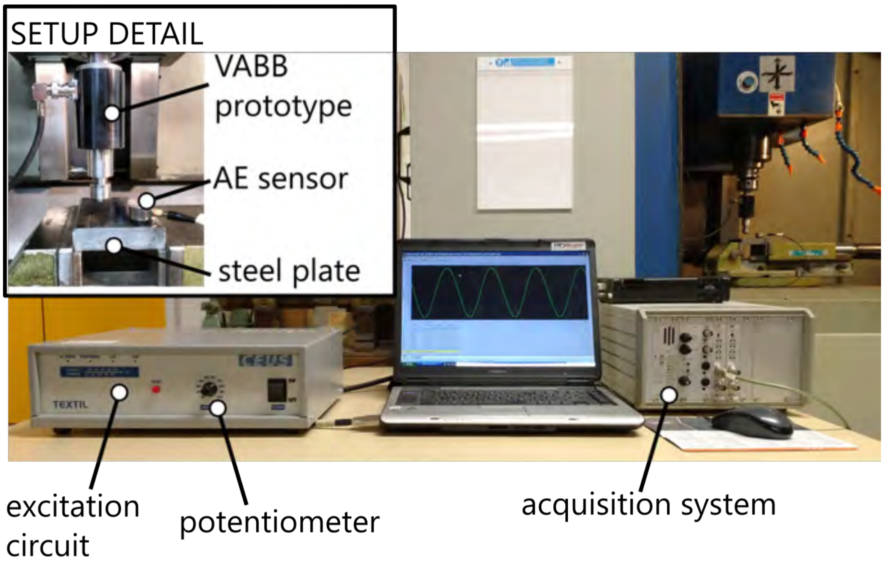

Figure 3.7. Experimental setup for the measurements through acoustic emission.

An initial set of experiments revealed sensor saturation when the highest amplitude allowed by the system was selected through the potentiometer at the power circuit. Therefore, $A = 100\%$ measurements were discarded from the experimental plan. The complete experimental setup can be seen in Figure 3.7.

The steel block was mounted on the vise and face milled, to ensure perpendicularity of the objective surface with regards to the central axis of the prototype. The external circuit which excites the VTU was installed next to the machine, so that the vibrations amplitude could be easily changed. AE measures were made with the following equipment:

- Vallen VS-150M acoustic emission piezoelectric transducer, fixed on the surface of the steel piece through a gel-type couplant.
- Vallen EAP4 34 dB pre-amplifier for signal conditioning.
- Vallen AMSY-5 acquisition system for signal recording.

All data was registered through the Vallen 32 Visual AE acquisition software. It was then processed through a Matlab script through which the signal was filtered and represented in the time domain. The power spectrum was calculated from the filtered signal. Results are presented in the next subsection.

3.2.2 Frequency of the ultrasonic signals recorded by AE

The signals recorded for the 0% amplitude case study did not reveal any data registration, as could be beforehand easily expected. On the other hand, all point and linear tests lead to similar conclusions. For instance, Figure **??** shows the graph of the signal obtained for the 270 N and 50% amplitude test.

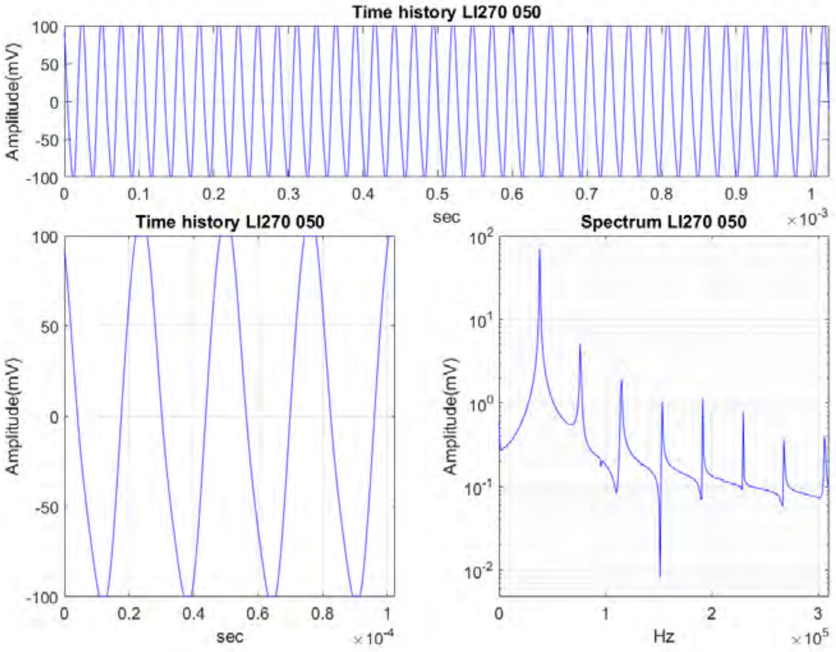

Figure 3.8. Time history and frequency spectrum of signals registered the burnishing line tests 270 N, A = 50%

The intensity of frequency peaks in the spectrum should actually not be considered, as they depend on the distance between the sensor and the measuring point, which has not been calibrated. Indeed, the objective of these measurements is the frequency characterisation of the signal emitted by the VABB prototype. Therefore, a slight saturation of signals does not bias the results expected from these measurements.

On the other hand, all recorded signals are represented by similar frequency spectrum, showing an harmonic response from the same fundamental frequency regardless of the preload level, or the presence of a feed movement during the process. This results leads to think that the tool actually vibrates equally in frequency terms during the execution of the process, and its behaviour does not change essentially when it is loaded.

To quantify the value of the fundamental frequency visible in the spectrum, the Matlab script was prepared so that it could return the value for each signal in a results array. Table 3.5 represents all these results. Regardless of the preload level or the amplitude of the vibration, all signals transmitted had the exact fundamental frequency of 39.1 kHz, very near from the 40 kHz defined at the initial specifications. The amplitudes do not reveal any profitable information, as the measurements were not calibrated.

Table 3.5. Fundamental frequency found for each measured signal and its amplitude.

Test	F_p (N)	A (%)	f_0 (kHz)	A_0 (mV)
burnishing point	90	25	39.1	70.1
	90	50	39.1	63.5
	270	25	39.1	55.9
	270	50	39.1	54.6
burnishing line	90	25	39.1	69.0
	90	50	39.1	61.4
	270	25	39.1	52.1
	270	50	39.1	69.1

3.3 Dynamometric characterisation

During the previous subsection, handicaps and technical limitations were found to measure the actual ball displacement during piezoelectric excitation. Having succeeded in finding a value of the frequency through the AE experimental analysis, an alternative method was considered to quantify that displacement by direct determination of the sinusoidal force overlapped on the preload while the piezoelectric is being excited, that is, F_v.

The quantification of F_v during this phase is completed by a second layer of objectives, as it allows the assessment of the effectiveness of the potentiometer installed in the external circuit for the piezoelectric excitation. On the other hand, it also delivers information about a possible dependence of this oscillating force on other process parameters.

3.3.1 Dynamometric experimental setup

The experimental application of the dynamometric measurements contemplated a total of 6 preload levels, which were tested at amplitudes 10%, 50% and 100%. Furthermore, the F_v was recorded at the highest preload level for amplitudes from 10% to 100% in steps of 10. A summary of all tested conditions are contained in Table 3.6.

Table 3.6. Conditions measured during the dynamometric tests.

F_p (N)	A (%)
100	10 – 50 – 100
200	10 – 50 – 100
300	10 – 50 – 100
400	10 – 50 – 100
500	10 – 50 – 100
600	10 – 20 – 30 – 40 – 50 – 60 – 70 – 80 – 90 – 100

Figure 3.9 shows the whole experimental setup next to the milling machine where it was conducted. The press force sensor was mounted on the vise on the milling machine, with the help of a copper shell to protect it. The tool would be directly compressed on the sensor surface to attain the different preload levels. With that aim, the following equipment was implemented:

- Kistler 9323A press force sensor, especially conceived for measuring dynamic and quasistatic forces (Natural frequency: 72 kHz).
- Kistler 5015A charge meter.
- Hameg HM2008 oscilloscope

A first set of measurements were taken to construct a calibrating line by progressively compressing the spring inside the prototype, and monitoring the static force. Figure 3.10 shows the equivalent calibration line obtained my linear regression, Compared to the equation obtained by continuous compression. Both stiffness coefficients can be considered equivalent, although the precompression force is slightly different. As that precompression is caused manually by the operator by tighting the nut at top

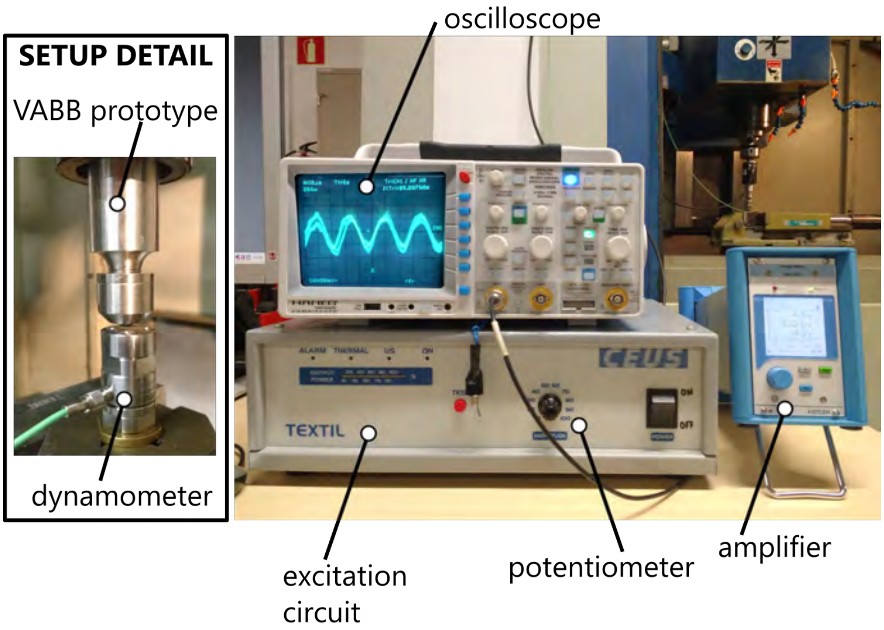

Figure 3.9. Experimental setup for the dynamometric measurements.

of the prototype, it can change from one situation to another. Consequently, this calibration should be performed before each application of the process. An alternative precompression method could be developed in future improvement activities.

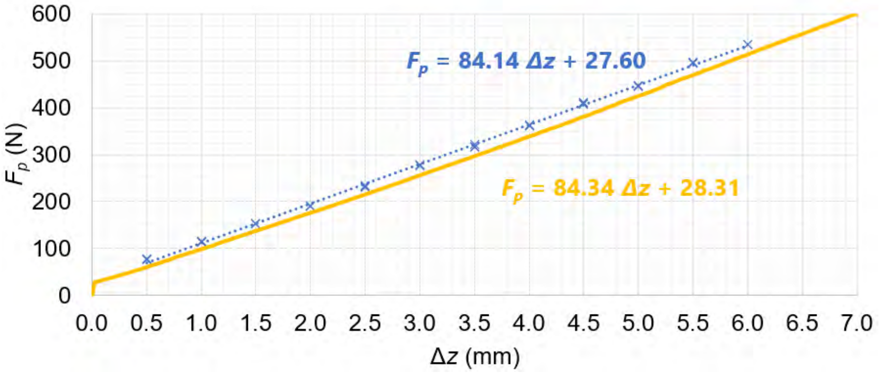

Figure 3.10. Comparison of calibration lines measured through continuous force acquisition and Kistler dynamometric measurements.

During the second phase, all preload levels and amplitudes were combined and registered. Preloads were managed by compressing according to the calibrating function deduced from the previous phase. For each preload level, the tool was compressed directly on the sensor, until the searched preload value was achieved. The measurement was then reset, and the piezoelectric was excited. That way, the only force detected by the sensor was the additional vibrating force, F_v. By the inverse piezoelectric effect, the sensor transformed that force acting on the quartz element inside the capsule into an analogue voltage signal, which was acquired and sampled by a Hameg HM2008 oscilloscope.

For a proper reconstruction of the signal, a 10-MHz sampling frequency was used to process the signal by the oscilloscope software. However, although the oscilloscope delivered the sampling and reconstruction of the signal at a satisfactory frequency, it also provided a technical limitation linked to the fact that only the portion of signal shown in the screen could be exported. In order to have a good representativeness of the force, each signal was acquired ten times, and processed by a Matlab routine to calculate a sine function fit.

3.3.2 Quantification of the superimposed vibratory force

The arguments of the fitted sine are the descriptors of the vibratory force, F_v, as represents Eq. 3.6.

$$F_v = \mathit{\Delta} F_v \sin\left(\omega t + \phi_0\right) \tag{3.6}$$

where $\mathit{\Delta} F_v$ is the force variation in one half cycle, ω is the angular frequency, and ϕ_0 is the phase.

Figure 3.11 shows an example of the sine fit calculated for one of the sampled signals for a 600-N preload at 100% amplitude. All fits have a Pearson R^2 parameter higher than 94%, thus confirming the reliability of the calculated parameters (Table 3.7). Only the fittings for the measurements at 100 N of preload are around 85%, probably because the signal is more unstable at this preload level. Still, this fitting can be considered as acceptable to quantify the level of force delivered by the vibrating s. Standard deviations have not been represented for the purposes of simplicity, as they are all below 0.01.

The Matlab routine returned all descriptors of the sine curves, which are actually the descriptors of the vibratory force overlaid on the preload. Of all those descriptors, the frequency and the amplitude of a half cycle are the most interesting ones to characterise F_v. Table 3.8 gathers all those descriptors averaged from the ten samples taken for each measuring condition, along with their standard deviation. The divergence between the mean half-cycle amplitude arising from the sine fitting and

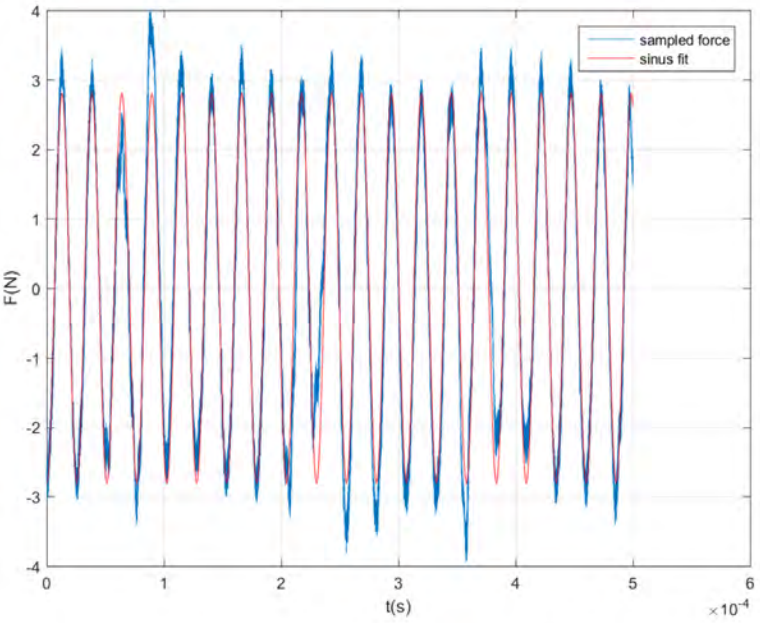

Figure 3.11. Sinus fit calculated for the recorded signal at F_p = 600 N and A = 100%.

the actual maximum and minimum registered forces confirms what can be visually detected in the signals: they show a random variability in time. Still, this function models well enough the behaviour of the vibratory force, as was shown in Figure 3.11.

For a better comprehension of the vibratory force scales, Figure 3.12 represents half cycle force amplitudes calculated from the sine fits, and both the maximum and minimum forces acquired through the dynamometer for the two highest tested amplitudes. All piezoelectric amplitudes regulated from the external power circuit generate a similar behaviour of the vibratory force, for all preload levels. The force variation in a half cycle is around ± 4 N, except for the case of 200 N preload force, where a slightly higher value of 5.5 N is observed.

This non-linearity can be associated to the fact that the stiffness of the prototype, k', changes as the spring is compressed different compression lengths, i.e. as the preload is changed. The most simple model to explain this is by assuming that the displacement of any mechanical system is directly proportional to the force causing it through its stiffness (Eq. 3.7). In the VABB prototype, this k' stiffness is the result of the mechanical combinations of all its components, including the spring. Therefore,

Table 3.7. Average goodness of fit of F_v sine fits through the Pearson R^2 parameter.

	$F_p(N)$					
A	100	200	300	400	500	600
10%	85.3%	97.3%	95.5%	95.5%	94.8%	94.0%
20%	-	-	-	-	-	94.4%
30%	-	-	-	-	-	94.0%
40%	-	-	-	-	-	93.4%
50%	85.5%	97.4%	95.1%	95.4%	94.1%	94.0%
60%	-	-	-	-	-	94.3%
70%	-	-	-	-	-	94.3%
80%	-	-	-	-	-	94.3%
90%	-	-	-	-	-	94.3%
100%	85.1%	97.4%	95.8%	95.5%	94.6%	94.0%

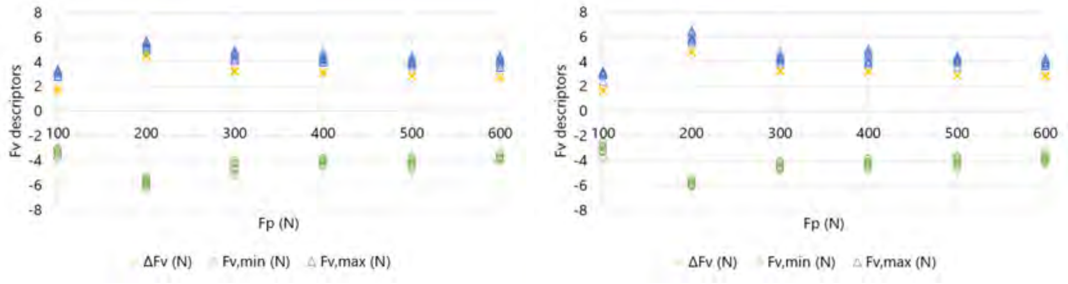

(a)

(b)

Figure 3.12. Half-cycle vibratory force variation, and extreme values, for different preload levels. **a**. A = 50%. **b**. A = 100%.

it is unknown.

$$F' = k'\delta \tag{3.7}$$

where F' is the force acting on the mechanical system, δ is the displacement, and k' is the system stiffness.

As the spring governing equation is linear, meaning that the variation of k' must come from other uncontrolled factors related to the mechanical composition of the tool, and it introduces the non-linearity observed in the experimental results, which lead to conclude that stiffness is minimum at a preload of around 200 N. The direct consequence is that it enables the whole FTU to vibrate along a higher displacement. Nevertheless, this variation should not be influential in the result, as the acoustoplas-

Table 3.8. Average descriptors of sine fits of F_v and maximum and minimum values registered.

$F_p(N)$	A	ΔF_v (N)	*SD* (N)	$F_{v,min}$ (N)	*SD* (N)	$F_{v,max}$ (N)	*SD* (N)
100	50%	1.70	0.079	-3.38	0.285	3.11	0.202
	100%	1.67	0.033	-3.06	0.388	3.03	0.247
200	50%	4.53	0.055	-5.77	0.298	5.47	0.248
	100%	4.80	0.040	-5.89	0.196	5.99	0.268
300	50%	3.23	0.051	-4.53	0.347	4.30	0.297
	100%	3.23	0.030	-4.41	0.250	4.39	0.279
400	50%	3.13	0.049	-4.41	0.250	4.33	0.279
	100%	3.17	0.042	-4.22	0.261	4.39	0.243
500	50%	2.87	0.040	-4.16	0.320	4.03	0.247
	100%	2.89	0.018	-4.07	0.324	4.12	0.244
600	10%	2.77	0.025	-3.75	0.178	4.11	0.203
	20%	2.78	0.031	-3.85	0.236	4.03	0.217
	30%	2.78	0.039	-3.64	0.331	4.39	0.264
	40%	2.76	0.028	-3.78	0.162	3.97	0.304
	50%	2.75	0.030	-3.76	0.178	4.11	0.329
	60%	2.76	0.026	-3.64	0.343	4.02	0.221
	70%	2.77	0.043	-3.64	0.321	4.02	0.221
	80%	2.76	0.054	-3.64	0.351	3.93	0.234
	90%	2.76	0.045	-3.65	0.187	3.86	0.202
	100%	2.84	0.048	-3.86	0.285	3.95	0.203

tic effect is not a matter of additive force, but the transmission of the ultrasonic wave inside the material, the source of which is confirmed for all preload levels. Furthermore, the reference values of 4 N and 5.5 N, over the different adopted preload levels provide a similar ratio, so that they can be considered at all effects equivalent.

As F_p = 600 N was object of more measurements at different amplitudes, it has been represented in Figure 3.13 along with 300 N for comparison. That Figure shows the stability of the vibratory force descriptors, even for the more discretised 600 N measurements. This behaviour is common for all preload levels.

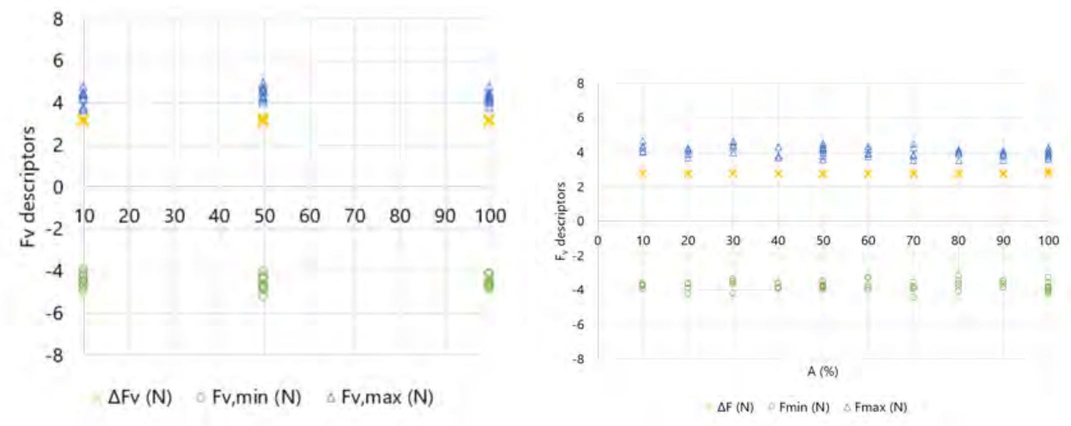

(a) (b)

Figure 3.13. Half-cycle vibratory force variation, and extreme values, for different preload levels. **a**. F_p = 300 N. **b**. F_p = 600 N.

As for the F_v frequencies, ν, they can be obtained from the angular frequency of the sine fits, according to Eq. 3.8. The frequencies corresponding to all the studied cases were calculated and averaged. Table 3.9 shows the high stability of the frequency at 39.2 kHz, regardless of the preload and the amplitude.

$$\nu = \frac{\omega}{2\pi} \tag{3.8}$$

In general, the dynamometric measurements have evidenced that the vibratory signal is stable for preloads lower and higher than 200 N, as this preload level shows a decrease in the stiffness of the system that slightly amplifies F_v. The next section tackles with the measurement of the mechanical integrity of all tool parts by the analysis of motion tracking.

Table 3.9. Average frequency of all sine fits that model the F_v, and standard deviation (SD).

	F_p (N)											
	100		200		300		400		500		600	
A	ν	SD	ν (Hz)	SD	ν	SD	ν	SD	ν	SD	ν	SD
10%	39.2	25	39.2	12	39.2	8	39.2	12	39.2	11	39.2	11
20%	-	-	-	-	-	-	-	-	-	-	39.2	25
30%	-	-	-	-	-	-	-	-	-	-	39.2	24
40%	-	-	-	-	-	-	-	-	-	-	39.2	26
50%	39.2	17	39.2	13	39.2	13	39.2	11	39.2	11	39.2	15
60%	-	-	-	-	-	-	-	-	-	-	39.2	16
70%	-	-	-	-	-	-	-	-	-	-	39.2	15
80%	-	-	-	-	-	-	-	-	-	-	39.2	13
90%	-	-	-	-	-	-	-	-	-	-	39.2	18
100%	39.2	25	39.2	8	39.2	17	39.2	16	39.2	9	39.2	23

Units: ν (kHz); SD (Hz)

3.4 Preliminary validation tests

Once the vibratory behaviour of the tool was measured, the next step was to confirm that the tool could actually modify the surface texture. With that aim, the prototype was tested on an AISI 1038 workpiece by performing a whole burnishing operation on a previously milled surface. Each burnishing cycle included precompression followed by successive parallel passes separated by a certain lateral offset were performed to obtain a whole burnishing patch. (Figure 3.14).

The initial surface was obtained by a surface milling operation with a ∅80 5-insert front mill, obtaining a surface characterised by $R_a = 2.735 \pm 0.473$ µm. The roughness was measured on the workpiece with a Mitutoyo S-210 Surftest profilometer, filtering the signal with $\lambda_c = 0.8$ mm cut-off length and 4 mm evaluation length, and by averaging 20 different measures along the burnishing direction. This first test proved to improve the surface roughness by 56.17%, confirming the positive effects of the tool. However, the prototype exhibited a slight bending effect during its displacement on the surface as the feed movement was induced, by effect of the friction. As an excessive geometric deviation between each pair of modules could prevent the tool to perform the process adequately, so it was decided to quantify it.

With that purpose, motion tracking was used to study the mechanical integrity of the burnishing tool, along with the relative movement and rotation of its constructive

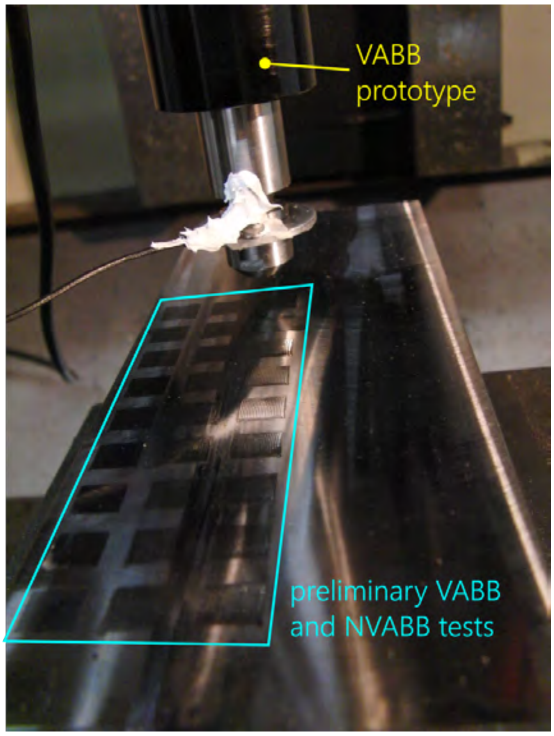

Figure 3.14. Preliminary burnishing imprints performed on a milled AISI 1038 surface.

parts. The tool was attached to a LAGUN 600 milling machine. An AISI 1038 block was fixed on the vise and surfaced to clean the working surface. A CNC code was written to perform successive going and returning burnishing passes along one line. The whole body of the tool was acquired with an HD video camera at 80 fps during 3 s, for two preload levels: 90 N and 270 N.

Each video was decomposed in 240 frames of 1280×720 pixels, which were processed through a Matlab routine that delivered the relative movement of specific predefined points throughout the different frames. Those marks were organised in a 237-point array composed by four sub-meshes (Table 3.10). Each sub-mesh corresponded to one component of the tool, as shows Figure 3.15.

Through the Matlab script, the x and y coordinates of all mesh points were located, and were followed along the next 239 frames, recalculating their x and y coordinates throughout the video sequence. The routine returns, for each of the four meshes, a matrix composed of those coordinates along the 240 frames. By coordinate subtraction, the slope of the lines composed by the points at each row with regards to the horizontal line were calculated. For instance, as mesh I is composed of 5 rows (points

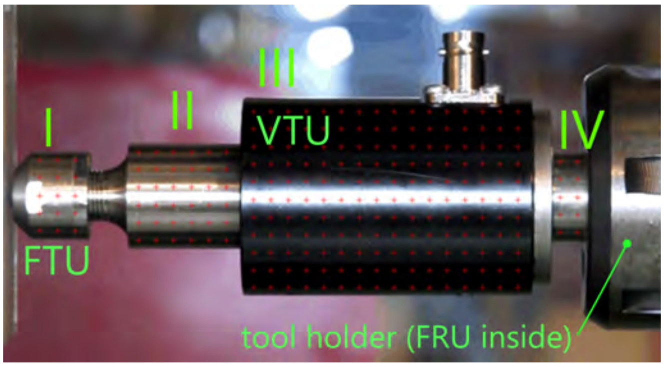

Figure 3.15. Meshes I-IV defined on the tool for the image treatment routine.

Table 3.10. Mesh size for the image processing of the tool.

Mesh	nodes	node distribution
I	15	3×5
II	36	6×6
III	176	16×11
IV	10	2×5

1-3, 4-6, 7-9, 10-12 and 13-15) (Figure 3.16), the respective five slopes were calculated for each of the 240 frames.

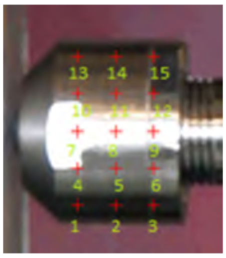

Figure 3.16. Points composing the mesh of part I.

Each frame is represented by one slope value calculated by the average of all points. For instance, Figure 3.17 shows the evolution of the slopes for the element I for each frame, along with a smoothed curve. Two clearly differentiated slopes can be observed in the graph, each one associated with the displacement of the tool in the corresponding direction, namely m_r and m_s. The former is associated in the represented case by the points comprised between frames #40 and #150, For our 80-fps acquisition, m_s is present during 1.375 s, which corresponds to the time that the tool takes to go along the 7-mm path at the established 300-mm/min feed.

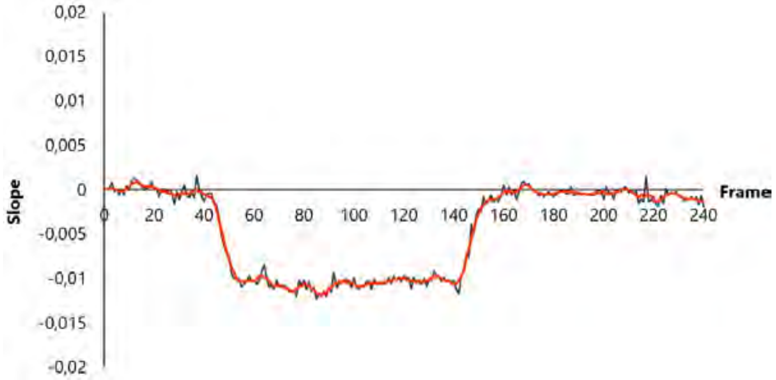

Figure 3.17. Raw and smoothed curves representing the slope presented by the mesh of part I with a 90-N preload.

For both registered preload forces, the presence of dual slope values is found at the four sub-meshes drawn on the tool geometry. Both m_r and m_s themselves are related to the rotation of the tool during the burnishing feed movement around a fixed point –the tool-holder origin– and can be calculated according to Eqs. 3.9 and 3.10.

$$\theta_r = \pi - \arctan m_r \tag{3.9}$$

where θ_r is the rotation of the tool when it moves in one sense.

$$\theta_s = \pi - \arctan m_s \tag{3.10}$$

where θ_s is the rotation of the tool when it moves in the opposite sense.

The maximum angle that the i component of the tool is pivoting when the feed direction changes, θ_i', is obtained as half the difference of angles θ_r and θ_s (Eq. 3.11). It can be seen in Figure 3.18. Although this calculation is based on the hypothesis that the tool swivels the same angle in both feed senses, this calculation method allows a good approximation to its value, and means that it is not necessary to take a vertical reference, which would be impossible to define properly due to the spherical deformation caused by the camera objective.

$$\theta_i' = \frac{\delta}{2} = \frac{\theta_r - \theta_s}{2} \tag{3.11}$$

where δ is the difference of the angles that the tool bends in both displacing directions.

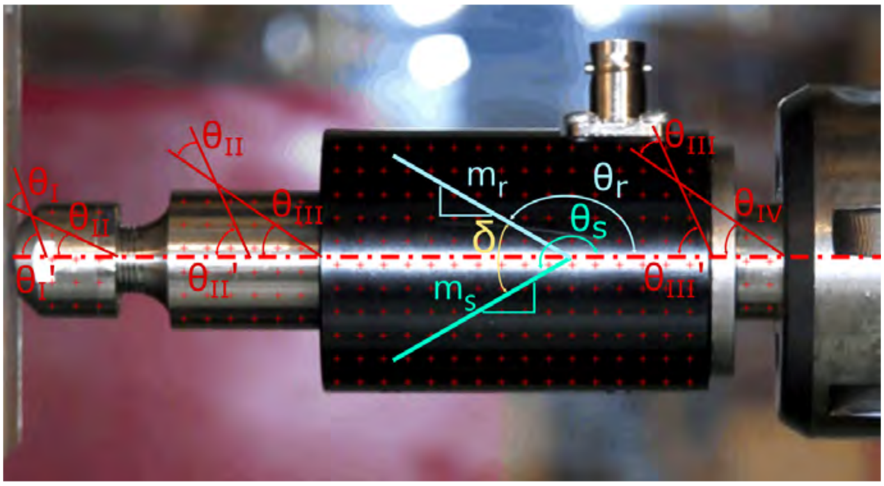

Figure 3.18. Angle and slope nomenclature related to the calculation of the relative angle between tool sections.

The relative pivoting angle of each part with regards to the part to which it is attached, θ_i , can be calculated by the difference of the angles already deduced, as follows:

$$\begin{cases} \theta_i = \theta_i' - \theta_{i-1} : i = 1, 2, 3 \\ \theta_i = \theta_i' : i = 4 \end{cases} \tag{3.12}$$

The absolute pivoting angles of the four distinguished parts of the tool change are higher as the preload grows, as expected, at sight of results contained in Table 3.11. The ball, as the furthest element from the tool holder, experiences the highest pivoting, being 0.2970° with the 90-N preload, and 0.4622° if the tool is preloaded 270 N. When it comes to relative angles, the transition between parts II and III exhibits the largest rotation angle, namely, 0.1688° and 0.3070° for both preloads. That is, respectively, 59% and 66% of the absolute angle, which means that this part is experiencing the highest rotation during the preload and feed movement of the prototype. However, in both cases the rotation angles are small enough to state that they shall not affect the application of the process through this prototype.

These results show that the prototype design is affected by friction force during the operation, which acts a shear interaction provoking the relative bending of the tool. It can be caused due to the fact that the piezoelectric actuator is supported on a 1-mm Ti-6Al-4V plate at the top of the sonotrode. This low thickness plate is highly

Table 3.11. Absolute and relative pivoting angles of each part of the prototype for both preload levels.

	90 N				270 N			
	I	II	III	IV	I	II	III	IV
θ_r (rad)	-0.0105	-0.0092	-0.0027	-0.0028	-0.0057	-0.0108	-0.0075	0.0094
θ_s (rad)	-0.0004	-0.0002	0.0005	-0.0002	0.0102	0.0063	-0.0023	0.0130
δ (rad)	-0.0102	-0.0091	-0.0032	-0.0026	-0.0154	-0.0171	-0.0052	-0.0037
θ' (deg)	**0.2907**	0.2601	0.0914	0.0734	**0.4622**	0.4560	0.1490	0.1048
θ (deg)	0.0305	**0.1688**	0.0180	0.0734	0.0061	**0.3070**	0.0442	0.1048

affected by the shear force provoked by friction during burnishing. However, this degree of rotation is not a problem for the execution of the process, and, therefore, the prototype shall not be modified and is ready to be tested in terms of dynamic behaviour. This conclusion shall be useful in future activities to improve the tool conception.

3.5 Synthesis

As no VABB tool is commercially available, a new design is proposed and was manufactured to apply the process on the target workpieces. Along this chapter an innovative design has been proposed and executed to successfully apply the process. The prototype was successfully tested on an AISI 1038 surface, confirming its feasibility for the application of the process. The main findings arising from the different characterisation activities of the prototype can be summarised as follows:

1. A spring-based ball burnishing tool equipped with a piezoelectric stack has been successfully designed to succeed in applying the process by using a vibratory force on the target surface.

2. The vibratory system is resonant at nearly 40 kHz. It sticks to this frequency even when the piezoelectric is loaded, by means of an electronic auto-tune circuit that forces it to work at minimum impedance. This frequency has been experimentally defined as slightly lower, of 39.1 kHz, by acoustic emission measurements.

3. The vibratory force introduced in the system follows a sine function, with minimum average half-cycle amplitude found for a 100-N preload, possibly due to the fact that this reduced force does not make the tool engage with the workpiece at the same extent as higher forces. For 200 N, a mean ± 5.5 N amplitude is found to be added in the system, but then it settles at a ± 4 N level for higher preloads. In all, this change should not be influential, as acoustoplasticity is not an effect based on stress addition. In all cases, the sine frequency is of 39.2 kHz, agreeing with the other performed measurements.

4. A slight relative pivoting of the sonotrode has been detected during the preliminary tests. However, it has been quantified to be of around 0.5 °, which is considered low enough to not be detrimental for the process.

4

Description of the experimental methodology

This chapter presents the different issues and techniques related to the VABB characterisation process. The first section tackles with the preparatory tasks developed to define the experimental plan. The different techniques and methods applied to assess the VABB results on surface integrity are then explained. A third section includes the characterisation of the materials on which ball burnishing tests are due to be applied. Finally, some aspects regarding the experimental execution are presented to report on the development of all VABB and NVABB tests.

It is important to note that no experimental results are included here, aside from some auxiliary tests that have been performed to assist design the whole experimental phase itself. The main results are included in the next chapter. This segregation has been done with the deliberate aim of not eclipsing the results assessment discussion with methodological data. Indeed, both contents could generate an excessively long chapter that could distract the attention of the reader, and prevent it to focus on the results and conclusions drawn from their discussion.

4.1 Experimental design

Design of experiments (DOE) constitutes one of the most used techniques to perform an in-depth assessment of different engineering issues. The ultimate objective of DOE is to determine the most influential factors in the case study, by performing an experimental campaign where those factors are tested at different levels. The definition of the DOE is the result of a series of strategic decisions leading to decide the whole experimental procedure, taken as follows:

1. Definition of the factors of study and the response variables on which results shall be evaluated.

2. Layout of the experimental plan that shows the order of the different tests to be undertaken. This plan is usually represented in an array, in which each row corresponds to a “run”, or a single experimental execution where the factors of study are combined conveniently.

3. Quantification of the response variables and statistical data analysis.

The variety of methods to define the experimental campaign introduces a high variability in the second step. The most simple –and rudimentary– approach to DOE, delivering the biggest volume of data, is a factorial design. However, it is only materially feasible if the number of levels or factors are low, or, as unusual as it is, the available time and budget are enough to extend the experimental phase indefinitely. Complex studies, seeking comprehensive interpretations of the case study, such as the one tackled in this dissertation, do not allow the performance of factorial designs. For that reason, an alternative strategy, namely fractional experimental design, can be followed to reduce the number of experiments, as is presented below.

4.1.1 Fractional design of experiments

Given the described circumstance, an alternative fractional design of experiments (FDOE) can be proposed to reduce the number of tests without losing considerable amount of information. That reduction in evidence of the variation of the response variable affects first to high-order interactions between factors, then second order interactions, and, in an extreme case, to the factors itself. Meaning that, the risks of using a too restrictive FDOE are (1) losing the capability of explaining non-linearities present in the system, and, (2) not being able to define the model itself. That being the price to pay to reduce the number of experimental repetitions, FDOE are highly extended and are usually chosen to tackle with research activities, as the effect of interactions is usually less relevant than the effects of first degree factors.

Now the question is, what experiments are to be removed form the complete factorial array to generate a reduced experimental plan from which drawing valuable conclusions? One could intuitively think that the design of the experimental plan cannot be randomly performed. Indeed, it depends on the number and nature of the actions, understanding by action any factor –first degree– or interactions –second and higher degrees– included in the model. To answer that question, it is necessary to consider that FDOE arrays must comply with two main properties, as explained below [111]:

- **Condition 1. Sufficient degrees of freedom.** The number of experiments composing the FDOE must be high enough to obtain all the coefficients taking part of the linear model associated to the system of study. Therefore, as an action is introduced into the case study, the total number of tests required to evaluate the influence of all actions on the response variable increases according to the degrees of freedom introduced by the new action. In practice, this condition establishes the minimum number of experiments to be executed to have enough information to complete the model.
- **Condition 2. Orthogonality.** The condition for the orthogonality of a FDOE as a whole is satisfied if each pair of uncoupled actions included in the model are also orthogonal. Therefore, its assessment is reduced to a two-by-two analysis of actions that do not have factors in common. That condition is invariably fulfilled for each pair of individual factors, but not so when interactions are included in the model. A pair of uncoupled actions are orthogonal if each level of the first one is combined the same number of times with the levels of the other, along the whole experimental array. The orthogonality condition guarantees that the effect of all actions can be analysed independently from the other ones.

The described conditions are necessary and sufficient to validate a FDOE as a proper method to conduct an effective study. Although their application and calculation might seem complicated, FDOE arrays are usually predefined as a result of decades of experimentation with this kind of arrays, and can be chosen from a great variety of literary sources. In fact, the strategies to reduce experimental plan to fractional designs are numerous. For this thesis, a Taguchi DOE approach has been selected [142]. Before detailing the construction and selection of the experimental array, the factors to be included in the model are defined in the next subsection.

4.1.2 Factors included in the study

The definition of the actions of interest, along with the levels that shall be object of study, is necessary to elaborate the experimental array, as the degrees of freedom to be covered by experimental results depend on them. Five different factors are established as object of study of this dissertation. They have been chosen at sight of the analysis of previous ball burnishing results presented in the state of the art revision. The five factors are explained along the following paragraphs.

Preload force – $\mathbf{F_p}$ The burnishing force, F_b, is the physical driver that describes the interaction between the burnishing ball, and the target surface. As was described at the previous chapter, during ultrasonic burnishing, F_b is the result of overlapping an oscillating force F_v to the preload. According to the characterisation tasks explained in the precedent chapter, that preload, F_p can be changed through the spring compression length, whereas the value of F_v is constant regardless of the preload level. These regulation operations are commanded by the NC programme, by selecting the appropriate negative Δz coordinate to compress the spring to the desired value.

Number of passes – $\mathbf{n_p}$ Total successive iterations performed during the burnishing operation on a specific surface position. If the interaction of the burnishing ball with the surface was ideally imagined as a line, this parameter represents the number of times that this line is traced on that position. Therefore, the higher its value, the more plastic deformation would be attained through burnishing. It must not be mistaken with the number of lines necessary to cover the whole surface dimension, which would be also dependent on the lateral offset taken between passes. The trajectory through which these passes are executed is described through the Strategy parameter, which is explained below.

Feed – v_f Linear velocity at which the tool is linearly translated over the surface. It is easily commanded through the NC code. Therefore, it corresponds to the conventional feed in a milling operation, with mm/min units.

Original surface topology – S^0 The influence of the initial surface texture on the burnishing results is of high interest, to associate the effectiveness of the process with a certain finishing degree achieved through machining. To that purpose, three different surfaces are to be tested. All of them shall be machined by ball-end milling operations with a hemispherical milling tool with a TiN coating. The ball-end strategy consists on following adjacent passes with the hemispherical milling tool. To vary the levels of this parameter, the offset distance between passes is increased from one strategy to the other, as shall be explained below.

Strategy – St. This parameter describes the trajectory followed by the burnishing ball to cover the whole target surface n_p times. The resulting strategies have been developed by combining different burnishing directions and protocols to cover the previously burnished areas. They are represented in Figure 4.1. First passes are in all cases performed perpendicular to the initial milling direction, hence its denomination as main burnishing direction. The “0” strategies are contemplated always along that direction, “0” denoting no angular change in the trajectory between passes. Alternatively, the “90/0” strategy is based on turning alternatively ±90° the burnishing direction between one pass and the next one. As for the relative order between lateral offset and number of passes, the “bn” strategies cover n_p times the whole target patch, whereas the “nb” strategy is performed by passing n_p times one line, and then taking the lateral pass until covering the whole target patch. By choosing these three strategies, the eventual influence of direction change during burnishing, as well as the effects of passing repeatedly on the same burnishing path, must be detected.

All strategies are executed according to a succession of linear interpolations defined in different NC codes written with that aim, and coded through capital letters as represented in Table 4.1. The combination of different n_p–St. pairs originates various burnishing patterns in the experimental array. For instance, the pair 3passes–bn90/0 covers the target surface through two complete passes along direction I, and one along II between both of them, and corresponds to tests #6, #14 and #22 [1]. All tests performed by 1 pass do not include further passes, and are therefore not affected

---

[1] “#” shall denote henceforth the number of test in the Taguchi experimental array

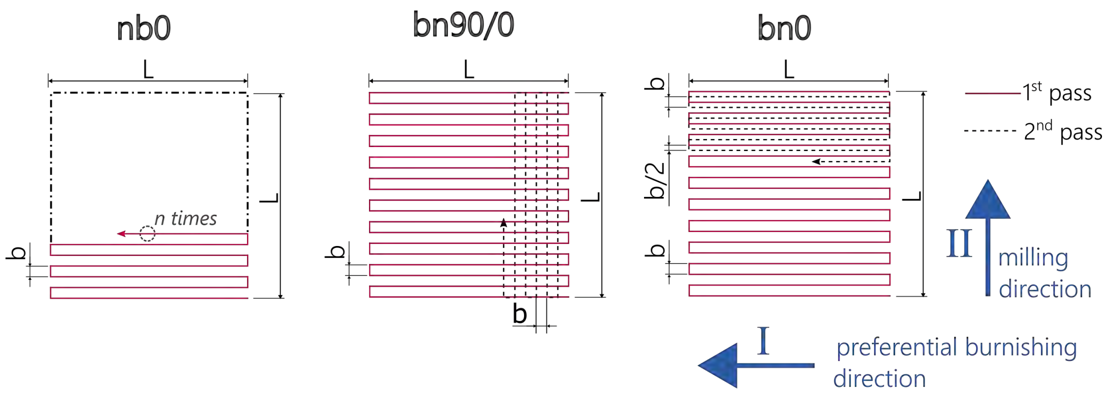

Figure 4.1. Burnishing strategies included in the DOE and nomenclature of the directions referenced in the text.

by the strategy. These are all coded by letter A. All seven codes were parametrised to facilitate the implementation of the feed and preload for each test.

Table 4.1. NC codes for every absolute strategy pattern resulting from the combination of the n_p and St. factors. In brackets the Taguchi run in which they are to be executed.

St.	n_p 1	3	5
nb0	A (#1,#12,#20)	B (#5,#13,#24)	C (#9,#17,#25)
bn90/0	A (#2,#10,#21)	D (#6,#14,#22)	E (#7,#18,#26)
bn0	A (#3,#11,#19)	F (#4,#15,#23)	G (#8,#16,#27)

The response variables that are going to be considered to assess the effects of these factors on the material are different parameters describing the surface topology and residual stress along the two main directions of the surface. These variables shall be discussed in upcoming sections.

4.1.3 Taguchi array

To implement the experimental plan according to the factors of interest, an L27 (3^{13}) Taguchi orthogonal array was chosen. Appendix A shows the whole matrix and its particularisation to the materials on which it shall be applied. This configuration allows the analysis of a maximum of 13 factors at 3 levels. However, as only 5 factors are to be included in the model, a large amount of degrees of freedom provided by the array are unused, making possible the inclusion of three different interactions among coupled factors in the model. The derived experimental design based is proposed as a linear graph in Figure 4.2, and shall be proved valid below.

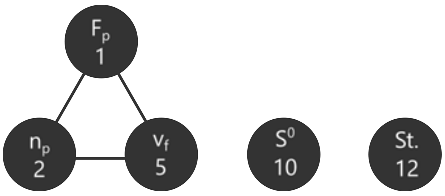

Figure 4.2. Linear graph associated to the L27 Taguchi array. Balls: factors. Lines: interactions.

To avoid aliasing effects among factors and interactions, these were located in the Taguchi array at the columns indicated in the linear graph. This procedure is standardised, and can be consulted at Taguchi et al. (2005) [142]. The final experimental array is represented in Table 4.2.

This L27 array is executed twice on both target materials, once with the VABB process, and the second one by executing the NVABB operation, to establish a comparative point. An overview of a standard workpiece, along with the reference directions considered in the dissertation, is represented at Figure 4.3.

The confirmation of the orthogonality and sufficient degrees of freedom conditions that were presented as necessary to validate the simplification of the experimental design provided by the L27 array is explained in Appendix A.

4.1.4 Particular DOE arrays for the studied materials

The methodology for experimental design exposed during the previous section was particularised for both chosen materials. As both of them exhibit different mechanical behaviour, the preload as main deforming source, was determined at sight of bibliographical review [117, 150] and a preliminary set of tests performed on both materials to confirm the deformation after those preload levels. The rest of the parameters were common for both the AISI 1038 and Ti-6Al-4V experimental execution. Table 4.3 shows the factors and levels which have been applied for the burnishing of the AISI 1038 surface.

Table 4.2. Experimental design derived from a $L27(3^{13})$ Taguchi orthogonal array.

Col.	1	2	5	10	12
No.	F_p	n_p	v_f	S^0	St.
1	1	1	1	1	1
2	1	1	2	2	2
3	1	1	3	3	3
4	1	2	1	2	3
5	1	2	2	3	1
6	1	2	3	1	2
7	1	3	1	3	2
8	1	3	2	1	3
9	1	3	3	2	1
10	2	1	1	3	2
11	2	1	2	1	3
12	2	1	3	2	1
13	2	2	1	1	1
14	2	2	2	2	2
15	2	2	3	3	3
16	2	3	1	2	3
17	2	3	2	3	1
18	2	3	3	1	2
19	3	1	1	2	3
20	3	1	2	3	1
21	3	1	3	1	2
22	3	2	1	3	2
23	3	2	2	1	3
24	3	2	3	2	1
25	3	3	1	1	1
26	3	3	2	2	2
27	3	3	3	3	3

The S^0 must be object of further explanation. Although this factor is defined in the DOE through three levels common to both materials, the respective three initial textures shall predictably different between both tested materials. Indeed, they shall be determined as a consequence of the machining process, by changing the lateral offset between every hemispherical tool passes.

The whole experimental array for both materials can be consulted in Appendix A. According to the provided materials, and the required high number of repetitions, a

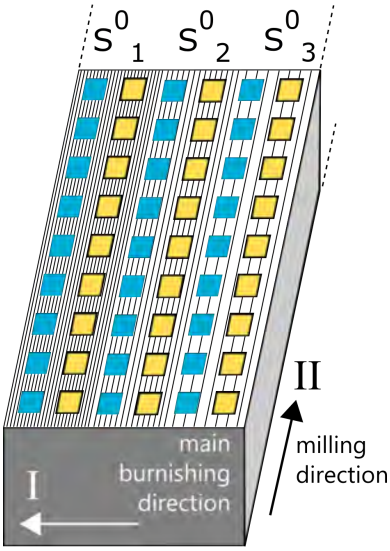

Figure 4.3. Schematic representation of the VABB (non-contoured yellow patches) and NVABB (contoured blue patches) tests performed on a general workpiece and reference directions considered in this work.

layout was proposed and planned before the execution for both surfaces. This plan is shown at Figure 4.4.

4.1.5 Unvaried process factors

The factors of study were varied along the different tests as the Taguchi array describes. However, there are some parameters that, while being eligible to be varied as process factors, were kept constant for all tests. These factors, along with other unvaried process descriptors, are included in Table 4.4. The burnishing ball material and diameter have been chosen to give continuity to the experimental execution followed in previous studies of our research group [43, 148].

The determination of a fixed lateral pass width was the result of a combination of different criteria, described as follows. As was described in the state of the art chapter, this value must be low small enough, not to leave any non-deformed material on the surface, regardless of the productivity loss that could be caused by taking a too low value. For that reason, a conservative value was chosen and kept constant for all tests, to discard it as a variability source. In the case of the AISI 1038 material, previous studies by Gómez-Gras *et al.* (2014) [45] recommended 0.36 mm as lateral pass

Table 4.3. Factors and levels at the Taguchi array for AISI 1038 and Ti-6Al-4V specimens.

		Levels		
Factors	Material	1	2	3
F_p (N)	AISI 1038	90	180	270
	Ti-6Al-4V	150	250	350
n_p	both	1	3	5
v_f (mm/min)	both	300	600	900
S^0	both	1	2	3
St.	both	bn0	bn90/0	nb0

Table 4.4. Descriptors and factors kept constant in the tests.

Factor	Value
lateral pass width	0.3 mm
burnishing ball diameter	∅10 mm
ball material	60Cr3 hardened chromium steel
lubrication	none

width for 90 N of preload. Consequently, a conservative value of 0.3 was taken. On the other hand, as no bibliographical data was identified for the Ti-6Al-4V material, a preliminary experimental test was performed on a milled surface. Burnishing tracks applying different preloads and number of passes were performed, and the resulting profiles were acquired and measured through an ALICONA Infinite Focus optical profilometer, as exemplifies Figure 4.5. The lowest imprint width was 0.732 mm, obtained by applying 150 N, proving that 0.3 mm was also a valid lateral pass width for this material.

4.1.6 Results assessment through Analysis of Variance

The methodology associated to the analysis of the Taguchi experimental setup contemplates the calculation and analysis of the results through two different approaches:

- Quantifying the mean effects that all actions (factors and interactions) have on the selected response variables.
- Evaluating the robustness of the actions associated to each response variable.

The parameter used to evaluate the robustness of a factor used in the Taguchi system is the signal-to-noise ratio (S/N) . Robustness refers to the neutralisation of the

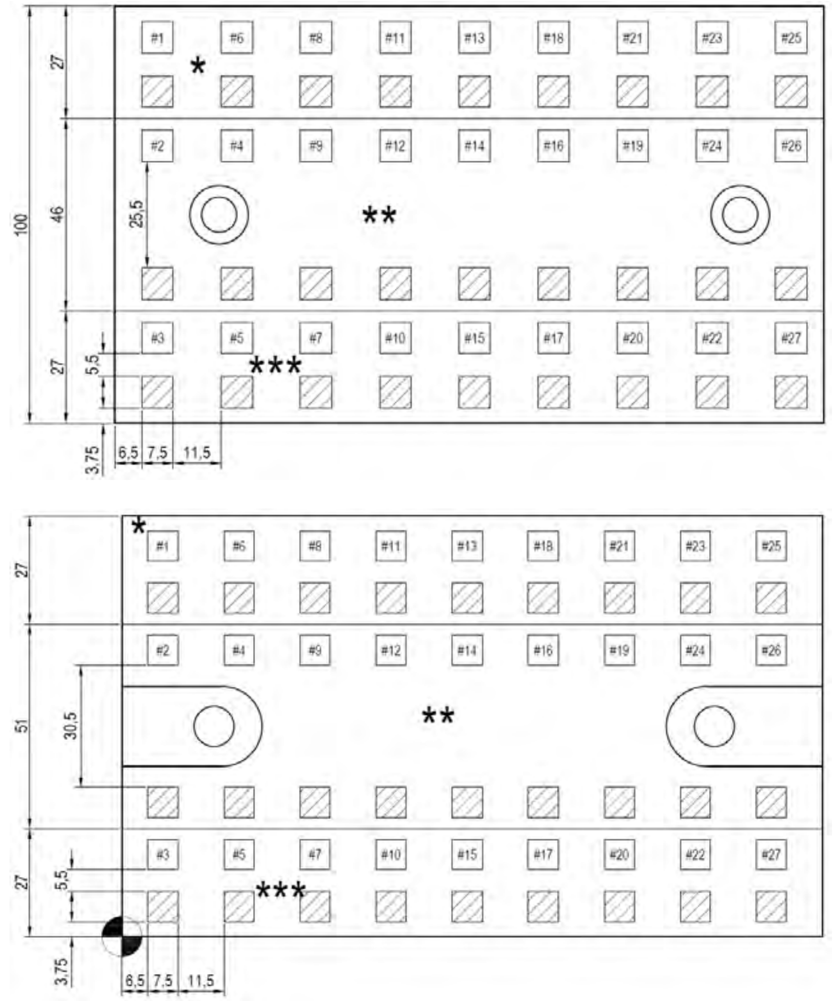

Figure 4.4. Planned experimental tests represented on the three different machined S^0. Striped patches: VABB tests. **a**. AISI 1038. **b**. Ti-6Al-4V.

effect of noise effects in the response, and is included in the Taguchi analysis because it is a fundamental aspect contained in its quality approach. The Taguchi experimental design focuses on achieving a desired response goal while minimising the variance of that response, that is, maximising its robustness. As S/N is an input-to-output relationship, it should be maximised. This perspective is based on the idea that a certain product or process should always respond the same way to an external signal. In our case, when a certain combination of burnishing parameters is applied on a workpiece, the process should always derive in the same result. Its calculation depends on the objective with regards to the response variable, according to the desired effect on the

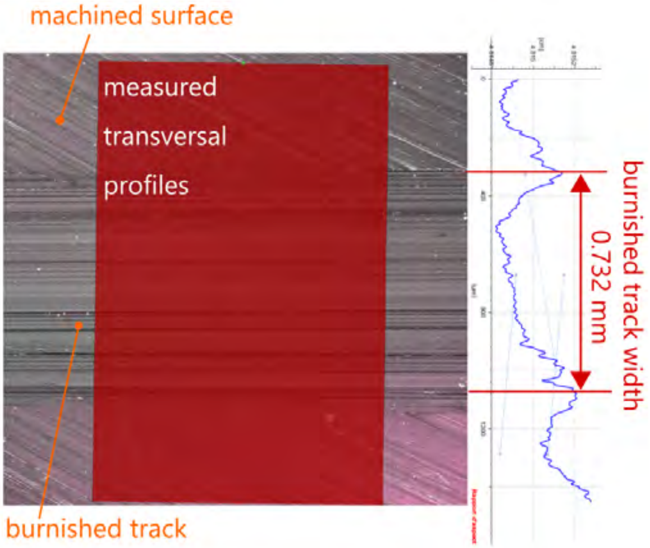

Figure 4.5. Measurement of burnished track width on Ti-6Al-4V applying 150 N.

response variable, as shows Table 4.5

Table 4.5. Calculation of the signal-to-noise ratio in function of the goal of the experiment.

S/N	Goal	Expression
Larger is better	Maximise response	$-10\log\left(\sum \frac{\frac{1}{Y^2}}{N}\right)$
Smaller is better	Minimise response	$-10\log\left(\sum \frac{Y^2}{s^2}\right)$

Y: responses for the given factor level combination, N: number of responses in the factor level combination, s: standard deviation of the responses for a given factor combination.

To analyse the influence of all factors on the response variables and the robustness associated to them, the results linked to a Taguchi experimental array can be assessed through an analysis of variance technique (ANOVA) . The purpose of ANOVA applied to experimental design analysis, is to compare the effect of single factors and interactions which are applied simultaneously on the response variable. Therefore, it allows the differentiation of the effects of the actions of interest from the residual variation, or noise. In other words, the ANOVA table delivers a hierarchy of the different sources of variation of the response variable. If all the observed means, i.e. the result for each run, are close together, then the differences between them can be attributed to residual variation. If, on the contrary, they are dispersed, then there is a reason to believe that the effects of different treatments are significantly different because of the application of different levels. The problem can be formulated as a hypothesis test:

$$\begin{cases} H_0 : \mu_1 = \ldots = \mu_i = \ldots = \mu_c \\ H_1 : \mu_i \neq \mu_j \quad for\, some\, i \neq j \end{cases} \tag{4.1}$$

where μ_i is the mean response for observation i.

The null hypothesis can be rejected if the p-value associated to it after the test is higher than a prefixed level of significance, α, in which case the null hypothesis can be rejected, and one can assume that the variation of the response is not caused by a variation of the related action. All ANOVA calculations shall be performed with the software Minitab 18.

4.2 Measurement of the surface integrity parameters

4.2.1 Acquisition of topological data

As explained in chapter 2, the evaluation of surface texture using two-dimensional parameters can be a biased and incomplete approach to assess VABB results. With the advances in surface metrology measurement, a new set of 3D parameters was progressively introduced to describe mathematically the nature of engineering surfaces [21]. Nowadays, optical systems allow the transformation of a surface into a mathematical function which assigns one height value to each sampled point (Figure 4.6). The publication of the ISO 25178 standard offered a wide set of tools to convert that mathematical function into functional descriptors grouped in two main categories, namely the 12 S parameter and the 13 V parameter sets [67].

To perform the calculation of those parameters, the sampled surface must be initially processed by establishing a reference plane, obtained through least squares [25]. Let $z(x_i, y_j)$ be a 3D equispaced sampled surface, formed by a set of points $x_i = i\Delta x : i = 1, 2, ..., M$, and $y_j = j\Delta y : j = 1, 2, ..., N$, being Δx and Δy the sampling intervals, and M and N the number of sampling points along the x and y axis, respectively. A least squares mean plane $f(x, y)$ calculated on the aforementioned dataset is calculated, and shall serve as the reference datum, so that all parameters

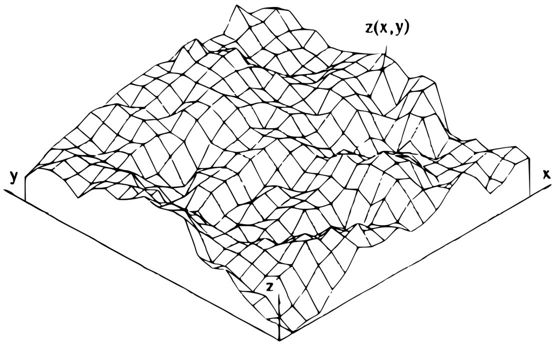

Figure 4.6. Sampled 3D surface transformed into a height function. After Dong *et al.*, 1992 [23]

are calculated on the resulting surface $\kappa(x, y)$, calculated as follows:

$$\kappa(x, y) = z(x_i, y_j) - f(x_i, y_j) \tag{4.2}$$

4.2.1.1 S parameter set

The first descriptor set that allows the exploitation of the topological data delivered by the $\kappa(x, y)$ dataset, is composed by the 12 S parameters. Table 4.6 summarises the mathematical expressions that lead to their calculation. The interpretation of each parameter is developed along the following paragraphs.

4.2.1.2 S amplitude parameters

They represent statistical characteristics of the surface height distribution, the scale of the irregularities, and the extreme points it presents. Due to their definition, all of them have a corresponding analogous parameter defined in 2D, calculated from the linear height distribution. Both the average surface texture, S_a, and the RMS height, S_q, are related to the scale of the surface texture, as already presented above for their two-dimensional counterparts. S_{10z} represents the amplitude of maximum deviations.

The skewness and kurtosis are actually defined in statistical analysis as the 3^{rd} and 4^{th} order central moments of the surface (Table 4.7). According to this definition, the RMS parameter is actually the second central moment, hence the statistical relevance already attributed to this parameter in detriment of S_a.

Table 4.6. 12 S parameter set for surface topography assessment, as defined in the ISO 25178.

Amplitude	
Root mean square height	$S_q = \sqrt{\left(\frac{1}{MN}\sum_{j=1}^{N}\sum_{i=1}^{M}\eta^2(x_i,y_j)\right)}$
Skewness	$S_{sk} = \frac{1}{MNS_q^3}\sum_{j=1}^{N}\sum_{i=1}^{M}\eta^3(x_i,y_j)$
Kurtosis	$S_{ku} = \frac{1}{MNS_q^4}\sum_{j=1}^{N}\sum_{i=1}^{M}\eta^4(x_i,y_j)$
Arithmetical mean height	$S_a = \frac{1}{MN}\sum_{j=1}^{N}\sum_{i=1}^{M}\mid\eta(x_i,y_j)\mid$
Ten-point height	$S_{10z} = \frac{1}{5}\left(\sum_{k=1}^{5}\mid\eta_{si}\mid+\sum_{k=1}^{5}\mid\eta_{vi}\mid\right)$
Maximum peak height	$S_p = \max\{\eta(x_i,y_j)\}$
Maximum pit height	$S_v = \min\{\eta(x_i,y_j)\}$
Spatial	
Fastest decay autocorrelation length	$S_{al} = \min\left\{\sqrt{t_x^2+t_y^2}\right\} : AACF(t_x, t_y \le 0.2)$
Texture aspect ratio	$S_{tr} = \frac{\min\left\{\sqrt{t_x^2+t_y^2}\right\}}{\max\left\{\sqrt{t_x^2+t_y^2}\right\}}$
Hybrid	
Root mean square gradient	$S_{dq} = \sqrt{\frac{\sum_{j=4}^{N-3}\sum_{i=4}^{M-3}\left(\frac{\kappa(x_{i+1},y_j)-\kappa(x_i,y_j)}{\Delta x}\right)^2+\left(\frac{\kappa(x_i,y_{j+1})-\kappa(x_i,y_j)}{\Delta y}\right)^2}{(N-6)(M-6)}}$
Developed interfacial area ratio	$S_{dr} = \frac{\sum_{j=1}^{N-1}\sum_{i=1}^{M-1}\sqrt{1+\left(\frac{\kappa(x_{i+1},y_j)-\kappa(x_i,y_j)}{\Delta x}\right)^2+\left(\frac{\kappa(x_i,y_{j+1})-\kappa(x_i,y_j)}{\Delta y}\right)^2}}{(N-1)(M-1)}-1$
Miscellaneous	
Texture direction	S_{td} Angle of texture's main direction

Table 4.7. Central moments of a surface height distribution. After King & Davis (1982) [69]

Function	Order	Statistical descriptor
$\mu_n = \int_{\infty}^{-\infty} y^n\, dy$	2	Root mean square
	3	Skewness
	4	Kurtosis

Figure 4.7 shows typical values of both parameters. The skewness value, S_{sk}, represents the proportion of negative and positive points in the profile, as it can take negative or positive values according to its definition. Skewness = 0 is the reference value for equilibrated Gaussian distributions. Negatively skewed surfaces are predominantly peak biased. Many processes, such as lapping or plateau honing generate these kind of surfaces, whereas positively skewed ones are not so easily obtained. On the other hand, Kurtosis, S_{ku} gives an idea of the abruptness of the surface. A Gaussian distribution is characterised by kurtosis value 3, which is its reference value. Higher values correspond to leptokurtic surfaces, typical of spiky surfaces, whereas kurtosis lower than 3 is typical of non-abrupt platykurtic surfaces.

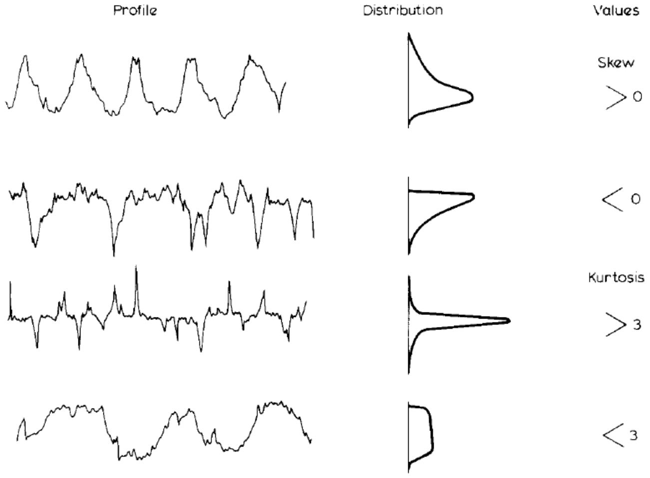

Figure 4.7. Surface profiles and height distributions showing the effects of skewness and kurtosis. *Top to bottom:* positively skewed, negatively skewed, leptokurtic and platykurtic distributions. After Thomas, 1981 [146]

Skewness and Kurtosis can be easily interpreted and, according to Stout & Davis (1984) [138], used to relate the characteristics of a surface with its functional performance. For instance, medical, food and antifatigue components require low kurtosis surfaces, which are related to unscratched surfaces desired for those applications.

4.2.1.3 S spatial parameters

These parameters represent a practical set to evaluate the texture of the surface, and they introduce the factor of directionality in topology characterisation. They do not have a 2D correspondence, as the spatial factor is not present if a directionality is fixed by a certain sampling line. They are calculated according to an areal autocorrelation function of the sampled surface, AACF , which describes the dependence of the height data at one position on the values at another position of the same dataset [26].

$$\begin{cases} AACF(t_i,t_j) = \dfrac{1}{(M-i)(N-j)} \sum_{l=1}^{N-j} \sum_{k=1}^{M-i} \eta(x_k,y_l)\eta(x_{k+i},y_{l+j}) \\ i = 0,1,...,m < M; j = 0,1,...,n < N \\ t_i = i\Delta x; t_j = j\Delta y \end{cases} \tag{4.3}$$

where m and n are the maximum numbers of the autocorrelation lengths in the x and y directions, respectively, and M and N are the number of sampled points along x and y.

The parameter S_{al} represents the shortest distance in which the value of the AACF decays under a threshold, normally 0.2. Large values of this parameter represent surfaces dominated by low frequency components, that is, the surface features are repeated along longer distances, and, therefore, are characterised by high scale features and irregularities. On the other hand, the S_{tr} parameter is useful to identify the existence of a preferential texture pattern. This ratio ranges between 0 and 1, being 0 for surfaces who show strong anisotropy, that is, an outstanding preferential direction in the texture.

4.2.1.4 S hybrid and miscellaneous parameters

These parameters combine spatial and amplitude features of the surface, by evaluating the degree of heterogeneity of the average slope shown by the surface features. S_{dr} represents the ratio of the increment of interfacial area of a surface over the flat sampling area. Large values of the developed interfacial area are related to rough surfaces. Therefore, its value tends to 0 as the surface presents a state nearer from a finishing. Superfinished surfaces usually show values smaller than 1%, which is the value usually taken as reference. Alternatively, S_{dq} calculates the root mean square of the surface slope within the sampling area. Whereas S_{dr} has an intuitive definition, S_{dq} has a strongest statistical meaning. However, both parameters provide similar information about the finishing state of the surface.

On the other hand, the S_{td} miscellaneous parameter is the value of the angle that indicates the main direction of the surface features with respect to the y axis. Therefore, it is useful in highly anisotropic surface that show a preferential texture direction.

4.2.1.5 V parameter set

The complementary 13 V parameter set (Table 4.8) is actually an evolution of the calculations proposed by Abbott-Firestone [1], by expanding their definition of bearing-area curve to a three-dimensional height dataset. The parametrisation of the bearing curve help to assess the topological features of a surface, while allowing the systematisation of the analysis of the curve by reducing it to a few parameters, which can be subsequently divided into two main groups. First, the amplitude descriptive parameters that represent the main geometrical features of the surface. Secondly, the volumetric parameters (void and material volumes), which are used to adopt a functional perspective of the height distribution of a surface, as the peak zone is associated to the material which shall eventually be the initial recipient of running-in wear, the core corresponds to the stationary bearing material, and the valley zone is related to the surface capability for lubricant retention and debris evacuation [67].

The approach of dividing the material into peak, core and valley zones requires a systematic method to establish the difference. In this dissertation, the ISO 13565-2 method is used. It is based on tracing a line secant to the Abbott-Firestone (AF) curve with the lowest gradient, with the restriction that the points defining the line must span 40% of bearing area percentage (x axis). Its intersection with the y axis defines the peak, core and valley areas, as is shown in Figure 4.8 [68].

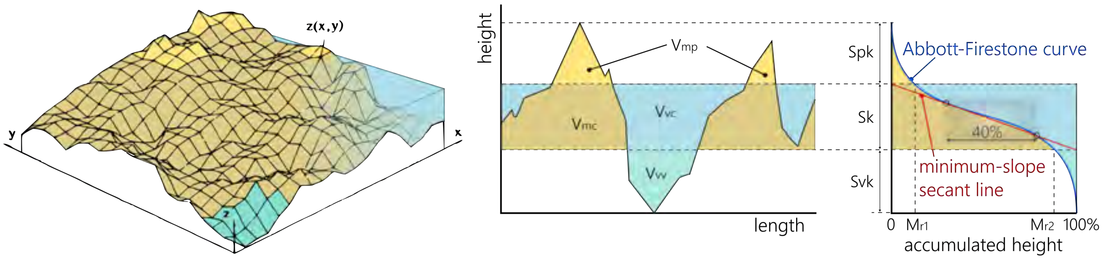

Figure 4.8. Main V parameters related to the bearing area curve, represented in 2D. Extrapolation to 3D can be easily visualised.

Table 4.8. The 13 V parameter set, as defined in the ISO 25178.

Name and symbol		Definition
		Areal parameters
Core distance	S_k	Distance between highest and lowest level of core
Reduced peak height	S_{pk}	Average height of protruding peaks above the core
Reduced valley height	S_{vk}	Average height of protruding valleys below the core
Peak material ratio	M_{r1}	Ratio of the area which separates the peak and the core
Valley material ratio	M_{r2}	Ratio of the area which separates the core and the valley
Plateau root mean square deviation	S_{pq}	Slope of linear regression on the plateau region
Dale root mean square deviation	S_{vq}	Slope of linear regression on the valley region
Relative material ratio	S_{mq}	Peak-to-valley material ratio
		Void volumes
Valley void volume	V_{vv}	Void volume in the valleys
Core void volume	V_{vc}	Void volume in the core material
		Material volumes
Peak material volume	V_{mp}	Material volume in the peaks
Core material volume	V_{mc}	Material volume in the core material
		Other
Peak extreme height	S_{xp}	Difference of heights at the average plane and peaks on the surface after especially high peaks on the surface are removed

4.2.1.6 Surface registration and influence of the acquired surface size

The burnishing patches derived from all tests were registered by an ALICONA Infinite Focus device. This device is able to register the topology of a surface by successive image acquisition along the vertical direction, without contact with the surface. Its functioning principle is focus variation achieved at different heights, assisted by a coaxial LED ring light, that assigns a height coordinate depending of the focal distance for each measured point. The 10x objective was used to perform this acquisition, delivering to the system a 100 nm vertical resolution.

In order to homogenise the measurement and discarding edge effects that could eventually distort the measurement, only the central areas of the burnishing patches were acquired. However, as standards do not define the exact area that guarantees an unambiguous characterisation of the target surface, a preliminary study was performed on the S_1^0, S_2^0 and S_3^0 machined surfaces (Figure 4.3), to determine the optimal size of the target area to be acquired. This operation was necessary in order to minimise the acquisition time of all burnishing surfaces, while not losing valuable data or aliasing the measurements for ulterior topological analysis.

As all three machined topologies consist on a highly periodic pattern formed by alternated peaks and valleys, it was decided to adjust the dimensions of each patch to include an integer value of coupled peak&valley pairs (henceforth P&V) . Due to the variation in the scale of topology features, this strategy involved capturing different sizes for each P&V set depending on the surface, as shows Figure 4.9.a.

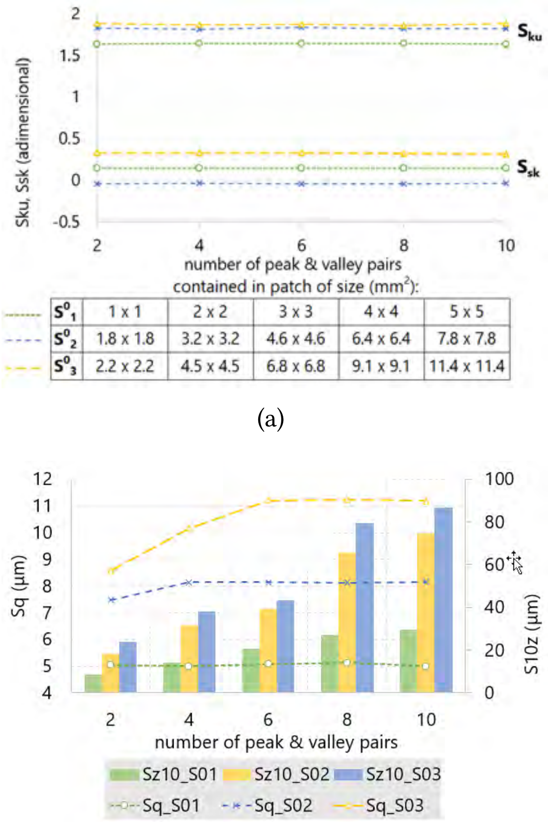

S^0_1	1 x 1	2 x 2	3 x 3	4 x 4	5 x 5
S^0_2	1.8 x 1.8	3.2 x 3.2	4.6 x 4.6	6.4 x 6.4	7.8 x 7.8
S^0_3	2.2 x 2.2	4.5 x 4.5	6.8 x 6.8	9.1 x 9.1	11.4 x 11.4

(a)

(b)

Figure 4.9. Evolution of some S parameters with respect to the sampling size. **a**. S_{sk} and S_{ku}. **b**. S_q and S_{z10}.

Table 4.9. Errors calculated from the repeatability of S parameters on the machined surfaces.

		S_q (µm)	S_{10z} (µm)	S_{sk}	S_{ku}	S_p (µm)	S_v (µm)	S_{dq}	$S_{dr}(\%)$
S_1^0	Av.	5.163	22.985	0.155	1.681	14.834	9.210	0.141	0.983
	St.Dev.	0.143	2.642	0.009	0.050	2.001	0.453	0.006	0.077
	Error	2.78%	11.49%	5.47%	2.94%	13.49%	4.92%	4.37%	7.80%
S_2^0	Av.	8.165	39.175	-0.058	1.814	38.0764	14.912	0.155	1.158
	St.Dev.	0.055	3.298	0.006	0.026	9.830	0.433	0.005	0.049
	Error	0.68%	8.42%	10.48%	1.45%	25.82%	2.90%	3.15%	4.19%
S_3^0	Av.	11.052	46.625	0.266	1.771	33.687	18.979	0.128	0.767
	St.Dev.	0.106	4.433	0.018	0.035	4.813	1.378	0.004	0.039
	Error	0.96%	9.51%	6.58%	1.95%	14.29%	7.26%	2.73%	5.09%

Whereas the S_{sk} and S_{ku} of the surfaces show stability for all sampling sizes, the evolution of S_q shows that the surfaces defined by larger features require larger areas to be fully characterised (Figure 4.9.a). For instance, S_1^0 shows the same S_q value for all sizes, so that 2 P&V, –that is, a 1 × 1 mm^2 surface– represent sufficiently the whole surface. On the contrary, a surface similar to type S_3^0, more abrupt, must be at least described by 6 P&V, or a 6.8 × 6.8 mm^2 surface. That is the value from which S_q stabilises and shows no variation with the sampling size.

Unlike the second, third and fourth moments of the surface, the S_{10z} extreme value does not show any signal of stabilisation, as it increases as the surface size grows. This effect is not atypical for this parameter, as explain Dong *et al.* (1994) [25]. Indeed, due to the fact that the summit heights are calculated by algorithms that depend on the evolution of the slope of the surface, so that atypical values can be discarded, they are sensitive to the sampling interval. Therefore, as that interval increases, the threshold to define a characteristic peak point increases, and the value of S_{10z} grows naturally.

At sight of the results, it is decided to take patches containing 6 P&V sets for all surfaces. A second measuring phase was carried out, by registering the three initial topologies five times at different positions of the whole machined surface. The descriptors measured at all patches were averaged, and the error associated to their repeatability was calculated (Table 4.9). For instance, the average value of S_{ku} for S_1^0 is 1.6816 µm, with a standard deviation of 0.0494 μm. That represents an error of 2.94% in terms of repeatability. This error is enclosed between 1.5% and 3% for all initial states. There is not an increase of error as the surface present more abrupt features, thus allowing the validation of the selected approach to perform the measurements.

All amplitude parameters show acceptable low error values, while, on the contrary, extreme parameters S_{10z}, S_p and S_v present a lower repeatability. This observed effect can be understood from the way these values are defined, their sensitivity with regards to the sampling area, and their higher dependence of extreme values which can be inconspicuously present as anomalous values in a certain acquired surface. Consequently, these extreme parameters must be taken carefully into consideration in the topological analysis to come.

4.2.1.7 Retained topological parameters from the S set

Given the high amount of 2D and 3D parameters available to describe the surface, it is worth reconsidering the possibility of discriminating parameters that might be redundant with regards to others, or that do not deliver any valuable information to the system of study. Table 4.10 shows the selected parameters for each surface feature.

Table 4.10. Retained topological parameters from the S set.

Surface feature	Retained parameter	Rejected parameters
Amplitude – scale	S_q	S_a
Amplitude – extreme points	S_{10z}	S_p, S_v
Spatial	S_{al}, S_{tr}	–
Hybrid	S_{dq}	S_{dr}
Miscellaneous	S_{td}	–

The mean square surface texture S_q shall be preferred over the average one S_a as the general amplitude descriptor of the surface finishing. As already explained, it can be consistently framed in the statistical analysis to be performed. Furthermore, King & Spedding (1982) [69] proved that both parameters were proportional to one another. Skewness and Kurtosis shall also be considered in the results discussion, for their uniqueness in surface characterisation. As for the extreme value parameters, S_{10z} is preferred over the peak and valley extreme values S_p and S_v.

The spatial and miscellaneous parameters, that is, S_{al}, S_{tr} and S_{td}, are also kept for analysis. However, not both hybrid parameters are required, for they give similar information about the surface, that is, its proximity to a finishing state. As the error associated to repeatability of both parameters is similar, it is decided to keep S_{dq}, due to its scale proximity to S_{tr}, that facilitates further representation. All these parameters shall be completed by other descriptors belonging to the V parameter set, as shall be specified in the result discussion chapter.

4.2.2 Metallurgical characterisation of subsurface layers

Analysing the metallurgical state of the surface and subsurface layers is fundamental to characterise the effects of VABB on surface integrity. Changes in metallography are usually explained through the hardness magnitude, as the phases that compose a certain metal have different structures, and consequently pose different behaviours towards indentation tests. For that reason, in addition to visual inspection of the microstructure of a metal, the mentioned tests are highly representative of this surface integrity descriptor.

Specimen preparation is common for both techniques. The protocol includes material cutting, so that the deep layers of the surface can be then studied. The next step consists on specimen encapsulation in resin (Figure 4.10) which is then polished. The result of the described process is a mirror-polished specimen encapsulated in a stable resin body. This kind of specimens can be used to assess the hardness of the specimen through microindentation testing.

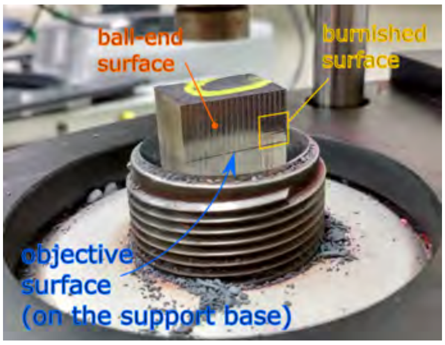

Figure 4.10. Overview of specimen positioned on the encapsulating machine plate.

A Buehler 5114 Vickers hardness testing machine was used to perform them (Figure 4.11.a). This measurement was undertaken according to the ASTM Standard E 384, which describes the calculation methods and establishes the characteristics of valid Vickers imprints.

This test, developed by Smith and Sandland in 1925, aimed to substitute the Brinell

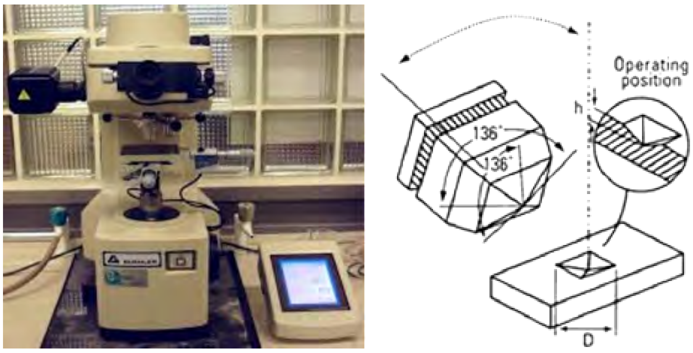

(a) (b)

Figure 4.11. Vickers microindentation hardness test scheme.

test, which was based on the usage of different indenters that made measurements non-comparable among them. The Vickers test uses a pyramidal diamond indenter, and contemplates a smooth application of the load, forcing the indenter into the piece, and keeping it inside it for 10 s (Figure 4.11.b). After the load is removed, the two impression diagonals are measured and averaged. The Vickers hardness (HV) is calculated as follows:

$$HV = \frac{1854.4\,p}{d^2} \tag{4.4}$$

where p is the load applied on the specimen in gf, and d is the average diagonal of the indentation in $\mu\mathrm{m}$.

Normally, the highest difficulty facing hardness measurements is the selection of the load. Indeed, although the actual hardness results should be stable regardless of its value, numerous studies about microindentation techniques have shown that results are not stable at low loads due to a higher experimental error and the indentation size effect. Therefore, excessive reduction of the indentation load can lead to a high error. The load selection is therefore an important factor to bear into account, especially for multiphase materials, which might show highly disperse hardness results if small loads are applied. If selective microstructural grains are spanned in the indentation, the average of all measurements could not be descriptive of the whole material.

Once hardness was measured, specimens were prepared for optical microscopy and SEM observation. An etching operation was performed to guarantee enough contrast between phases, and fully reveal the microstructure of the target specimen. Although etching techniques are varied, chemical attack is often selected for this aim because of its easiness of application. Chemical etching is based on the fact that metal phases react at different speeds with chemical reagents. Therefore, by putting them in contact with different chemical inorganic substances, the most vulnerable phases shall dissolve, revealing grain boundaries that differentiate them from the most stable ones that remain creating a nearly three-dimensional image of the material structure. As the AISI 1038 and Ti-6Al-4V are subjected to different etching operations, this stage is detailed in particular for each of them at subsequent subsections.

4.2.2.1 Error estimation for Vickers hardness measurements

For this dissertation, a minimum of 10 indentation tests are performed for each desired hardness measurement. As hardness is not an absolute measure, and depends on the point on which the indentation is performed, an error term must accompany the hardness value. In this case, the Student's t-distribution delivers the estimation the mean HV value for small size samples from which the mean and standard deviation of the population is unknown, as is the case. Therefore, the statistical uncertainty, E_s, associated to the HV measurement, can be calculated as:

$$E_s = \frac{s}{\sqrt{N_{HV}}} t_{\alpha, N_{HV}-1} \tag{4.5}$$

where s is the standard deviation of the HV sample and N_{HV} is the sample size, and $t_{\alpha, N_{VH}-1}$ is the Student's t statistic at a α confidence level.

A second term arising from experimental execution must be added. This term includes the error introduced by the limitation in optical resolution given by the microscope used to measure the indentation imprint diagonals, E_{opt}, considering that the maximum resolution achievable by the system is restricted by the light wavelength, as establishes the Rayleigh principle (Eq. 4.6) [9]. This term is fix for all measures, and depends on the equipment.

$$E_{opt} = 1.220 \frac{f\lambda}{D_l} \tag{4.6}$$

where f is the focal length of the objective, D_l is the diameter of the light beam, and λ is the light wavelength.

A third term related to the bias in the diagonal measurement caused by the spherical deviation of the operator's eyeball, E_e, must be considered in the experimental error. This term is calculated with a previous calibration phase performed on a standard block for hardness testing. The total error is, therefore, the addition of the three terms:

$$E = E_s + E_{opt} + E_e \tag{4.7}$$

4.2.3 Residual stress measurement

The methods to measure the residual stress (RS) state of a material are numerous, including both destructive and non-destructive techniques. The decision of what method to use is conditioned by the technical constraints that each of them pose, as well as the type of residual stress to be measured, as explain Withers & Badeshia (2001) [157]. For instance, the deep hole drilling technique is an effective method to assess type-I residual stress gradient along progressively deeper layers of the material, by the adhesion of strain rosettes and gauges on the surface. In previous works, this method has been successfully used by the author of this dissertation to evaluate residual stress on AISI 1038 and AA2017-T4 surfaces [40]. However, specimen preparation is highly time consuming, comprising delicate gauge adhesion onto the target workpiece. Furthermore, the low repeatability of the method makes it infeasible for the purposes of this thesis, where 108 burnishing tests must be measured.

Alternatively, the X-ray diffraction method has been selected to evaluate the superficial residual stress after VABB. The technique is based on applying Bragg's law while quantifying the change of interplanar spacing inside crystals which conserve elastic strain confined inside plastically deformed crystals due to VABB. As elastic strain results in a change of the lattice dimension, crystalline planes inside the grains are actually used as intrinsic strain gauges in this method. Albeit the major drawback of this diffraction method is the low depth to which compressive residual stresses measurements can be performed, its technical availability and feasibility makes it proper to evaluate VABB results in this experimental plan.

Bragg's law states that when an X-ray beam with a certain wavelength is incident onto a crystal, it is diffracted by the same angle. This is only true for certain waves that verify the analytical expression of the law (Eq. 4.8). Let us consider an X-ray beam irradiating a surface with incidence angle θ, on a set of crystalline planes defined by an interplanar distance, d, then all magnitudes are related as follows:

$$2\,d\,\sin\theta = n\,\lambda \tag{4.8}$$

where d is the interplanar distance between planes, θ is the diffraction angle, λ is the wavelength of the beam, and $n \in \mathbb{N}$ is the order of diffraction.

Let us consider a crystal in an non-deformed state, characterised by an interplanar spacing d_0. In that case, the diffraction angle shown by an X-ray beam is θ_0. After experiencing a deformation, that distance has diminished due to plastic strain and compression to d_ψ, and reflexes the X-ray wave a θ_ψ angle (Figure 4.12).

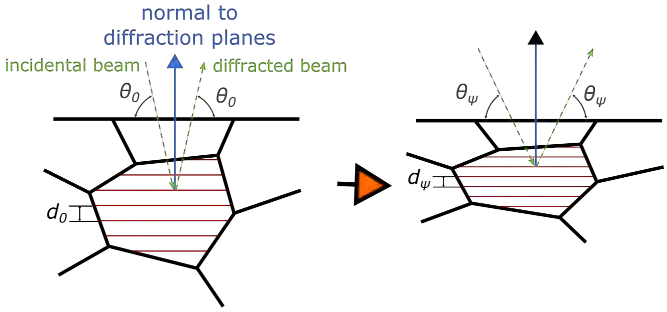

Figure 4.12. X-ray diffraction in a non-deformed crystal (*left*) and a deformed crystal (*right*).

As in both states is Bragg's law true, the initial state and the state after modification can be related as expressed in Eq. 4.9. That initial state is characterised by reference interplanar distance d_0, and diffraction angle, θ_0, which are determined by applying the technique to reference standard specimens obtained by powder metallurgy, which are free of residual stress.

$$d_0 = d_\psi \frac{\sin\theta_0}{\sin\theta_\psi} \tag{4.9}$$

The explained principle allows the calculation of deformation of crystals and link it to the stress state that generates that deformation, i.e. the residual stress, as follows. The multiangle technique used in this dissertation consists on irradiating the surface with an X-ray collimator mounted on a goniometer. That device is equipped to adjust the azimuth angle, ϕ , in which the measure shall be performed. Once this angle has been fixed, the collimator irradiates the surface with X-ray at different incidence angles, θ. Of all those beams, only the one complying with Bragg's law shall be detected by a receiver coupled to the system. This operation is repeated for several negative and positive tilt angles, ψ, regulated through the motorised workpiece base. Once this operation has been completed, the goniometer is used to change the azimuth angle and take a subsequent measurement.

Along the described process, for each tilt angle at each azimuth position, the intensity registered by the receiver is saved for every explored angle $2\theta_\psi$ is represented in a diffraction spectrum. Each pair $\phi-\psi$ has an associated diffractogram on which an intensity peak is present for the irradiation angle for which Bragg's law is satisfied, $2\theta_\psi$ (Figure 4.13).

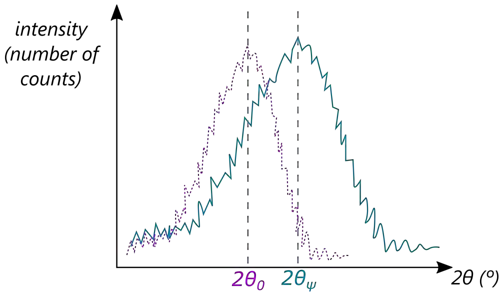

Figure 4.13. X-ray diffraction spectrum showing a diffraction peak at $2\theta_\psi$ position, with regards to the spectrum registered for the reference material, $2\theta_0$.

The residual stress quantification is based on the analysis of a set of those spectra. The calculation of the interplanar distance for every tilt angle $\phi-\psi$, and its comparison with the reference non-deformed distance, delivers the deformation to which the crystal is being subjected, through the following equation:

$$\varepsilon_{\phi\psi} = \frac{d_\psi - d_0}{d_0} = \frac{\sin\theta_0}{\sin\theta_\psi} - 1 \tag{4.10}$$

If the strain state of the crystal is considered tridimensional, then that deformation can be related to the stress state that generates it, that is, the residual stress, through the elastic mechanics equations in a continuum:

$$\varepsilon_{ij} = \frac{1+\nu}{E}\sigma_{ij} - \frac{\nu}{E}\delta_{ij}\sigma_{ij} \tag{4.11}$$

where $\delta_{ij} = 1$ if $i = j$ and $\delta_{ij} = 0$ if $i \neq j$

As this elastic strain in measured along the normal direction to the diffracting planes at a certain tilt position of the collimator, $\ltimes$. It can be quantified by projecting the strain tensor on the $\mathbf{n}$ direction, as follows:

$$\varepsilon_{\phi\psi} = \mathbf{n}\,\varepsilon\,\mathbf{n}^T = \frac{1+\nu}{E}\left(\sigma_\phi - \sigma_{zz}\right)\sin^2\psi + \frac{1+\nu}{E}\sigma_{zz} - \frac{\nu}{E}Tr\left(\sigma\right) + \frac{1+\nu}{E}\tau_\phi\sin\left(2\phi\right) \tag{4.12}$$

Eq. 4.12 actually represents a function, namely $\varepsilon_{\phi\psi} = f(\sin\psi)$. Therefore, if $\varepsilon_{\phi\psi}$, i.e. 2θ by Eq. 4.10, is graphically represented against $\sin^2\psi$), the characteristic parameters of the linear fit (slope and intercept) can be compared to the graphical representation to deduce the values of the residual stress tensor (Figure 4.14). Specifically, normal stress σ can be calculated by determining the slope, whereas tangential stress τ are by the overture of the parabolic function fitted on the measured points. A measure at $\phi = 0^o$ delivers σ_x and τ_{xy}, whereas $\phi = 90^0$ allows the calculation of σ_y and τ_{yx}. Therefore, in practice, normally only these two azimuth angles are irradiated for one measurement.

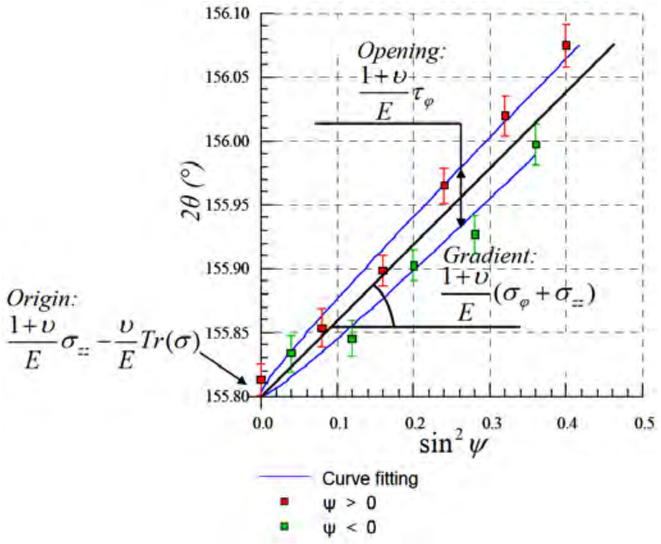

Figure 4.14. Linear representation of the $\sin^2\psi$ method. After Guillemot (2010) [49].

The technological application of the X-ray diffraction measurements changes according to the objective material. Table 4.11 shows the technological parameters used for both considered materials in this thesis. All tests were performed with a SET-X goniometer and the STRESSDIFF software was used to automatically register all diffraction measurements and calculate the stress tensor associated to the analysed burnishing patch. However, the data postprocessing was different. As the AISI 1038 diffractometer spectres hardly showed noise, the approximative FWHM-peak height method was used to estimate the diffraction angle. On the contrary, the spectres presented by Ti-6Al-4V spectres were postprocessed through polynomial fitting, to overcome the high noise presented by the measurement. Consequently, the incertitude associated to Ti-6Al-4V was higher, as shall be presented in the next chapter.

Table 4.11. Experimental characteristics of X-ray diffraction measurements.

Item	AISI 1038	Ti-6Al-4V
Anode type	CrKα	Vα
Exposition time	40 s	360 s
# measures	13	13
$2\theta_0$	156°	143.5°
$\{hkl\}$	Fe(α) $\{211\}$	Ti(α) $\{213\}$
estimated depth	15 µm	10 µm
post-processing method	FWHM and peak height	curve fitting

4.3 Material characterisation

4.3.1 AISI 1038 alloy

AISI 1038 is a medium-carbon steel alloy with medium-high machinability. It has been chosen for this experimental execution for two main reasons. The first one is to give continuity to previous works [43]. Secondly, the 1038 alloy is used for an extensive range of industrial applications such as gears, axes, shafts, or moulds, as well as larger components such as power shovels, due to its high versatility. Therefore, it is a steel prone to be found in numerous industrial workshops of different scale. Table 4.12 shows its composition according to the AISI standard.

Table 4.12. AISI 1038 weight composition.

Component	Fe	Mn	C	S	P
Weight (%)	98.6–99.05	0.6–0.9	0.35–0.42	≤0.05	≤0.04

The material has been provided as laminated bars of 100×60 mm section. A 170-mm long piece was cut from the bar to obtain the workpiece to be burnished, so that all planned essays could be carried out. The mechanical properties of that material were characterised by Travieso-Rodríguez (2010) (Table 4.13). They are considered as valid for this thesis, as the material was taken from the same bar.

To observe the metallurgical structure of the material, a sample from its core was extracted from the bar, and was cut along the lamination direction, coincidental with the milling direction, or direction II, according to the criterion established in Figure 4.3. A second specimen to observe the microstructure along direction I, was also

Table 4.13. AISI 1038 properties, as characterised by Travieso-Rodríguez (2010) [148].

Property	Value
Density	7.84 g/cm^3
Young's Modulus	211 GPa
Poisson's Modulus	0.29
Yield strength	416 MPa
Self-hardening coefficient	0.19

extracted. Both of them were prepared as explained at the precedent subsection, and etched by chemical action of a Nital solution. Figure 4.15.a shows the core material along direction I, as a matrix of pearlite and ferrite, usual in this kind of carbon steels. On the other hand, Figure 4.15.b shows that grains are aligned along direction II, as a clear effect of the lamination operation through which the raw material was obtained.

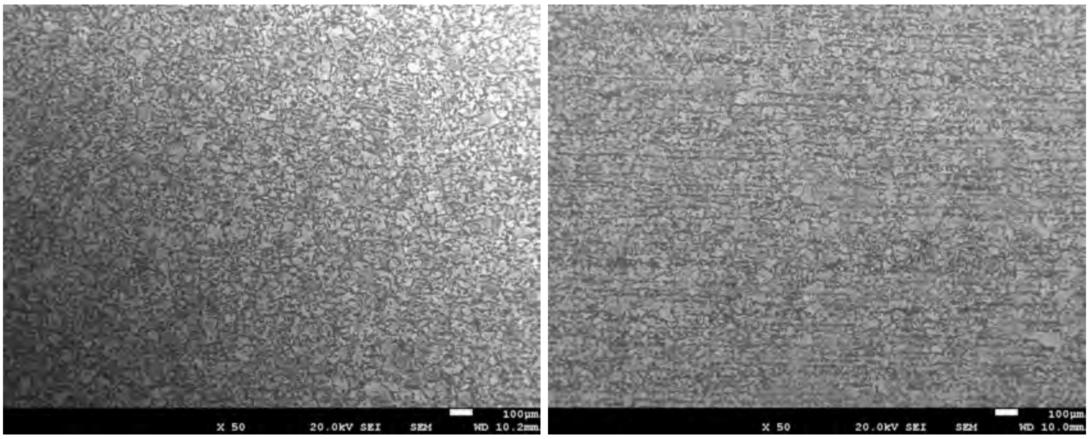

Figure 4.15. Metallographic observations of the AISI 1038 specimen at 50x. **a**. Direction I. **b**. Direction II (lamination).

The metallurgical characterisation of the material was completed through Vickers microindentation hardness tests, after polishing the specimens a second time to erase the effect of etching. Figure 4.16.a shows a detail of pearlite grain in the core material, leading to establish that the reference grain size is of the order of 20 µm. By applying a 100-gf load, burnishing imprints had an average size of around 30 µm, and, therefore, this load was confirmed as adequate. Indeed, as ferrite is considerably ductile and less hard than cementite, and therefore, pearlite formations, the indentation imprints were not localised on single isolated phases and no bias of the overall hardness measurement was detected. Figure 4.16.b confirms that Vickers indentations spanned a mix of both phases in the material core.

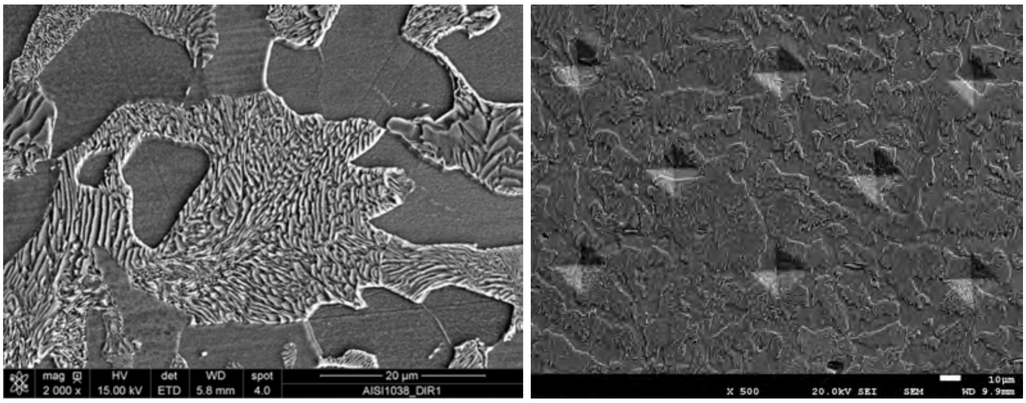

Figure 4.16. . **a**. SEM image of pearlite nucleation. **b**. Imprints after Vickers indentation spanning ferrite and pearlite structures.

Table 4.14 shows the average result of 15 hardness measurements along each direction. At sight of these results, the material can be considered isotropic in terms of hardness.

Table 4.14. Hardness measurements performed on the AISI 1038 specimens.

Direction	HV100	Error	Average d (µm)	max d (µm)	min d (µm)
Direction I	175	10.6	32.08	30.12	32.86
Direction II	180	10.5	31.86	29.99	32.74

4.3.2 Ti-6Al-4V alloy

The titanium alloy Ti-6Al-4V is a biphase material composed of $\alpha + \beta$ structures. The presence of both phases is achieved by the equilibrated combination of α-stabiliser interstitial Al, and β-stabiliser element V and Fe, as is shown in Table 4.15. The presence of both allotropic phases makes Ti-6Al-4V a versatile alloy offering an exceptional balance of strength, ductility, fatigue and fracture properties with application in the aeronautical industry to manufacture pressure vessels, gas turbine disks or compressor blades.

Table 4.15. Ti-6Al-4V weight composition according to AFNOR L14-601.

Component	Ti	Al	V	Fe	O	C	N	H
Weight (%)	88.1–91	5.5–6.75	3.5–4.5	≤0.25	≤0.2	≤0.08	≤0.05	≤0.01

The raw material used for the experimental phase was provided as a $105 \times 95 \times 165$ mm forged block. The standard properties are included in Table 4.16. Compared to the AISI 1038 alloy, this material presents a higher yield strength, what leads to think that higher forces should be applied to achieve permanent plastic strain via VABB.

Table 4.16. Grade 23 Ti-6Al-4V properties.

Property	Value
Density	4.4 g/cm^3
Young's Modulus	110 GPa
Poisson's Modulus	0.32
Yield strength	870 MPa
Self-hardening coefficient	0.3

As the historic of the material is unknown, the structure of the alloy along with its hardness were determine in a preliminary phase. A specimen was extracted from the core material, cut along the longitudinal direction and its perpendicular. Both resulting surfaces were then subjected to encapsulation and polishing treatments explained above. An indentation test was performed to calculate the hardness of the material. Table 4.17 contains the resulting hardness measurements, evidencing the original isotropy of the material.

Table 4.17. Hardness measurements performed on the Ti-6Al-4V specimens.

	HV100	Error	Average d (µm)	max d (µm)	min d (µm)
Direction I	311	9.1	24.5	16.19	23.16
Direction II	308	7.4	24.7	15.64	22.98

After the Vickers microindentation tests, chemical etching through Kroll's reagent was performed. The microstructure was then analysed through SEM observation. Figure 4.17.a confirms the biphase composition of the Ti-6Al-4V, equally distributed in both main directions. The α-titanium is depicted as the white regions, whereas the β-titanium is darkened by the used reagent. Both structures are organised as intergranular α embedded in a β matrix. As the β phase has a BCC structure, a large number of slip planes makes it more ductile and less resistant than the α hexagonal crystal structure, hence the relatively low hardness presented by the raw material, with regards to other metallurgical states of the same alloy [22].

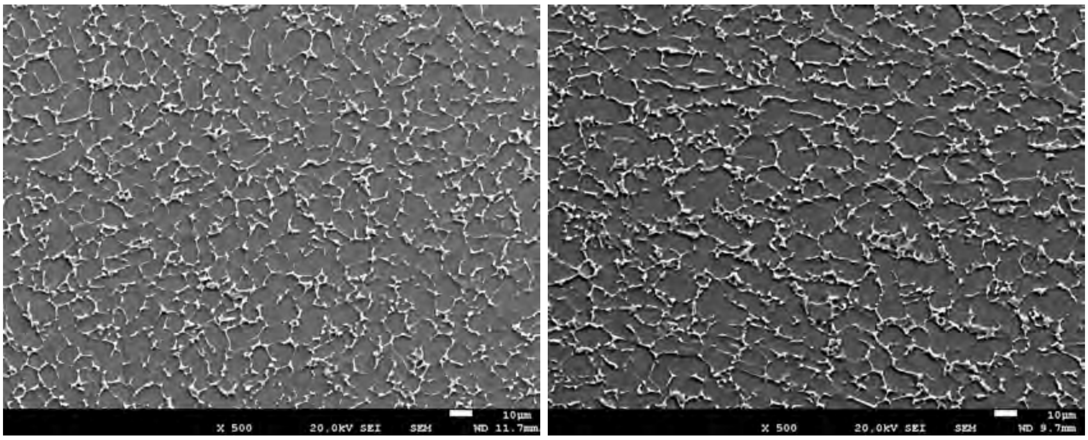

Figure 4.17. Metallographic observations of the Ti-6Al-4V specimen along direction I (**a**) and direction II (**b**).

Since the microstructure patterns of the alloy present an approximate grain size of 15 µm, the Vickers imprints derived from the indentation tests can be considered representative enough to characterise the material hardness. In fact, Figure 4.18 confirms that both phases can be adequately spanned by applying a 100-gf load.

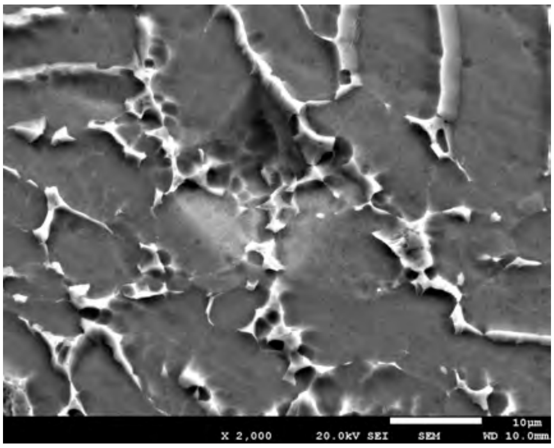

Figure 4.18. Detail of Vickers indentation performed on the Ti-6Al-4V.

4.4 Experimental execution

The tests were performed on a HURON KX10 3-axis milling machine equipped with a Kistler 9257B dynamometer located at the *École Nationale d'Ingénieurs de Tarbes*. To fix the workpieces to the machine table, they were drilled and screwed to it in order to monitor the forces applied during the burnishing tests (Figure 4.19.a). The data measured through the Kistler 5019A amplifier was registered through the DynoWare software. The experimental setup was completed by the external power circuit to which the VABB tool is connected and excited (Figure 4.19.b).

(a) (b)

Figure 4.19. Experimental setup. **a**. Detail of workpiece attached to a Kistler dynamometer. **b**. HURON KX10 milling machine where experiments were developed.

The workpieces were not removed from that position during the whole machining and burnishing processes. Like that, the perpendicularity of the burnished surface to the VABB tool was guaranteed, and references were kept constant. The workpiece preparation process started by a first surfacing operation with a multi-insert front milling tool. On that flat surface, the different ball-end milling strategies were applied to obtain the desired different surfaces, as explained in the next subsection.

4.4.1 Machining of the original surfaces

The influence of the original surface texture on the burnishing results is of high interest for this thesis, to associate the effectiveness of the process with a certain finishing degree that can be found in an actual industrial context. To that purpose, three different surfaces were planned to be tested. All of them were obtained by executing a face milling operation using a hemispherical milling tool with a TiN coating. The cutting speeds selected to perform the machining were 120 m/min and 70 m/min for the AISI 1038 and the Ti-6Al-4V workpieces respectively. Table 4.18 shows the geometrical machining parameters selected for all three surfaces. The generation of the original surfaces by choosing these parameters is fundamental to control and master the peak height and the material distribution on the surface, and, therefore, the expected texture. Furthermore, the chosen parameters can be undoubtedly identified with realistic machining conditions applied in an industrial context. Defining these parameters by adopting this approach is not casual, since it is of high importance to take profit of the derived results for potential industrial applications.

Table 4.18. Machining parameters applied to obtain the three original surface topologies.

	Machining parameters		
Original surface	a_e (mm)	a_p (mm)	tool diameter (mm)
S_1^0	0.5		
S_2^0	0.8	0.2	∅10
S_3^0	1.1		

To calculate the spindle velocity to be applied during machining through Eq. 4.13, the effective radius of cut r_e, that is, the contact between the hemispherical tool and the material plane, must be determined. This value represents the actual dimension which characterises the contact between the cutting tool and the objective material, as a function of the selected geometrical cutting parameters, as shows Figure 4.20. Its determination is important to optimise the tool life, avoid surface integrity defects due to detrimental chip removal mechanism, and preventing the coating to be worn out prematurely.

$$n = \frac{1000\, v_c}{2\, \pi\, r_e} \tag{4.13}$$

where n is the spindle speed in min^{-1}, v_c is the cutting speed in m/min.

All geometrical parameters can be mathematically related through a rectangle

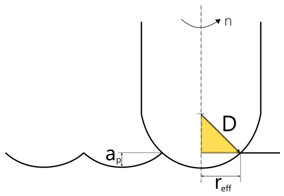

Figure 4.20. Hemispherical front milling geometric system.

triangle. Therefore:

$$D^2 = r_e^2 + (D - a_p)^2 \tag{4.14}$$

where D is the milling tool diameter and a_p is the depth of cut.

As $a_c^2 \ll D a_c$, Eq.4.14 can be simplified, and the effective radius can be calculated as:

$$r_e = \sqrt{2\,D\,a_c} \tag{4.15}$$

4.4.2 Burnishing force measurement

Being able to register the forces while the burnishing operation is being executed allows the control of the force level that is being applied, as well as quantifying the force fluctuation during the test. This is the reason why the test pieces are attached to the Kistler dynamometer. The device delivers a register of the forces applied according to a Cartesian reference system, where F_z represents the burnishing force, whereas F_x is the tangential force that appears during the execution of the process, opposed to the feed movement of the tool. Although it cannot be formally defined as a friction force, it shall be referred to as pseudo-frictional due to its dynamic opposition to the feed motion.

As the sampling frequency of the Kistler amplifier is 2 kHz, the registered signals cannot evidence the vibratory component delivered by the piezoelectric. Under this circumstance, the forces acquired during the VABB and the NVABB tests should have in essence the same behaviour, as only the force governed by the spring, F_p, is registered. The first 15 s of each test were acquired to reduce the amount of data to manipulate. This portion of registered forces were exported as `.csv` files, and processed through a Matlab routine composed of different scripts.

The observation of the NVABB and VABB forces registered for each testing conditions showed a similar pattern. Figure 4.21.a shows test #25 performed on Ti-6Al-

4V as an example. All forces were equal to zero during an initial timespan during which the VABB tool was plunging onto the target surface. As soon as contact was established between them, the force increased linearly, proportional to the plunging velocity, until the programmed spring compression was achieved. From that point, the registered forces show a repetitive pattern. F_z exhibits an oscillatory behaviour, while F_x changes its sign as the different burnishing passes are completed in one direction, and the next one starts. The point in which F_x achieves value 0 is used in the script to determine the original point of each burnishing pass, and isolate a single burnishing cycle (two passes in opposite directions), as shows Figure 4.21.a.

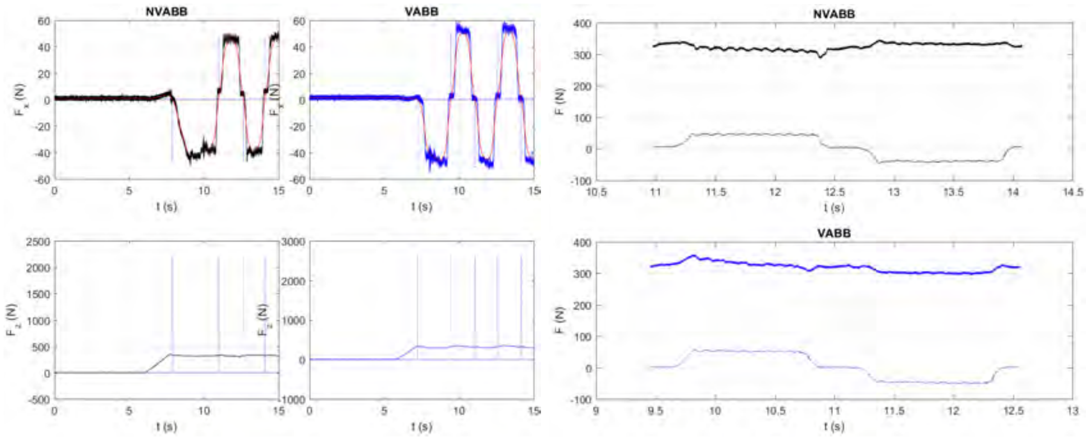

(a) (b)

Figure 4.21. F_x and F_z measurement during the VABB and NVABB tests #25 in Ti-6Al-4V workpiece. **a**. Identification of burnishing cycles through fitted signal (red). **b**. Extracted forces at two burnishing cycles.

The objective of this strategy is quantifying the singular values that describe the registered forces for all tests and characterise the nature and evolution of that preload to ultimately declare equivalent force level during VABB and the complementary NVABB test. Without this confirmation, the comparability of tests could be questioned. Figure 4.22 shows all mean forces, along with the maximum and minimum values computed for all tests. All means show a consistent correspondence with the objective mean preload established at the experimental design. Furthermore, they present maximum and minimum values of the oscillating cycle which are of similar order of magnitude for all tests. Whereas it is impossible to keep force perfectly constant along all executions according to the desired level, this comparative representation leads to the conclusion that all forces were comprised inside similar levels.

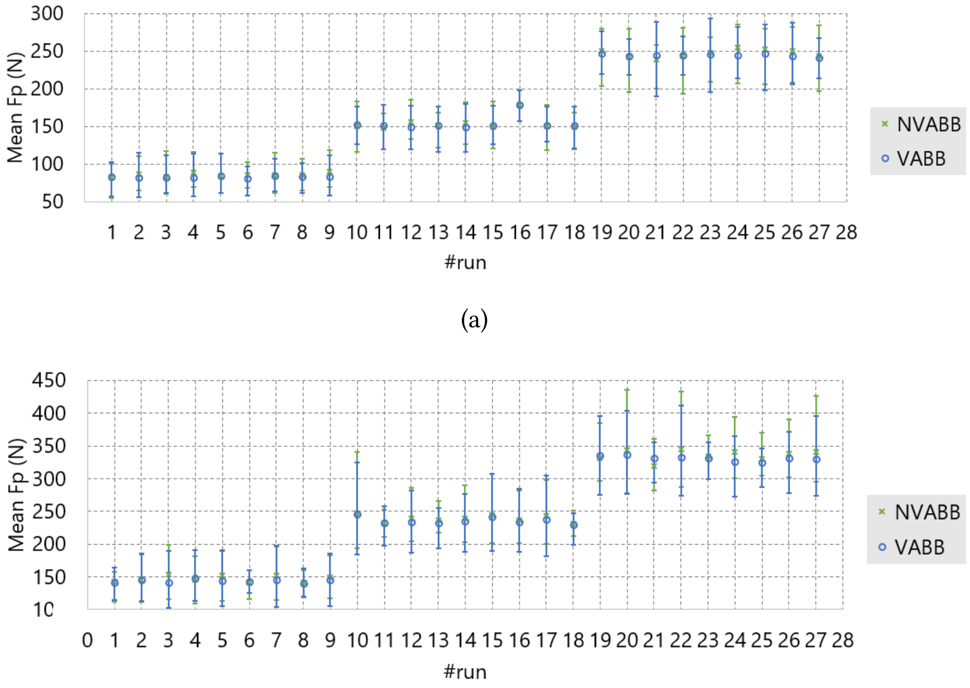

(a)

(b)

Figure 4.22. Mean F_z registered for all burnishing cycles, and maximum and minimum forces registered. **a**. AISI 1038. **b**. Ti-6Al-4V.

4.5 Recapitulation

In this chapter, the issues related to the experimental development of this thesis is presented, including two main types of information which are summarised in this recapitulation section.

1. An L27 Taguchi orthogonal array has been chosen to develop the experimental plan to test the VABB prototype on both AISI 1038 and Ti-6Al-4V workpieces. This arrange allows the analyse of five different factors at three levels, along with three paired interactions among three of them.

2. The X-ray diffraction technique has been selected to perform residual stress measurement, due to the availability of the equipment and the amount of measurements to be carried out.

On the other hand, albeit the descriptive nature of this chapter, some partial results have been presented as auxiliary data to validate and set up the experimental strategy. They can be presented as follows:

1. A trial-error approach has been applied to decide the size of the patches to acquire of each burnishing test to obtain relevant information about its texture parameters. Finally, it has been decided to acquire patches containing 6 peaks & valleys of each surface. The actual size of the patch changes depending on the target surface, due to the different machining strategies from which each of them was obtained.
2. A detailed study considering numerous descriptors of surface topology has lead to the determination of the parameters that adequately can describe the changes in the surfaces. They shall be included in the result discussion in the next chapter.
3. A metallurgical analysis of the materials was performed, along with an initial hardness measurement assessment through Vickers microindentation tests. A 100 gf load has been set as an adequate level to assess hardness, as it is able to quantify the effects of all microstructural structures present in both materials.
4. The analysis of forces acquired during all VABB and NVABB specimens revealed that, in mean and absolute terms, both processes do not show a remarkable different behaviour. All mean forces representing an approximate value of the preload force show a stable value along all tests. However, if the pseudo-frictional force is analysed, the initial surface state shows a conspicuous influence on its value, reaching the highest relative values for the less finished one, S_3^0. On the other hand, an increase in the preload force shows a relative decrease of the pseudo-frictional one. From this point of view, the process shows a more effective behaviour for higher forces.

The next chapter includes the main results arising from the experimental plan that has been designed and explained along the previous pages.

5

Experimental results and discussion

In this chapter, the results derived from the execution of the Taguchi experimental array on the AISI 1038 and the Ti-6Al-4V alloys are presented and discussed. The chapter is organised by surface integrity parameters, including first the results regarding the steel alloy, and then those corresponding to the titanium alloy. Figure 5.1 summarises the different areas included in the result discussion.

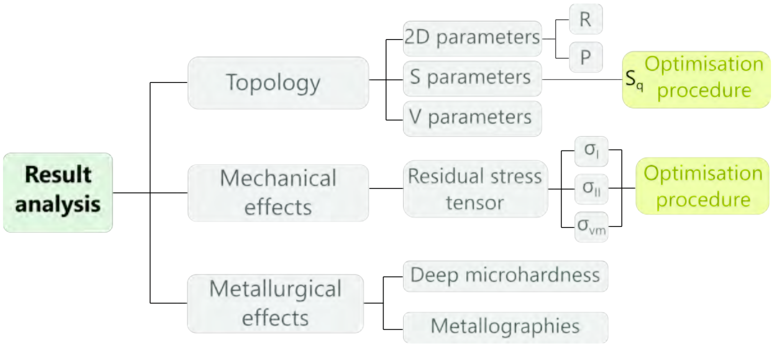

Figure 5.1. Summary of items included in the result analysis.

Of all aspects of surface integrity that are analysed, some of them are qualitative.

On the other hand, specific quantitative indicators shall be subjected to an optimisation procedure, since one of the aims of this chapter is defining the parameter sets that deliver the best surface integrity results. "Optimal" is understood here as the factor levels that can be found in the DOE, that have the most enhancing effects on the surface. The criteria to define the term "best", depends on the optimisation target, and shall be specified according to the area of study.

5.1 Geometrical parameter: surface texture

This section tackles with the influence of the VABB process on the topological state of both materials, being later compared with the NVABB effects. The aim of this section is exploring a new approach for texture assessment after ball burnishing. With that purpose, the parameters included in Table 5.1 are from a start considered. However, the reader shall notice that, due to the nature of the surfaces derived after VABB and NVABB, not all parameters are able to systematically represent the way the material is distributed on the surface after their execution.

To perform the study, and discriminate the best set of parameters to fully describe the topological effects of ball burnishing, the first subsection of each material aims to characterise the three machined surfaces, S^0. The surface analysis is then performed by considering all S parameters. As the amplitude S parameters shall show to be the best ones to describe the VABB surfaces, they shall be used to find the optimal parameter set in terms of topology enhancement. The next subsection shall tackle with the V or Abbott-Firestone parameter set, to evaluate whether they deliver additional information to the system of study, or whether, on the contrary, they are redundant in this analysis.

5.1.1 AISI 1038

5.1.1.1 Topologies of the original surfaces

The first approach to topology characterisation of all three original surface finishing textures is undertaken by considering a simple set of two-dimensional parameters, represented in Figure 5.2. This kind of parameters can be considered highly representative of the initial surface texture, due to the planar symmetry that they exhibit

Table 5.1. Summary of retained two- and three-dimensional topological parameters.

Two-dimensional parameters	
Roughness parameters	R_a: average; R_q: RMS
Profile parameters	P_a: average, P_q: RMS
S parameters	
Amplitude	
Root mean square height	S_q
Skewness	S_{sk}
Kurtosis	S_{ku}
Ten-point height	S_{10z}
Spatial	
Fastest decay autocorrelation length	S_{al}
Texture aspect ratio	S_{tr}
Hybrid	
Root mean square gradient	S_{dq}
Miscellaneous	
Texture direction angle	S_{td}
V parameters	
Areal parameters	
Core distance	S_k
Reduced peak height	S_{pk}
Reduced valley height	S_{vk}
Peak material ratio	M_{r1}
Valley material ratio	M_{r2}
Volumetric parameters	
Valley void volume	V_{vv}
Core void volume	V_{vc}
Peak material volume	V_{mp}
Core material volume	V_{mc}

as a consequence of the machining strategy performed to obtain them. To calculate the R and P parameters –roughness and profile respectively–, a set of 20 evaluation lengths traced along parallel paths perpendicular to direction II were acquired and averaged to obtain a representative value. The roughness parameters were obtained by filtering the whole profile P through a low-pass filter with a λ_c = 0.8 mm cut-off length was applied to filter the height signals.

All parameters show an increasing trend from S_1^0 to S_3^0. This behaviour was predictable, as surface roughness and topography are expected to be harsher as the offset distance between ball-end milling passes is increased. Furthermore, it is shown that

P_a and P_q, as well as their R correspondents, are related by a factor of proportionality 0.87. This relationship between both factors was already observed by King & Spedding (1982) [69] on manufactured surfaces, and proves that both of them can deliver the same information about the surface state. On the other hand, extreme points are also of higher magnitude as the surface becomes more abrupt.

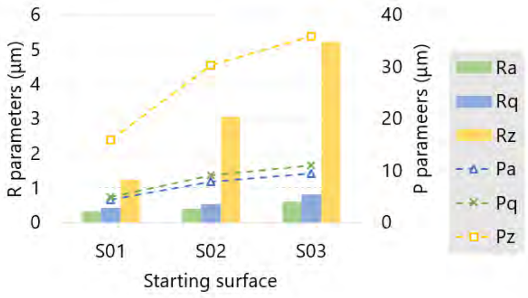

Figure 5.2. Two-dimensional descriptors of original surfaces (AISI 1038).

If instead of two-dimensional parameters, the three-dimensional parameters that represent surface are considered, results are consistent with the previous observations. These parameters have been calculated by establishing a least square mean plane on the acquired height datasets, and without applying filter to retain the texture features. S_q in Figure 5.3.a grows until reaching its maximum value for S_3^0. Extreme points are also maximum for that surface. Spatial parameters also evidence the larger scale of the S_3^0 surface, with regards to the other two finishing regions because of their characteristic highest correlation length S_{al} (Figure 5.3.b). That means that, by calculating of the autocorrelation function, the surface must be folded and displaced along a longer distance on itself to exhibit an actual decay of its value.

S_{tr} is for the three cases well below 0.1, and proves that all machining strategies have lead to highly anisotropic surfaces, with a preferential direction. That direction is defined by the S_{td} parameter common to all surfaces, not represented in the graph due to its uniform value of $-90°$ regardless of the considered surface. On the other hand, the S_{dq} hybrid parameter shows that the three machined surfaces are next to a finishing state, although the S_1^0 surface is the smoothest one, and, therefore, this parameter increases as surfaces S_2^0 and S_3^0 are considered.

Volumetric parameters also show the higher abruptness of the S_3^0 surface with regards to the opposite end of the sequence S_1^0 (Figure 5.4.a). Indeed, all core, peak and valley volumes, are maximum for S_3^0, and minimum for S_1^0. The descriptors of

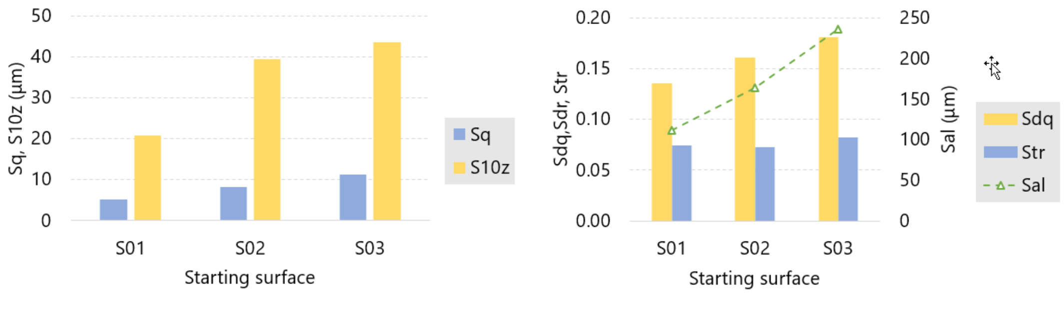

(a) (b)

Figure 5.3. S parameters describing the initial surfaces of AISI 1038. **a**. Amplitude parameters. **b**. Spatial and hybrid parameters.

the AF curve show the same behaviour with regards to the core and peak material, but not so at the valley proportion, which is virtually equal for all surfaces (Figure 5.4.b).

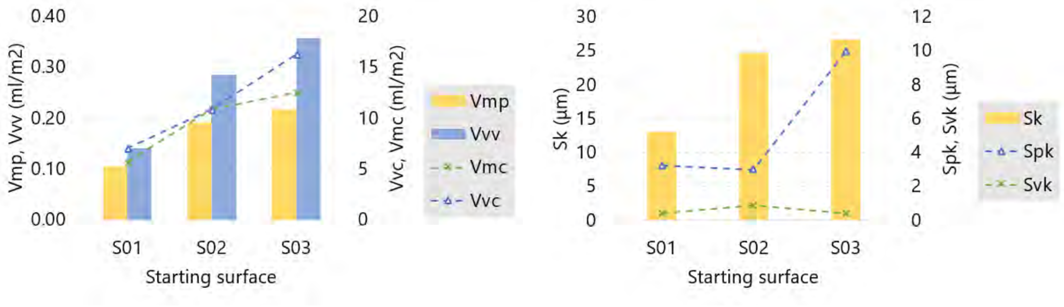

(a) (b)

Figure 5.4. V parameters describing the initial surfaces of AISI 1038. **a**. Volumetric parameters. **b**. AF parameters.

The visual inspection of the AF curves helps understanding the uneven trend of its descriptors, as not all three surfaces show different bearing area distributions, as shown in Figure 5.5. Whereas the bearing capacity of positive heights proves to be higher for S_1^0 and increases progressively towards S_3^0, explaining the behaviour of S_k and S_{pk}, the points corresponding to the valleys machined on the material show an overlapping of S_2^0 and S_3^0 at high M_r values, and a change in concavity difficult to interpret at this point, but that could help explaining the unpredicted behaviour of S_{vk}.

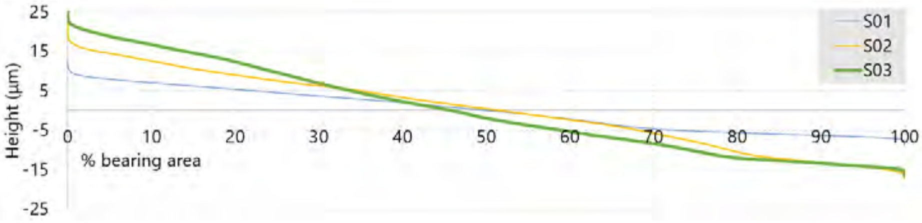

Figure 5.5. AF curves for the three original surfaces on AISI 1038.

The different original surfaces were characterised through two- and three-dimensional parameters. Both of them allowed the identification of a sequential decrease in the surface scale, and a slightly different material distribution, at sight of the Abbott-Firestone curves and the S_{sk} and S_{ku} parameters. However, the uneven evolution of some of the bearing area curve descriptors questions their adequacy to represent systematically the evolution of these surfaces. The next subsections tackle with the results of the 27 VABB tests, and shall reveal whether these original conditions have an impact on the final results delivered by the process.

Synthesis **Original AISI 1038 surfaces**

Due to the periodical peak pattern presented by the original surfaces, obtained through ball-end milling, the basic two-dimensional factors represent well enough the bigger scale of the topologies as the lateral offset between passes is increased, i.e. from S_1^0 to S_3^0. The three dimensional factors also denote that evolution, except for some volumetric descriptors, that shall be taken into account cautiously in the analysis of ball-burnished surfaces.

5.1.1.2 Two-dimensional Rq parameter

Following the traditional approach to the analysis of ball burnishing results, this first phase of topological analysis focuses on the two-dimensional roughness. However, a preliminary visual inspection of the burnished patches evidences that the repeatability of two-dimensional R parameters cannot be expected to be high. As an example, Figure 5.6 shows the surfaces after tests #25 and #18, performed on the S_1^0 surface. Test #25 exhibits a higher heterogeneity of the height distribution, compared to #18, which is clearly still governed by the original machining marks. In fact, the S_{td} parameter, which indicates the main texture direction, is inverted in the former. Therefore, the hypothesis of planar symmetry that was considered in the previous subsection cannot be equally applied to analyse the VABB surfaces. Consequently, the use of this kind of parameters must be taken cautiously.

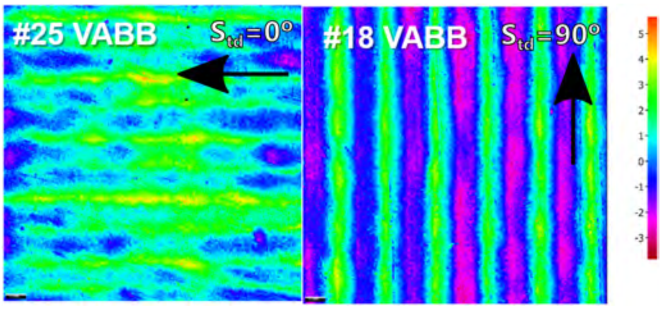

Figure 5.6. Topological images of VABB tests #25 and #18 performed on AISI 1038.

Regardless of having exposed the risks of focusing the analysis exclusively in two-dimensional parameters, the traditional approach to burnishing analysis is considered by calculating all R parameters, measured 20 times along direction I by applying a $\lambda_c = 0.8$ mm filtering cut-off length. To control the error, and guarantee the representativeness of those values, outliers have been discarded through Chauvenet's criterion. This method assumes normality of the sample, enabling the calculation of an interval based on the error so that every point outside it is discarded. This method of outliers control is controversial, due to the fact that it removes from consideration points that were actually measured on the sample. However, it delivers a fast and uniform sample with a highly representative average value [144].

The mean R_q parameters were subjected to an ANOVA. Figure 5.7 shows the graphical results derived from that analysis. The VABB process proves to decrease roughness, being the preload the most influential value, followed by the number of passes. On the contrary, the strategy and initial surface state show no influence in roughness reduction. Nor does the feed considering a 0.05 confidence level, at sight of the associated p-value calculated through the ANOVA test (0.087). The S/N ratio reaches its highest values at those levels that have a higher mean average effect on the response, confirming that they are also the most robust ones. Finally, no interactions are observed between F_p, n_p and v_f.

The only influence of F_p and n_p on R_q, and the result independence from S^0 agrees with results obtained previously by other researchers, such as Lee *et al.* (1993) [78]. One possible reason for this independence could be due to the fact that, by removing the low frequency features of the surface through the filtering operation to which

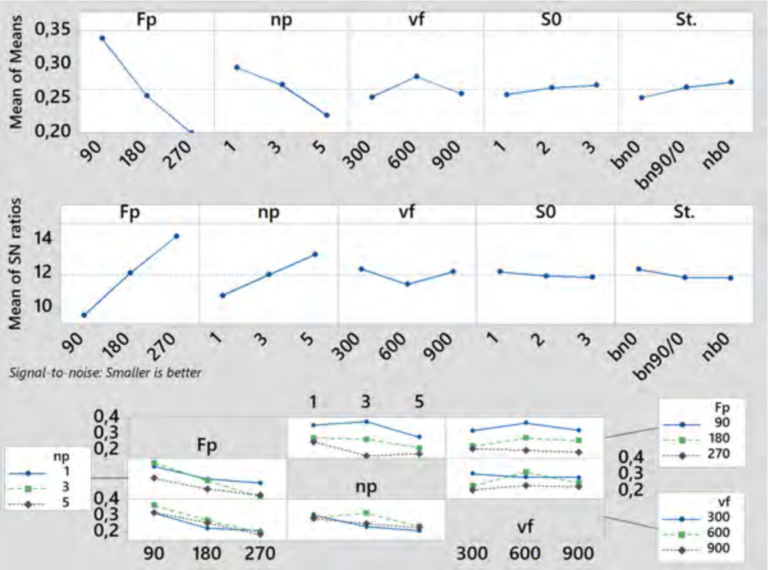

Figure 5.7. VABB mean effects, S/N ratios and interaction plots. ANOVA response variable: R_q of AISI 1038.

the sampled P profile must be subjected to extract the R profile, the material that actually interacts with the ball is being obviated. The filtered resulting profile is less representative of the surface, and does not model the material that interacts with the burnishing ball. The next subsection deepens into texture assessment by analysing a wider set of three-dimensional parameters.

Synthesis **Description of VABB results on AISI 1038 through 2D parameters**

The direct visual inspection of the height maps caused by VABB has evidenced that VABB operation does not have a homogeneous effect on the whole target patch. Therefore, the two-dimensional scale factor, R_q, lacks quantitative accuracy to describe the VABB effects. If no other measuring devices are available, two-dimensional parameters could be considered as an alternative by averaging big datasets to make it interpretable.

5.1.1.3 Sq and S10z amplitude parameters

The first approach to analyse the three-dimensional amplitude parameters is by performing an ANOVA, taking S_q as response variable. Results are depicted in Figure 5.8, proving that the VABB system influences S_q differently with regards to R_q. Indeed, the initial surface texture is the most influential parameter, followed by the preload and the number of passes. The strategy and feed do not show a significant influence. Again, no interaction between factors can be judged as relevant in this case, and the S/N ratio proves that robustness increases as the factors reach their optimal levels, confirming the low impact of noise variables in the system.

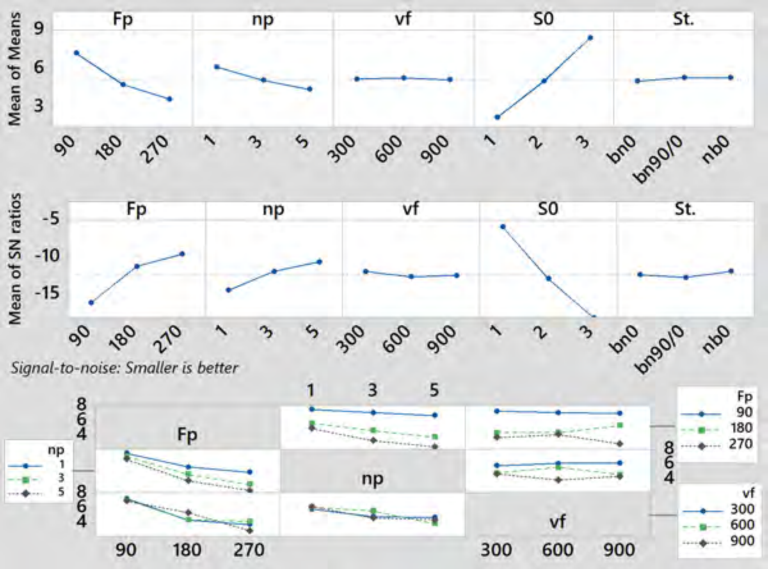

Figure 5.8. VABB mean effects, S/N ratios and interaction plots. ANOVA response variable: S_q of AISI 1038.

The revelation that the initial surface state is more influential on texture results than F_p and n_p leads to a reconfiguration of the strategy for result interpretation, by considering a different pattern for their representation. Accordingly, all topological parameters are rearranged and represented henceforth according to their respective initial surface texture, instead of by their position in the Taguchi experimental array. This layout reconfiguration of the experimental array allows the arrangement of the tests by increasing F_p, and by reiterative cycles of 1, 3 and 5 n_p values. This simplification obviates the feed and the strategy as influential factors, and leads to consider the burnishing results as a discrete sequential evolution departing from the original texture, towards surfaces generated by increasing degree of plastic strain, i.e. the F_p–n_p pair.

Following the described pattern, Figure 5.9 shows the S_q and S_{10z} amplitude parameters. Both of them behave similarly, as they generally decrease as the degree of plastic strain increases, that is, by a rise in F_p and n_p. The only exception to that trend is when shifting from the 180N–5passes test to 270N–1pass, where S_q and S_{10z} increase. This is due to the fact that rising the preload from 180 N to 270 N is not enough to compensate the decrease of number of passes from 5 to 1. Thus the lower degree achieved regardless of the higher preload.

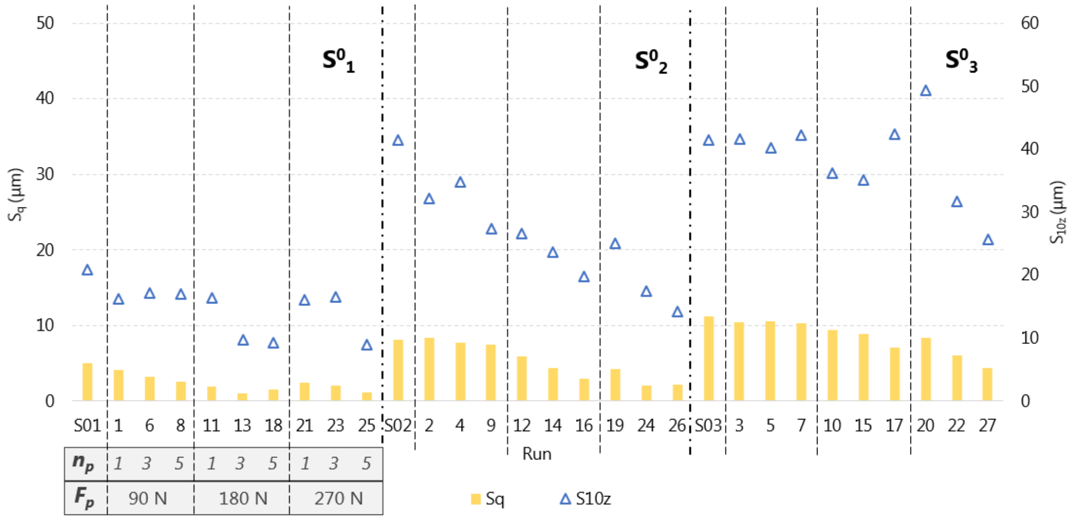

Figure 5.9. S_q and S_{10z} amplitude parameters of AISI 1038 VABB patches.

The lowest S_q at the S_1^0 surface is attained by applying 180N–5passes (test #18). In fact, further plastic deformation leads to surface harm, revealed by a reproduction of new protuberances on the surface by pile-up due to strain hardening, that could be understood as a recreation of the surface texture along the burnishing direction. 180 N should not be surpassed to treat this kind of surfaces, to prevent a detrimental effect of the process. This idea shall be further discussed in following subsections. Therefore, this surface has a different behaviour with regards to the other two. The process seems to be cyclic, at least in terms of scale of the amplitude, as the 270N–5passes test derives in similar texture amplitudes, but, obviously, consuming a larger amount of time. On the contrary, this effect is not observed in S_2^0 or S_3^0, since these surfaces admit VABB with the highest level of preload and number of passes to achieve the largest amplitude reduction. This fact can be explained due to the higher amount of plastic strain required to compress residually a surface where a higher material volume is present at the peaks of the texture pattern.

It is also remarkable the high sensitivity of the S_{10z} parameter to outliers, at sight of some anomalous points observed, for instance in tests #7 or #17. Consequently, it can be considered as less appropriate than S_q to define the amplitude effects of VABB.

5.1.1.4 VABB optimal parameters according to Sq

The mean effects calculated through the ANOVA shown at Figure 5.8 allow the best parameters for S_q minimisation to be found. That criterion can be considered the optimisation target in this case. Figure 5.10 shows the procedure that shall be followed in this subsection to perform that optimisation.

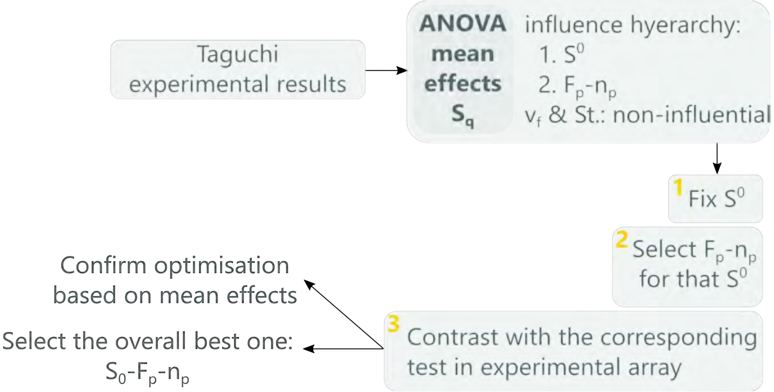

Figure 5.10. Procedure to find the best VABB parameters based on S_q reduction.

Results have proved that the optimal set of parameters is different for each initial texture. The mean effects graph confirms that observation, as an optimal F_p–n_p pair can be found for each S^0, being the strategy and the feed non-influential for the results. Furthermore, no interaction can be found in the system, what simplifies the optimisation procedure. Table 5.2 shows the optimal parameters that result from the analysis.

To confirm the condition of these sets as the best combination, they are compared to experimental results, as tests #18, #26 and #27 correspond to the defined combinations. Indeed, the relative reduction of S_q included in the table shows that they correspond to the best obtained conditions, being S_1^0 where the highest improvement is registered.

The topological study continues in the next subsection by considering the skewness and kurtosis of the generated height distributions. The optimal values defined here shall be also considered in that analysis.

Table 5.2. Parameters to apply VABB on AISI 1038 end-milled surfaces, based on ANOVA mean results. Optimisation target: minimum texture amplitude.

Initial surface	F_p (N)	n_p	vf (mm/min)	Strategy	test	scale reduction: ΔS_q
S_1^0	180	3	300-900	nb0, bn90/0 or bn0	#18	81.3%
S_2^0	270	3	300-900	nb0, bn90/0 or bn0	#26	73.4%
S_3^0	270	5	300-900	nb0, bn90/0 or bn0	#27	61.5%

5.1.1.5 Ssk and Sku amplitude parameters

Skewness and kurtosis parameters are plotted in Figure 5.11. Both S_2^0 and S_3^0 exhibit a uniform increase of S_{ku} as the degree of plastic strain increases, with exception of the singular step from 180N–5passes to 270N–1pass. This trend interruption was already detected in the amplitude parameters. Although S_{ku} increases towards the Gaussian value of 3 in both cases, it is only achieved at S_2^0, when the highest levels of preload and number of passes are applied. It seems that higher plastic deformation could modify S_3^0 towards a Gaussian state. On the other hand, the evolution of S_{sk} proves that the first burnishing passes shifts the height distribution towards positive values, whereas further plastic strain balances the peak-to-valley proportion of the resulting surface again, as it reaches value zero.

S_1^0 exhibits a different behaviour, again consistently with the observations made for S_q. S_{ku} reaches a value of 3 for testing conditions 180N–3passes, then falls once again when increasing to 5 passes. Its behaviour is irregular in the following tests, but reaches 3 again at tests 270N–3passes and 270N–5passes, although the former is clearly positively skewed. The evolution of skewness has similarities with the results on the other two initial textures, as it first decreases, whereas a value next to 0 is achieved when burnishing with 180N–1pass. It then increases and decreases once again to a minimum value at 270N–5passes.

According to the discussed results, both parameters show a certain cyclic evolution in S_1^0, clearly linked to the surface regeneration detected in the other amplitude and spatial parameters. As the surface is reconfigured along the burnishing direction, with a consequent transient phase where it presents detrimental effects, the height distribution is unbalanced until achieving another enhanced state, represented by

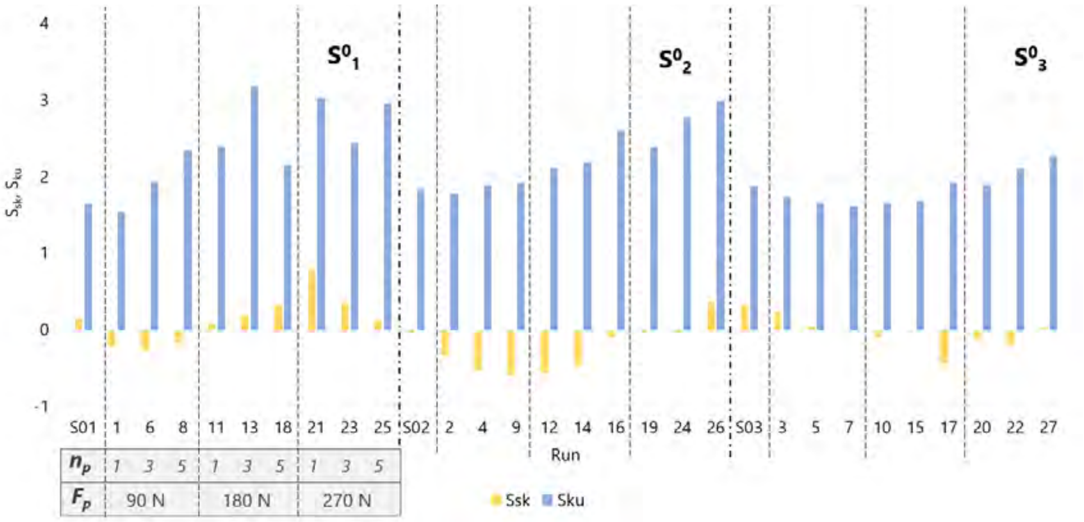

Figure 5.11. S_{sk} and S_{ku} amplitude parameters of AISI 1038 VABB patches.

270N-5passes. On the contrary, S_2^0 and S_3^0 reveal an evolution towards a Gaussian state, and the referred cyclic effect has not been observed. It would seem that it could be achieved by applying higher preload and number of passes.

Furthermore, the effect of VABB on kurtosis and skewness can hardly lead the surface to states far from Gaussian, probably because of the interaction of the ball with the surface, which creates new peaks but is able to convert them into valleys with subsequent passes. These new peaks are originated by the pile-up effect that materials present when they are plastically deform, due to strain hardening.

This analysis can be complemented by checking on the VABB surface height distributions. Figure 5.12 includes the histograms of the original surfaces in the first column, followed by the ones resulting from the best burnishing conditions that were already included in Table 5.2, along with another singular surface state after VABB for the purposes of comparison. A Gaussian-bell distribution can be observed at the height histograms obtained after the best VABB parameters to treat surfaces S_1^0 and S_2^0. The histogram obtained for the optimal test for S_3^0, #27, suggests that the surface could still accept a higher force to increase the kurtosis without biasing the skewness, and therefore the Gaussian bell is not totally shaped yet.

Although skewness values are easily identified in the histogram shape –positive values are depicted by the concentration of heights at the negative side, and vice versa–, interpreting the kurtosis values is not trivial. Indeed, no purely platykurtic

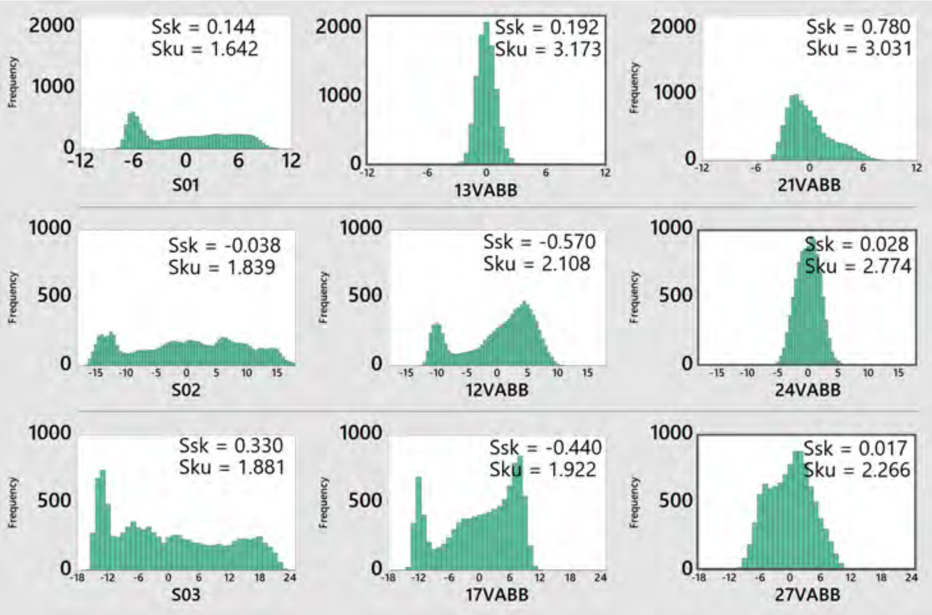

Figure 5.12. AISI 1038 height histograms of VABB tests on S_1^0 (*top*), S_2^0 (*middle*), and S_3^0 (*bottom*), optimal results (*framed*), and another reference test.

or leptokurtic distributions can be observed at the depicted histograms. The answer lies in the fact that kurtosis is actually a measurement of the relative weight of the tails with regards to the distribution central areas. As Darlington (1970) [19] pointed out, kurtosis can be also associated to distribution bimodality, which is the case of burnishing surfaces far from the ideal finishing state (for instance, test #27 with S_{ku} = 2.266). Therefore, the evolution of kurtosis can be understood as a description of the evolution from multimodal height distributions to unimodal ones. The described disappearance of bimodality as the optimal testing conditions are reached, along with a balancing effect of positive and negative heights can be easily distinguishable by comparing the complete sequence of histograms, which is included in Appendix B for every initial surface.

Synthesis **S amplitude parameter optimisation in AISI 1038**

The optimal VABB parameters defined considering S_q minimisation as the optimisation target, also result in Gaussian or quasi-Gaussian height distributions –unskewed and kurtosis near to 3. In other words, texture enhancement through VABB implies minimal RMS of heights with respect to the average centre plane $\min\{S_q\}$ combined with an balanced Gaussian height distribution $-S_{sk} = 0$ & $S_{ku} = 3-$. This kind of surfaces combine good lubrication and bearing characteristics, and can be therefore considered appropriate optimisation targets.

Having explored all amplitude parameters, the next subsection considers whether the VABB process changes the directionality of the surface features, or has any impact on the spatial height distribution.

5.1.1.6 Sal, Str spatial, Sdq hybrid and Std miscellaneous parameters

The S_{dq} hybrid parameter, as the RMS slope of the surface irregularities, reveals a similar decreasing trend with the increasing level of plastic deformation, which proves that higher deformation leads the surface to a more near-to-finished state (Figure 5.13). On the contrary, both spatial parameters prove to be modified to a lower extent by effect of VABB. On one hand, S_{al} shows little variation with the increase of F_p and n_p. On the other hand, S_{tr} values range between 0.06 and 0.1, confirming that the orthotropic nature of the original surfaces is kept after VABB.

As for the texture direction parameter, S_{td}, it is kept at -90° for all tests, except for #21, #23 and #25, whereby the value is zero. Those tests are the ones performed on the S_1^0 with the highest preload. The only change of S_{td} in these specific tests means that VABB reduces effectively the texture amplitude descriptors in all cases, but it is only able to reconfigure the directionality of the main superficial features on the finest surface when a high preload is applied. This observation is an evidence of what was already observed, about the VABB process being detrimental to the surface texture when a too high preload is applied.

The described effect is not observed in the S_2^0 and S_3^0 surfaces, because the maximum preload applied on them is not enough to cause it. Consequently, the initial machining marks are maintained. As an example, Figure 5.14 shows both the initial S_3^0 surface, and its state after burnishing with 270N–5passes (test #27). Although the effects of burnishing are conspicuous, the reader may note that the original finishing grooves caused by the nose of the hemispherical tool, are unaltered after burnishing. It is the initial peaks the ones that are actually affected by the plastic deformation, whereas valleys remain untouched. Hence the maintenance of the original preferential direction, clearly driven by these unaltered paths generated during machining. For further graphical evidence of the unchanged texture direction in most of the surfaces except for tests #21, #23 and #25, all sequential colour maps of all VABB surfaces

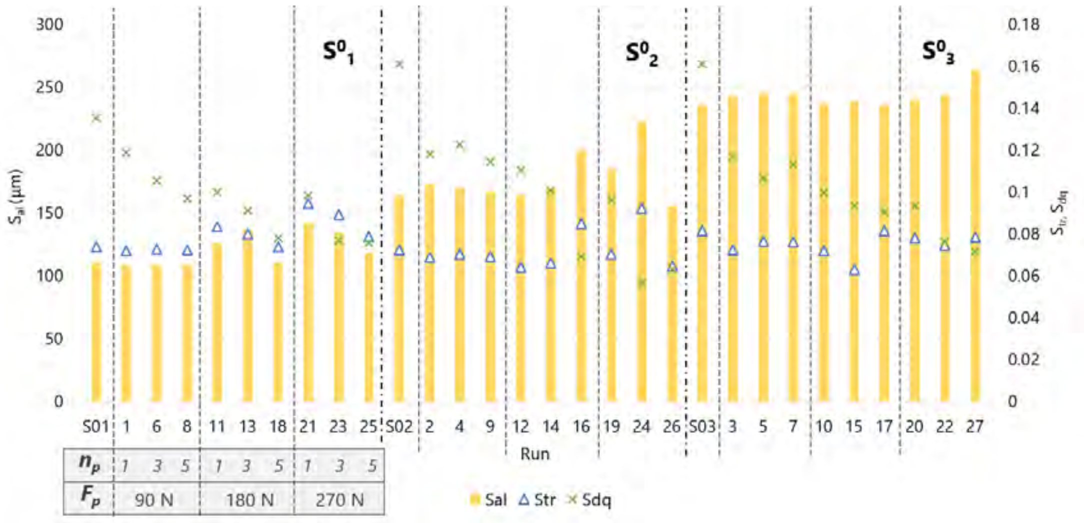

Figure 5.13. S_{al} and S_{tr} spatial parameters and S_{dq} hybrid parameter of AISI 1038 VABB patches.

can be consulted in the appended Figures B.1 to B.3.

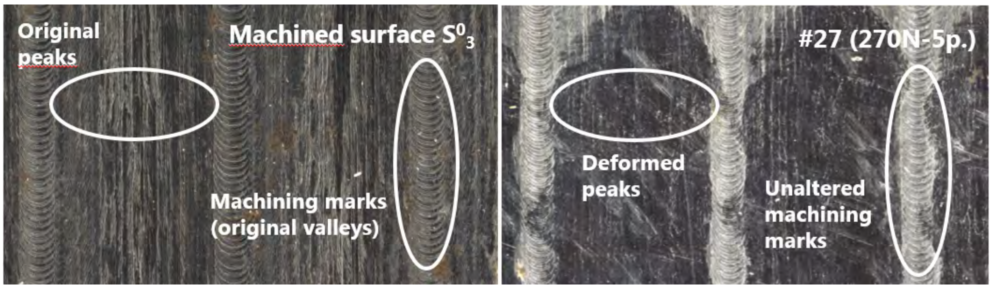

Figure 5.14. Optical images of S_3^0 and #27VABB surfaces.

Synthesis **S spatial parameter discussion in AISI 1038**

The VABB process is only capable of changing the directionality of ball-end milled surfaces if a threshold preload value is surpassed. The immediate consequence is a detrimental effect on the surface that is again corrected as more plastic deformation is performed. An ulterior enhanced surface state is observed, but the preferential direction of the surface features results inverted according to the direction of VABB. That threshold value is lower the more fine the initial surface is. For that reason it has only been found for S_1^0. The insufficient plastic deformation applied on S_2^0 or S_3^0 is exemplified by the machining marks being still visible after VABB.

5.1.1.7 Abbott-Firestone descriptive curves

So far, the analysis of amplitude parameters has proved that the VABB process reduces the scale of the target surface, and succeeds in redistributing the height histogram towards a Gaussian distribution. The next issue to tackle is finding an answer the following question: do the AF curves reveal further information about the nature of the VABB surfaces? For a first approach, let us consider those corresponding to the optimal and singular tests in each original surface that were included above in Figure 5.12. Graphically, surface improvement is brought to light by the AF curves as they are sequentially flattened (Figure 5.15). The highest surface enhancement delivered by VABB was observed in test #13 on surface S_1^0. The ulterior harm at the surface by increasing the preload and number of passes, exemplified by test #21, is depicted by a rebound of the whole AF curve towards the original state. As usual, S_2^0 and S_3^0 exhibit a different behaviour, as the bearing curves become flatter as plastic strain increases, and no harmful effect is observed in any test. Figure B.5 in the Appendix shows the sequential evolution of all AF curves for a higher comprehension of the effect. In overall, the highest improvement seems to be attained at the S_1^0 surface by applying 180N–3passes, which also derives in the highest bearing capacity.

The skewness and kurtosis descriptors of the surfaces also have a representation in the AF curves. This is obvious, as these are an alternative representation of heights, showing the accumulated function from the same dataset. Zero skewness (unbiased height distributions) is associated to curves that cross the x axis at the middle point (M_r= 50%). For instance, test #17, negatively skewed, is represented by a bearing curve which intersect the x axis at 55%.

Identifying the platykurtic or leptokurtic nature of the surface on these curves is not such a direct task. Platykurtic burnishing patches are characterised by S_{ku} < 3, which also denotes the bimodality of the height distribution. Consequently, they should be reflected in the AF curves as an abrupt gradient change, which could even derive in convexity alternations. At sight of the exemplifying curves shown in Figure 5.15, there are visible convexity changes present at low and high M_r values. As the preload and number of passes increase towards the optimal value, the texture evolves towards a Gaussian value of kurtosis, which is reflected by an increase of flatness of the curve, while the slope decreases at every point and no convexity change is further present.

To visualise this effect of VABB on the accumulated height distribution, Figure 5.16

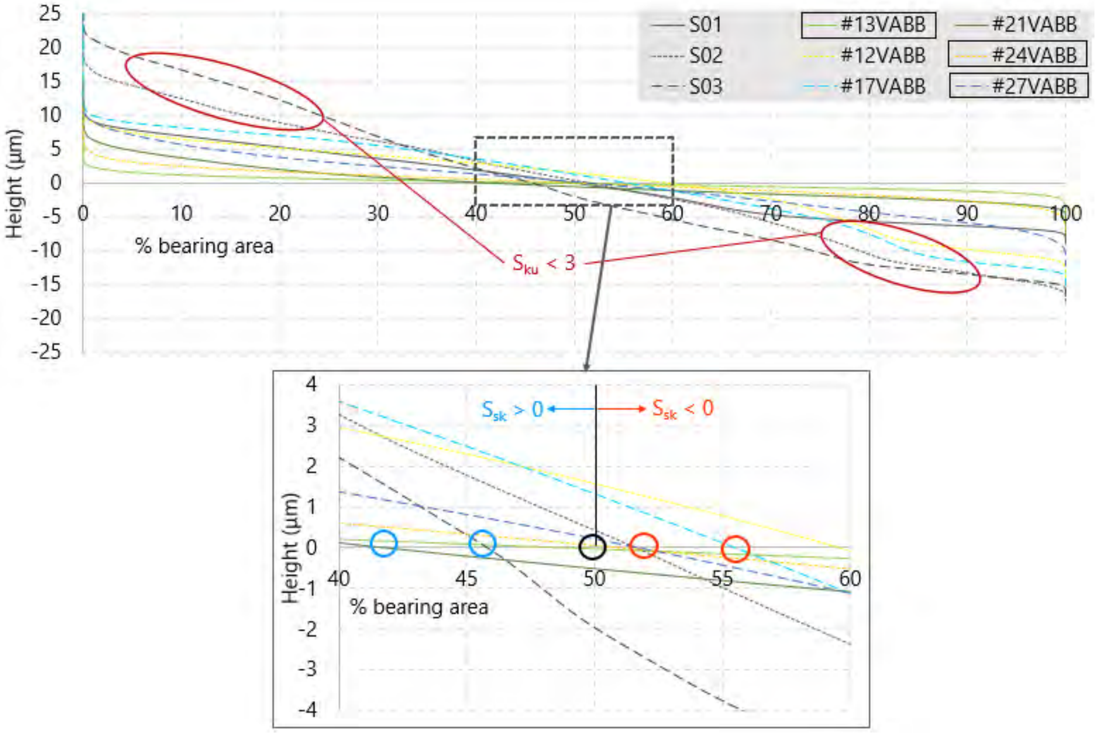

Figure 5.15. Singular AF curves with convexity change linked to platykurtic surfaces, and detail showing S_{sk} related to x intersection point.

represents the slopes of all tests in surfaces S_1^0 and S_3^0, calculated through numerical derivative of their corresponding AF curves. In S_1^0, slope functions are in general more regular as the F_p–n_p pair increases until test #18. From that point, the slopes keep a regular behaviour, meaning that although higher plastic deformation leads to surface harm, it does not redistribute the surface towards the initial distributions, that show an abrupt convexity change at high M_r values. Indeed, bimodality is permanently discarded due to VABB execution. In the case of S_3^0, slopes stabilise as more plastic strain is applied, until reaching the optimal conditions in test #27, where convexity change in the AF curve is totally erased.

The change in convexity is depicted in the slope representation as a local minimum or maximum. Geometrically, it can be related to a higher area between these curves and the x axis. Let Σ_s be the area confined between the slope numerical function of each test and the x axis. It can be calculated by numerical integration of the slope functions. The representation of S_{ku} against Σ_s in Figure 5.17, evidences a clear linear correlation between them, confirming the hypothesis that allows the identification

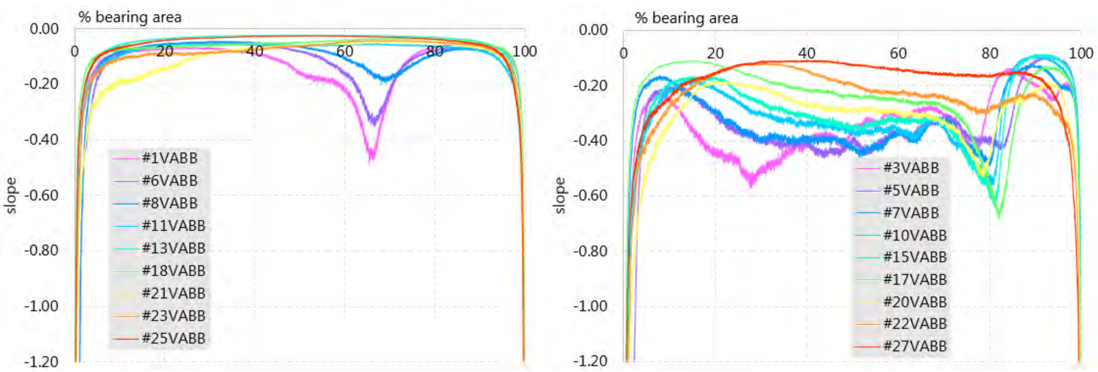

Figure 5.16. AF curve slopes of all S^0_1 and S^0_3 tests.

of kurtosis with convexity changes in the AF curves. This finding shall be especially relevant for the analysis to come in the next subsection, where the curves are reduced to quantitative parameters.

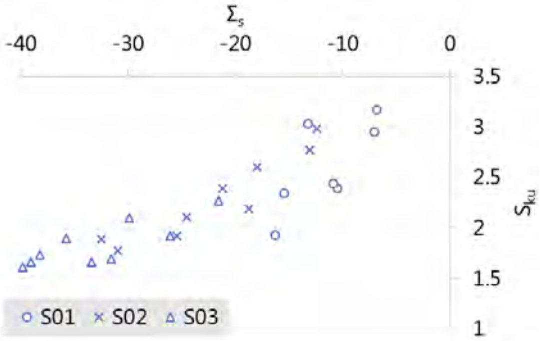

Figure 5.17. Linear correlation between S_{ku} and Σ_sVABB tests.

5.1.1.8 Abbott-Firestone descriptive parameters

The representation of the AF curves by a set of specific parameters can help to simplify them in a functional fashion, and can help to systematise the analysis of VABB results through these curves. Volumetric descriptors have been represented in Figure 5.18. The value of both core parameters, V_{mc} and V_{vc}, fall as the degree of plastic deformation increases, with the regular rebound when changing from 180N–5passes to 270N-1pass. This trend is consistent with the decrease in surface texture amplitude detected through the S amplitude parameter analysis. For S^0_2 and ${}^0_3$, the evolution of

V_{vv} is not so regular. Although it seems to decrease in general as the optimal parameters are achieved, its evolution has ups and downs that make it uneven. Similarly, V_{mp} is evidently minimum for the best burnishing conditions, but it exhibits an errant evolution as the degree of plastic strain increases, lacking a defined pattern. On the contrary, for S_1^0, it seems to account well enough for the creation of new peaks and valleys corresponding to the cyclic phenomenon explained for the finest surfaces. As a consequence, these parameters do not exhibit a specific relation between process parameters for all surfaces, and their effect on the resulting extreme volumetric descriptors. Not all V parameters serve to represent the effects of VABB on a certain surface.

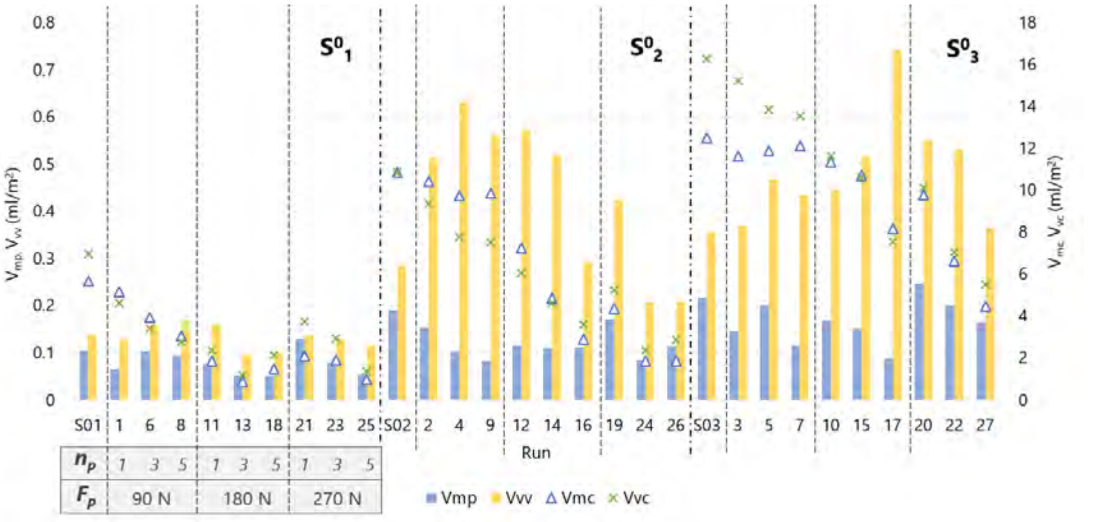

Figure 5.18. Volumetric parameters of AISI 1038 burnishing patches.

The extreme amplitude descriptors of the AF curve are according to the volumetric parameters, as shows Figure 5.19. The core material amplitude, S_k, decreases as the preload and number of passes increase, and is minimum for optimal tests #13, #24 and #27. On the contrary, S_{pk} and S_{vk} do not provide reliable information about the evolution of the bearing profiles. For instance, S_{vk} stabilises in a single value from test #13 to #25 in surface S_1^0, and does not experience variation from test #3 to #7 tests in S_3^0. It then rebounds, achieving a maximum value in test #17. Again, the core parameter agrees with the effects observed before, but the extreme descriptors are not so clearly related to the process parameters.

The bearing potential of the derived surfaces can also be checked through the values of the lowest and highest bearing area percentages, M_{r1} and M_{r2} (Figure 5.20). As

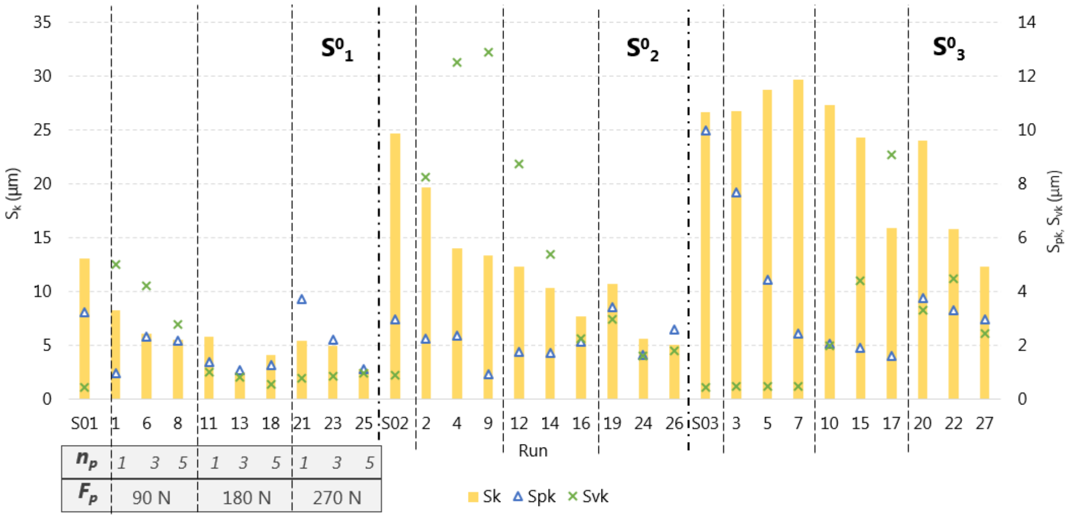

Figure 5.19. AF amplitude parameters of AISI 1038 burnishing patches.

expected, they also lead, in some cases, to dubious conclusions about the evolution of the surface after VABB. M_{r2} evolves in all S_1^0 tests by growing and stabilising from test #13, consistently with S_{vk}. That effect is obvious, since M_{r2} denotes the dominion of S_{vk} in the curve. In S_1^0 and S_2^0, M_{r2} increases until the optimal parameters are applied. However, this effect is not observed in S_3^0, where M_{r2} is maximum in tests performed with 90 N, and then decreases. M_{r1} is not more regular. Intuitively, it should increase as the optimal conditions are achieved, since it is associated to an increase in the bearing capacity. However, it does not happen like that. Furthermore, it is also uneven in its pattern, following different trends in all three surfaces, hindering the task of finding a correlation with VABB parameters.

In overall, the V parameters have proved that only the core descriptors seem to represent well enough the scale reduction of the surfaces, whereas the reliability of the change scale reduction of surface texture can be questioned. Neither do the M_r values prove descriptive potential of the process results. This is obvious, as these extreme parameters do not depend on the 40% minimum slope secant method used to calculate the boundaries between the core and the peaks and valleys. They depend directly of the AF curve, which can have any extreme values. This idea can be related to the observation done about S_{10z} at the beginning of this chapter. For that reason, it is worth questioning at this point whether the V parameter set can help to explain in a systematic fashion the evolution of surface topology after increasing plastic strain through VABB. The word systematic is here crucial, as the ultimate aim of this analysis

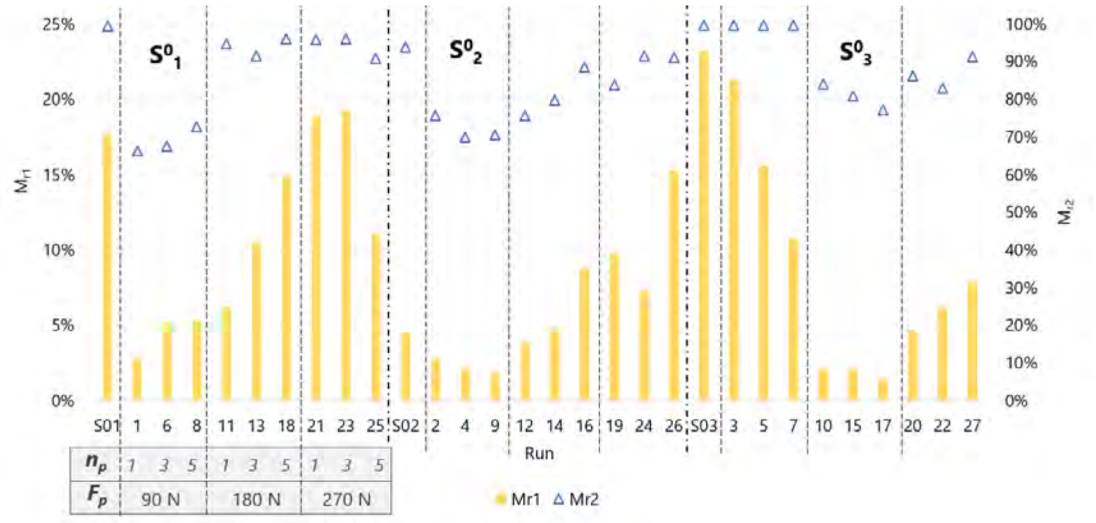

Figure 5.20. AF bearing percentages parameters of AISI 1038 burnishing patches.

is detecting a pattern in the evolution of the surface heights as the preload and number of passes increase.

Can the source of this lack of definition be in the method through which the descriptors are obtained? In the previous subsection, the evolution of kurtosis was associated to convexity change reduction in the AF curves. That irregular shape could be the reason of the errant behaviour of most of the V parameters. To prove it, the least 40%-slope method has been reproduced by importing the different datasets in a Matlab routine, and calculating the value of the least gradient secant line spanning 40% of bearing area or each of them, denoted m_{min}, , as well as the x coordinate of the first secant point, M_{min} (Figure 5.21). Defined m_{min}, the S_k parameter is unambiguously defined:

$$S_k = 40\, m_{min} \tag{5.1}$$

To check whether the least slope secant method offers a systematic calculation of the AF curves, a possible correlation between m_{min} and M_{min} and each curve descriptor is verified in Figure 5.22. The parameters which reliably reflected the evolution of VABB surfaces, V_{mc}, V_{vc}, S_k, show clear linear correlations with the m_{min} descriptor. Specifically, the perfect fit between S_k with m_{min}, direct consequence of the way it is calculated (Eq. 5.1), serves as a confirmation of the adequacy of the reproduced method, and the doubt about the reliability of extreme values that was already commented above. Secondary inverse correlations can be observed against M_{min}, which

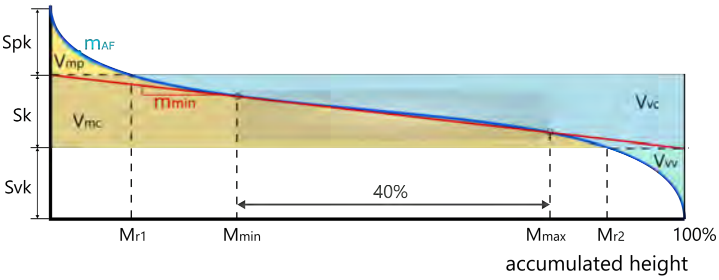

Figure 5.21. Nomenclature of parameters describing the AF curve and the least slope method applied to obtain the core area.

could evidence a certain relation but in no case a regular pattern. As M_{min} depends on the shape of the curve, this could lead to think. M_{r1} and M_{r2} are directly correlated to M_{min}, but only the former shows a linear relationship. On the contrary, the parameters showing an errant behaviour (V_{vv}, V_{mp}, S_{vk}, S_{vk}) are not related to m_{min} or M_{min}. In overall, this analysis leads to think that not all items inside the V parameter set can be considered as relevant descriptors of the evolution of VABB results as the F_p-n_p pair increase.

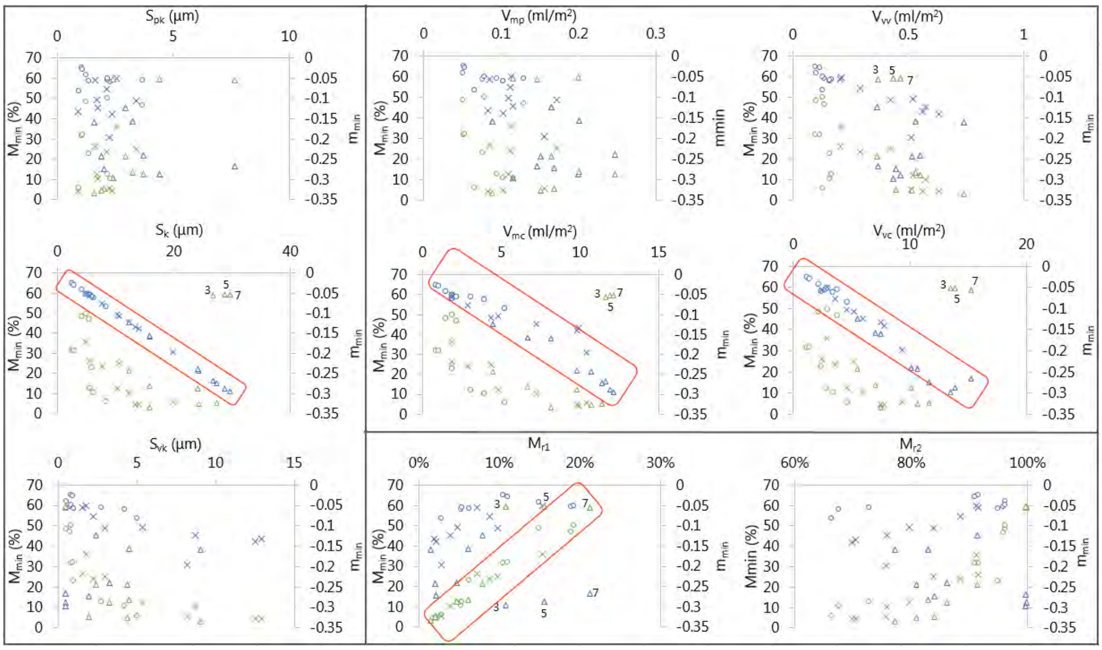

Figure 5.22. Correlation between AF parameters and the least slope curve traced to calculate them. *Surfaces:* S_1^0: ○ S_2^0: × S_3^0: △. *Descriptors:* Blue: m_{min}. Green: M_{min}.

In the analysed graphs, it is especially remarkable the divergence of the points of tests #3, #5 and #7 in many of them, meaning that these are singular cases that should be taken into consideration, and can help to clear out the way the method should be interpreted. Figure 5.23 represents graphically the least slope secant method through the calculated lines on each of the aforementioned AF curves. Apparently, an abrupt change in convexity of the curves at low M_r values displaces the position of the least slope secant line to the other extreme of the curve. Inversely, the AF curve resulting from test #17, that presents that convexity change at its tail, has caused an inverse effect. The AF curves for the optimal tests #13 and #27, essentially flat, derive in secant lines positioned in intermediate sections of the AF curve.

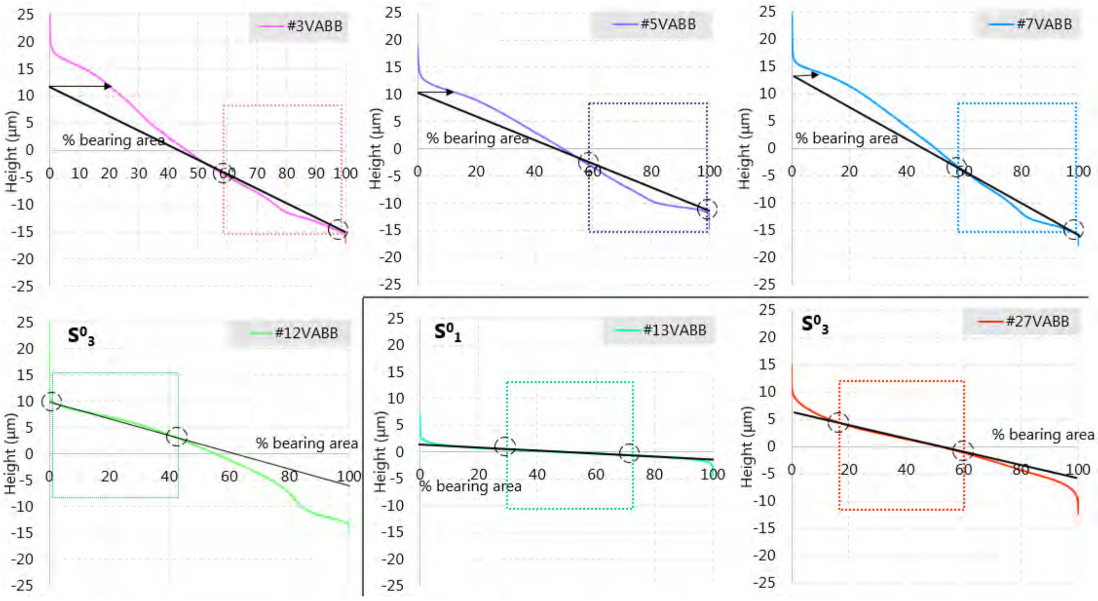

Figure 5.23. Secant according to ISO 10350 to calculate the AF descriptive parameters.

If, in fact, convexity change has to do with a miscalculation of m_{min} and M_{min}, it can be checked by using the kurtosis parameter, that was presented in the previous subsection as an indicator of that convexity change associated to bimodality. The correlation of m_{min} and M_{min} with the S_{ku} statistic in Figure 5.24.a, except for tests #3, #5 and #7, could leads to the conclusion that irregular convexity changes in the AF curves can lead to a lack of reproducibility of the method, and, therefore, an incorrect comparative between tests. This result does not imply that this method is not valid to analyse surfaces individually, but must be taken into account to compare different topologies, especially if the kurtosis value is not regular enough. The calculation of the minimum slope method parameters can also prove that the reduction of S_q is also linked to a flattening effect of the AF curves, as the absolute value of m_{min} increases with an increase of S_q, at sight of Figure 5.24.b.

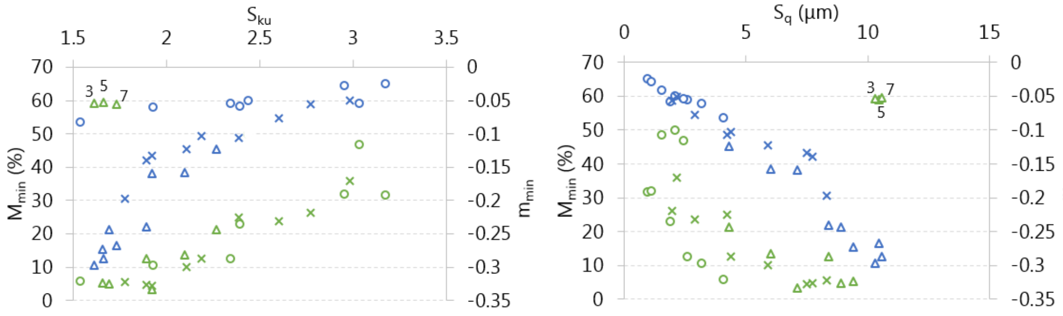

(a)

(b)

Figure 5.24. Correlation between AF parameters with **a**. S_{ku}, and **b**. S_q.

Synthesis **Abbott-Firestone curves of AISI 1038 VABB tests**

The V parameter analysis has proved that only the core descriptors of the AF curves represent well enough the evolution of surface textures after VABB. Although they do not add further information with regards to the S amplitude parameters, they can be considered for lubrication or wear applications where the expression of surface texture is more conveniently represented in volumetric terms. Furthermore, the reliability of the extreme parameters to explain the sequential evolution of surface texture has been evidenced, due to a lack of uniformity to apply the 40% minimum slope secant method proposed by the standard to establish the differentiation between core, peak and valley areas of the surface.

5.1.1.9 Comparison of VABB to the NVABB process

The direct comparison of VABB results with the NVABB tests included in this subsection allows the relative effect of each process on the final texture. Figure 5.25) represents all S_q results of both processes, exhibiting that the NVABB can lead to lower values, especially on the S_2^0 and S_3^0 surfaces. The results seem to be of the same order for S_1^0. At sight of this observation, it can be concluded that the vibration-assisted process leads to detrimental results in higher scale surfaces. Its negative effect is reduced as the surface has smaller amplitude features, as is the case of S_1^0. The causality of this phenomenon cannot be known, but some clues can be inferred from previous results. For instance, the higher infuence of the process on the directionality of the S_1^0 could lead to think that the engagement of the ball and the material of the surface is higher in this kind of textures, thus increasing the effect of the vibration-assistance.

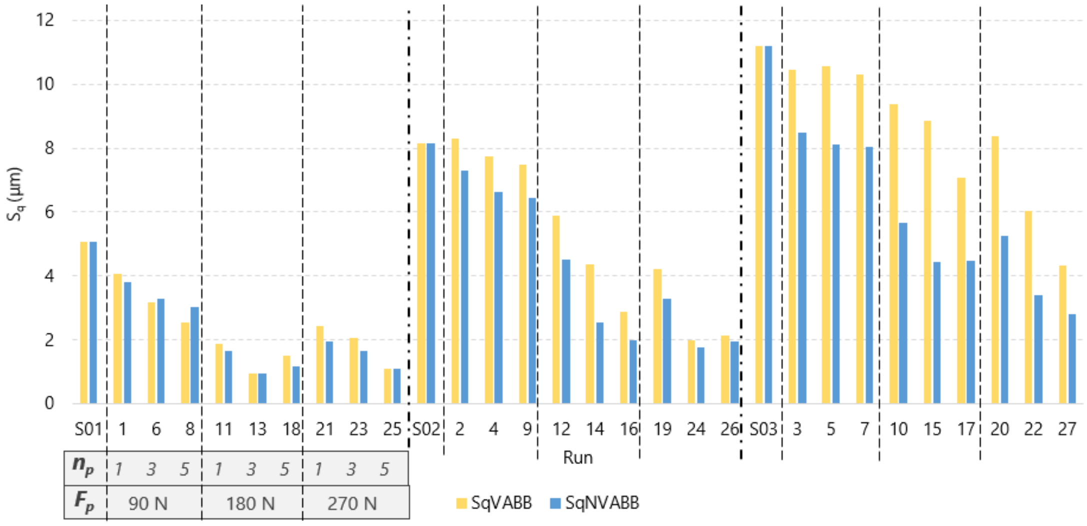

Figure 5.25. Direct comparison of the S_q parameter of VABB and NVABB tests on AISI 1038.

From a qualitative point of view, both surface states have been observed by SEM inspection. The initial machined surface shows a typical repetitive pattern caused by the plastic deformation of the remaining material on the surface. Figure 5.26 shows a detail of that pattern, which appears to be completely deformed after VABB and NVABB. Although the surface appears to be similarly deformed by both processes, NVABB seems to lead to characteristic scratches on the material along the burnishing sense. These scratches could be the source of crack nucleation during functioning in service. Their prevention through the VABB process could be explained by the alternative vertical displacement experienced by the ball during the process, that decreases the detrimental interaction with the surface, and, therefore, prevents the creation of these marks.

At sight of the absence of these marks on the VABB process, the vibration-assisted process can be presented as a more convenient operation to finish an unharmed surface with lower roughness, albeit the slightly higher texture amplitude parameters.

As for the heights distribution, compare the S_{sk} and S_{ku} parameters after VABB and NVABB are directly compared in Figure 5.27, by representing both parameters in

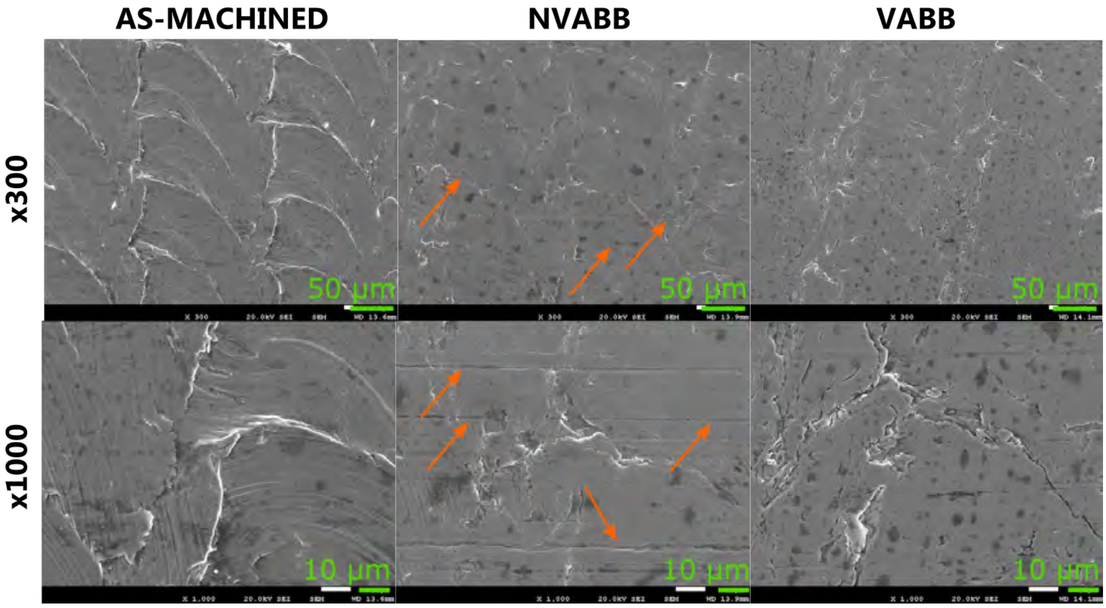

Figure 5.26. SEM images of the S_1^0 surface burnished by 5 passes and the nb strategy. NVABB surfaces show scratches along the feed direction.

the Cartesian plane. This technique can help to characterize the nature of surfaces after finishing through a certain process, as explained by Griffiths (1986) [47]. All results prove to be contained inside a tear-shaped enclosed area. Therefore, both processes are similar in terms of heights distribution after the operation, although the concentration of VABB tests at negative skewness positions shows that NVABB is able to generate less skewed surfaces. In the same graphic, two outliers can be observed: tested conditions #13 and #21. The first set of burnishing parameters executed by the NVABB shows a high kurtosis, whereas the second ones show an especially positive-skewed surfaces.

5.1.1.10 Synthesis of topological results on AISI 1038

Both the VABB and the NVABB have proved to enhance the different surface integrity aspects of AISI 1038 ball-end milled surfaces. The topological state of VABB and NVABB surfaces have been analysed, proving that two-dimensional parameters cannot represent their condition from a functional point of view. Furthermore, not all three-dimensional parameters succeed in accounting for the evolution of textures, which can be explained as follows:

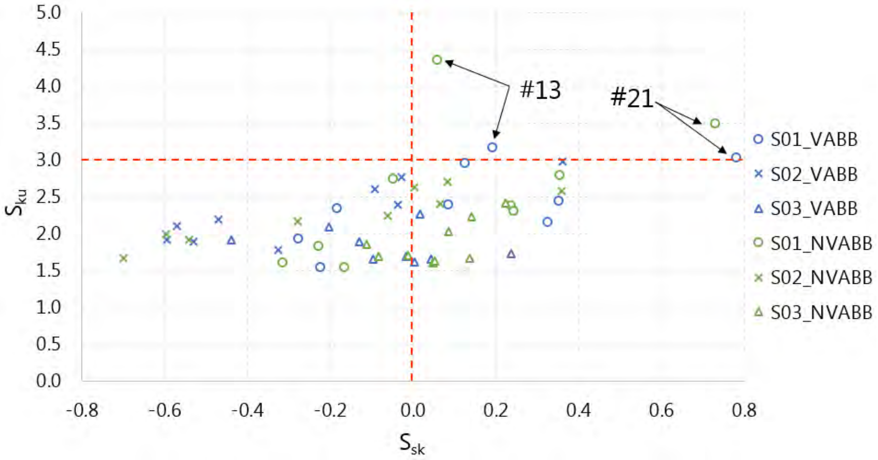

Figure 5.27. Skewness and kurtosis amplitude parameters represented for all VABB and NVABB tests.

- Amplitude S parameters (S_q, S_{10z}, S_{sk} and S_{ku}) reveal that VABB and NVABB succeed in reducing the surface scale of different AISI 1038 ball-end milled surfaces, and lead to Gaussian or quasi-Gaussian height distributions.
- Spatial and miscellaneous S parameters (S_{al}, S_{dq}, and S_{tr}) are not sensitive enough to describe the evolution of surfaces after VABB and NVABB, due to the fact that the process only deform the peaks of the surfaces, and cannot erase the mill-nose marks caused during machining
- Core Abbott-Firestone parameters (S_k, V_{vc}, and V_{mc}) exhibit the surface scale reduction, consistently with the amplitude S parameters.
- The rest of the Abbott-Firestone parameters cannot account for the evolution of the surfaces due to VABB or NVABB, either because they are not sensitive enough to detect that change, or because the 40% minimum slope secant line method used to divide the AF curve in core, peak and valley zones cannot be applied on surfaces represented by bimodal height distribution. That bimodality is exhibited in the AF curves by abrupt convexity change.

In summary, the best burnishing conditions found for the NVABB process are the same ones as for VABB. The original texture has proved to be the most influential parameter, achieving the lowest surface scale on S_1^0, and only the F_p–n_p pair exhibited influence on the results. Considering all these observations, the best burnishing parameters to finish different AISI 1038 surfaces can be established as Table 5.3 shows. In absolute terms, the lowest surface texture after both processes is obtained on S_1^0 (shadowed in green in the table).

Table 5.3. Recommended parameters to ball-burnish AISI 1038 end-milled surfaces. Optimisation target: Gaussian surface with minimum texture amplitude.

Initial surface	Process	F_p (N)	n_p	vf (mm/min)	Strategy	test	scale reduction: ΔS_q
S_1^0	VABB or NVABB	180	3	300-900	nb0, bn90/0 or bn0	#18	81.3%
S_2^0	NVABB	270	3	300-900	nb0, bn90/0 or bn0	#26	73.4%
S_3^0	NVABB	270	5	300-900	nb0, bn90/0 or bn0	#27	61.5%

The previous table is based on the quantitative results delivered by VABB and NVABB processes, which have lead to similar results. However, from a qualitative point of view, SEM observations lead to conclude that the NVABB process exhibited scratching defects, apparently prevented through VABB. Consequently, for a functional point of view, it is the latter that should be preferred to avoid these surface defects that can harm the in-service performance of workpieces treated through NVABB.

The evolution of the amplitude parameters, height distribution histograms and AF curves has evidenced that the process always achieves its best results by simultaneously reducing the texture scale, while generating Gaussian height distributions. The evolution towards Gaussian surfaces can be explained due to the selective effects of the ball burnishing process on the peaks of the surface topology. As they are deformed plastically to reduce their scale, a secondary effect of piling up due to strain hardening also happens, generating new irregularities in the surface. This process of peak generation followed by peak compression being generated simultaneously by the burnishing ball accounts for the described cyclic effect of VABB and NVABB, which can be defined as characteristic of both processes. In contrast, other other finishing operations based on chip removal, eliminate the material causing the escalation of the surface kurtosis towards high values.

This cyclic effect is represented by the existence of a critical F_p–n_p pair for each surface, i.e. the optimal pair found for each surface, from which higher plastic deformation leads to immediate surface harm. Further plastic strain degree results in a return to an optimal state. This effect was evidently observed for the S_1^0 surface, where a first optimal level was found at 180N–3passes, and the ulterior return to the same surface texture was achieved with 270N–5passes. On the contrary, that point was not reached in the S_3^0 texture, leading to think that the maximum plastic strain delivered by 270N-5passes could be still achieved by a higher preload.

5.1.2 Ti-6Al-4V

The analysis of topological results on the AISI 1038 workpiece has lead to identify the key parameters with which it is necessary to tackle to wholly define the topological effects of VABB on different surfaces. Consequently, the results shown in this subsection for the Ti-6Al-4V patches take advantage of those observations to synthesise the study and focus on the descriptors that actually deliver information about the process results. First, the three original surfaces are described.

5.1.2.1 Topologies of the original surfaces

The surfaces machined on the Ti-6Al-4V workpiece present the two-dimensional parameters represented in Figure 5.28. These values represent the increasing scale of the surface features, being the surface S_1^0 the smallest. Although the trend is similar as the one presented in the AISI 1038 workpiece, the absolute magnitudes are lower for all surfaces. For instance, S_2^0 of Ti-6Al-4V can be can be considered in the same way as S_1^0 in the AISI 1038 workpiece. This issue shall not be momentarily considered, and shall be resumed at the end of the section.

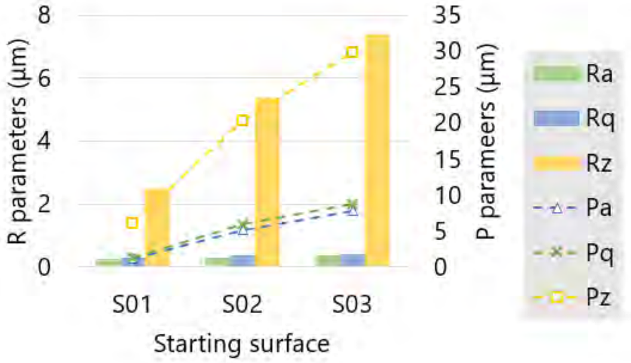

Figure 5.28. Bidimensional descriptors of original surfaces (Ti-6Al-4V).

Surface parameters depicted in Figure 5.29.a and 5.29.b are also highly descriptive of the increasing trend of all surfaces as they were machined with higher offset between end-ball milling passes. The maximum decay length of the autocorrelation function S_{al} also grows, showing the larger spacing between the surface features. The second spatial parameter S_{tr} presents values lower than 0.1 in all cases. Although this value is lower for the S_3^0, the anisotropy of all three surfaces can be acknowledged. As for the descriptors of the AF curves, the ones referring to the core material are highly consistent with the observations commented above, as shows Figure 5.29.c. Both the core material and the peak material increase from surface S_1^0 to S_3^0.

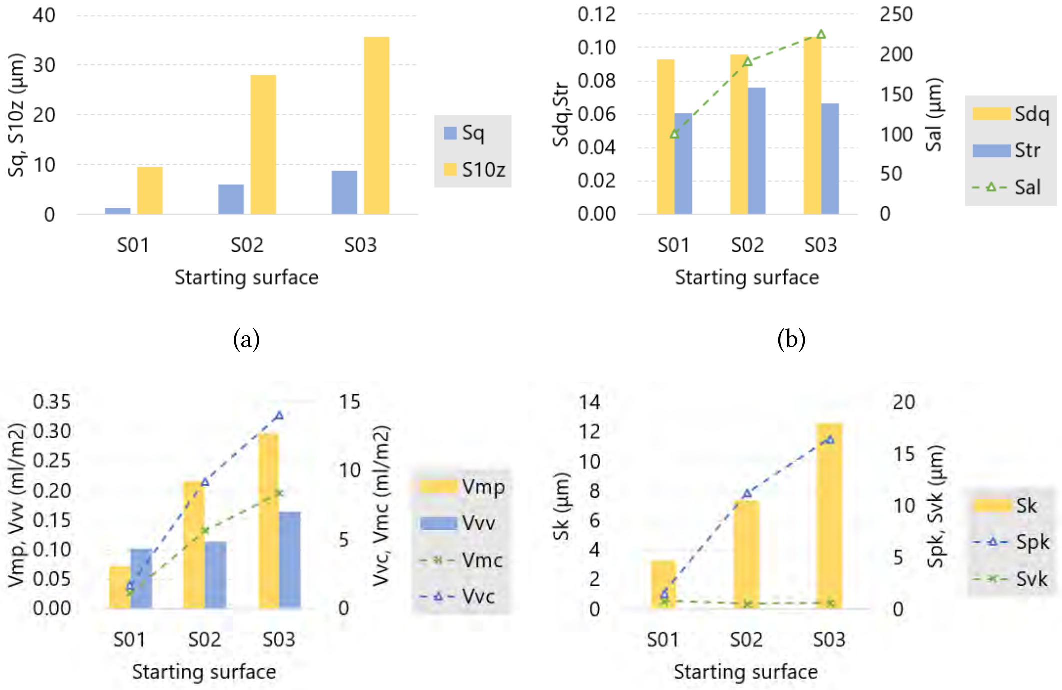

(a) (b)

(c) (d)

Figure 5.29. S parameters describing the initial surfaces of Ti-6Al-4V. **a**. Amplitude parameters. **b**. Spatial and hybrid parameters. **c**. AF parameters. **d**. Volumetric parameters.

Synthesis **Original Ti-6Al-4V surfaces**

It is confirmed that the surfaces machined on the Ti-6Al-4V workpiece are comparatively of higher scale as the lateral offset between hemispherical tool passes was increased, at sight of the S amplitude parameters and the Abbott-Firestone curves. Therefore, it can be stated that all surfaces have been conveniently machined, and are representatively different to represent the influence that they introduce in the application of VABB.

5.1.2.2 Sq and S10z amplitude parameters

The graphical results of the ANOVA considering S_q as response variable are represented in Figure 5.30. The initial topology is again the most important factor on the variation of the amplitude parameters. In fact, its effect is so remarkable, that the sources of variation due to the rest of the factors are hidden by it. Alternatively, the p-values associated to the statistical tests were consulted, revealing that only the preload is an influential effect on the response, if a 5% significance level is considered.

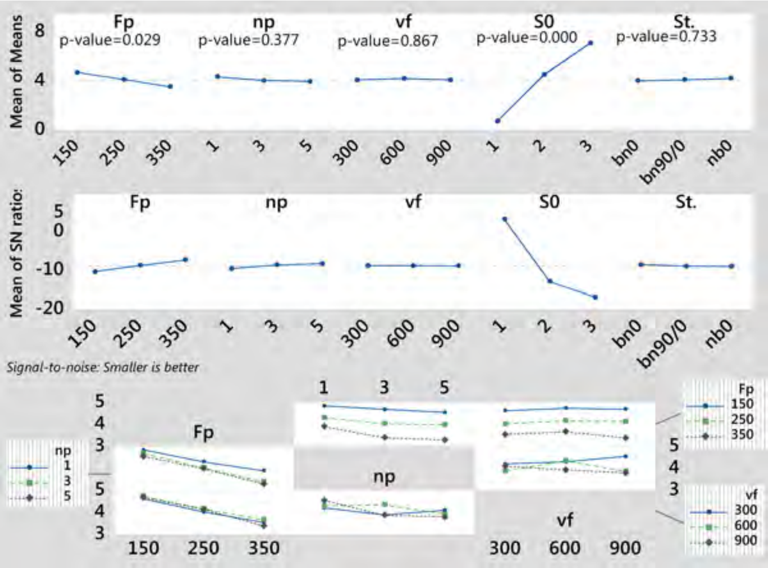

Figure 5.30. VABB mean effects, S/N ratios and interaction plots. ANOVA response variable: S_q of Ti-6Al-4V.

All texture parameters have been ordered by increasing preload, as were during the AISI analysis, consistently with the resulting ANOVA calculations. Figure 5.31.a shows that the continuous decrease of extreme points, represented by S_{10z}, as well as of the general amplitude parameter S_q, can be observed in all surfaces. However, no limit value is achieved in any of the three surfaces, revealing that further improvement could be achieved by a higher degree of plastification. An alternative representation of S_1^0 is presented in Figure 5.31.b to appreciate the decrease of the amplitude values in a proper scale. In essence, the maximum 350N–5passes pair has proved to deliver the best results in terms of topological scale reduction in the three initial textures.

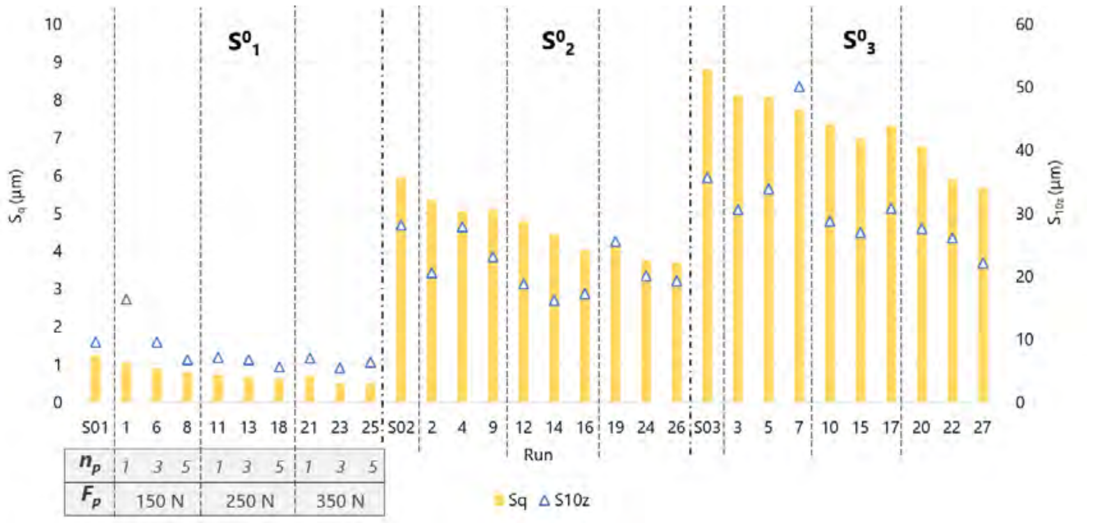

(a)

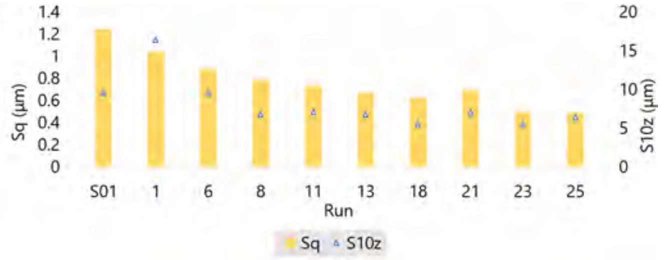

(b)

Figure 5.31. a. S_q and S_{10z} amplitude parameters of Ti-6Al-4V burnishing patches. **b**. Detail of S_1^0 results.

5.1.2.3 VABB optimal parameters according to Sq

Due to the fact that the influence of the different factors on the surface texture in the Ti-6Al-4V is similar as the one found for the steel alloy, the same optimisation procedure proposed in Figure 5.10 can be followed. The term optimal parameters refer to those factors that generate the lowest scale on the surface. They are included in Table 5.4. Their identification with the real experiments #23, #26 and #27 allow the calculation of the relative texture reduction with regards to the initial surface, and prove quantitatively that they are indeed maximum for each initial texture. At sight of the results, the surface S_1^0 exhibits a higher affectation after VABB, with a 60.3% S_q reduction. Conjoint to the evolution of the factor observed in the previous subsection, these results suggest that surfaces S_2^0 and S_3^0 can still accept further plastic deformation.

Table 5.4. Parameters to apply VABB on Ti-6Al-4V end-milled surfaces, based on ANOVA mean results. Optimisation target: minimum texture amplitude.

Initial surface	F_p (N)	n_p	vf (mm/min)	Strategy	test	scale reduction: $\varDelta S_q$
S_1^0	350	3	300-900	nb0, bn90/0 or bn0	#23	60.3%
S_2^0	350	5	300-900	nb0, bn90/0 or bn0	#26	28.9%
S_3^0	350	5	300-900	nb0, bn90/0 or bn0	#27	25.7%

The origin of the lower affectation of the Ti-6Al-4V, if compared with the AISI alloy, can lie on the higher yield strength of the first one, which requires higher preload levels to experience residual plastic strain. The following subsection tackles with the characteristics of the height distributions generated after VABB, to add more information to this observation. Furthermore, it is necessary to contrast the optimal parameter set found above, based on S_q reduction, with the aim of obtaining Gaussian distributions through that set.

5.1.2.4 Ssk and Sku amplitude parameters

The evolution of skewness and kurtosis amplitude descriptors as more plastic strain is performed on each initial texture are represented in Figure 5.32. In all cases, the application of VABB rectifies the skewness of the original surfaces, by reducing to levels near zero. In S_1^0, skewness is partially lead to a negative value for test #11, but the absolute value is so small that it can be assimilated to an unskewed state. In the case of S_2^0 and S_3^0, the fact that they depart from a higher positive skewness is more representative of the effects of VABB, since this parameter is reduced as the preload and number of passes are increased, until it reaches zero with the maximum F_p–n_p pair.

The kurtosis factor is not so sensitive to the increase of plastic strain. In fact, the values along the different tests are kept practically equal to the original values in the case of S_2^0 and S_3^0. Therefore, the VABB process can only account for the scale reduction in this kind of textures, but does not essentially change the height distribution.

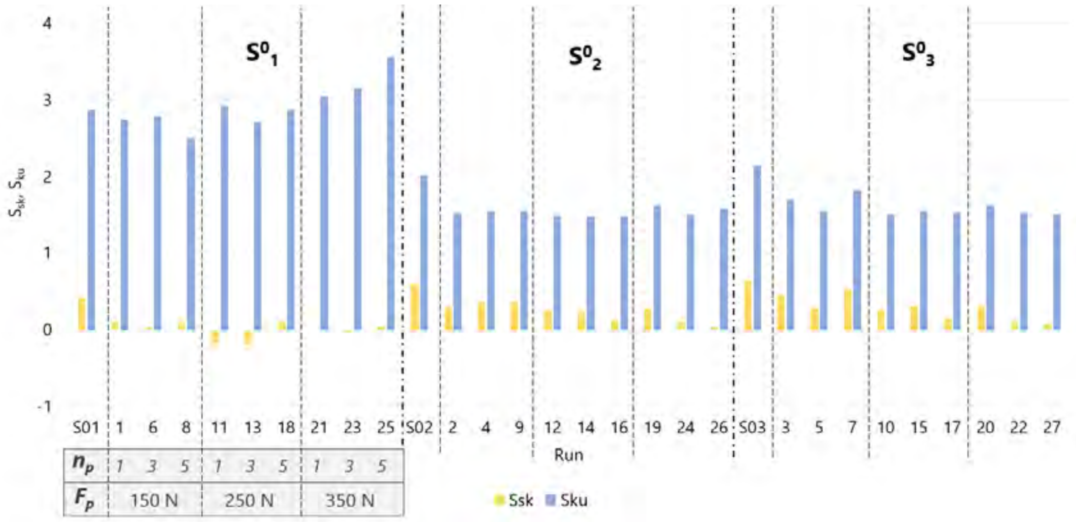

Figure 5.32. S_{sk} and S_{ku} amplitude parameters of Ti-6Al-4V burnishing patches.

On the contrary, S_1^0 presents an increase of the kurtosis parameter as the maximum F_p–n_p pair is reached. Nevertheless, 270N−1pass is the pair that can be associated to the Gaussian state of S_1^0 after VABB.

Now, let us identify the explained S_{sk} and S_{ku} behaviour with the evolution of height histograms as plastic strain is increased. Figure 5.33 depicts a sequential representation of the histograms of the tests corresponding to the optimal parameter set (shown above in Table 5.4), along with an intermediate test to depict the evolution from their respective raw states. Only is in S_1^0 the effect of VABB conspicuous, in terms of bimodality neutralisation and surface scale reduction. Indeed, test #21 presents a Gaussian height distribution with lower extreme points.

Much on the contrary, bimodality cannot be erased from surface S_3^0, as it is present along all tests. Consequently, for this kind of surface, the VABB process proves to reduce the scale of its texture, as revealed the analysis of S_q factor, but it is not able to change the height distribution. The behaviour is similar for the S_2^0 surface. The maintenance of a low kurtosis value on the most abrupt surfaces in Ti-6Al-4V, regardless of the applied preload, could be due to two reasons. First of all, as the Ti-6Al-4V can be described as ductile, the pile-up effect is more accused, and, therefore, a predominance of extreme height values is always present, no matter the degree of plastic deformation achieved on the surface. That predominance is represented in the height histogram as peaks at the lowest and highest points. For additional graphical information about this matter, the complete histogram sequence can be found in the

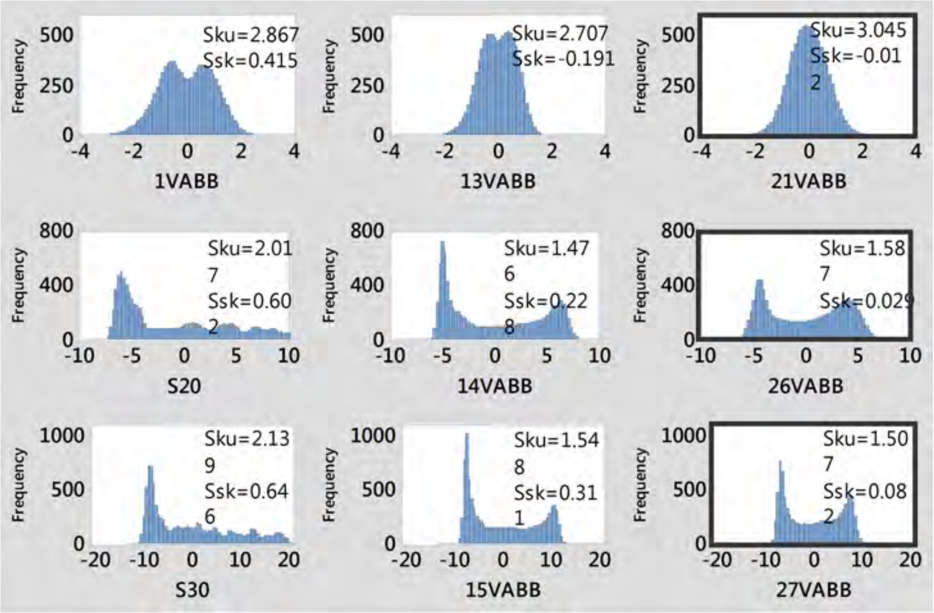

Figure 5.33. Ti-6Al-4V height histograms of VABB tests on S_1^0 (*top*), S_2^0 (*middle*), and S_3^0 (*bottom*), optimal results (*framed*), and another reference test.

Appendix at Figure C.4.

Synthesis **S amplitude parameter optimisation for Ti-6Al-4V**

The optimal parameters have been found for each surface machined on the Ti-6Al-4V workpiece. Results support the idea of surface enhancement is attained through simultaneous scale reduction while obtaining Gaussian height distribution, but only in the finest surface S_1^0. On the contrary, while S_2^0 and S_3^0 surfaces register scale reduction, its effects are not so remarkable, and the nature of height distributions are hardly modified as plastic deformation is increased. In general terms, the titanium alloy has proved a lower affectation by VABB than the steel alloy, although the applied preloads have been higher.

Having analysed the amplitude parameters, the next subsection tackles with spatial and hybrid parameters, to evaluate their representativity of the VABB effects. Prospects are not very clear, at sight of the antecedent observed for the AISI surfaces, where, although higher amplitude affectation was confirmed, spatial parameters were insensitive to plastic deformation.

5.1.2.5 Sal, Str spatial, Sdq hybrid and Std miscellaneous parameters

The visual inspection of spatial parameters do not deliver fundamental information about the variation of the surface directionality, as can be observed in Figure 5.34. S_{al} reveals stable values at each test, always enclosed inside a range near the value corresponding to the original surface. Therefore, it cannot be considered as a representative descriptor of the surface. S_{tr} is similar in its incapability to describe the surface. Only the miscellaneous parameter S_{dq} seems to fall consistently with the aforementioned amplitude parameters, evidencing a stabilisation of the surface characteristics from a certain plastification level in surfaces S_1^0 and S_2^0, and a continuously decreasing trend for S_3^0, in which VABB seems to be able to keep still an improving potential by applying a higher preload.

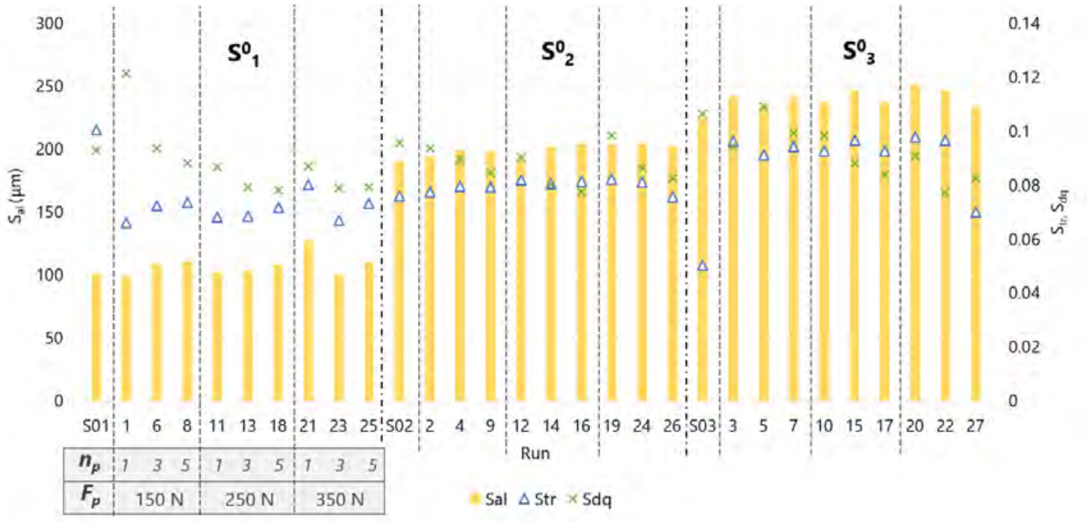

Figure 5.34. S_{al} and S_{tr} spatial parameters and S_{dq} hybrid parameter of Ti-6Al-4V burnishing patches.

In this case, the value of the main texture direction given by S_{tr} is kept at -90°, with no direction inversion as was observed in the AISI alloy. It confirms the lower affectation of the Ti-6Al-4V alloy by the VABB process. To exemplify this statement, Figure 5.35 represents the raw S_1^0 surface along with tests #18, performed with a succession of perpendicular passes due to the bn90/0 strategy, and #25, executed through the nb0 strategy. The raw Ti-6Al-4V surface shows clearly the marks of the end-ball milling tool nose, which are not erased after VABB processing, neither through constant passes along one direction, nor with a change of directionality.

Figure 5.35. Optical images of S_1^0 surface, and VABB tests #18 and #25.

The colour map representation of the height distributions also depicts this lack of influence on the directionality of the surface. In order to exemplify it, Figure 5.36 represents how the initial pattern that defines S_3^0 is practically maintained, even with the test performed with the highest F_p–n_p pair, although the effects of deformation on the peaks is clearly observed through the evolution of the height scale. Furthermore, even being the texture most affected by the process, S_1^0 is hardly redistributed by effect of VABB with 350N–5passes. For further reference, Figures C.1 to C.3 in the appendix show the complete whole colour map collection.

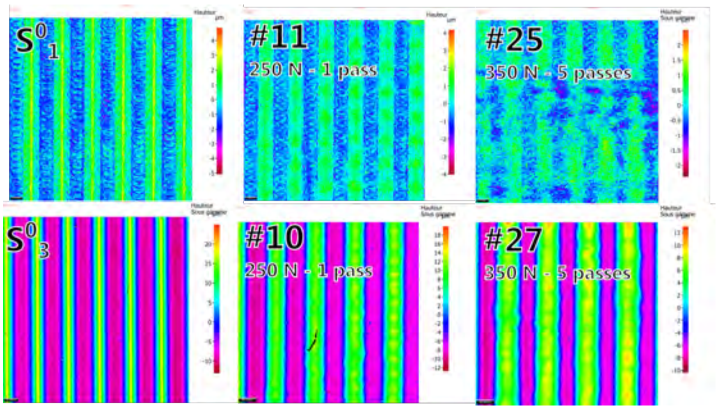

Figure 5.36. Colour map of heights composing the VABB surfaces of singular tests.

Synthesis **S spatial parameter discussion in Ti-6Al-4V**

The Ti-6Al-4V surfaces keep in practice the same spatial and hybrid parameter levels after VABB, with regards to their original surfaces. This conclusion can be easily identified with the AISI results, since both of them show that the trails caused by the hemispherical tool on the surfaces are not erased by VABB. That pattern determines the preferential direction of the surface, regardless of the applied burnishing strategy.

5.1.2.6 Abbott-Firestone descriptive curves and parameters

The complete analysis performed through on the AISI 1038 material revealed that the AF curves do not reveal extra information about the resulting surface. However, they constitute an alternative approach to quantify the distribution of material according to a peak–core–valley differentiation that can be useful for functional calculations. The 40% least gradient method applied to calculate the volumetric parameters also proved to be highly biased for surfaces showing a specially low kurtosis values, which could be translated into undesired convexity changes in the curve that invalidated the method to systematise the topological analysis of the surface through the majority of the AF parameters.

The described remarks are taken in this subsection as the basis to facilitate tackling with the titanium alloy results. First, the correlation between the S_{ku} parameter and the slope change of the AF curves is confirmed. Albeit the low values of kurtosis, the parameter representing the area confined between the slope curves and the x axis, Σ_s, proves to be correlated with the core parameters derived from the processing of the AF curves, as shows Figure 5.37. Again, only the core parameters derived from the minimum slope method should be considered as reliable descriptors of the evolution of the surface by effect of the VABB process. Indeed, only V_{mc} and V_{vc} (Figure 5.38), along with S_k (Figure 5.39), show a decreasing trend as more plastic deformation is attained. This observation evidences the scale reduction that was already evidenced through the amplitude S parameters.

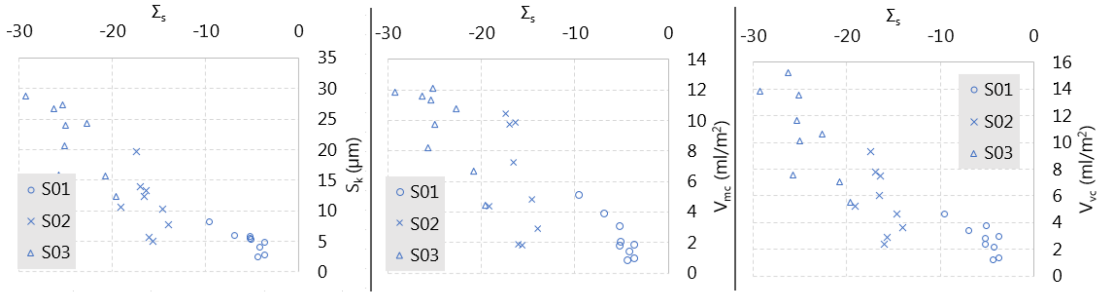

Figure 5.37. Correlation between Σ_s and S_k, V_{mc} and V_{vc} of VABB tests on Ti-6Al-4V.

A very different case is evidenced by the rest of the extreme volumetric parameters, that show the errant behaviour typical of surfaces represented by AF curves with abrupt slope change, as the one that we are dealing with. The case of the material ratios are hardly exploitable, as M_{r2} is practically constant for all tests, and M_{r1}

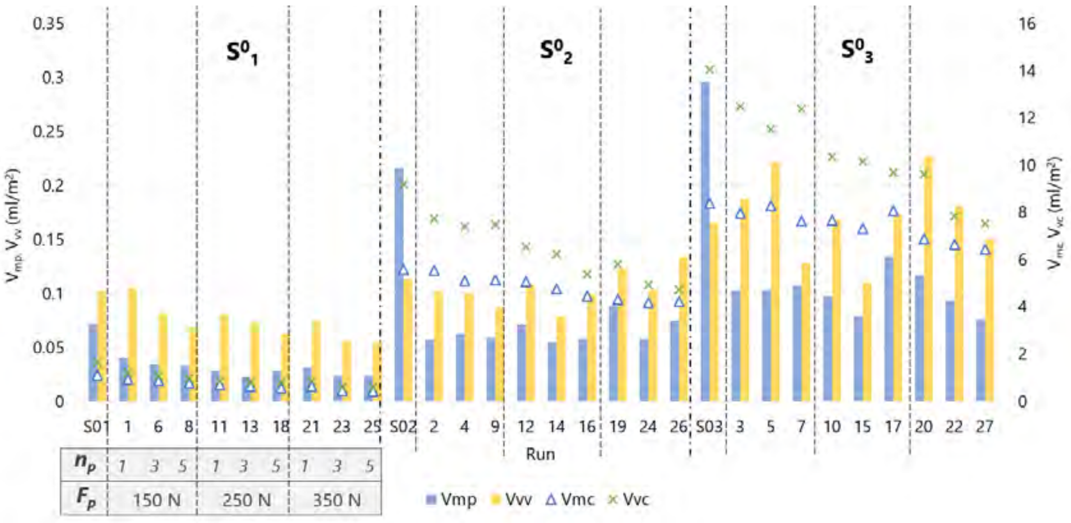

Figure 5.38. Volumetric parameters of Ti-6Al-4V burnishing patches.

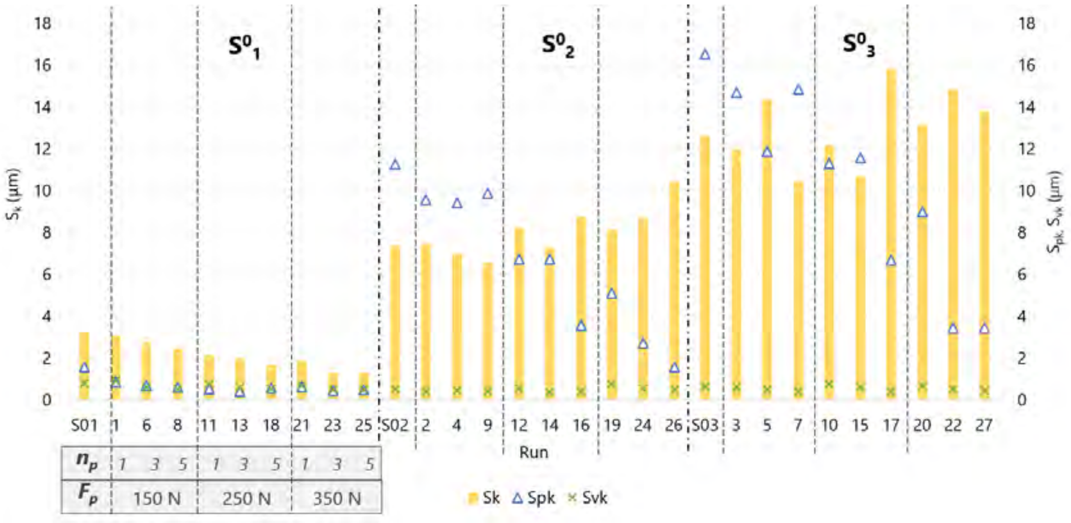

Figure 5.39. Abbot-Firestone amplitude parameters of Ti-6Al-4V burnishing patches.

reveals a contradictory behaviour, since it decreases in S_2^0 and S_3^0, while it increases in S_1^0 tests. The reduction of M_{r1} should be the expected behaviour of the parameter, as is associated to AF curve flattening, what can be translated into an increase of bearing potential of the surface. The unexpected behaviour of the parameter for the two roughest surfaces can only be explained by the inadequacy of the least slope method evidenced above.

The slopes of the AF curves have been calculated, and represented in Figure 5.41.

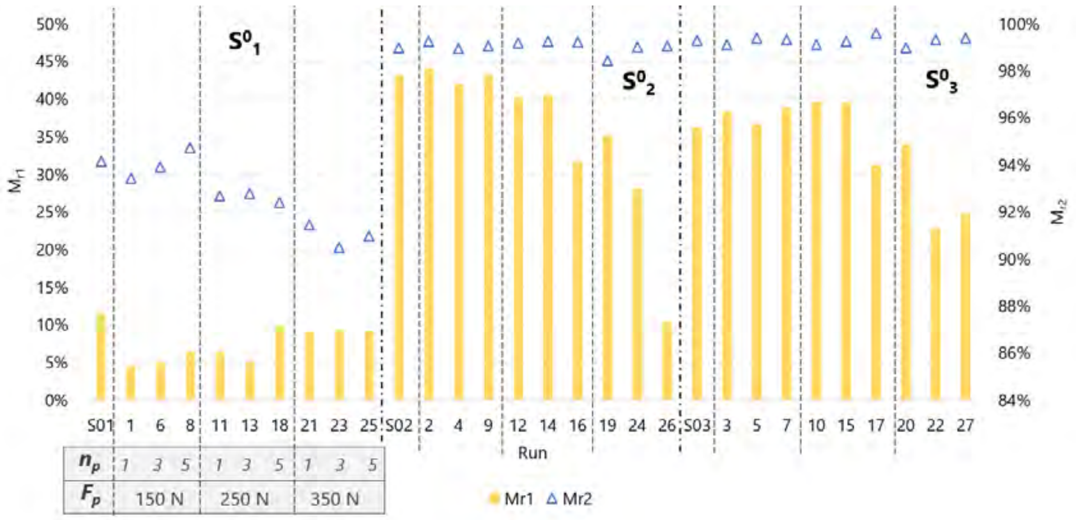

Figure 5.40. AF bearing percentages parameters of Ti-6Al-4V burnishing patches.

Tests corresponding to surface S_1^0 present a regular slope, except for the tests performed with the lowest preload. On the contrary, all the resulting surfaces on S_3^0 show constant convexity change, revealing that, indeed, the minimum slope method is due to lead to biased results.

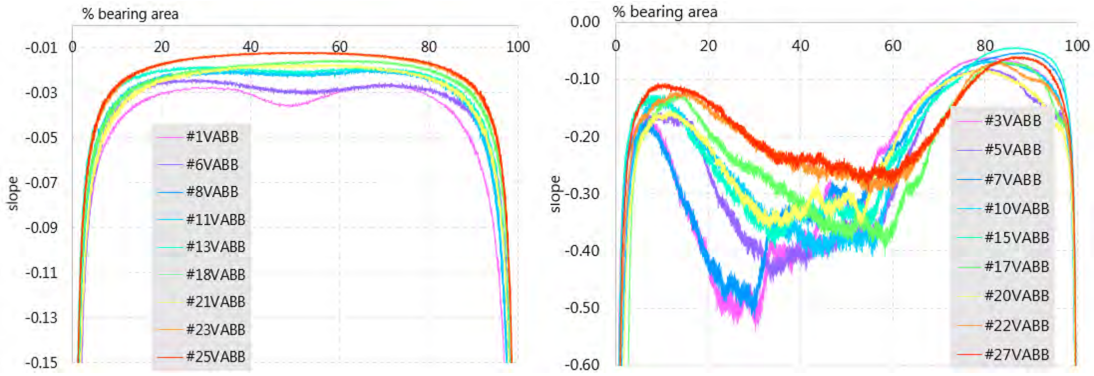

Figure 5.41. Slopes of AF curves resulting from VABB on the Ti-6Al-4V material, on S_1^0 (*left*) and S_3^0 (*right*).

The analysis of the adequacy of the V parameter set, based on the method developed in the analogous section of the AISI 1038 analysis, leads to conclude that thy cannot be considered stable enough to deliver reliable information about the evolution of material distribution in the surface as more plastic deformation is achieved. For further reference, AF curves can be observed in the Appendix Figure C.5.

Synthesis **Abbott-Firestone curves discussion in Ti-6Al-4V**
The core parameters inside the V parameter set have proved to be representative of the evolution of Ti-6Al-4V surfaces after VAB. Their evolution support the idea of surface enhancement by scale reduction and, in the case of S_1^0, final Gaussian height distributions. Considering the volumetric parameters does not add new information about the final surfaces, but offers an alternative approach to the subject for functional applications of surface metrology.

5.1.2.7 Comparison of VABB to the NVABB process

The direct comparison of the S_q parameter in of all VABB and NVABB tests performed on the Ti-6Al-4V workpiece leads to interesting results. Whereas S_2^0 and S_3^0 evidence similar results, the process is capable of producing lower surface scale in S_1^0 (Figure 5.42). This result suggests that the introduction of vibrations as a mean of reducing the surface scale is only effective on surfaces that are characterised by S_q around 1 $\mu\mathrm{m}$. Furthermore, the potential beneficial effects of the process increases as the amplitude of the surface decreases. This statement was also true for the AISI surfaces. This statement reinforces the incidence that the initial texture has on the ball burnishing results, as well as the effectiveness of the vibration-assistance.

5.1.2.8 Synthesis of topological results on Ti-6Al-4V

The topological results obtained on the Ti-6Al-4V surfaces have been analysed based on the strategy that was outlined after the AISI results. Indeed, the S amplitude parameters and the V core parameters have been proved to describe correctly the sought amplitude reduction and redistribution of the titanium surfaces to quantify texture improvement. Again, the most influential parameter on the results was the initial surface, followed by the F_p–n_p pair. Table 5.5 shows the best parameter combination from a topological point of view. It can be observed that the maximum preload is required in all cases to achieve the best improvement.

The influence of the initial surface on the Ti-6Al-4V material has exhibited interesting results in terms of process assistance. First of all, the introduction of vibrations has proved to be positive to increase texture reduction only if the initial surface has a reduced scale similar to the one shown by S_1^0. Secondly, no boundary F_p–n_p value

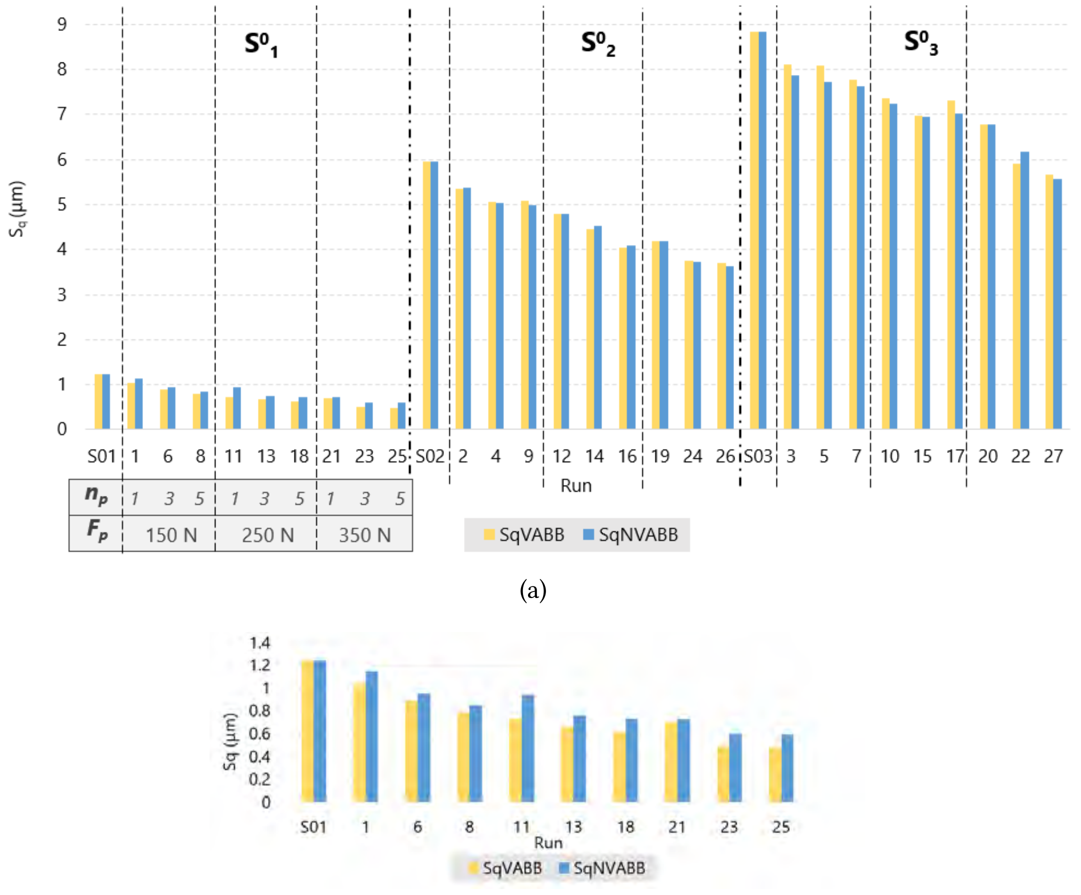

(a)

(b)

Figure 5.42. **a**. Direct comparison of the S_q parameter of VABB and NVABB tests on Ti-6Al-4V. **b**. Detail of S_1^0 results.

was observed in these surfaces, what leads to think that the Ti-6Al-4V could still accept higher preload to achieve higher plastic deformation.

5.1.3 Comparison of topological results of AISI 1038 and Ti-6Al-4V

The results that were analysed for both materials individually have lead to conclude that they are differently affected through the VABB and NVABB processes. On one hand, AISI 1038 surfaces were not affected by the introduction of the vibration-assistance, while Ti-6Al-4V exhibited enhanced results by VABB only in the initial surface that

Table 5.5. Recommended parameters to ball-burnish Ti-6Al-4V ball-end milled surfaces. Optimisation target: Gaussian surfaces with minimum texture amplitude.

Initial surface	Process	F_p (N)	n_p	vf (mm/min)	Strategy	test	scale reduction: $\varDelta S_q$
S_1^0	VABB	350	3	300-600	nb0, bn90/0 or bn0	#23	60.3%
S_2^0	VABB or NVABB	350	5	300-900	nb0, bn90/0 or bn0	#26	28.9%
S_3^0	VABB or NVABB	350	5	300-900	nb0, bn90/0 or bn0	#27	25.7%

showed smallest features. In overall, the S_1^0 surface were the ones delivering the best results in both materials, by applying a different set of burnishing parameters.

The descriptors of the different initial surface topographies were compared, as is shown in Table 5.6. This direct contrast reveals that applying the same ball-end milling parameters on both of them did not generate the same surfaces. In fact, the steel S_1^0 surface cannot be directly compared with its titanium homonymous. On the contrary, it seems more alike S_2^0 surface (aquamarine values inside the table). That means that the titanium S_1^0 has no direct equivalent in the AISI 1038 workpiece. Since it has been the topology that has proved to deliver better results by the introduction of vibrations in the process, it can be questioned whether the lack of influence of vibration assistance in the AISI material has been caused by an insufficient surface reduced scale, being the AISI S_1^0 surface excessively abrupt to perceive the influence of vibration-assistance. For this reason, a second experimental phase was executed to tackle with this issue, as is described in the next subsection

Table 5.6. Main topology descriptors of machined surfaces, including S_0^0 (AISI 1038).

	S_q (µm)		S_{10z} (µm)		S_{sk}		S_{ku}	
	AISI	TA6V	AISI	TA6V	AISI	TA6V	AISI	TA6V
S_0^0	1.662	–	7.9547	–	0.653	–	2.3040	–
S_1^0	5.058	1.243	20.839	9.503	0.144	0.415	1.642	2.686
S_2^0	8.154	5.956	39.448	28.071	-0.038	0.602	1.839	2.017
S_3^0	11.205	8.836	43.446	35.631	0.330	0.341	1.881	2.139

5.1.3.1 Second experimental execution: S_0^0 on AISI 1038

A second test piece was machined by reducing the offset length between passes during the milling operation, setting it to a_e = 0.3 mm. This surface has been called S_0^0 to follow the sequential denomination of textures. Its main descriptors are included in Table 5.6, confirming that it can be assimilated to the Ti-6Al-4V S_1^0 surface. This newly machined surface was subjected to VABB and NVABB by fixing the feed at 600 mm/min and strategy at nb0. The preload was varied at the same three levels −90, 180 and 270 N− and n_p was tested at 3 and 5 passes. A total of 12 new burnishing patches resulted from this full factorial plan.

Figure 5.43 shows the main amplitude parameters of all tests performed on S_0^0. All results are congruent with the observations that were discussed above. First, the inflection point from where surface is damaged due to an excessive degree of plastic deformation is found at 90N−5passes, lower than 180N-3passes found for S_1^0, proving that lower scale surfaces require lower F_p−n_p pairs to achieve positive results. If a threshold level is surpassed the already described cyclic process of surface recreation and re-correction happens, by increasing the processing time unnecessarily from the texture point of view. Furthermore, this pair is associated to S_{ku} near 3 and an unskewed surface, confirming that surface texture improvement is also achieved in terms of attaining a Gaussian height distribution by the application of these parameters.

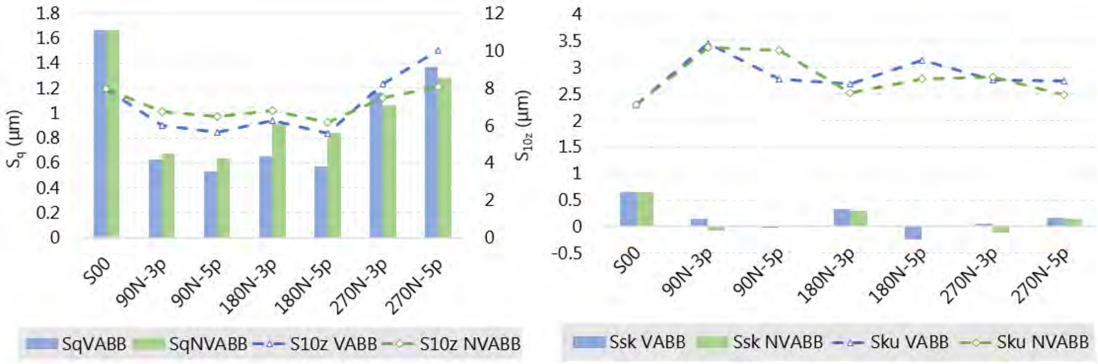

Figure 5.43. Amplitude parameters defining the surfaces.

The second main result obtained from this analysis is that, indeed, the vibration-assisted process leads to similar height distributions, but delivers better results in terms of scale. At sight of this result, it could be concluded that the lack of effect of vibrations on the AISI surfaces, while present on the least rough Ti-6Al-4V texture, was not caused by an insensitivity of the material towards acoustoplasticity, but because of the need to soften the texture features to guarantee the good contact between the burnishing ball and the material. In fact, the introduction of vibrations prove to be detrimental in tests applied with 270 N, suggesting that an excessive preload can lead to further surface degradation if the VABB process is applied, probably due to excessive plastification arising from the vibration-assistance. Indeed, Figure 5.44 shows that the VABB process consistently generates deeper grooves due to the explained effect. Consequently, F_p should be limited to avoid detrimental effects of the acoustoplasticity during the VABB process.

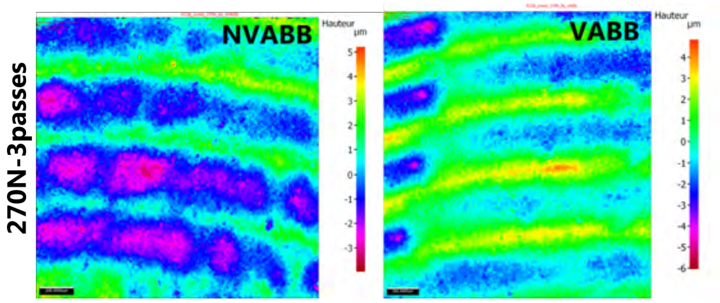

Figure 5.44. Colour maps of NVABB and VABB tests performed on S_0^0, applying 270N-5passes

The AF curves represented in Figure 5.45 confirm that 90N–5passes correspond to the best VABB parameters that could be applied on S_0^0, and lead to similar results as 350N-5passes on the S_1^0 surface of Ti-6Al-4V. Both original surfaces are slightly different in terms of bearing area ratio, as proves this figure, but were highly comparable at sight of their main S descriptors. The rebound of the AF curves present at surfaces burnished through 180 N is the graphical manifestation of the detrimental effects that were detected on S_0^0 at sight of the parameters represented above.

5.1.3.2 Kurtosis and skewness comparison

The comparison of the VABB and NVABB effects on the AISI 1038 and the Ti-6Al-4V workpieces must not just be read in terms of scale reduction, but also as a means of material redistribution at the surface of the workpiece. The conjoint representation of the S_{sk}-S_{ku} pair shows of all VABB and NVABB surfaces obtained on both materials are differently distributed in the plane (Figure 5.46). Whereas most surfaces are

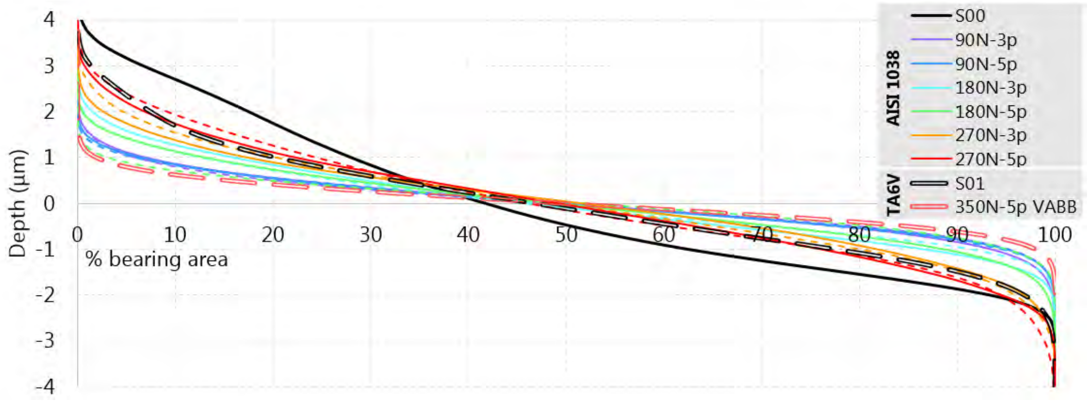

Figure 5.45. AF curves of S_0^0 tests on the AISI 1038 material. Discontinuous lines: VABB process.

platykurtic, different values of skewness are taken by the different results. The kurtosis parameter shows a higher variation in the AISI tests, whereas it is practically unvaried in Ti-6Al-4V surfaces. This can be understood as the highest affectation of the steel alloy by the process. Nevertheless, all VABB and NVABB results are contained inside a certain area of the space which is near to Gaussian surfaces. Now, the question is whether this variation is significant enough to state that both processes are different among them, or that both materials react differently to them?

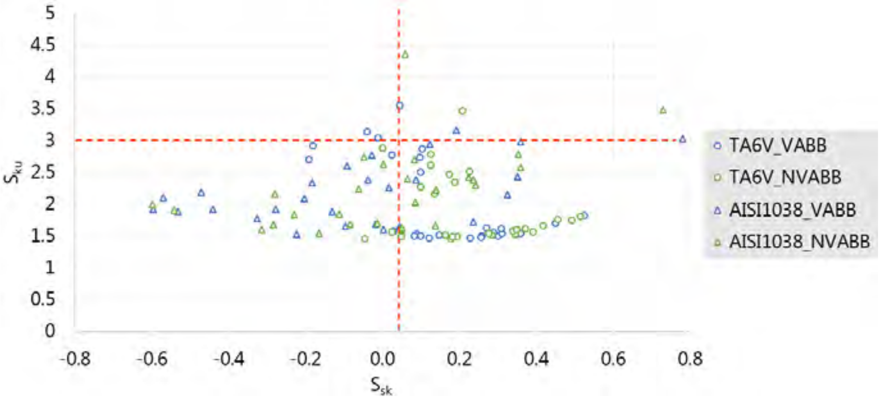

Figure 5.46. S_{sk} - S_{ku} plot of VABB and NVABB results obtained on AISI 1038 and Ti-6Al-4V tests.

To establish a referential point, all the obtained S_{sk} - S_{ku} points have been represented along with other results corresponding to other machining and finishing processes, taking the results compiled by Griffiths *et al.*(1986) [47] (Figure 5.47). NVABB and VABB show the unique capability of generating both positively and negatively skewed surfaces, as well as unskewed ones, whereas other processes lead to clearly negatively skewed (e.g. honing) or positively skewed surfaces (e.g. turning). Furthermore, ball burnished surfaces can be characterized by low kurtosis values. Although the Gaussian value 3 can be attained with the correct application of parameters in AISI surfaces and Ti-6Al-4V S_1^0 surface, it is hardly modified in harsher textures of the last material.

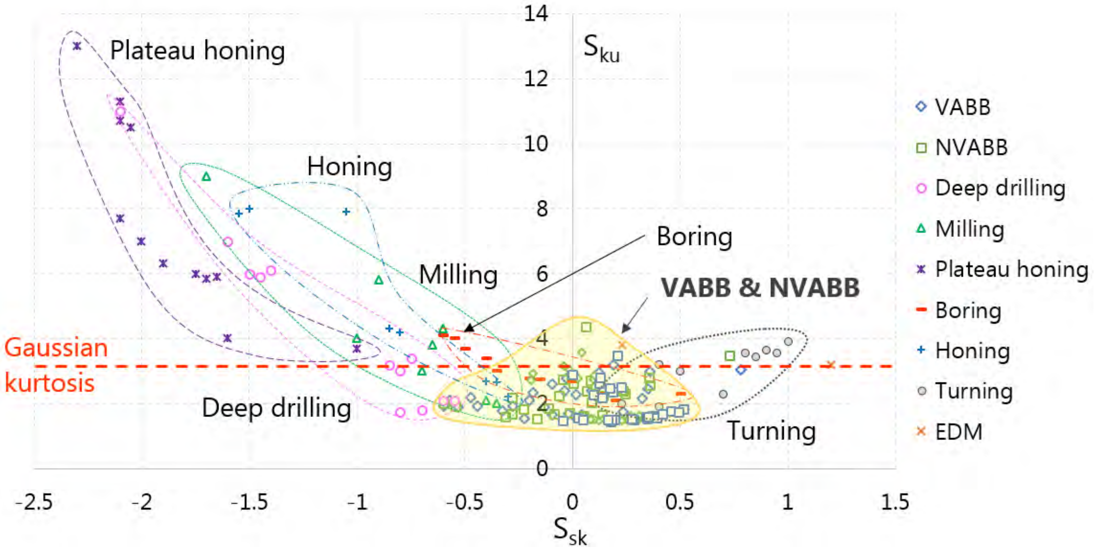

Figure 5.47. Position of the VABB and NVABB process with respect to other finishing process. After data found at Griffiths (1986) [47].

The clearly controlled area in which ball burnishing results are enclosed with regards to other finishing processes is a direct consequence of the mechanism on which each one is based. For instance, chip-removal operations, such as honing, remove the peaks of the material texture, generating a certain flattening effect that leads to high kurtosis values and a predominant weight of positive heights (negative skewness). On the contrary, ball burnishing actually redistributes the target material that composes the surface texture, as the excerpted compression mechanism causes its flow towards the burnished track, thus creating new irregularities on the surface, only of a lower scale. As was shown in the previous subsection, too high plastic strain can lead the surface to over-strain, generating new irregularities that can be detrimental to its surface texture, by regenerating the initial peaks and valleys of the milled areas. Therefore, the effect of ball burnishing can be then described as a self-reproducing or cyclic process, that redistributes material causing similar lower-scaled surfaces. By this effect, kurtosis and skewness values are always kept inside a specific enclosed area of the Cartesian plane, whereas the scale may vary from test to test.

5.1.4 Approach to the surface-ball interface through a finite element model

The initial topology has proved to determine to what extent it can be modified after ball burnishing, as well as the effectiveness of the vibration assistance, which has proved to be negligible for surfaces conformed of relatively more abrupt height distributions. In other words, the introduction of vibrations has proved to be more effective as the surface texture has a smaller scale. The first hypothesis concerning this observation is that the interaction of the ball with the surface material changes substantially with the scale and distribution of the surface features.

It would be desirable to observe and measure this contact by optical means, enabling its quantification. Unfortunately, this task is technically complex and costly, due to the scale of the contacts and the reduced accessibility to the manufacturing environment. At sight of this limitation, and seeking evidence to confirm this hypothesis, the idea of developing a Finite Element Model (FEM) to have comparative data to compare the interface between the ball and the surfaces was embraced. The development of this model is however not at all the aim of this dissertation. Its complete and comprehensive development would be the object of an entire thesis. Therefore, the results presented here have a preliminary condition, and constitute a first approach to the issue to bring light from a theoretical point of view to the effects that are being experimentally observed through the topological analysis.

Many ball burnishing FEM can be found in the bibliography. They are mostly based on lathe ball burnishing, being the objective of all of them identifying the results in terms of residual stress distribution with experimental results. Rodríguez *et al.* (2012) found a model that could predict deep residual stress of ball burnished AISI 1042 cylinders, but no initial surface texture was considered. Yen *et al.*(2004) [160] developed two 2D and 3D FE model to predict the final roughness after ball burnishing. Other authors, such as Balland *et al.* (2013) [5], considered saw-shaped periodic roughness, but the unrealistic condition of the surface makes results non-comparable with real results. As an alternative, the model developed for this dissertation, and presented below, implements the real surface texture obtained after machining in 3D, based on a similar 2D approach developed by Sartkulvanich *et al.* (2007) [124], represented in Figure 5.48.

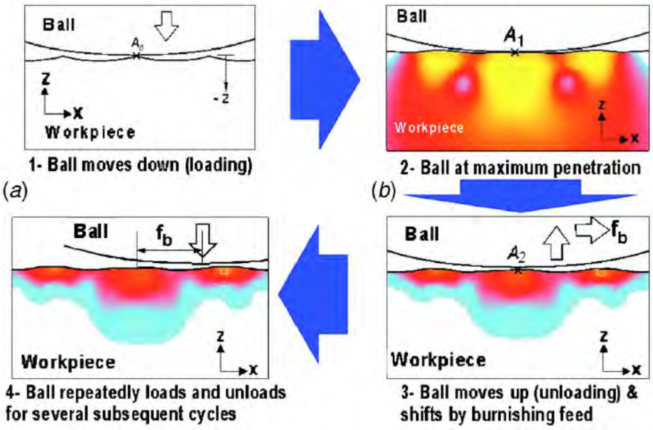

Figure 5.48. 2D periodical texture profile used by Sartkulvanich *et al.* (2007) [124].

Another critical issue in modelling the ball burnishing process is the method used to pilot the preload. Authors have usually controlled the preload by geometrical means, imposing a depth of penetration of the ball inside the material [10, 122]. This solution is often adopted because of its easiness of implementation. However, an improved model should discard this option, as the real depth of penetration of the ball in the material changes as it moves, due to the surface irregularities. Furthermore, as the material is deformed, the hardening effect can have an impact on the initially programmed depth. In the model proposed here, the preload is directly imparted on the burnishing ball, and is kept constant along the whole process.

The bibliographical review reveals that there is still work to do about ball burnishing FE models, by making them more adapted to real burnishing conditions. The model that has been developed here to support the result analysis of this dissertation, constitutes the first step of a more sophisticated model that shall be developed in the future, and that includes the following main differential features:

- It incorporates a 3D ball-end periodical texture pattern, based on real machined surfaces used in the experimental phase of this thesis.
- It allows preload control by direct application of the force on the burnishing ball, preventing the results of being influenced by self-hardening effects or variations due to the topology height variations of the material.

The ball burnishing model shall be executed for surfaces S_1^0 and S_3^0 textures, on which 270 N and 1 pass shall be executed. Only the NVABB process shall be modelled, as the 40-kHz vibration-assisted operation includes dynamical interactions that should be object of a more thorough study, far from the scope of this dissertation. The ANSYS software was used to perform the model.

5.1.4.1 Model geometry and material properties

A 5.5 × 1.7 × 2 mm AISI 1038 block was generated and meshed as the target material of NVABB. The S_1^0 and S_3^0 textures were overlapped on top of the volume by reproducing a simplification of their original profiles along the width coordinate, thus generating two respective blocks that exhibited planar symmetry and periodical texture features. The base curves were generated by juxtaposing spline curves characterised by their opening width and their depth, extracted from the real P profile traced on the real surface, as shows Figure 5.49. The mechanical properties of the steel alloy were taken from Table 4.13, whereas its plastic behaviour was modelled through the von Mises yield criterion (Eq. 5.2). The meshing was generated through `solid186` elements, that allow us to model three-dimensional solids with quadratic displacement behaviour.

$$\tau_{max} = \frac{\sigma_y}{\sqrt{3}} \tag{5.2}$$

where τ_{max} is the maximum shear stress due to friction force, and σ_y is the yield strength of the material.

The ∅ 10-mm ball was modelled as an rigid solid characterised by the mechanical properties of a standard hardened chromium steel taken from a standard material database (Table 5.7).

Table 5.7. 60Cr3 chromium steel mechanical properties.

Property	Value
Young's Modulus	200 GPa
Poisson's Modulus	0.3

The contact between the two solids was modelled through `conta174`- and `target170`-type elements, to adequately represent the sliding mechanism between the ball and the surface, governed by the Coulomb-Mohr classical friction law. The friction is deliberately introduced in the model, as although it does not have effect on the

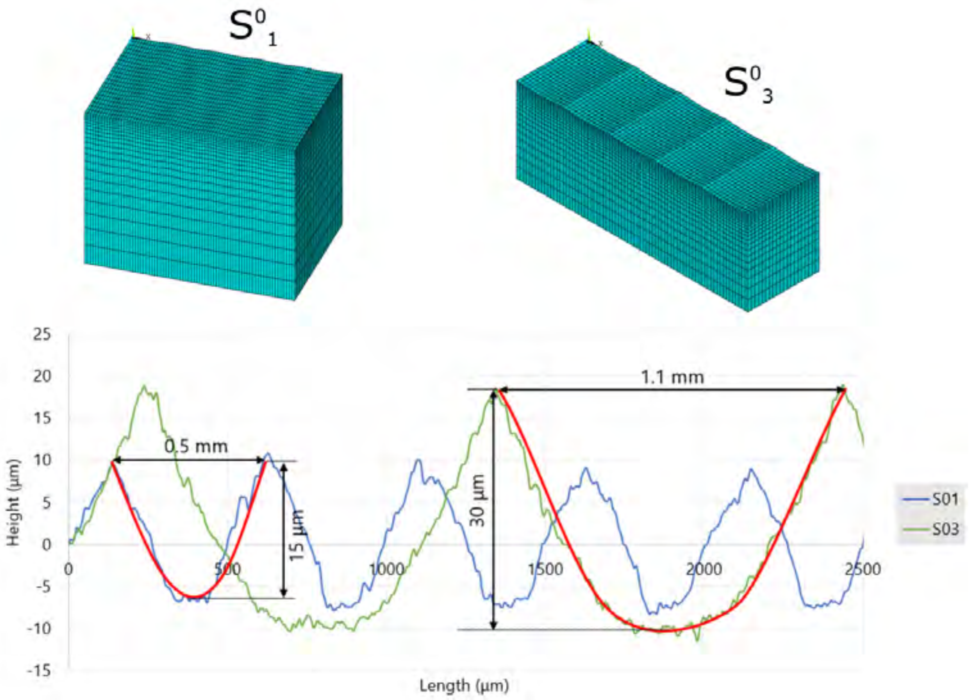

Figure 5.49. 3D periodical textures modelling S_1^0 and S_3^0. Red line: spline curves modelling the initial texture peaks.

force variation, it is an important drive for material pile-up after deformation, which is fundamental for the final texture after the process.

5.1.4.2 Boundary conditions and model development

The boundary conditions of the model comprise no displacement at the bottom and the three sides of the block, as shows Figure 5.50. The execution of the model was programmed through the implicit ANSYS software, due to the lack of effect of inertial forces, so that a succession of three main steps were considered as follows:

1. Loading phase: preload is actuated on the burnishing ball to plunge it into the material.
2. Burnishing phase: displacement of the burnishing ball through frictional sliding continuously along a longitudinal path formed by 3 peaks of the surface, with a 600-mm/min feed, and a 0.3-mm lateral offset displacement. Repeat the process five times to obtain 5 parallel burnishing paths.

3. Unloading phase: the ball is raised, ending its contact with the surface.

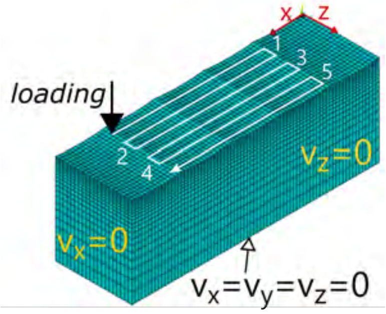

Figure 5.50. Steps comprising the FEM and boundary conditions imposed on the material.

5.1.4.3 FEM results

Figure 5.51 represents the vertical displacement of all points after NVABB. Warm colours represent the nodes that are in a higher position than before applying the procedure. Therefore, the ball trajectory can be clearly represented by the blue valleys that have been created. The highest positive displacement is registered at the borders of the burnishing patch, showing the transient boundary effects caused by the pile-up of the material after self-hardening due to plastic deformation.

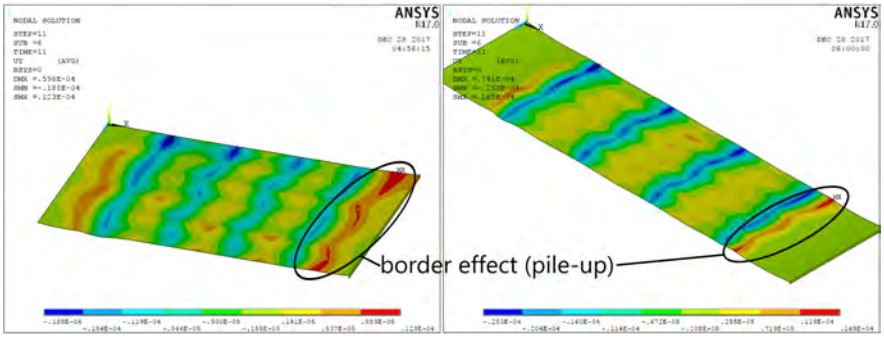

Figure 5.51. Texture after burnishing modelled by vertical displacement of the FEM nodes due to plastic deformation on S_1^0 (*top*) and S_3^0 (*bottom*). Scale in m.

The shown displacement values correspond to the relative change of position of each node after the NVABB process, and should be added or subtracted to each correspondent coordinate before the operation. However, this is not the aim of the analysis, and, therefore, shall not be tackled here. On the contrary, it shall focus on the quantification of the contact area of the ball and the nodes that compose the surface is sought. To do that, instantaneous states of the whole simulation were considered during the lateral displacements along the offset length between adjacent passes, coded according to the numbers represented at Figure 5.50. For that instant, the nodes that were simultaneously in contact with the ball and the surface solids were retained. Being known the instantaneous size of the elements, the addition of all single areas allows the calculation of the contact surface between the ball and the surface material. Figure 5.52 shows one set of retained elements to calculate the area as an example, as well as a graphical representation of the areas retained for each analysed simulation step.

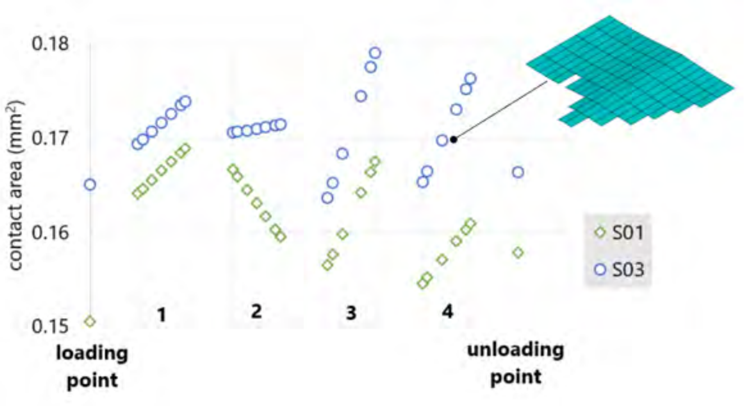

Figure 5.52. Contact areas between ball and S_1^0 and S_3^0 surfaces in different stages during lateral displacements.

Considering that all treating conditions are the same ones, the areas calculated for the two calculated cases are comparable among them. In overall, the contact are of the ball with the material surface is not constant, and evolves as the lateral pass width is progressively taken. However, the interaction area between the ball and the S_1^0 surface is in all cases lower with regards to S_3^0. This area difference can explain the different effects of the process depending on the kind of surface on which it is actuating. Being the contact surface smaller in S_1^0 can account for the higher effectiveness of the process in affecting this kind of texture, as the total actuated stress is higher. It can also give clues about the higher effectiveness of the VABB process, although this should have to be investigated by developing a model which is able to incorporate the vibration movement.

The finite element model has evidenced a different affectation of the surfaces, just by the fact that the interface contact area between both solids changes with the different scale of the texture features. It was only calculated on an AISI 1038 workpiece to serve as a starting point for future works, and to observe the effects of the process on the material that exhibited the highest contrast between results depending on the initial surface. The next subsection starts the study of mechanical effects of the VABB and NVABB, by studying the results on the superficial residual stress.

5.2 Mechanical parameter: residual stress

The residual stress (RS) results calculated by applying the $\sin^2\psi$ method through X-ray diffraction were provided by the lab as a two-dimensional tensor represented as in Eq.5.3. It contains the normal stress along the two main reference directions (I and II), and the shear stress associated to the measured patch. The error associated to each stress value was automatically quantified by the calculation software as a result of noise estimation and uncertainty in the identification of the Bragg's diffraction peak registered through the equipment. All errors are lower than 5%, meaning that the measurements are highly reliable to represent the RS of every machined and burnished surface.

$$\sigma_{\mathbf{RS}} = \begin{pmatrix} \sigma_I & \tau_{12} \\ \tau_{21} & \sigma_{II} \end{pmatrix} \pm \begin{pmatrix} e_I & e_{12} \\ e_{21} & e_{II} \end{pmatrix} \tag{5.3}$$

where σ_i is the normal component of the tensor along direction i, τ_{ij} is the shear stress components of the tensor, e_i is the error associated to σ_i, and e_{ij} is the error associated to τ_{ij}.

5.2.1 AISI 1038

5.2.1.1 Residual stress state of the original surfaces

All three machined surfaces result in compressive RS, as is shown in Figure 5.53. This condition is not rare in this kind of machined materials, which are obtained by perpendicular ball-end milling, due to the near-zero cutting velocity at the tool nose, which is detrimental for clean chip removal. Instead, the tool presses on the surface as it traverses the material along the programmed trajectory [49]. S_1^0 shows higher compressive RS than for S_2^0 and S_3^0. As this surface is obtained by parallel passes with the lowest offset between them, the aforementioned detrimental cut dynamics are actually substituted by a compressive action that deforms the surface near to the tool nose. The low offset length makes more passes necessary to cover a certain amount of surface, increasing the described compressive action.

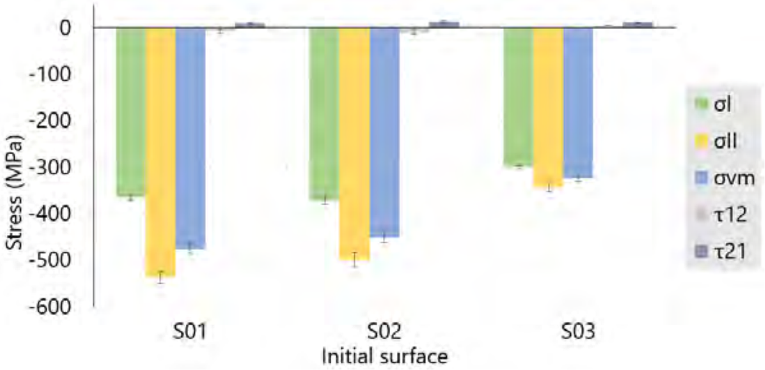

Figure 5.53. Residual stress descriptors at S_1^0, S_2^0 and S_3^0 AISI 1038 surfaces.

The material presents a remarkable anisotropy, as $\sigma_{II} > \sigma_I$, meaning that the higher residual compression on the surface is accounted along the feed direction followed by the hemispherical tool. The shear components of the tensor, τ_{12} and τ_{21}, are almost negligible if compared to the normal ones, and considering the incertitude associated to them. Therefore, the machined surfaces can be described through a biaxial stress state, being directions I and II its principal directions.

Figure 5.53 also represents the von Mises stress, which has been calculated for the three surfaces through Eq. 5.4, provided their biaxial stress state. The von Mises stress can be considered as a comprehensive descriptor of the RS state of the material [51].

$$\sigma_{vm} = \sqrt{\sigma_I^2 + \sigma_{II}^2 - \sigma_I \, \sigma_{II} + 3 \, \tau_{12} \, \tau_{21}} \tag{5.4}$$

The incertitude associated to the von Mises stress can be calculated by error propagation:

$$e_{vm} = \sqrt{\sum_1^n \left(\frac{\partial \sigma_{vm}}{\partial x_i} e_{r,i}^2 \right)} \tag{5.5}$$

Applying Eq. 5.4 to 5.5, the von Mises stress incertitude, e_{vm}, can be calculated as follows:

$$e_{vm} = \frac{1}{2\,\sigma_{vm}}\sqrt{\left[e_I\left(2\sigma_I - \sigma_{II}\right)\right]^2 + \left[e_{II}\left(2\sigma_{II} - \sigma_I\right)\right]^2 + 9\left(\tau_{12}e_{21} + \tau_{21}e_{12}\right)^2} \tag{5.6}$$

Comparing the von Mises stress calculated on all three initial surfaces, a general decrease in the stress state is detected as a higher offset distance is taken between adjacent passes, while the incertitude is of a similar same order of magnitude.

5.2.1.2 Overview of residual stress results after ball burnishing

A first approach to the VABB and NVABB RS results analysis is performed by colour-coding and representing the normal components of the stress tensors of each test (Figure 5.54). Whereas RS are still compressive, the absolute values of some of them are lower than their as-machined correspondents, meaning that certain some burnishing conditions can lead to stress relaxation. Now, would this effect be the same one in surfaces that are not in such a compressive state? That would mean a net positive effect of ball burnishing, that should be checked on another set of workpieces in future works.

The anisotropy that was observed in the initial surfaces is however maintained after the VABB and NVABB processes. The higher values of σ_{II} with regards to σ_I are in general confirmed for all burnishing states, except for specific conditions where this trend is reverted: tests #7, #18, #22 and #26. These testing conditions have in common that they are all executed with 3 or 5 passes combined with the bn90/0 strategy. Consequently, whereas the strategy proved not to be influential in topological results, it can actually affect the directionality of RS. Indeed, applying a burnishing strategy based on more than 3 criss-crossed passes, turns out to have the effect of reverting the anisotropy that was detected after machining.

The von Mises stress calculated for all patches, and represented against σ_{II}, reveals that the latter dominates the overall RS state of every VABB and NVABB surfaces, except for the singular group of tests that were detected as significantly influential (Figure 5.55). This fact reinforces the idea of the strategy as a modifier of the preferential direction of RS. On the other hand, the highest von Mises stress are attained at the tests performed on the S_1^0 and S_2^0 surfaces.

This first visual analysis has delivered valuable information, but cannot describe

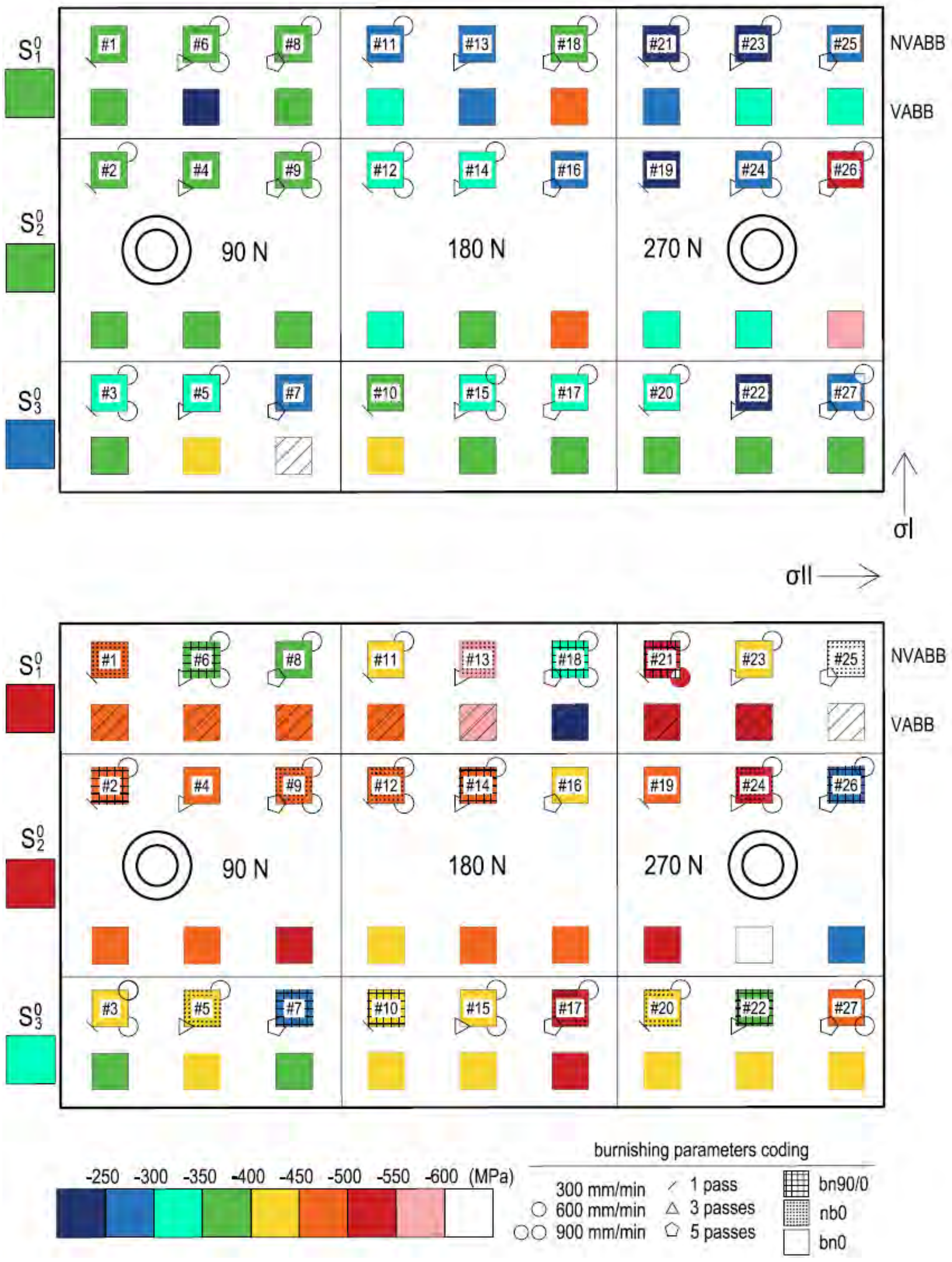

Figure 5.54. Normal components of the residual stress tensor measured for all VABB and NVABB patches of the AISI 1038 workpiece.

the effect of each burnishing factor on the final RS. For that reason, an ANOVA has been performed and explained in the next section to assess the influence of the

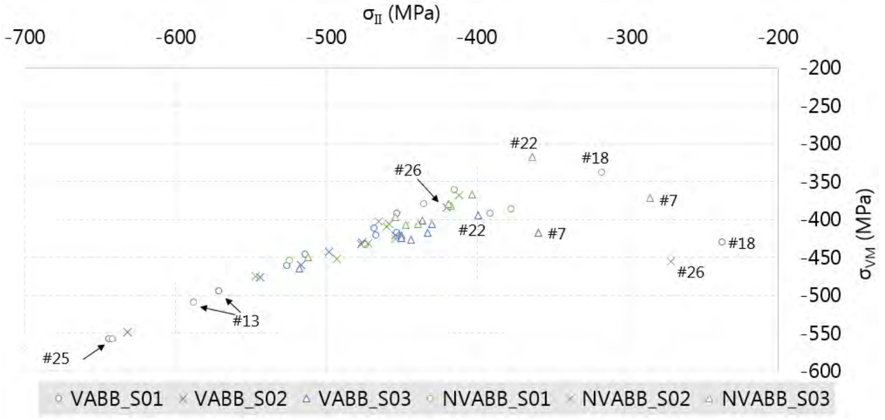

Figure 5.55. Correlation between σ_{II} and σ_{vm}.

preload, number of passes, strategy, initial surface texture and feed velocity on the normal stress components and the von Mises stress. This analysis shall lead to parameter optimisation in order to maximise compressive residual stress on the surfaces.

5.2.1.3 Parameter optimisation for RS maximisation based on ANOVA mean effects

The analysis performed in the previous section evidenced that the anisotropy of the machined surfaces was maintained after the execution of both NVABB and VABB processes. A direct deduction of this observation is that the optimisation target is not unique in this case. Indeed, many variables could fulfil that role, namely σ_I, σ_{II}, or σ_{vm} as a general descriptor of the RS state. Although the ideal objective would be maximising σ_I and σ_{II} simultaneously, the reader shall realise that this is not possible at sight of the results that are to be presented throughout the next subsections.

The optimisation procedure that shall be followed is represented graphically in Figure 5.56. First, the set of optimal values shall be decided based on the mean effects and interactions graphs delivered by the ANOVA calculations considering as response variables the absolute RS components, and their relative improvement with regards to the reference values related to the machined surfaces. The "higher is best" criterion is considered to calculate the S/N ratios. To complete the analysis, the parameter set found through this deduction shall be compared to experimental values.

ANOVA mean effects on absolute residual stress

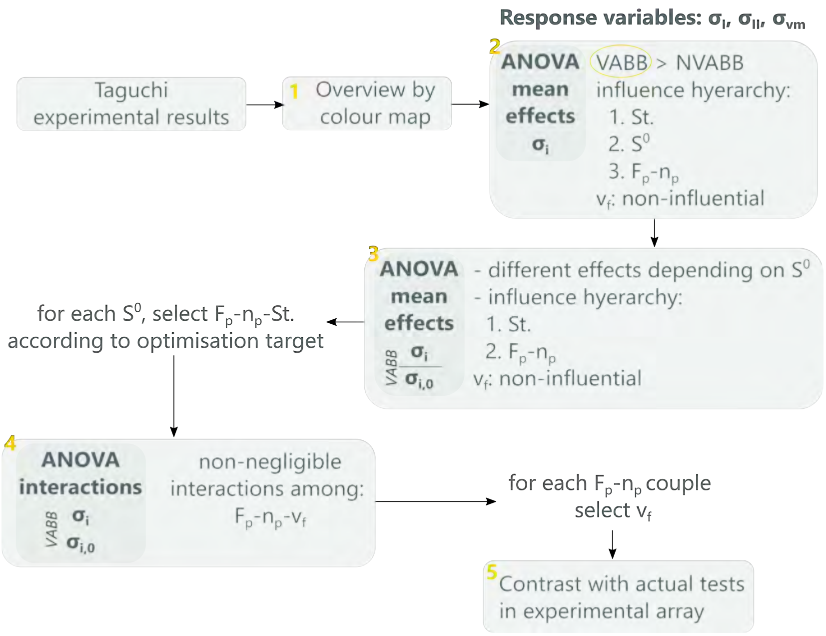

Figure 5.56. Procedure to find the best ball burnishing parameters to maximise residual stress.

The mean effects of each parameter on the different RS components calculated through ANOVA are represented in Figure 5.57. The first observation that can be made agrees with the general remarks performed in the previous subsection, by identifying the strategy as a modifier of the preferential direction. While bn90/0 reinforces σ_I, σ_{II} is enhanced by nb0. Being true for both VABB and NVABB, this consideration is a fundamental finding in terms of productivity, as it implies that by planning correctly the trajectory of the burnishing tool, for instance concentrating all ball passes along one direction, the surface orthotropy can be modified conveniently, sparing productive time.

Secondly, the VABB process generates higher compressive RS in average, especially along direction I. Therefore, VABB can be considered as thee preferential process over the NVABB one. Focusing then on te VABB factors, the F_p can be fixed in 270 N, whereas 5 passes should be recommended for σ_I and 3 passes for σ_{II}. Ironically, the low influence of the initial texture is also an interesting result in this case, due to the fact that the surfaces departed from very different stress states. Indeed, as the original RS values of S_3^0 are lower than those of S_1^0 and S_2^0, its enhancement can be described as more remarkable after VABB. Consequently, S_3^0 can be declared as the surface that has been more positively influenced by the VABB process.

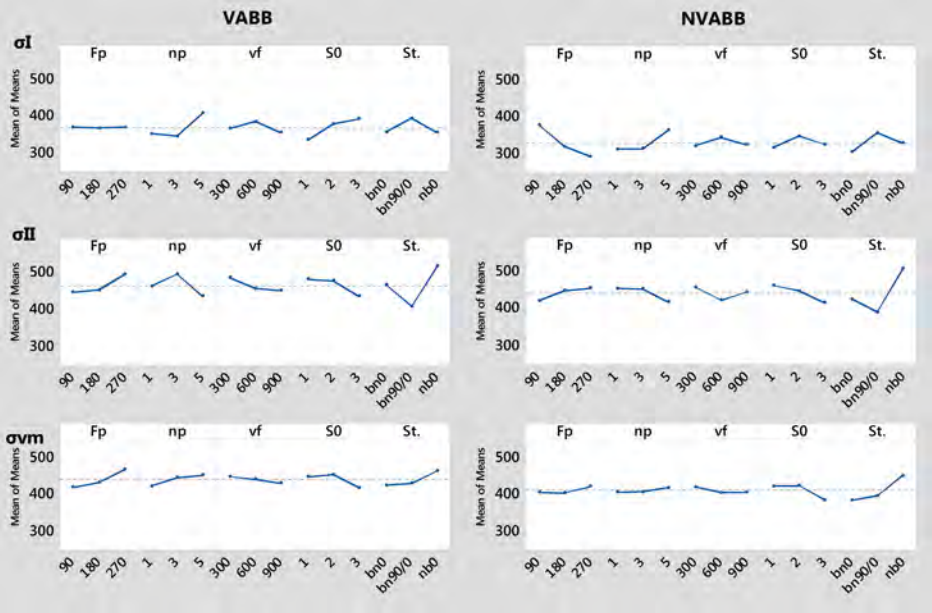

Figure 5.57. VABB and NVABB mean effects. ANOVA response variable: RS stress components of AISI 1038.

Taking into consideration the results delivered by the absolute RS states leaves many questions open. Therefore, an additional approach to the subject is undertaken in the next subsection by considering the factors that deliver the highest profit from the introduction of vibration-assistance.

ANOVA mean effects on the residual stress relative improvement

To consider the influence of the introduction of vibration-assistance in the R results, the ANOVA has been performed taking the final-to-initial ratio of each RS component as response variables:

$$\Delta\sigma_i = \frac{\sigma_i}{\sigma_{i0}} \tag{5.7}$$

where $\Delta\sigma_i$ is the final-to-initial RS ratio, being $i = \{I, II, vm\}$

The mean effect graphs are represented in Figure 5.58. The red line delimits the boundary between the area where RS is improved after burnishing that is, $\Delta\sigma > 1$. Again, the VABB process shows superior effects on the RS, as it is able to deliver a higher improvement to the surface with regards to its non-assisted complementary. Results also show that this superiority must be read differently according to the initial surface texture, that, again proves to be a remarkable focus of response variation. The S_3^0 surface shows that it experiences the highest RS improvement by the introduction of vibrations. On the other hand, results on surfaces S_1^0 and S_2^0 show that the NVABB process causes stress relaxation. However, by introducing the vibration-assistance, the VABB maintains in average the initial RS level of S_2^0 tests, and reduces stress relaxation in S_1^0. This statement reinforces the idea of discarding the NVABB process, and considering the VABB process as the most adequate to deliver positive RS results on AISI 1038 surfaces.

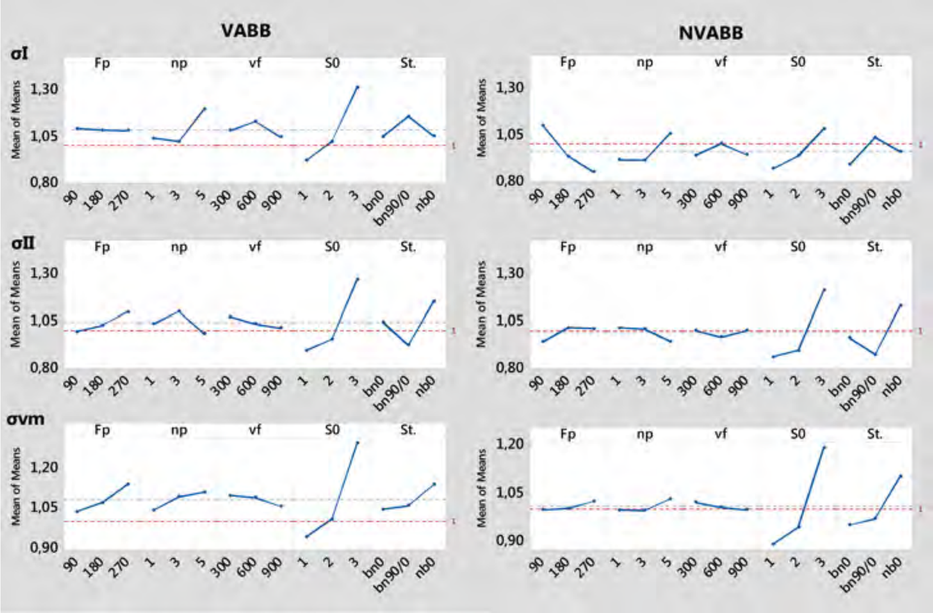

Figure 5.58. VABB and NVABB mean effects, S/N ratios and interaction plots. ANOVA response variable: final-to-initial stress components ratio of AISI 1038.

In this case, it seems that a 900 mm/min feed should be discarded, as the only values that improve RS are 300–600 mm/min. The rest of the results are consistent with the observations made in the previous absolute RS analysis: 270N–3passes is recommended to increase σ_I, while 270N–5passes should be the selected pair to achieve the highest enhancement of σ_I. The strategy evidences again its effects in the same sense as when the absolute RS values were considered: bn90/0 reinforces σ_{II}, while nb0 affects positively to σ_I.

Interaction analysis through ANOVA results on the residual stress relative improvement

The ANOVA calculations evidence that, in this case, the $F_p{}^*v_f$ and $n_p{}^*v_f$ interactions cannot be neglected from the analysis (5.59). Starting by σ_I, for which 270N–5passes were established as best, the interactions seem to favour 600 mm/min. For σ_{II}, the observed 270N–3passes combination is more adequate to be applied with 300 mm/min. Finally, the overall RS represented by σ_{II}, should be executed by 270N–5passes, and the feed interval 300–600 mm/min is adequate.

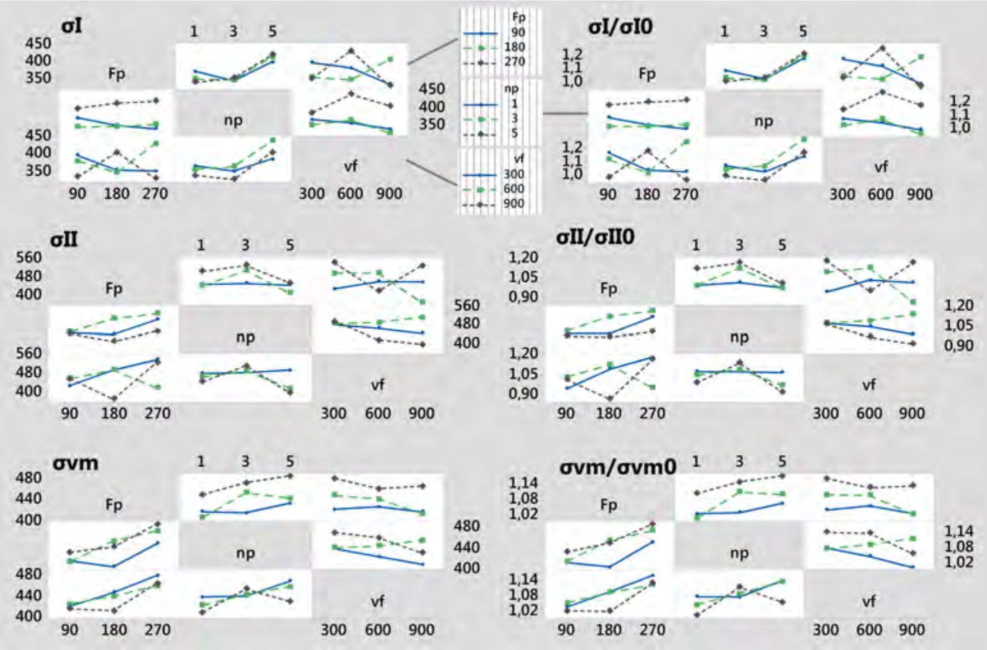

Figure 5.59. VABB interaction charts. ANOVA response variables: RS components of AISI 1038.

The feed values defined by this deductive process might seem different, but can be actually read from a single scope: they discard 900 mm/min as a possible value, and accept in general, al feeds lower than 600 mm/min. This means that the efficiency of the process is delivered by a sufficiently low ball displacement on the surface.

All S/N ratios figures can be observed in Appendix D. The higher values of the S/N ratios for every level that has been found optimal prove their higher robustness in terms of results.

The optimal values that must be taken to maximise compressive residual stress after VABB, at sight of the mean effects of the factors calculated through an ANOVA, can be found in Table 5.8. Of all the values, the initial texture must be taken very carefully. The S_3^0 has proven to be extraordinarily enhanced by VABB, reaching also the highest σ_I. However, the S_1^0 and S_2^0 have proved to deliver the maximum σ_{II} and σ_{vm}, although RS have been relaxed. This is due to the fact that they depart from a higher compressive state, so that their superior RS results are actually not caused by the VABB process, but because it is able to keep the same level as the machined surfaces.

Table 5.8. Optimal parameters to apply VABB on AISI 1038 surfaces according to different RS targets, based on ANOVA mean effects.

Opt. target	Process	F_p (N)	n_p	vf (mm/min)	S^0	Strategy	test	RS increase: $\Delta\sigma_i$
σ_I	VABB	270	5	600	S_3^0	bn90/0	–	–
σ_{II}	VABB	270	3	300	S_1^0 or S_2^0	nb0	–	–
σ_{vm}	VABB	270	5	300-600	S_1^0 or S_2^0	nb0	#25	21.1%

The fact that all factors have been declared influential in the RS results makes it difficult to find the exact experimental realisation in the Taguchi array. Only the test #25 can be found to represent the optimal parameter set to maximise σ_{vm}, which is, indeed, the test for which that parameter achieves its highest improvement. Albeit the positive result, this test is performed on S_1^0, where RS should be relaxed at sight of the mean effect analysis. This observation does not invalidate the previous results, as they proceed from real experimental data. However, it leads to think that there might be tests that, although do not fit the found optimal factor combination, could also derived in positive results. These tests are discussed in the following subsection.

5.2.1.4 Optimal parameter set for RS maximisation based on individual Taguchi experimental results

Figure 5.60 shows the RS components of the experimental tests were they resulted to be maximum. The respective parameter sets that characterise those tests are included in table 5.9. It is evident that these combinations are not exactly coincident with the optimal sets obtained from the ANOVA mean effect deductive process. The feed is the factor showing a highest disagreement, as it presented better mean results for low values, but some of the real best tests are performed with 900 mm/min. A possible source of variation could be identified with the fact that there are still 6 second-order interactions that are not being studied through the L27 experimental design, and that could indeed be relevant for the case study.

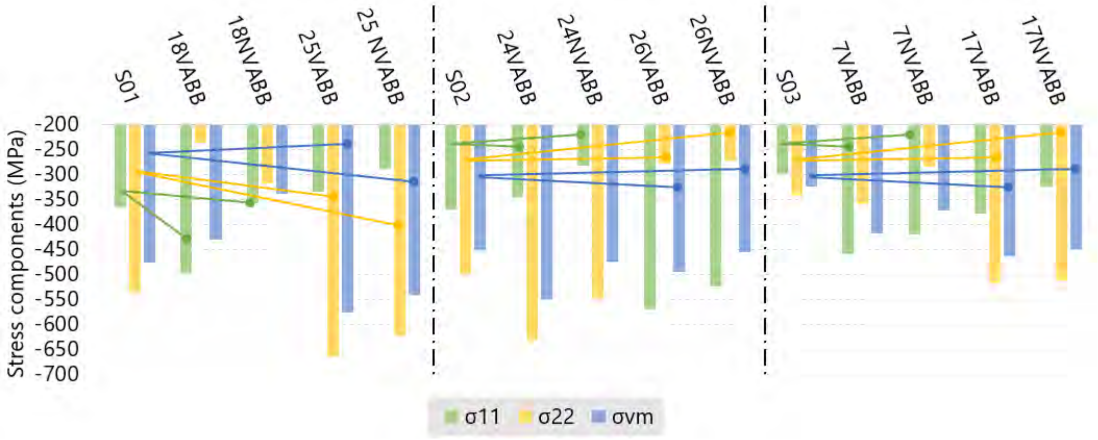

Figure 5.60. AISI 1038 experimental tests with highest compressive residual stress.

Table 5.9. Optimal parameters to ball burnish AISI 1038 surfaces based on real experimental results

Initial surface	Opt. target	Process	F_p (N)	n_p	vf (mm/min)	Strategy	test	VABB $\varDelta\sigma_i$	NVABB $\varDelta\sigma_i$
S_1^0	σ_I	VABB	180	5	900	bn90/0	#18	36.6%	2.2%
	σ_{II}	VABB	270	5	300	nb0	#25	23.6%	15.8%
	σ_{vm}	VABB	270	5	300	nb0	#25	21.1%	13.5%
S_2^0	σ_I	VABB	270	5	600	bn90/0	#26	53.9%	41.5%
	σ_{II}	VABB	270	3	900	nb0	#24	26.4%	9.4%
	σ_{vm}	VABB	270	3	900	nb0	#24	21.8%	5.4%
S_3^0	σ_I	VABB	270	5	900	bn90/0	#7	50.3%	40.0%
	σ_{II}	VABB	270	3	600	nb0	#17	51.2%	49.3%
	σ_{vm}	VABB	270	3	600	nb0	#17	43.4%	38.7%

At this point, it seems that a reasonable strategy to obtain conclusions about ball burnishing for compressive RS maximisation, is finding the facts that are common between both theoretical and experimental approach. These

- The VABB process has proved to deliver superior results both in mean terms, and also in the specific experimental tests.
- The strategy is a fundamental factor to define the preferential RS stress direction. On one hand, bn90/0 reinforces direction I, while nb0 reinforces direction II. However, it must not be forgotten that the reinforcement of one direction proves to be detrimental to the perpendicular one, at sight of the experimental results.

- 270 N is the preload level that derives in the best results. Although the best VABB conditions for S_1^0 is obtained with 180 N, it is still a high preload level. Therefore, in general terms, it can be stated that a high preload are desired to achieve higher compressive RS in the workpieces.
- The number of passes is not exactly the same one in all tests. However, in all cases, 3 o 5 passes are considered, agreeing that 1 pass is not suitable. A general conclusion to this matter is that the best n_p is between 3 and 5.

The RS analysis on the AISI material has proved to be more complicated than the result discussion performed for the texture issue. Indeed, the relevance of all parameters on the responses, as well as the interactions, has complicated this task. In the next subsection, the titanium alloy results in terms of RS are analysed, by following a similar proceeding.

5.2.2 Ti-6Al-4V

5.2.2.1 Residual stress state of the original surfaces

The assessment of the residual stress of the initial surfaces machined on the Ti-6Al-4V workpiece was performed by performing the X-ray diffraction method on three different points for each surface. The resulting 9 measurements show that the residual stress condition of each one is stable at all assessed coordinates, since although σ_I and σ_{II} can slightly vary from one point to another, the equivalent von Mises stress is equivalent for all of them (Figure 5.61). That means that the influence of the machining operation on RS can be considered uniform, but that a variation of the relative weight of the two normal stress components in the overall RS state might occur depending on the specific measuring point. All in all, anisotropy is detected in all measurements, being $\sigma_I > \sigma_{II}$. This observation is contrary to the one found in the AISI 1038 workpiece, where the direction showing the higher RS was σ_{II}. This difference can be easily explained by considering the different background of both raw materials, which were processed through lamination and forge respectively, and the consequent variation in residual stress state. In any case, this difference should be considered when comparing and discussing the results found for both materials.

In absolute terms, it is S_1^0 the surface with highest RS components, which descend sequentially as the offset distance between passes is reduced to generate S_2^0 and S_3^0. This effect was also observed on the AISI 1038 surfaces, and can be attributed to the

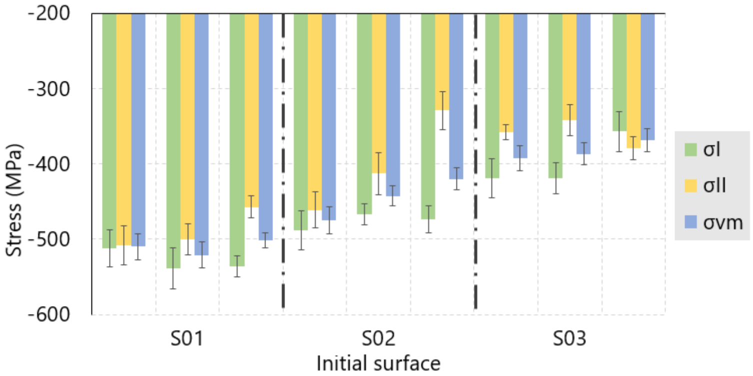

Figure 5.61. Residual stress descriptors at S_1^0, S_2^0 and S_3^0 Ti-6Al-4V surfaces.

pressing force performed by the tool nose in this kind of orthogonal ball-end milling operation, increased as the passes are less separated among them.

5.2.2.2 Overview of residual stress results after ball burnishing

The resulting normal components of the RS tensor associated to every burnishing patch are represented in Figure 5.62. As warm colours are associated to higher compressive residual stress level, it is evident that the resulting σ_I values are maintained higher after the VABB and NVABB process, in most of the cases. Consequently, it can be stated that neither of the two processes succeed in reverting the preferential direction presented by the original residual stress state. This effect was also observed on the AISI 1038 burnishing patches, where the main direction was kept in all cases along II, except for those tests performed by combining the bn90/0 strategy with 3 and 5 passes −#7, #18, #22 and #26−, which reverted the preferential direction. For the Ti-6Al-4V patches, where the initially favoured direction is I, the effect of VABB and NVABB tests is the reinforcement of this initially preferential direction. Indeed, tests #7, #18, #22 and #26 show the highest σ_I inside their initial texture groups.

The σ_{II} results also show a more clear progressive increase as the degree of plastic deformation grows, represented by a degradation from cool to warm colours. The effect of the preload can be expected to be more remarkable in this case, as show the ANOVA results included in the next subsection. On the other hand, the singular tests #7, #18, #22 and #26 do not seem to modify the level of stress, and no inversion can be detected in this case. Instead, the preferential RS directions presented by the raw material were reinforced by the application of these tests. Although this result seems

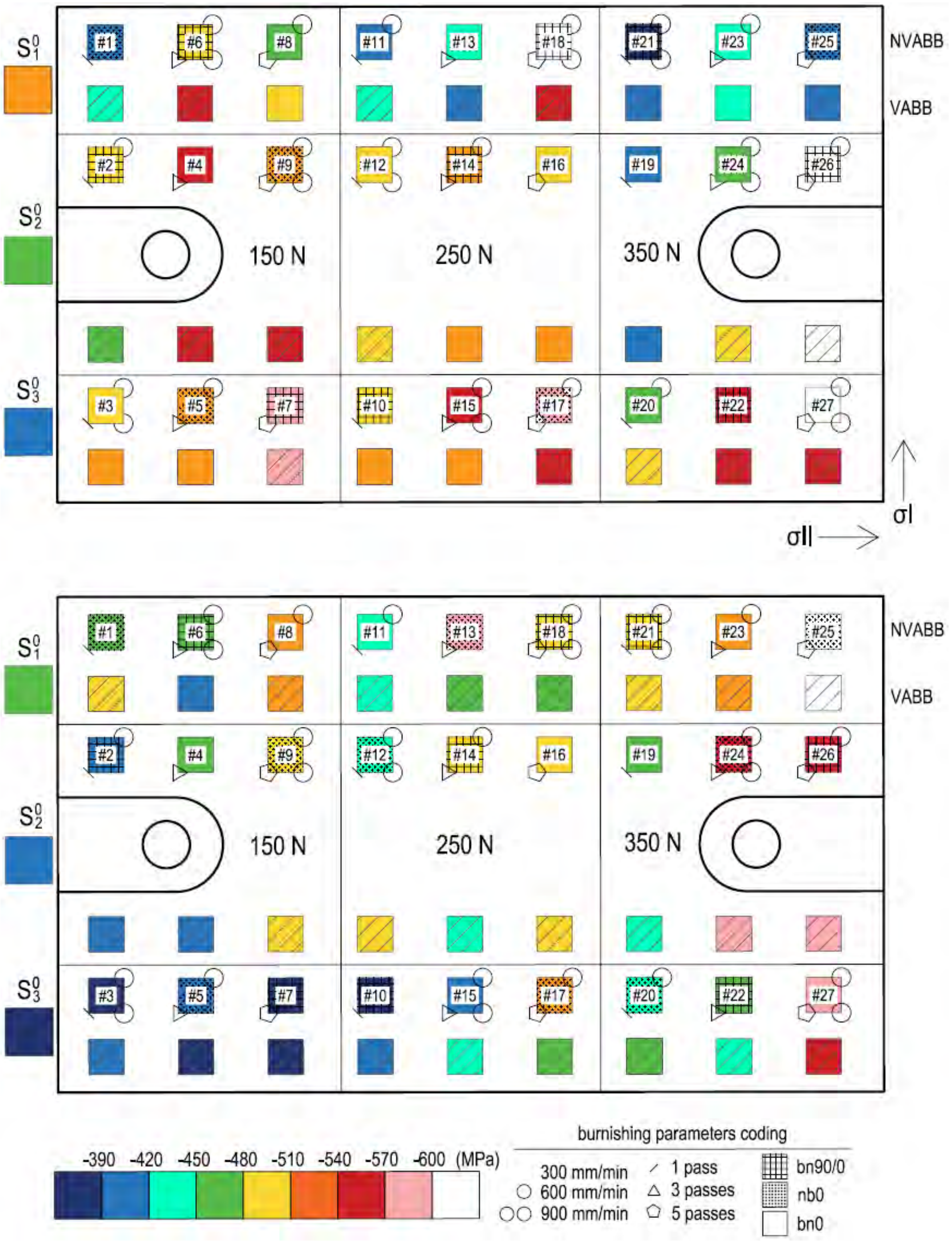

Figure 5.62. Normal components of the residual stress tensor measured for all VABB and NVABB patches of the Ti-6Al-4V workpiece.

opposed to the one obtained on the AISI workpiece, they are both very consistent. The favoured directions of both materials after machining were inverted. Since the preferential burnishing direction was maintained along I, the effect of applying each strategy must be consequently changed. What was inverted in the AISI surfaces is reinforced in the Ti-6Al-4V workpiece.

5.2.2.3 Parameter optimisation for RS maximisation based on ANOVA mean effects

The overview of all RS results has reinforced the idea of VABB and NVABB as processes able to reinforce the orthotropy presented by a machined surface. The following step is finding out whether an optimal parameter set can be found in order to take advantage as much as possible of VABB and NVABB to increase the compressive residual stress on the material surface. The sequential proceeding that is followed below is based on the same approach that was taken for the AISI results, shown in Figure 5.56. First, the optimisation shall be tackled by considering the mean effects of the factors and interactions included in the model, all of them calculated through ANOVA. These ideal parameter sets shall be then compared to experimental results. Finally, the best experimental results shall be identified, to compare them to the ideal set and extracting conclusions about this matter.

ANOVA mean effects on absolute residual stress

The mean effect of each factor included in the Taguchi design is assessed by performing the ANOVA taking the different RS components as response variables. The mean effect graphs are represented in Figure 5.63. The first immediate remark to do about the result is that both VABB and NVABB seem to deliver comparable mean effects. Secondly σ_{vm} is only influenced by the F_p–n_p pair, meaning that the overall RS modification is basically dependent on the degree of plastic deformation. Specifically, 350N−5passes are the best conditions to be applied in both VABB and NVABB.

As for σ_I and σ_{II}, the strategy proves again to be an effective driver through which reinforcing a desired surface direction, being bn90/0 the strategy favouring the former, and nb0 the latter. This result is identical to the case observed in the AISI workpiece.

The mean effects of the initial surface on the results is also inverted from σ_I and σ_{II}. The interpretation must be related to the initial surface state. After burnishing, the relationship $\sigma_I > \sigma_{II}$ is maintained in average as in the machined surfaces. However, S_1^0 being more residually compressed than S_3^0 is only maintained in σ_{II} after VABB and NVABB whereas it is inverted in σ_I. The only reason why this happens is

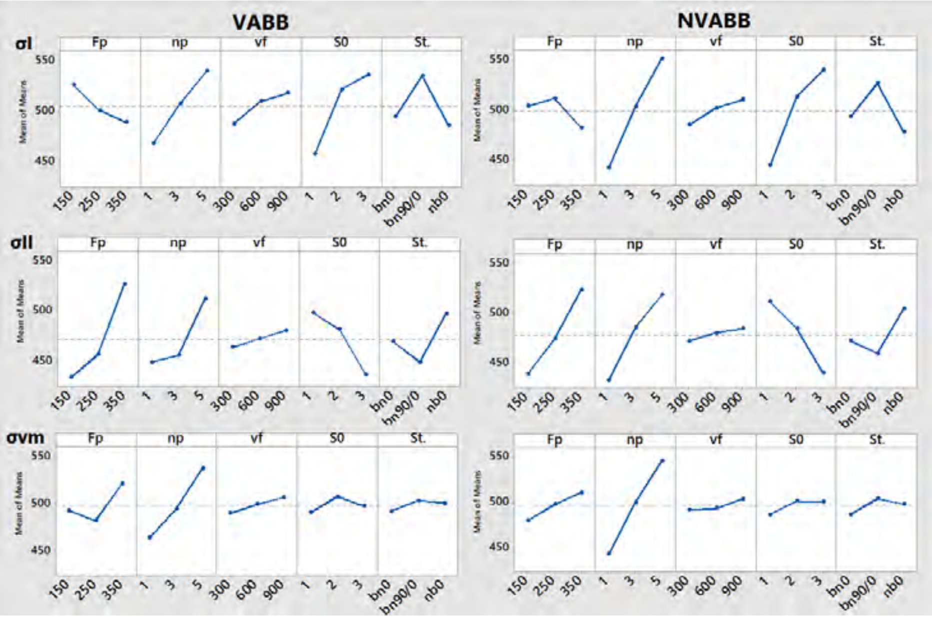

Figure 5.63. VABB and NVABB mean effects. ANOVA response variable: RS stress components of Ti-6Al-4V.

because S_3^0 is more positively affected by VABB and NVABB, and its σ_I (main burnishing direction) is increased to a higher extent.

Finally, the combination 350N−5passes is the best in meand terms to maximise σ_{II}. On the contrary, σ_I reflects better results by the application of 90 or 180 N with 5 passes. This observation could imply that a certain stress relaxation can be associated to both processes as the preload is increased. This effect contradicts the results obtained in the AISI 1038 results, were relaxation was only detected for the NVABB process.

The RS assessment after the mean effects calculated through the ANOVA has shown that the influence of all factors is relevant for the case study. However, there are still some issues to tackle with, such as the different influence of the process depending on the initial surface texture. Therefore, the relative improvement caused by the processes is analysed in the next subsection.

ANOVA mean effects on the residual stress relative improvement

The initial-to-final residual stress component ratio calculated through Eq. 5.7, has been subjected to an ANOVA calculation. Figure 5.64 shows that both processes are able to influence positively all surfaces, being the red line the boundary from where surface stress relaxation is caused after the process. It is remarkable that, in general terms, σ_{vm} is kept constant before and after ball burnishing, while it increases the most in S_3^0, through 350N-5passes, and independently from the strategy.

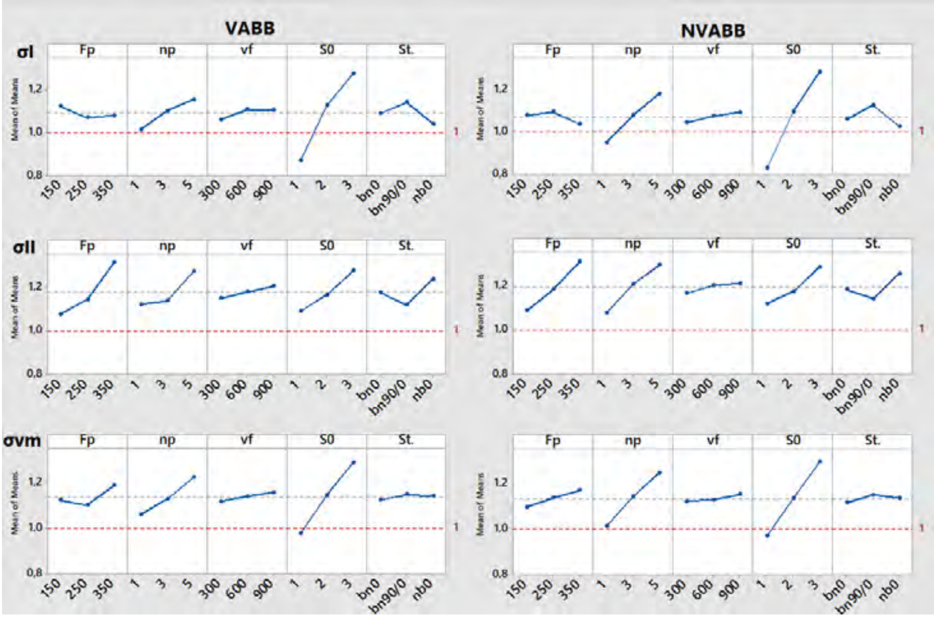

Figure 5.64. VABB and NVABB mean effects, S/N ratios and interaction plots. ANOVA response variable: final-to-initial stress components ratio of Ti-6Al-4V.

Other direct results arise from this analysis. First, no substantial difference between VABB and NVABB can be observed. Secondly, the strategy influence follows exactly the same pattern than in the absolute results. Third, no influence of the feed is observed. Last of all, the same F_p–n_p that were identified as ideal to maximise the final RS, also delivers the highest advantage of the process. The only difference, is that 270 N proves to be more effective in the VABB than in the NVABB process. That means that a high preload is required to take advantage of the vibration assistance.

These ANOVA results are highly interesting to understand the effect of the initial surface on the process effectiveness. S_3^0 is the most positively affected by VABB and NVABB. However, S_1^0 experiences RS relaxation along direction I, confirming what was observed in the analysis of the absolute results: this relaxation justifies the lower σ_I in S_1^0 than in S_3^0, being the only relative trend that is inverted after ball burnishing. The direct consequence of this observation is that applying the bn90/0 process on the S_1^0 surface, which defines σ_I should be avoided.

The last step to confirm the definition of the best parameters must be completed by checking the interactions between factors, that proved to be relevant in the case of the AISI alloy. This study is presented below.

Interaction analysis through ANOVA results on the residual stress relative improvement

The interaction analysis shown in Figure 5.65 proves that these are not so relevant in this case as they were for the AISI 1038 material. The $F_p{}^*v_f$ interaction for σ_I, makes recommendable to chose a 900 mm/min feed for the 150 N preload that was selected. The lack of remarkable interactions for the other two RS components allows the confirmation that all feeds could be eligible to apply the process, at sight of the lack of influence on the result

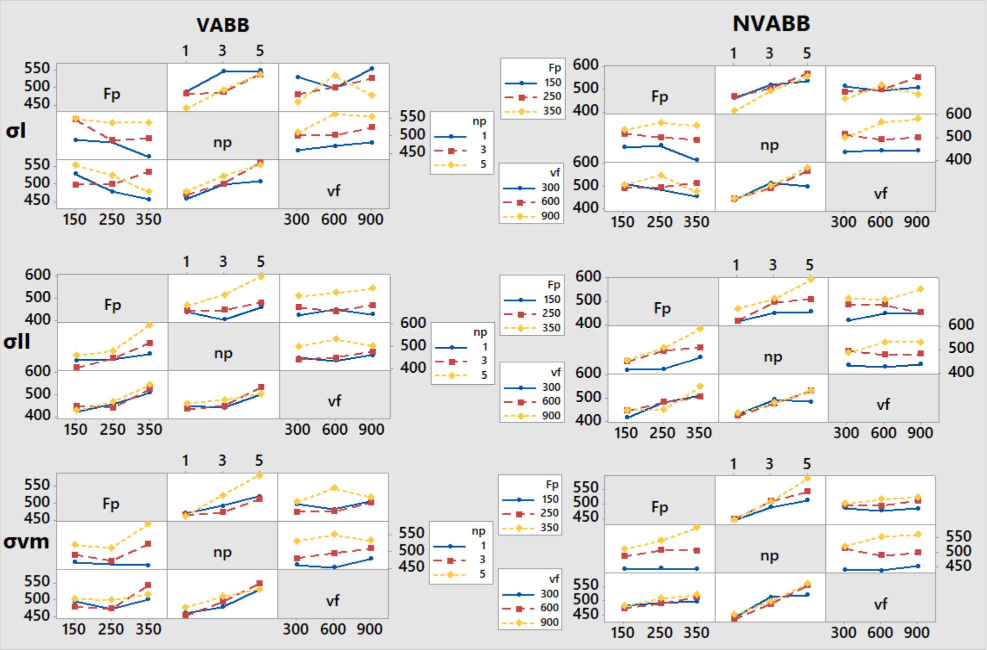

Figure 5.65. VABB and NVABB interaction charts. ANOVA response variables: RS components of Ti-6Al-4V.

The search for optimal parameter set according to the mean effects of each factor on the different RS components has resulted in the respective parameter sets included in Table 5.10. Both processes can be recommended to improve the RS state of the material, due to their similar mean effects, and the strategy is again the main facilitator for the reinforcement of a specific surface direction. As this solution is based on mean effects, it is necessary to compare them to actual experimental results. Only the sets determined for the σ_{II} and σ_{vm} can be found in the Taguchi array, confirming that they are able to increase the compressive residual stress over 40%. Now, to complete this validation, the direct consideration of the experimental results is undertaken in the next subsection.

Table 5.10. Optimal parameters to ball burnish Ti-6Al-4V surfaces according to different RS targets, based on ANOVA mean effects.

Opt. target	Process	F_p (N)	n_p	vf (mm/min)	S^0	Strategy	test	RS increase: $\Delta\sigma_i$
σ_I	NVABB	150	5	900	S_3^0	bn90/0	–	–
σ_{II}	VABB or NVABB	350	5	300–600	S_1^0	nb0	#25	21.0%
σ_{vm}	VABB or NVABB	350	5	300–600	S_1^0 or S_2^0	nb0, bn0 or bn90/0	#26	39.1%

5.2.2.4 Optimal parameter set for RS maximisation based on individual Taguchi experimental results

The direct inspection of all RS results has delivered the identification of the highest compressive residual stress results on the tested surfaces. These singular tests are represented in Figure 5.66. The processing parameters corresponding to these tests can be found in Table 5.11.

These selected tests confirm that, indeed, both VABB and NVABB can improve the RS state of all surfaces. Also, it is indifferent to apply the NVABB or the VABB processes due to their similar results, although S_3^0 exhibits a tendency to register better results with the NVABB process.

- Both the VABB and NVABB are able to cause similar effects in terms of residual stress on the Ti-6Al-4V surfaces.
- The highest preload 350 N is recommended to improve any of the different RS components, except for σ_I in the S_1^0 texture, for which 250 N is recommended. Although the main effect results fixed that recommended preload at 150 N, both cases indicate that a lower preload should be applied on S_1^0, so that it does not have a detrimental effect on the RS along direction I.

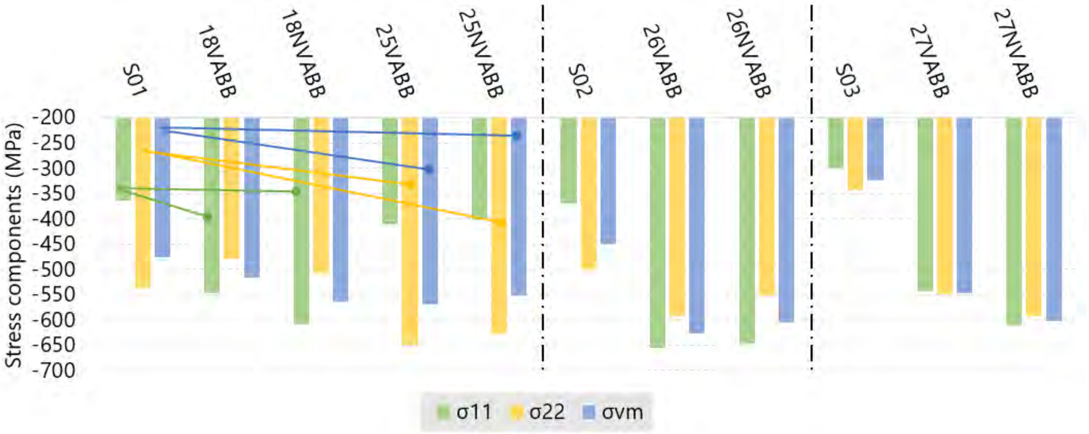

Figure 5.66. Ti-6Al-4V experimental tests with highest compressive residual stress.

- 5 passes should be performed in all cases to achieve the highest RS improvement.
- The bn90/0 surface favours direction I, and bn0 favours direction II, although this fact had an inverse effect on the Ti-6Al-4V workpiece due to the fact that the relative weight of each RS component was reverted after machining in both materials.
- No specific feed seems to be more adequate to perform the NVABB or the VABB processes.

5.3 Optimal parameter sets according to texture and RS criteria: synthesis

Having reached this point in the result discussion chapter, it is necessary to make a synthesis of all the results derived from the topological and RS analysis, with the aim of deciding whether they can be unified to establish one or various priority parameter set to apply the VABB process; and, in those cases where NVABB is recommended over it, propose an alternative.

The derived ball burnishing parameter sets have been organised by material, in two different Tables: 5.12 and 5.13. These charts are organised by initial surface texture, which should actually be considered as a contextual requisite for burnishing application, and no longer as a factor of study. Indeed, it was concluded that the

Table 5.11. Optimal parameters to ball burnish Ti-6Al-4V surfaces based on real experimental results

Initial surface	Opt. target	Process	F_p (N)	n_p	vf (mm/min)	Strategy	test	VABB $\Delta\sigma_i$	NVABB $\Delta\sigma_i$
S_1^0	σ_I	NVABB	250	5	900	bn90/0	#18	49.8%	66.6%
	σ_{II}	VABB or NVABB	350	5	300	nb0	#25	21.0%	16.9%
	σ_{vm}	VABB or NVABB	350	5	300	nb0	#25	19.7%	15.9%
S_2^0	σ_I	VABB or NVABB	350	5	900	bn90/0	#26	76.8%	74.6%
	σ_{II}	VABB or NVABB	350	5	600	bn90/0	#26	18.4%	10.2%
	σ_{vm}	VABB or NVABB	350	5	600	bn90/0	#26	39.1%	34.4%
S_3^0	σ_I	NVABB	350	5	900	bn0	#27	81.0%	100.3%
	σ_{II}	NVABB	350	5	900	bn0	#27	66.3%	71.9%
	σ_{vm}	NVABB	350	5	900	bn0	#27	68.8%	85.7%

application of the VABB process requires not only calibration and testing on a specific target material, but the process parameters should also be decided according to the initial surface presented by the specific workpiece. The aforementioned tables include all optimal parameter set, obtained after diverse criteria, including statistical and experimental evidence. In the case of texture enhancement, the optimal burnishing parameter combination arising from the observation of individual experimental texture results are in agreement with those derived from the ANOVA analysis. Therefore, no differentiation is made in this regard. On the contrary, those two criteria lead to different solutions in the case of RS component maximisation, thus having been specified in the Table as "Taguchi" –direct observation in the experimental results–, and "ANOVA" –concluded after the mean effects calculation.

The inspection of both tables leads to conclude that, although not all parameter sets lead to the same target, some factors are recommended in the same or similar values regardless of the objective. It is the case of the preload and the number of passes, which are in most of cases recommended at their highest levels. For that reason, the last column of the tables propose a unified parameter and process descriptors that could be applied in a general case to enhance texture and residual stress at the same time. However, it should not be forgotten that one direction of the space is prone to be less affected. A special mention should be done regarding the case of the

Table 5.12. Summary of optimal parameters to ball burnish AISI 1038 surfaces based on texture and RS criteria.

Initial surface	Opt. target	Process	F_p (N)	n_p	vf (mm/min)	Strategy	Overall optimal set
S_1^0	Texture	VABB or NVABB	180	3	300–900	nb, bn0 or bn90/0	VABB
	σ_I Taguchi	VABB	180	5	900	bn90/0	270 N
	σ_{II} Taguchi	VABB	270	5	300	nb0	5 passes
	σ_{II} ANOVA	VABB	270	3	300	nb0	300–900 mm/min
	σ_{vm} Taguchi	VABB	270	5	300	nb0	Strategy according to target
	σ_{vm} ANOVA	VABB	270	5	300–900	nb0	
S_2^0	Texture	VABB or NVABB	270	3	300–900	nb, bn0 or bn90/0	VABB
	σ_I ANOVA	VABB	270	5	600	bn90/0	270 N
	σ_{II} Taguchi	VABB	270	3	900	nb0	5 passes
	σ_{II} ANOVA	VABB	270	3	300	nb0	300–900 mm/min
	σ_{vm} Taguchi	VABB	270	3	900	nb0	Strategy according to target
	σ_{vm} ANOVA	VABB	270	5	300–600	nb0	
S_3^0	Texture	NVABB	270	5	300–900	nb, bn0 or bn90/0	VABB
	σ_I Taguchi	VABB	270	5	900	bn90/0	270 N
	σ_I ANOVA	VABB	270	5	600	bn90/0	5 passes
	σ_{II} Taguchi	VABB	270	3	600	nb0	300–900 mm/min
	σ_{vm} Taguchi	VABB	270	3	600	nb0	Strategy according to target

Table 5.13. Summary of optimal parameters to ball burnish Ti-6Al-4V surfaces based on texture and RS criteria.

Initial surface	Opt. target	Process	F_p (N)	n_p	vf (mm/min)	Strategy	Overall optimal set
S_1^0	Texture	VABB	350	3	300–600	nb, bn0 or bn90/0	VABB
	σ_I Taguchi	NVABB	250	5	900	bn90/0	350 N
	σ_{II} Taguchi	VABB or NVABB	350	5	300	nb0	5 passes
	σ_{II} ANOVA	VABB or NVABB	350	5	300–600	nb0	300–900 mm/min
	σ_{vm} Taguchi	VABB or NVABB	350	5	300	nb, bn0 or bn90/0	Strategy according to target
	σ_{vm} ANOVA	VABB or NVABB	350	5	300–600	nb0	
S_2^0	Texture	VABB or NVABB	350	5	300–900	nb, bn0 or bn90/0	VABB or NVABB
	σ_I Taguchi	VABB or NVABB	350	5	900	bn90/0	270 N
	σ_{II} Taguchi	VABB or NVABB	350	5	900	nb0	5 passes
	σ_{vm} Taguchi	VABB or NVABB	350	5	600	nb0	300–900 mm/min
	σ_{vm} ANOVA	VABB or NVABB	350	5	300–600	nb, bn0 or bn90/0	Strategy according to target
S_3^0	Texture	NVABB	350	5	300–900	nb, bn0 or bn90/0	NVABB
	σ_I Taguchi	NVABB	350	5	900	bn0	270 N
	σ_I ANOVA	NVABB	150	5	900	bn90/0	5 passes
	σ_{II} Taguchi	NVABB	350	5	900	bn0	600–900 mm/min
	σ_{vm} Taguchi	NVABB	350	5	900	bn0	Strategy according to target

AISI 1038 S_1^0 surface improvement. The unified parameter set has been set in 270N-5passes, what seems to be incoherent with the 180N–3passes recommended in terms of texture. Thee explanation is simple: in the already known cyclic effect of VABB, 270N-5passes was found to deliver also good surface texture, although being a longer process, and it allows in addition the RS enhancement. The reader shall notice that the strategy is not included in the cell that gathers a unified parameter set. Since one of the main conclusions derived from this result discussion was that they were indifferent for texture scale reduction, they should be chosen according to the preferential direction that must be reinforced.

5.4 Metallurgical parameter: hardness and metallography

The previous section has shown that, although not all aspects of surface integrity can be simultaneously improved, a certain optimal set can be established to find a balanced solution for all of them. In this section, a third aspect of surface integrity is tackled to complete the assessment of the impact of VABB. Although it is not expected to observe specially remarkable results from the metallurgical point of view, SEM metallographic observations have also been performed.

Due to the highly time-consuming sequence of specimen preparation and hardness measurement execution, this section focuses on a specific parameter set derived from the previous analysis. Since the strategy has proved to modify the directionality of the material, this parameter has been included in two different levels, to assess its effects of VABB on both materials. NVABB tests are also performed to establish a comparison point.

5.4.1 AISI 1038

A new AISI 1038 workpiece was machined to generate an S_1^0-type surface. This texture was chosen due to the fact that is the one that evidenced higher affectation by the VABB process. The influence of strategy in the directionality of the RS results lead into consider both bn90/0 and nb0 strategies, to evaluate whether there can also be a reinforcement effect in the case of the hardness. In total, four new patches were burnished on the machined surface, as shows Table 5.14.

To study the in-depth affectation of the material due to VABB and NVABB processes, every burnishing patch was cut in the middle in both directions I and II, thus generating the respective surfaces parallel to both of them (Figure 5.67.a). After pol-

Table 5.14. Tested conditions for hardness tests on AISI 1038 S_1^0.

Process	Strategy	Fixed parameters
VABB	nb0	F_p = 270 N ; n_p = 5 ; v_f = 600 mm/min
NVABB	bn90/0	

ishing, a Vickers imprint indentation matrix was performed, at different deep layers every 50 μm, until 300 μm, from where three more 100 μm steps were measured (Figure 5.67.b). At every depth level, a minimum of 10 indentations were performed. Outliers were discarded through the Chauvenet's criterion, and the resulting samples were averaged to obtain the representative value. The error was calculated as explained in subsection 4.2.2.1.

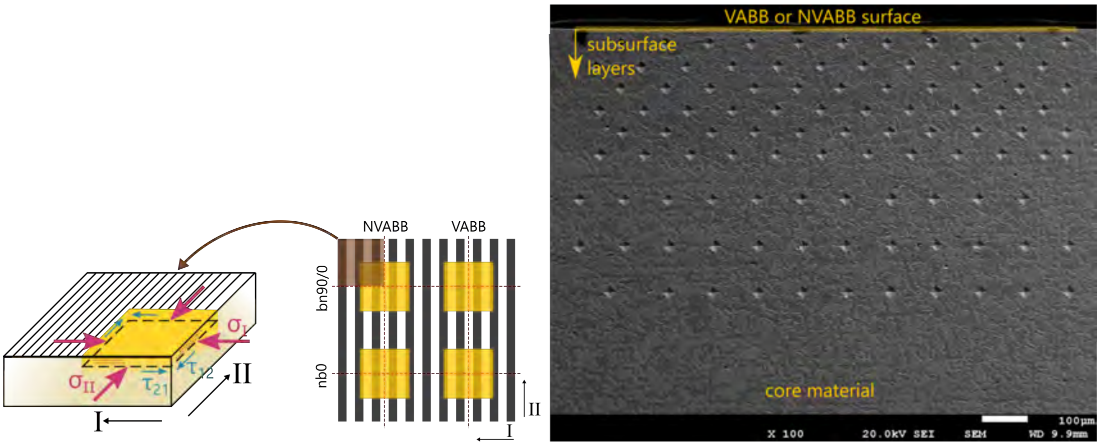

(a) (b)

Figure 5.67. Hardness profiles of VABB and NVABB S_1^0 AISI 1038 surfaces. **a**. Along direction I. **b**. SEM view of the Vickers microindentation matrix performed on the subsurface layers of the non-burnished AISI 1038 specimen.

5.4.1.1 AISI 1038 deep affectation: Vickers hardness profiles

Figure 5.68 shows the resulting hardness profiles along with their respective error bars. The comparison of the as-machined subsurface hardness measurements confirm the original anisotropy: along direction II, the core hardness is achieved at around 250 μm, whereas this value is reached at 500 μm along direction I. The lack of further data does not allow us to state a definitive explanation to this fact. However, a certain link between RS and hardness could be proposed as possible, as RS can be understood as elastically deformed grains confined inside plastified boundary grains. Under this perspective, hardness measured on the plane parallel to direction I could be dominated by the compressive σ_{II} residual stress (Figure 5.67.a.). σ_I presents lower values, and so do the hardness datasets measured on that plane. Although there seems to be a link between both magnitudes, the main drawback to this approach is that, as the X-ray diffraction method applied to calculate RS has only a few μm of penetration, it is not sure that they keep that level to a 50-μm depth, which is the first available hardness measurement.

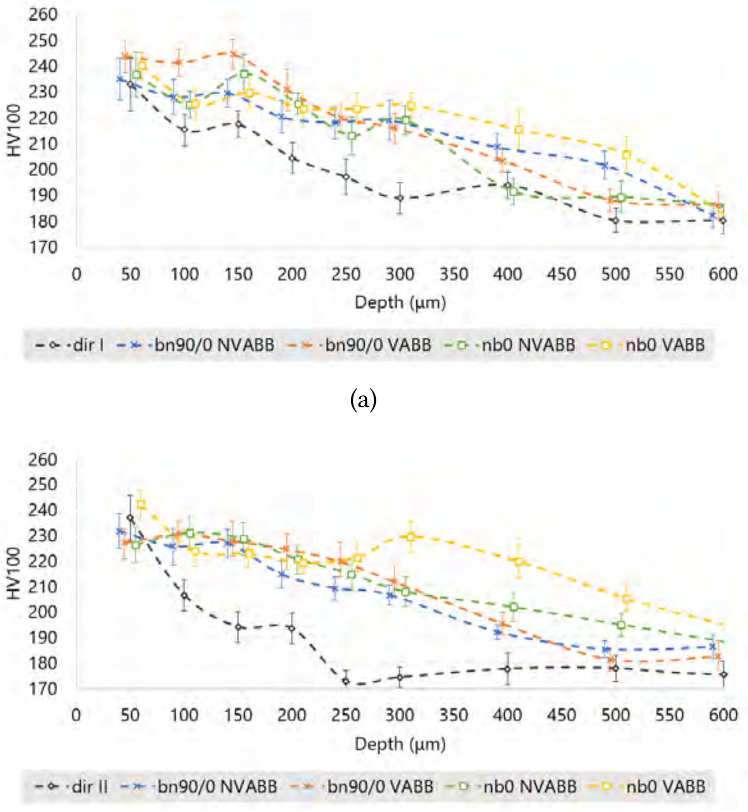

(a)

(b)

Figure 5.68. Hardness profiles of VABB and NVABB S_1^0 AISI 1038 surfaces. **a**. Along direction I. **b**. Along direction II.

Neither VABB nor NVABB modify substantially the hardness level at the near-surface depth, considering the error bars. This observation was already confirmed by evidence presented previously by other researchers, included in the state of the art chapter. The material hardness is, however, affected at deeper layers, spanning from 250 to 500 µm along direction II and 150 to 250 µm along I. Direction II must be considered as the one affected to a highest extent in terms of hardness. This deep effect of ball burnishing can be explained by the elastic-plastic Hertzian contact mechanics, that characterise stress propagation inside solids by effect of a superficial load [37].

The strategy has a clear effect on the hardening effects after both processes, being nb0 the one resulting in higher hardness, especially along direction II. Only the bn90/0 strategy seems to have a slight more positive effect along direction I, from 100 to 150 µm. The nb0 strategy clearly favours the same direction as it did in RS terms, and so does bn90/0 at the near subsurface layers, although its effect is more modest.

Now, considering the difference between vibration-assistance and conventional ball burnishing, results change. The VABB process executed according to the nb0 strategy exhibits in overall a more remarkable positive effect, from 250 to 500 µm depths. To visually detect the different result delivered by vibration-assistance, if present, an alternative representation is proposed through the VABB-to-NVABB ratio, $\varDelta HV$, calculated as follows:

$$\varDelta HV = \frac{HV_V}{HV_N} \tag{5.8}$$

where HV_V is the average Vickers hardness obtained through the VABB process, and HV_N is the average Vickers hardness obtained through the NVABB process.

The incertitude bars have been calculated by error propagation on $\varDelta HV$, as was indicated in Eq. 5.5. The resulting expression can be formulated as follows:

$$e_r = \varDelta HV\sqrt{\left(\frac{e_{HVV}}{HV_V}\right)^2 + \left(\frac{e_{HVN}}{HV_N}\right)^2} \tag{5.9}$$

where e_{HVV} is the error associated to HV_V, and e_{HVN} is the error associated to HV_N.

Figure5.69 represents the values of the $\varDelta HV$ ratio for all the explored depths. It is the bn0 strategy the one that delivers better results through VABB, from 250 µm depth, whereas bn90/0 hardly takes advantage of vibration-assistance. Therefore, it can be stated that, in terms of deep affectation, it is the nb0 strategy the one that registers more advantage from vibration-assistance. As repeated passes along the same path, clearly help take profit of the vibrations incorporated to the process, whereas this effect is dissolved for the bn90/0 by the change of direction of the passes. The described higher residual hardening after VABB can be associated to the transmission of the ultrasonic waves inside the material, as the Blaha effect explains, at sight of the results found by Siu *et al.* (2013) [136].

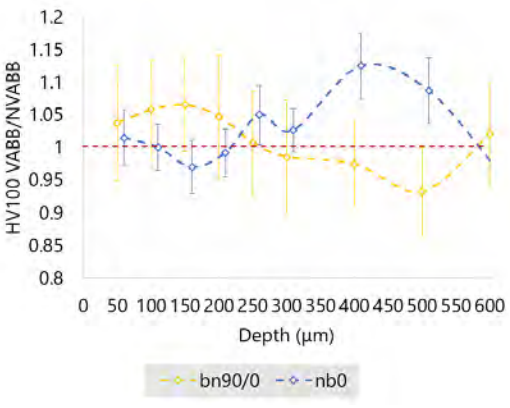

(a)

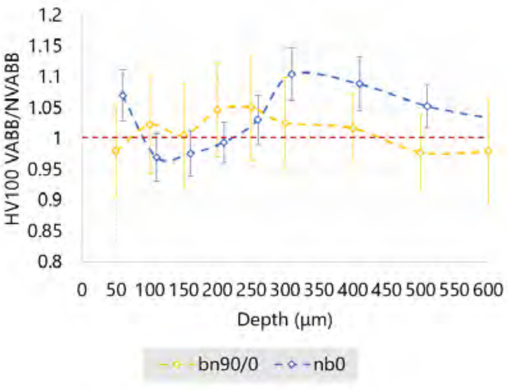

(b)

Figure 5.69. HV ratio between VABB and NVABB tests of S_1^0 AISI 1038 surfaces. **a**. Along direction I. **b**. Along direction II.

5.4.1.2 SEM examination of the AISI 1038 surface and sub-surface layers

The specimens that were subjected to the previously described hardness tests were chemically etched to perform SEM observations. Figure 5.70 exhibits a surface layer of deformed material, being the grains of ferrite and cementite reduced due to the plastic residual strain. Some shear marks can be observed in the ferrite phase after VABB, which leads to conclude that the depth of affectation due to this process is slightly higher. However, this is not necessarily positive for the surface, as this effect cannot be momentarily assessed in functional terms. The only metallography that exhibits a substantial different result is the one corresponding to direction I of the nb0 strategy performed through VABB. The cementite at the surface seems to be smashed and mixed with the ferrite matrix. The reason could be, again, the repetitive passes caused by this kind of strategy along the same direction while the ultrasonic signal is transmitted inside the material. The consequence of this change should be further assessed in future works.

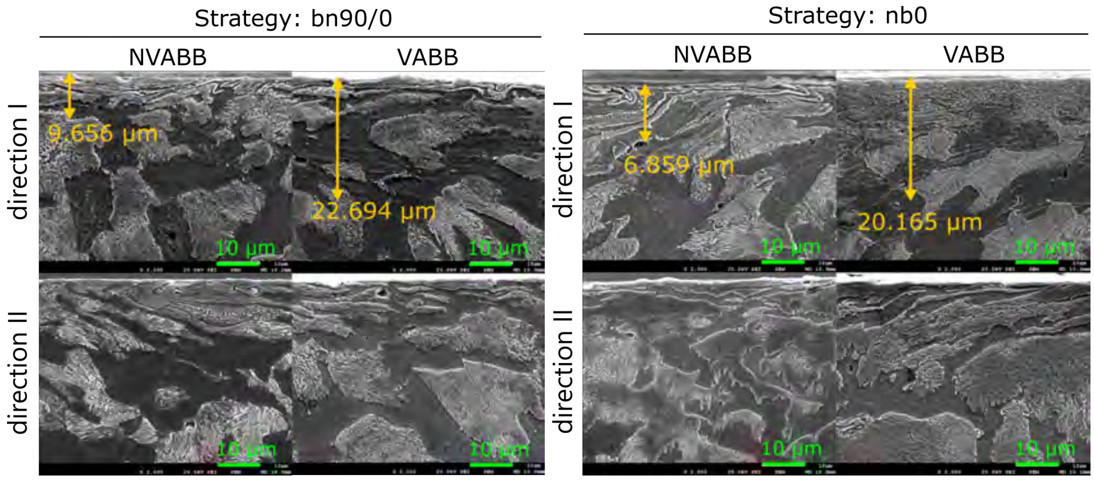

(a) (b)

Figure 5.70. x2000 SEM observations of ball-burnished AISI 1038.

5.4.2 Ti-6Al-4V

To complete the characterisation of the effects of VABB on the Ti-6Al-4V surfaces, a metallurgical analysis was performed on a new specimen. The S_1^0 surface was taken as basis, and the parameters that were defined as most appropriate were selected to perform the operations (Table 5.15). Specimens were prepared as specified for the steel alloy, to subject them to hardness measurement through a matrix as the one represented at Figure 5.67.

Table 5.15. Tested conditions for hardness tests on Ti-6Al-4V S_1^0.

Process	Strategy	Fixed parameters
VABB	nb0	F_p = 350 N ; n_p = 5 ; v_f = 600 mm/min
NVABB	bn90/0	

5.4.2.1 Ti-6Al-4V deep affectation: Vickers hardness profiles

Figure 5.71 shows the resulting deep hardness profiles of the explored surfaces. In this case, the machining process has a hardening effect on the workpiece that spans to a 100-µm depth. However, the hardness profiles are substantially more similar among them than in the case of the AISI alloy.Both the NVABB and VABB processes cause a residual hardening along direction I, but that effect is inconspicuous along direction II, except for one processing condition: nb0 and VABB. The combination of both is in overall positive along both directions, although the depths where it can be observed, is different: the effect along direction II seems more superficial. It must be considered the error introduced my the manual measurement with the Vickers microindenter, which is not automatised, and might deliver undesired bias in the depth control. Therefore, it should be highlighted the positive impact of nb0 and VABB, regardless of the exact depth represented in the Figure.

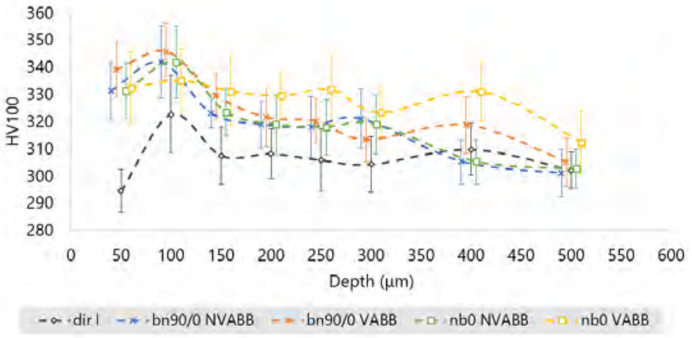

(a)

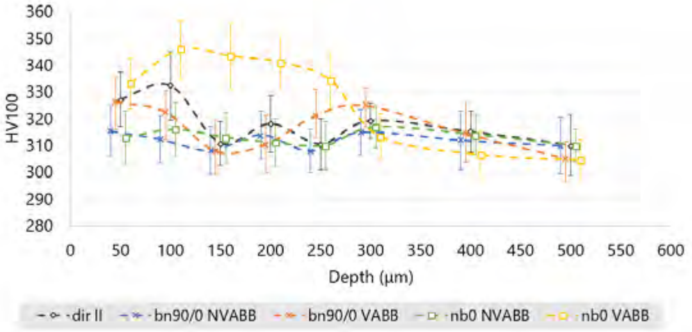

(b)

Figure 5.71. Hardness profiles of VABB and NVABB S_1^0 Ti-6Al-4V surfaces. **a**. Along direction I. **b**. Along direction II.

5.4.2.2 SEM observation of the Ti-6Al-4V surface and sub-surface layers

The specimens that were used for the hardness measurements were chemically etched to distinguish the different phases of the Ti-6Al-4V material, and assess a possible change in microstructure caused by VABB and NVABB. Figure 5.72 represents the subsurface layers of the nb0 patches, exhibiting the typical white layer formed by this kind of alloys [155], mixed with some oxygen fluorides coming from the chemical etching with Kroll's reagent. The main effect of ball burnishing is represented by the α phase oriented along the surface, by effect of the plastic deformation. However, the depth of affectation is lower than in the case of the AISI material, and, in all cases, difficult to distinguish.

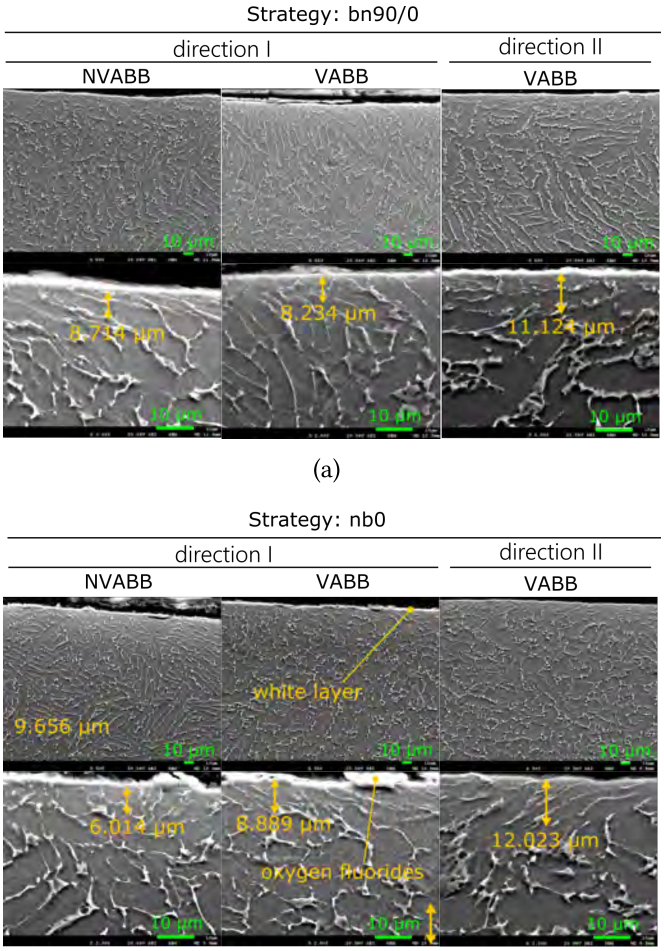

(a)

(b)

Figure 5.72. x2000 SEM observations of ball-burnished Ti-6Al-4V.

5.5 Synthesis of metallurgical results

The performed metallurgical analysis allowed the assessment of the effects of VABB and NVABB in deep layers of the AISI 1038 and Ti-6Al-4V tested alloys. It proved that both processes affect positively the hardness of the subsurface layers of the target material. The only relevant result is the remarkably more effective combination of nb0 strategy with the VABB process, that achieves higher hardness. It even has a metallurgical effect, as it is able to break the cementite phase.

The implications of the metallurgical analysis, which has not been so extensive due to the time-consuming activities required with that aim, reveals that the effect of both VABB and NVABB is present down to around 500 μm. Deeper material layers can be considered to have the properties of the bulk material, and cannot be described through the surface integrity approach.

6

Conclusions and perspectives

The present dissertation tackled with the issue of executing the vibration-assisted ball burnishing process through a designed tool, and has explored its application on two different industrial alloys: AISI 1038 and Ti-6Al-4V.

Being 40 kHz the frequency of the signal transmitted by the prototype designed to execute the process, the most complex technological challenge was being able to acquire, sample and postprocess this kind of high frequency signal. Acoustic emission tests allowed the measurement of the signal transmitted inside an AISI 1038 block. It evidenced to be characterised by a 39.1-kHz frequency, independent of the preload excerpted by the tool. A second characterisation phase was undertaken by direct dynamometric measurement, to quantify the vibratory force overlapped on the spring preload. This force resulted to experience relatively low variations with regards to the preload value, inside a ± 4−5.5 N interval. Since the Blaha effect is not based on stress addition but on signal transmission through the material while it is deformed, this range of forces is considered as valid. These characterisation activities proved that the prototype was able to function inside stable levels, with no dependence on process parameters.

The test of VABB on AISI 1038 and Ti-6Al-4V surfaces proved to have a highly positive impact in the surface integrity of the treated surfaces. However, the industrial implementation of the process requires a preliminary study to determine the adequate parameters that must be applied, considering the target material and the topology of the target surface. Additionally, both the topological and residual stress results showed that the search for the best process parameters cannot be detached from the original surface texture on which they shall be applied. This statement is based on several evidence, explained along the following paragraphs.

From a topological point of view, VABB has a triple effect on the surfaces where it is applied, as follows:

- General scale reduction.
- Surface height redistribution according to Gaussian or quasi-Gaussian surfaces.
- Change of the main directionality of the surface texture features, if enough preload is applied.

The results showed that plastic deformation performed through VABB delivers a net reduced scale surface. Furthermore, as the process is not based on chip removal, the resulting topologies are always represented by Gaussian or quasi-Gaussian height distributions, which are known for their balanced characteristics of lubricant retention and low wear. That result can be explained due to the fact that the ball has a simultaneous effect on the texture: it reduces its original peaks while generating new low-scale valleys. The AISI 1038 material registered texture scale reductions higher than 80% in the finest tested original surface, whereas the improvement was of around 60.3% for the Ti-6Al-4V alloy.

On the other hand, given a specific texture machined on a material, a single preload and number of passes pair of values, F_p–n_p, can be found to achieve the best texture scale reduction. From that point, higher combinations delivering more plastic deformation lead to detrimental effects on the surface. Nevertheless, a cyclic effect of VABB can be observed as further plastic deformation always leads to a reconfiguration of the surface. In this sense, a second threshold that delivers again good texture results can be found. That reconfiguration includes texture scale reduction with Gaussian height distributions, accompanied with a change in the directionality of the surface topology features, which are reoriented according to the main VABB direction. The singular F_p–n_p values must be selected regarding the target material and the texture machined on it.

The topological characteristics of the original surfaces also have an impact in the effectiveness of vibration-assistance to generate lower scale textures. This observation was confirmed in both materials. If the initial surface presented an S_q parameter of 1 $\mu\mathrm{m}$ or less, the VABB presented superior results, compared to NVABB. This observation reinforces the idea of the initial surface being a fundamental variable to consider when selecting VABB process parameters. The results also showed that, as the scale of the texture increases, both the VABB and the NVABB lead to similar results. A second threshold is found for the singular value of around 10-$\mu\mathrm{m}$ S_q, from which NVABB starts to deliver better results. Vibration assistance can only be taken advantage of on fine enough surfaces, whereas it is detrimental in too high scale ball-end milled textures.

The second response evaluation parameters that were considered is the change of the compressive residual stress tensor components after VABB. The effects of VABB were not always positive in this regard, as the original surfaces were originally residually compressed as a consequence of the machining process. The finest surface presented the highest residual stress from the beginning. The VABB process proved to avoid stress relaxation in that surface, which was on the contrary observed after the non-assisted process. The other original surfaces, less compressed originally, registered remarkable higher RS after VABB, proving its positive effects with regards to the non-assisted operation (e.g. in some cases, compressive RS increased by 36%). Results are slightly different in the Ti-6Al-4V workpiece, where both NVABB and VABB resulted in similar results, also more modest compared to those on the AISI 1038 alloy. These results lead to think that the materials react completely different to the vibration-assistance, besides their original texture. For the explored values, the Ti-6Al-4V was less sensitive to vibration-assistance.

Regarding the residual stress results, it must be highlighted the relevance of the burnishing strategy to define the direction of the surface that should be reinforced. All original surfaces exhibited a high anisotropy after machining that could be corrected or balanced by choosing the direction along which VABB should be applied. This result is fundamental to simplify the implementation of the VABB process, according to the state of the machined surface on which it shall be executed.

Last of all, the deep hardness analysis exhibited that the VABB process delivered deeper affectation of the material, especially if the process was always performed along the same direction (nb0 strategy). Therefore, the transmission of the ultrasonic signal during the VABB process seems to result in a higher penetration of the effects of the process. However, the direct consequence of this result should be addressed in future research lines, as is highlighted in the next subsection.

The presented evidence, found after the different experimental outcomes, lead to the conclusion that the industrial application of the process can only successfully be performed if the processing parameters are linked to the outcomes of the previous machining procedure. A previous assessment to characterise the original surface integrity shall always be necessary, including two main variables: the target material and initial surface (Figure 6.1). As a result of that combination, the F_p–n_p pair should be fixed to achieve the best topological and RS results. The strategy must be then selected according to the preferential direction that is expected to be subjected to higher load and stress during its functioning in service.

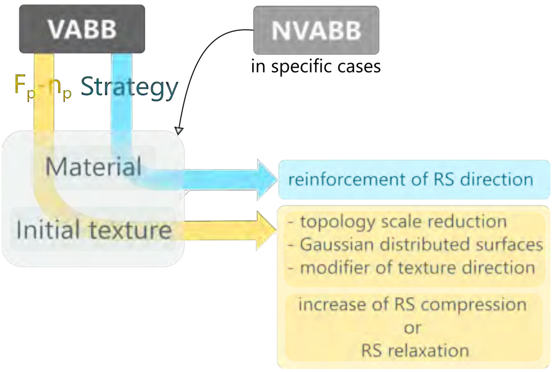

Figure 6.1. Summary of the conclusions regarding VABB.

6.1 Future works

The experimental database and the holistic approach taken in this dissertation to the VABB process must be used in future works to succeed in developing new insights into the process. Many questions remain open about the phenomenology of associated to the process, and the direct consequences of the vibration assistance on the material. The ultimate result of that assessment should be its industrial implementation. Under this perspective, the following activities are proposed as next steps:

- Performing similar analysis on a greater variety of topologies, particularly those being originally neutral in terms of residual stress. Furthermore, to study in detail the described cyclic effect of VABB on the surface texture, higher preloads could be applied on the already assessed surfaces, to establish that threshold value in more abrupt topologies.

- Development of a new version of the prototype, to overcome the mechanical drawbacks provided by the one presented in this dissertation. For instance, to reduce the relative movement between its components.

- An improved FEM that allows to understand in depth the interaction of the burnishing ball with the surface features. This study must derive in a phenomenological explanation of the effects of NVABB based on the way that the ball performs the pressure to cause the residual plastic strain.

- An optimisation procedure should be performed, to find real optimal values for the operation. The results presented in this thesis are based on different optimisation methods. But the term "optimal" refers to the best parameters inside the explored boundaries included in the design of experiments.

6.2 Publications derived from this dissertation

Publications in JCR indexed journals

Jerez-Mesa, R., Landon, Y., Travieso-Rodriguez, J.A., Dessein, G., Lluma-Fuentes, J., Wagner, V. (2017) Topological surface integrity modification of AISI 1038 alloy after vibration-assisted ball burnishing. *Journal of Surface and Coatings Technology*. Under review.

Jerez-Mesa, R., Travieso-Rodriguez, J.A., Gomez-Gras, G., Lluma-Fuentes, J. (2017) Development, characterization and test of an ultrasonic vibration-assisted ball burnishing tool. *Journal of Materials Processing Technology*. Accepted with major revisions.

Contributions in international congresses with peer review

Jerez-Mesa, R., Landon, Y., Travieso-Rodriguez, J.A., Gomez-Gras, G., Lluma-Fuentes, J. Ultrasonic burnishing of AISI 316L stainless steel curved surfaces. *13° Congreso*

Iberoamericano de Ingeniería Mecánica, Lisboa (Portugal), 23-26 October 2017.

Patent

Jerez-Mesa, R., Travieso-Rodríguez, J.A., Gómez-Gras, G., Llumà-Fuentes, J. Herramienta de bruñido con bola asistida por vibraciones ultrasónicas. Published en el Boletín Español de la Propiedad Intelectual, 2 de junio de 2017. Número de publicación: 2 615 002.

A

L27 Taguchi arrays for experimental design

Table A.1. L27(3^{13}) Taguchi orthogonal array. After Taguchi *et al.*, 2005 [142]

No.	1	2	3	4	5	6	7	8	9	10	11	12	13
1	1	1	1	1	1	1	1	1	1	1	1	1	1
2	1	1	1	1	2	2	2	2	2	2	2	2	2
3	1	1	1	1	3	3	3	3	3	3	3	3	3
4	1	2	2	2	1	1	1	2	2	2	3	3	3
5	1	2	2	2	2	2	2	3	3	3	1	1	1
6	1	2	2	2	3	3	3	1	1	1	2	2	2
7	1	3	3	3	1	1	1	3	3	3	2	2	2
8	1	3	3	3	2	2	2	1	1	1	3	3	3
9	1	3	3	3	3	3	3	2	2	2	1	1	1
10	2	1	2	3	1	2	3	1	2	3	1	2	3
11	2	1	2	3	2	3	1	2	3	1	2	3	1
12	2	1	2	3	3	1	2	3	1	2	3	1	2
13	2	2	3	1	1	2	3	2	3	1	3	1	2
14	2	2	3	1	2	3	1	3	1	2	1	2	3
15	2	2	3	1	3	1	2	1	2	3	2	3	1
16	2	3	1	2	1	2	3	3	1	2	2	3	1
17	2	3	1	2	2	3	1	1	2	3	3	1	2
18	2	3	1	2	2	3	1	1	2	3	3	1	2
19	3	1	3	2	1	3	2	1	3	2	1	3	2
20	3	1	3	2	2	1	3	2	1	3	2	1	3
21	3	1	3	2	3	2	1	3	2	1	3	2	1
22	3	2	1	3	1	3	2	2	1	3	3	2	1
23	3	2	1	3	2	1	3	3	2	1	1	3	2
24	3	2	1	3	2	1	3	3	2	1	1	3	2
25	3	3	2	1	1	3	2	3	2	1	2	1	3
26	3	3	2	1	2	1	3	1	3	2	3	2	1
27	3	3	2	1	3	2	1	2	1	3	1	3	2

Table A.2. Taguchi array followed for the experimental testing of AISI 1038.

#	F_p (N)	n_p	v_f (mm/min)	S^0	St.
1	90	1	300	1	nb0
2	90	1	600	2	bn90/0
3	90	1	900	3	bn0
4	90	3	300	2	bn0
5	90	3	600	3	nb0
6	90	3	900	1	bn90/0
7	90	5	300	3	bn90/0
8	90	5	600	1	bn0
9	90	5	900	2	nb0
10	180	1	300	3	bn90/0
11	180	1	600	1	bn0
12	180	1	900	2	nb0
13	180	3	300	1	nb0
14	180	3	600	2	bn90/0
15	180	3	900	3	bn0
16	180	5	300	2	bn0
17	180	5	600	3	nb0
18	180	5	900	1	bn90/0
19	270	1	300	2	bn0
20	270	1	600	3	nb0
21	270	1	900	1	bn90/0
22	270	3	300	3	bn90/0
23	270	3	600	1	bn0
24	270	3	900	2	nb0
25	270	5	300	1	nb0
26	270	5	600	2	bn90/0
27	270	5	900	3	bn0

Table A.3. Taguchi array followed for the experimental testing of Ti-6Al-4V.

#	F_p (N)	n_p	v_f (mm/min)	S^0	St.
1	150	1	300	1	nb0
2	150	1	600	2	bn90/0
3	150	1	900	3	bn0
4	150	3	300	2	bn0
5	150	3	600	3	nb0
6	150	3	900	1	bn90/0
7	150	5	300	3	bn90/0
8	150	5	600	1	bn0
9	150	5	900	2	nb0
10	250	1	300	3	bn90/0
11	250	1	600	1	bn0
12	250	1	900	2	nb0
13	250	3	300	1	nb0
14	250	3	600	2	bn90/0
15	250	3	900	3	bn0
16	250	5	300	2	bn0
17	250	5	600	3	nb0
18	250	5	900	1	bn90/0
19	350	1	300	2	bn0
20	350	1	600	3	nb0
21	350	1	900	1	bn90/0
22	350	3	300	3	bn90/0
23	350	3	600	1	bn0
24	350	3	900	2	nb0
25	350	5	300	1	nb0
26	350	5	600	2	bn90/0
27	350	5	900	3	bn0

A.1 Compliance of the sufficient degrees of freedom condition

Interactions are represented as lines connecting the factors which take part of them in the linear graph at Figure 4.2. As all factors are studied in 3 levels, 2 degrees of freedom are associated to each one. Therefore, second level interactions have 4 degrees of freedom, as shows Table A.4. Consequently, the designed experimental plan requires $\sum dof_i = 22$ degrees of freedom. Therefore, a 27-run plan based on the L27 array as proposed complies satisfactorily with this condition.

Table A.4. Actions included in the model and their degrees of freedom.

factors	#levels	#d.o.f.
F_p	3	2
n_p	3	2
v_f	3	2
S^0	3	2
St.	3	2
F_p*n_p	9	4
v_f*F_p	9	4
n_p *v_f	9	4

A.2 Compliance of the orthogonality condition

A common methodology to prove that all actions in the model are orthogonal among them, and consequently prove the orthogonality of the experimental array, is to represent the Sisson-Vigier incidence matrix (Table A.5). It depicts the necessary minimum runs to analyse the effect of every uncoupled actions, which is the product of their levels inside the proposed array. For instance, the combination of F_p and n_p, at three levels each, requires the execution of 3^2 tests to have enough information about their effects. The orthogonality between the n_p & v_f interaction and the S^0 factor is satisfied if $3 \cdot 3^3$ runs are executed. The experimental plan to analyse the desired model must be a multiple of the least common multiple of all of them, that is $lcm\,(9, 27)$ = 27, which confirms the orthogonality condition for the designed experimental setup based on the L27 array.

Table A.5. Sisson-Vigier incidence matrix of orthogonality of the experimental design. ∪: coupled actions.

	F_p	n_p	v_f	S^0	St.	$F_p{}^*n_p$	$F_p{}^*v_f$	$n_p{}^*v_f$
F_p	–							
n_p	9	–						
v_f	9	9	–					
S^0	9	9	9	–				
St.	9	9	9	9	–			
$F_p{}^*n_p$	∪	∪	27	27	27	–		
$F_p{}^*v_f$	∪	27	∪	27	27	∪	–	
$n_p{}^*v_f$	27	∪	∪	27	27	∪	∪	–

B

VABB AISI 1038 texture figures

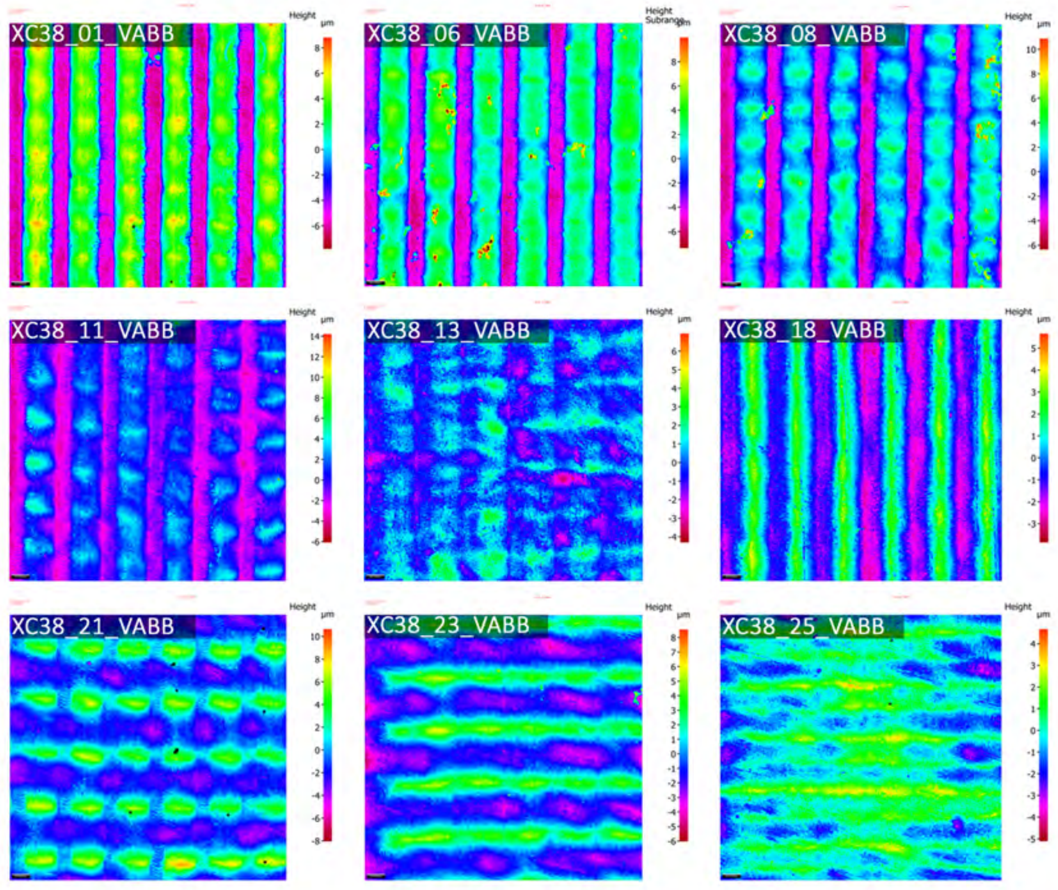

Figure B.1. Sequential height colour map of all VABB tests on AISI 1038 S_1^0 surfaces.

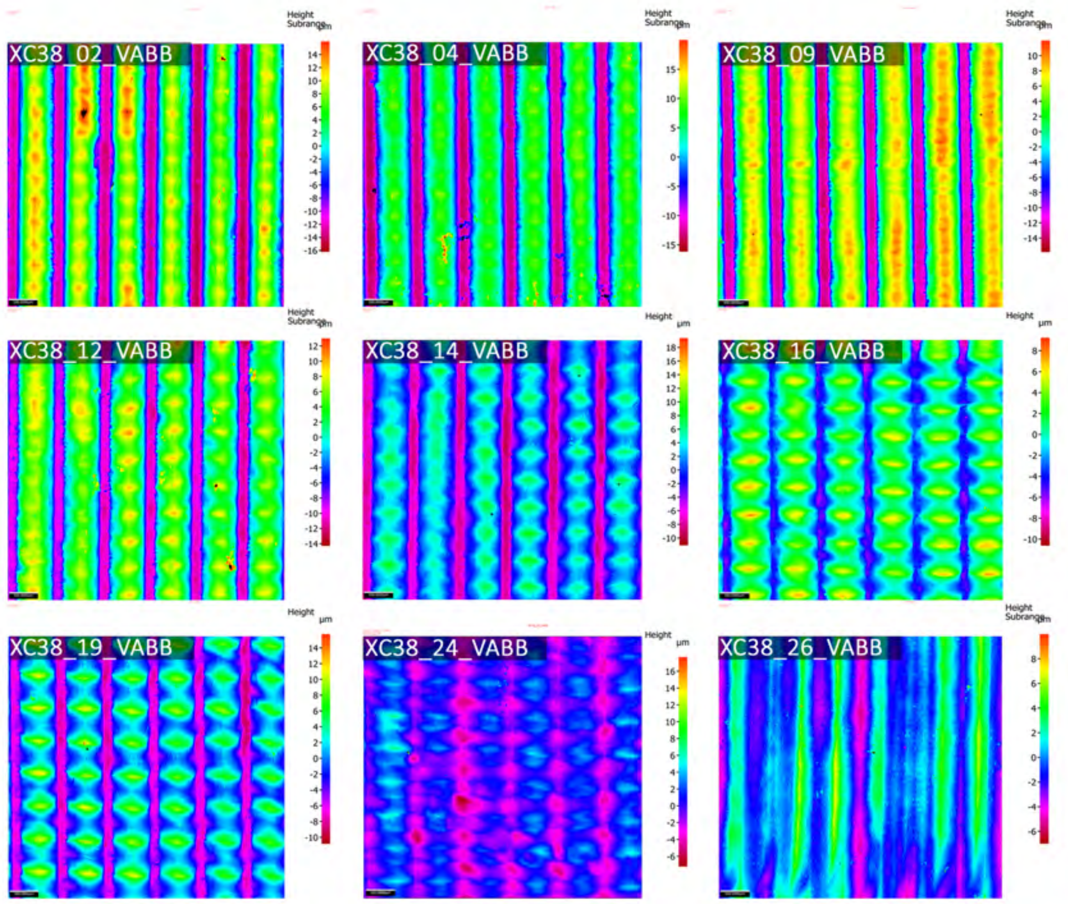

Figure B.2. Sequential height colour map of all VABB tests on AISI 1038 S_2^0 surfaces.

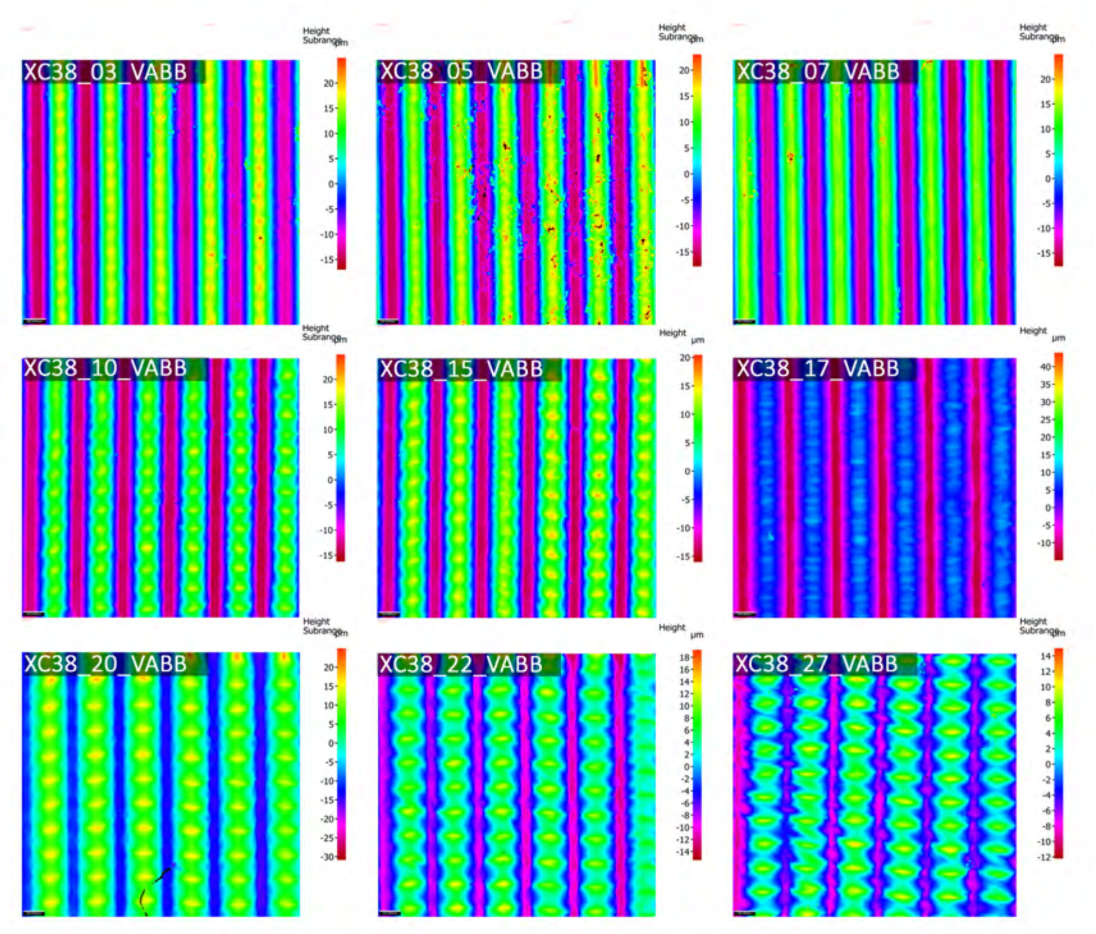

Figure B.3. Sequential height colour map of all VABB tests on AISI 1038 S_3^0 surfaces.

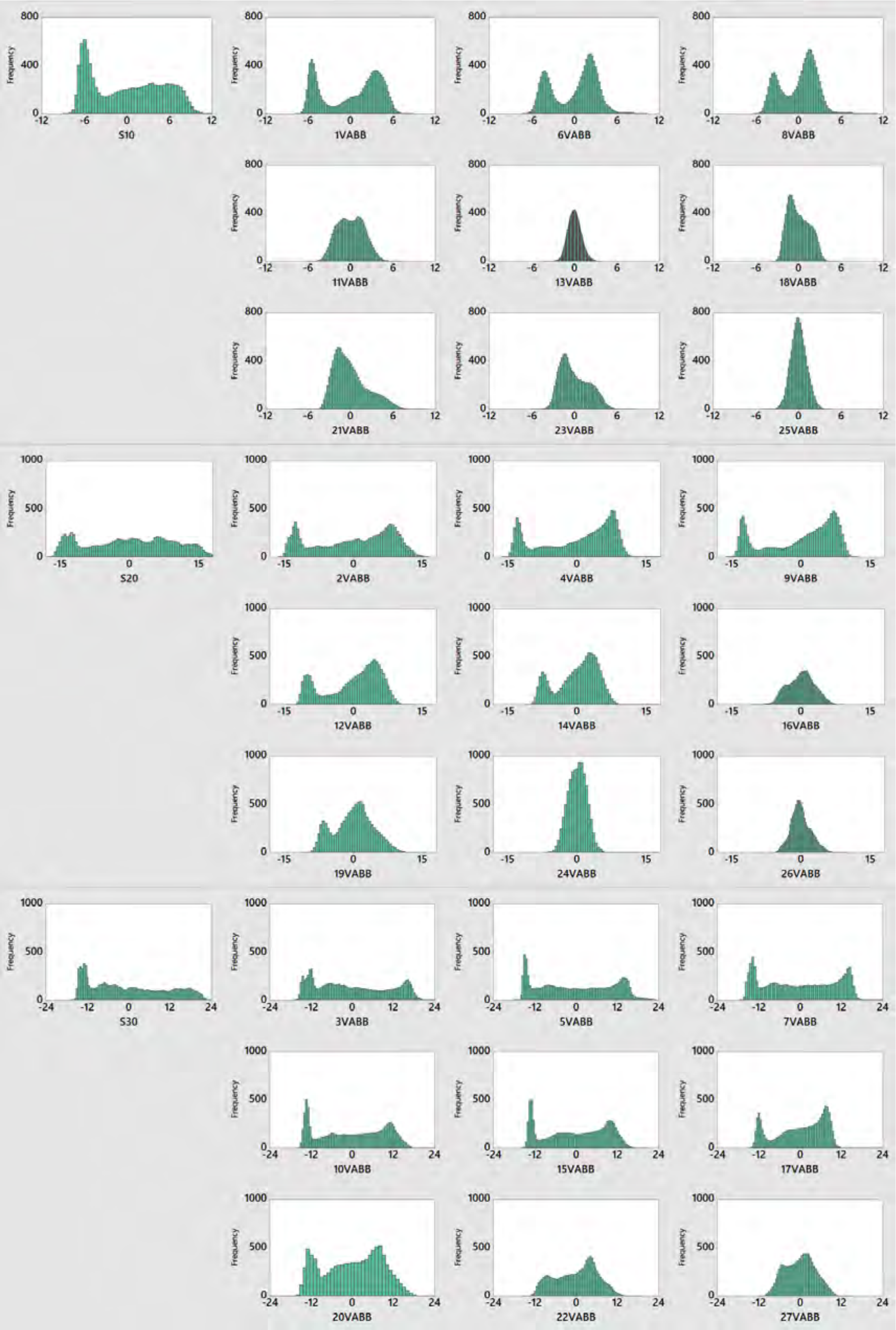

Figure B.4. VABB height distributions of AISI 1038 surfaces.

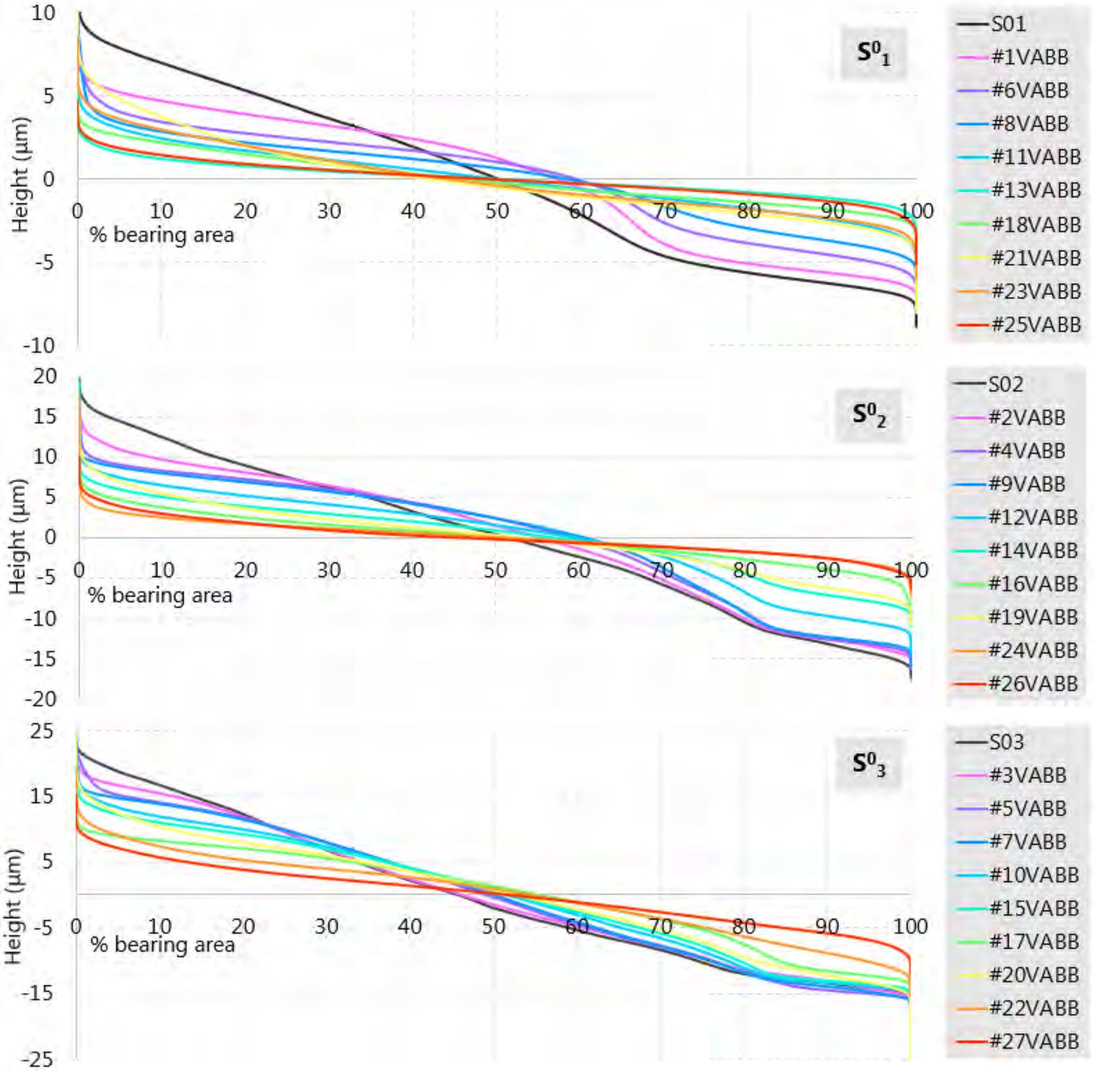

Figure B.5. VABB Abbott-Firestone curves of AISI 1038 surfaces.

C

VABB Ti-6Al-4V texture figures

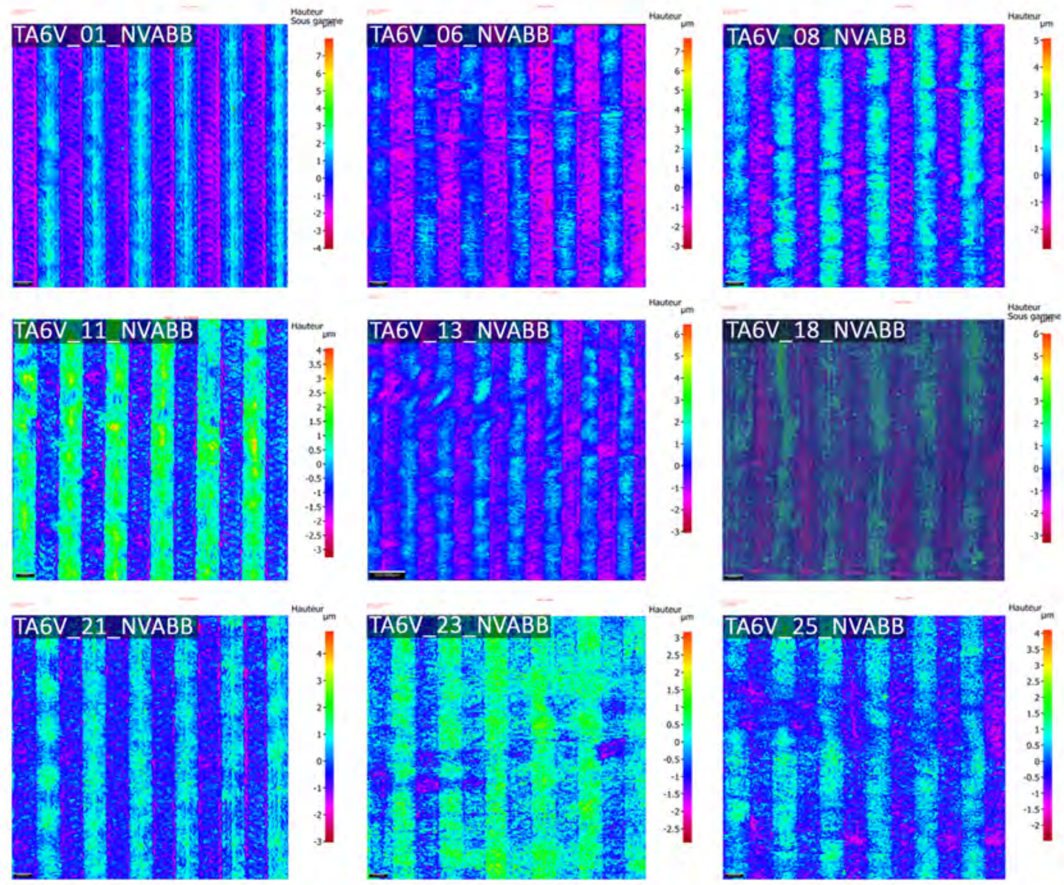

Figure C.1. Sequential height colour maps of all VABB tests on Ti-6Al-4V S_1^0 surfaces.

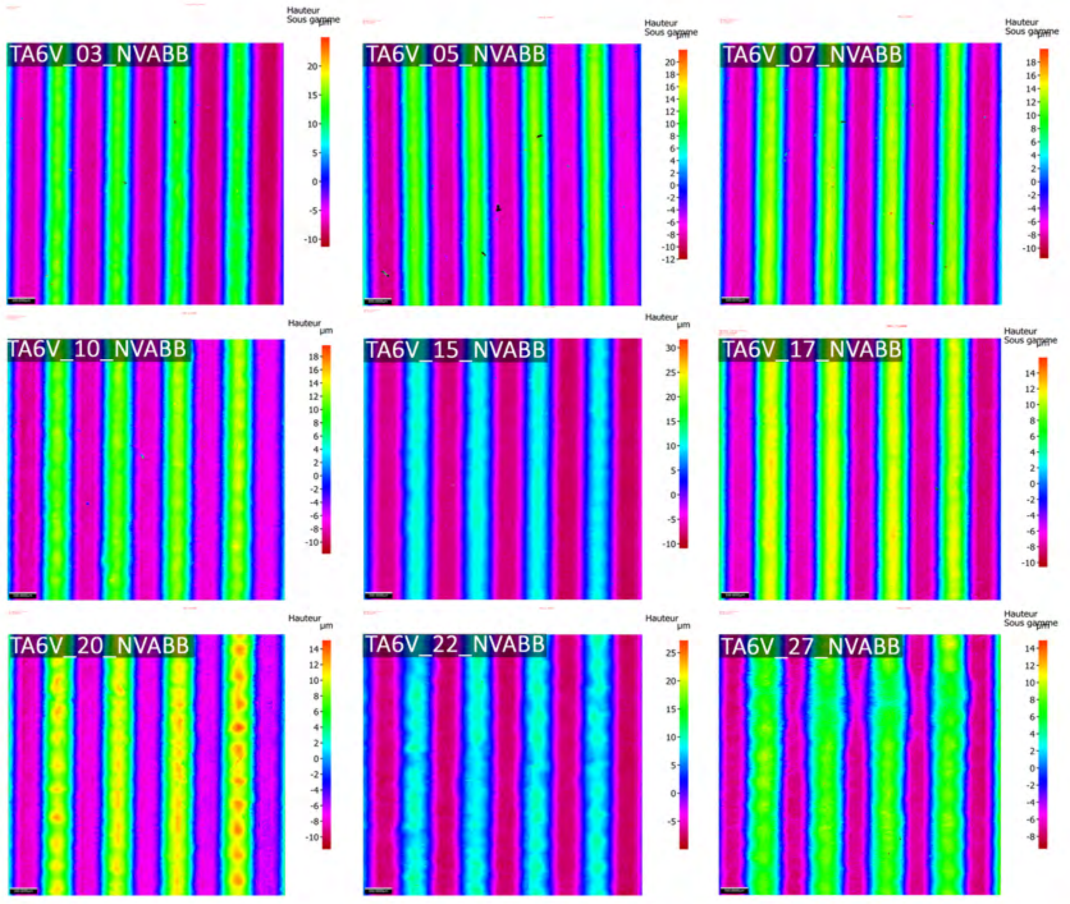

Figure C.2. Sequential height colour maps of all VABB tests on Ti-6Al-4V S_2^0 surfaces.

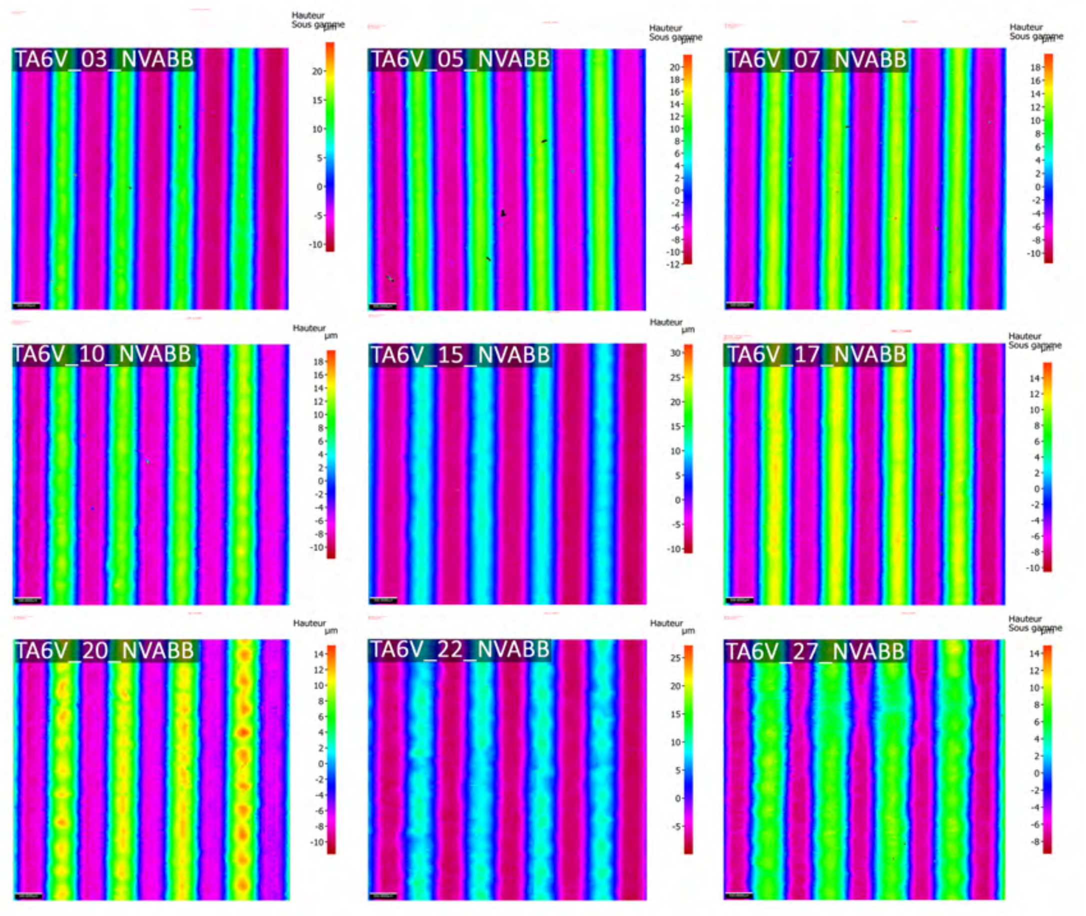

Figure C.3. Sequential height colour maps of all VABB tests on Ti-6Al-4V S_3^0 surfaces.

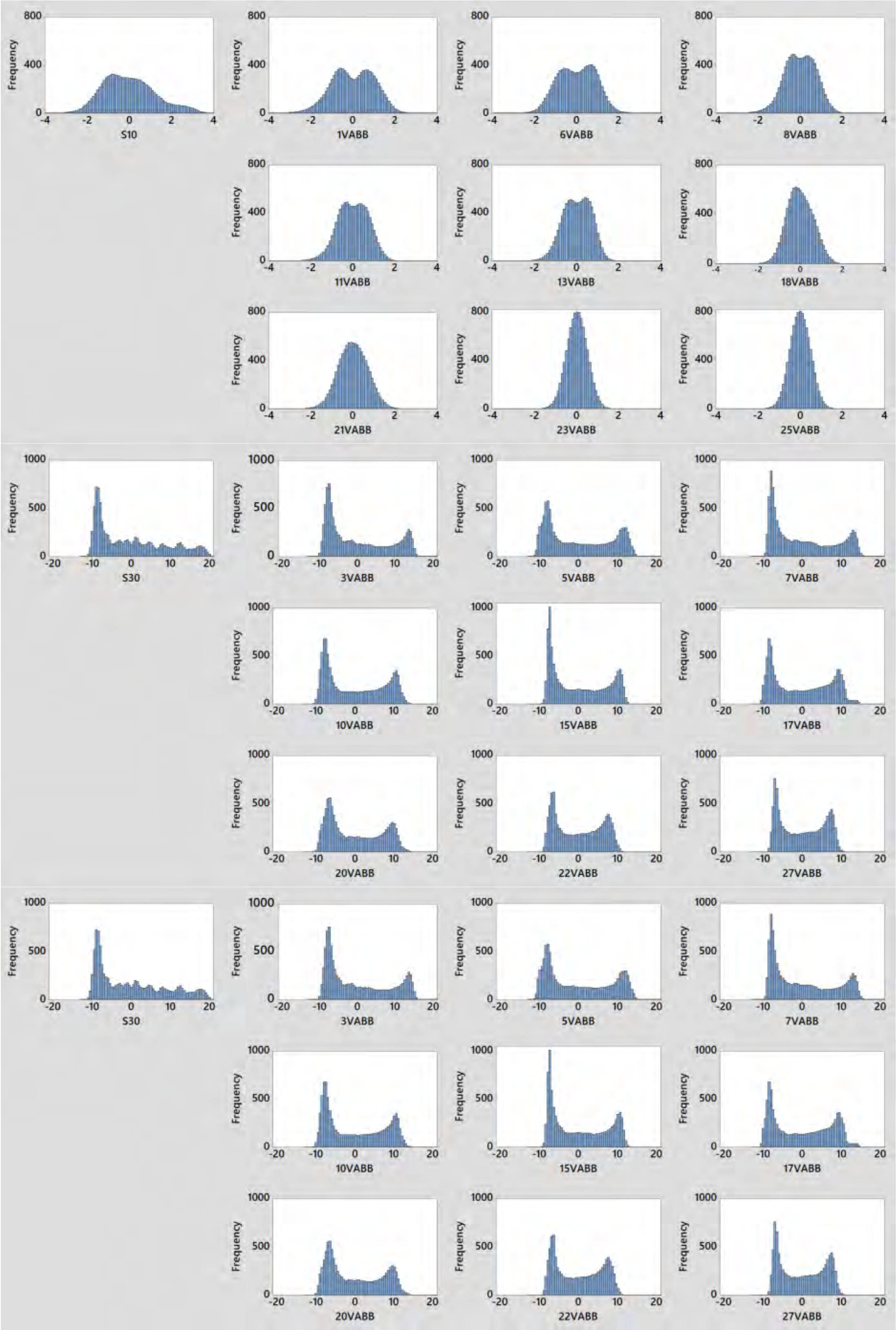

Figure C.4. VABB height distributions of Ti-6Al-4V surfaces.

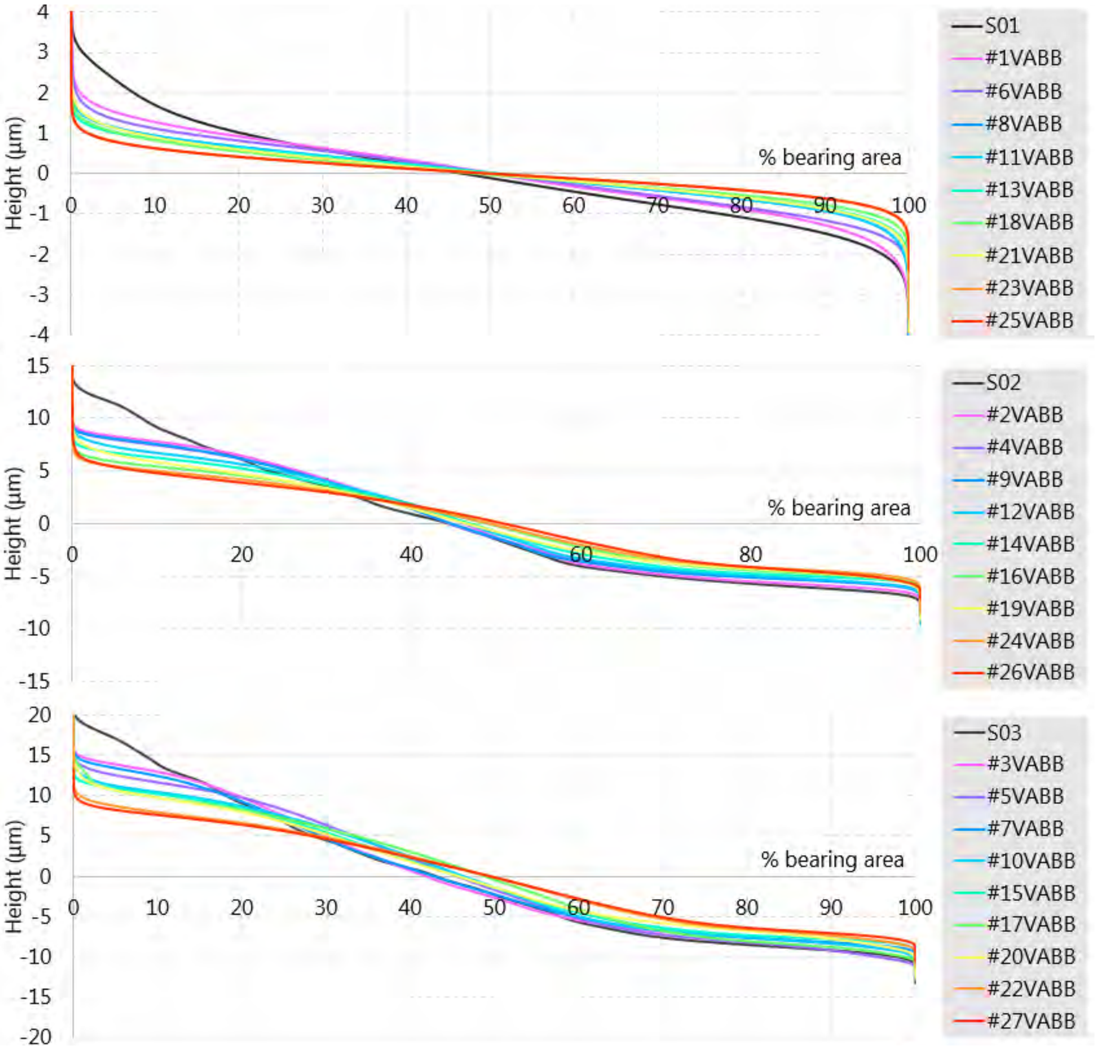

Figure C.5. VABB Abbott-Firestone curves of Ti-6Al-4V surfaces.

D

S/N ratios of residual stress ANOVA

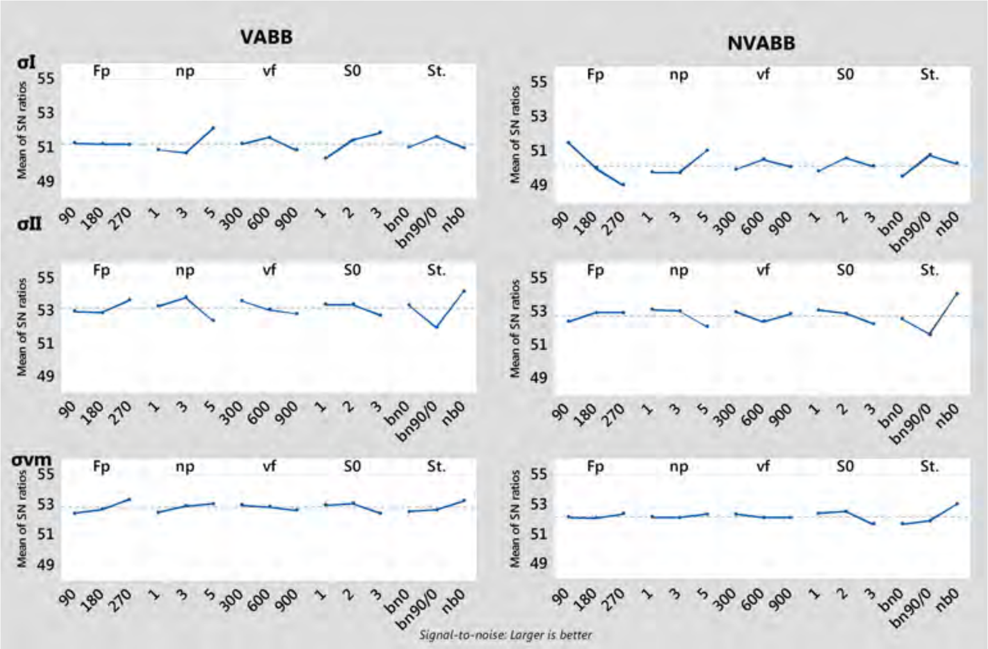

Figure D.1. S/N ratios for the ANOVA analysis of RS in AISI 1038 surfaces.

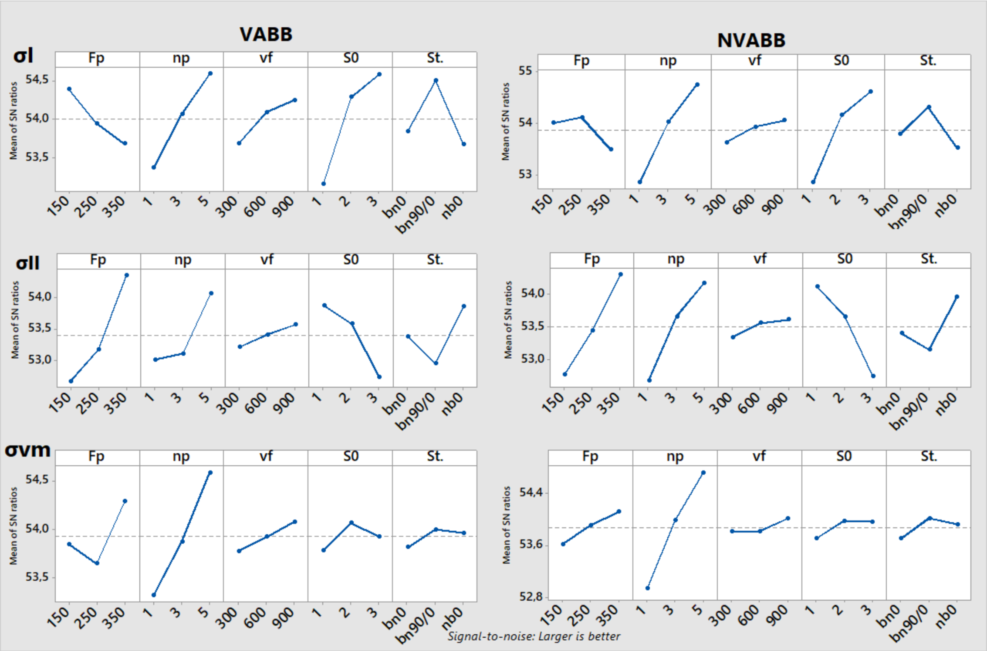

Figure D.2. S/N ratios for the ANOVA analysis of RS in TA6V surfaces.

Bibliography

[1] Abbott, E., and Firestone, F. Specifying surface quality. *Mechanical Engineering 55*, 9 (1933), 569–572.

[2] Altenberger, I., Nalla, R. K., Sano, Y., Wagner, L., and Ritchie, R. O. On the effect of deep rolling and laser peening on the stress-controlled low and high-cycle fatigue behavior of Ti-6Al-4V at elevated temperatures up to 550°C. *International Journal of Fatigue 44* (2012), 292–302.

[3] Amdouni, H., Bouzaiene, H., Montagne, A., Van Gorp, A., Coorevits, T., Nasri, M., and Iost, A. Experimental study of a six new ball-burnishing strategies effects on the Al-alloy flat surfaces integrity enhancement. *The International Journal of Advanced Manufacturing Technology 90*, 5-8 (2017), 2271–2282.

[4] Avilés, R., Albizuri, J., Rodríguez, A., and López de la Calle, L. N. Influence of low plasticityf ball burnishing on the high-cycle fatigue strength of medium carbon AISI 1045 steel. *International Journal of Fatigue 55* (2013), 230–244.

[5] Balland, P., Tabourot, L., Degre, F., and Moreau, V. Mechanics of the burnishing process. *Precision Engineering 37*, 1 (2013), 129–134.

[6] Basak, H., and Goktas, H. H. Burnishing process on Al alloy and optimization of surface roughness and surface hardness by fuzzy logic. *Materials & Design 30*, 4 (2009), 1275–1281.

[7] Blaha, F., and Langenecker, B. Dehnung von Zink-Kristallen unter Ultraschalleinwirkung. *Naturwissenschaften 42*, 20 (1955), 556–556.

[8] Blaha, F., and Langenecker, B. Plastizitätsuntersuchungen von Metallkristallen in Ultraschallfeld. *Acta Metallurgica 7*, 2 (1959), 93–100.

[9] Born, M., and Wolf, E. *Principles of optics: electromagnetic theory of propagation, interference and diffraction of light.* Elsevier, 2013.

[10] Bougharriou, A., Saï, K., and Bouzid, W. Finite element modelling of burnishing process. *Materials Technology 25*, 1 (2010), 56–62.

[11] Bouzid, W., Tsoumarev, O., and Sai, K. An investigation of surface roughness of burnished AISI 1042 steel. *The International Journal of Advanced Manufacturing Technology 24*, 1-2 (2004), 120–125.

[12] Bozdana, A., and Gindy, N. Comparative experimental study on effects of conventional and ultrasonic deep cold rolling processes on Ti–6Al–4V. *Materials Science and Technology 24*, 11 (2008), 1378–1384.

[13] Bozdana, A. T., Gindy, N. N., and Li, H. Deep cold rolling with ultrasonic vibrations–a new mechanical surface enhancement technique. *The International Journal of Machine Tools and Manufacture 45*, 6 (2005), 713–718.

[14] Brehl, D., and Dow, T. Review of vibration-assisted machining. *Precision engineering 32*, 3 (2008), 153–172.

[15] Callister, W. D., and Rethwisch, D. G. *Fundamentals of materials science and engineering.* Wiley London, 2000.

[16] Celaya, A., Rodríguez, A., Albizuri, J., Lopez de la Calle, L., and Alberdi, R. Finite element model of burnishing. In *9° Congreso Iberoamericano de Ingeniería Mecánica* (2009), Asociación Española de Ingeniería Mecánica, pp. 147–154.

[17] Cheng, B., Leung, H., and Ngan, A. Strength of metals under vibrations-dislocation-density-function dynamics simulations. *Philosophical Magazine 95*, 16-18 (2015), 1845–1865.

[18] Chomienne, V., Valiorgue, F., Rech, J., and Verdu, C. Influence of ball burnishing on residual stress profile of a 15-5PH stainless steel. *CIRP Journal of Manufacturing Science and Technology* (2016).

[19] Darlington, R. B. Is kurtosis really “peakedness?”. *The American Statistician 24*, 2 (1970), 19–22.

[20] Davim, J. P. *Surface integrity in machining.* Springer, 2010.

[21] De Chiffre, L., Lonardo, P., Trumpold, H., Lucca, D., Goch, G., Brown, C., Raja, J., and Hansen, H. N. Quantitative characterisation of surface texture. *CIRP annals-manufacturing technology 49*, 2 (2000), 644–652.

[22] Donachie, M. *Titanium: a technical guide.* ASM International, 2000.

[23] Dong, W., Sullivan, P., and Stout, K. Comprehensive study of parameters for characterizing three-dimensional surface topography I: Some inherent properties of parameter variation. *Wear 159*, 2 (1992), 161–171.

[24] Dong, W., Sullivan, P., and Stout, K. Comprehensive study of parameters for characterizing three-dimensional surface topography II: Statistical properties of parameter variation. *Wear 167*, 1 (1993), 9–21.

[25] Dong, W., Sullivan, P., and Stout, K. Comprehensive study of parameters for characterising three-dimensional surface topography III: Parameters for characterising amplitude and some functional properties. *Wear 178*, 1-2 (1994), 29–43.

[26] Dong, W., Sullivan, P., and Stout, K. Comprehensive study of parameters for characterising three-dimensional surface topography IV: Parameters for characterising spatial and hybrid properties. *Wear 178*, 1-2 (1994), 45–60.

[27] Dutta, R., Petrov, R., Delhez, R., Hermans, M., Richardson, I., and Böttger, A. The effect of tensile deformation by in situ ultrasonic treatment on the microstructure of low-carbon steel. *Acta Materialia 61*, 5 (2013), 1592–1602.

[28] El-Axir, M., and Ibrahim, A. Some surface characteristics due to center rest ball burnishing. *Journal of Materials Processing Technology 167*, 1 (2005), 47–53.

[29] El-Axir, M., Othman, O., and Abodiena, A. Improvements in out-of-roundness and microhardness of inner surfaces by internal ball burnishing process. *Journal of materials processing technology 196*, 1 (2008), 120–128.

[30] El-Axir, M., Othman, O., and Abodiena, A. Study on the inner surface finishing of aluminum alloy 2014 by ball burnishing process. *Journal of Materials Processing Technology 202*, 1 (2008), 435–442.

[31] El-Helieby, S., and Rowe, G. Influences of surface roughness and residual stress on fatigue life of ground steel components. *Metals Technology 7*, 1 (1980), 221–225.

[32] El-Khabeery, M., and El-Axir, M. Experimental techniques for studying the effects of milling roller-burnishing parameters on surface integrity. *The International Journal of Machine Tools and Manufacture 41*, 12 (2001), 1705–1719.

[33] El-Tayeb, N., Low, K., and Brevern, P. Influence of roller burnishing contact width and burnishing orientation on surface quality and tribological behaviour of aluminium 6061. *Journal of Materials Processing Technology 186*, 1 (2007), 272–278.

[34] Endo, T., Suzuki, K., and Ishikawa, M. Effects of superimposed ultrasonic oscillatory stress on the deformation of Fe and Fe-3% Si alloys. *Transactions of the Japan Institute of Metals 20*, 12 (1979), 706–712.

[35] Ezugwu, E., Da Silva, R., Bonney, J., and Machado, A. Evaluation of the performance of CBN tools when turning Ti-6Al-4V alloy with high pressure coolant supplies. *The International Journal of Machine Tools and Manufacture 45*, 9 (2005), 1009–1014.

[36] F, R. *ASM Handbook Volume 5: Surface engineering*. 1994.

[37] Fischer-Cripps, A. C. *Introduction to contact mechanics*. Springer, 2000.

[38] Fontaine, M., Devillez, A., Moufki, A., and Dudzinski, D. Predictive force model for ball-end milling and experimental validation with a wavelike form machining test. *The International Journal of Machine Tools and Manufacture 46*, 3 (2006), 367–380.

[39] Fu, C., Sealy, M., Guo, Y., and Wei, X. Austenite–martensite phase transformation of biomedical nitinol by ball burnishing. *Journal of Materials Processing Technology 214*, 12 (2014), 3122–3130.

[40] García-Granada, A. A., Gómez-Gras, G., Jerez-Mesa, R., Travieso-Rodriguez, J. A., and Reyes, G. Ball-burnishing effect on deep residual stress on AISI 1038 and AA2017-T4. *Materials and Manufacturing Processes 32*, 11 (2017), 1279–1289.

[41] Gharbi, F., Sghaier, S., Al-Fadhalah, K., and Benameur, T. Effect of ball burnishing process on the surface quality and microstructure properties of AISI 1010 steel plates. *Journal of Materials Engineering and Performance 20*, 6 (2011), 903–910.

[42] Gindin, I., Malik, G., Neklyudov, I., and Rozumnyi, O. Effect of ultrasonic vibrations on the parameters of the hardening curve for copper single crystals. *Soviet Physics Journal 15*, 2 (1972), 192–196.

[43] Gomez-Gras, G. *Estudio del proceso de bruñido con bola asistido por una vibración.* PhD thesis, Universitat Politècnica de Catalunya, 2015.

[44] Gómez-Gras, G., Travieso-Rodríguez, J., Jerez-Mesa, R., Lluma-Fuentes, J., and Gomis de la Calle, B. Experimental study of lateral pass width in conventional and vibrations-assisted ball burnishing. *The International Journal of Advanced Manufacturing Technology* (2016), 1–9.

[45] Gómez-Gras, G., Travieso-Rodríguez, J. A., González-Rojas, H. A., Nápoles-Alberro, A., Carrillo, F. J., and Dessein, G. Study of a ball-burnishing vibration-assisted process. *Proceedings of the Institution of Mechanical Engineers, Part B: Journal of Engineering Manufacture 229*, 1 (2015), 172–177.

[46] Gorlenko, O. Assessment of surface roughness parameters and their interdependence. *Precision Engineering 3*, 2 (1981), 105–108.

[47] Griffiths, B. Problems in measuring the topography of machined surfaces produced by plastic deformation mechanisms. *Wear 109*, 1-4 (1986), 195–205.

[48] Grzesik, W., and Żak, K. Modification of surface finish produced by hard turning using superfinishing and burnishing operations. *Journal of Materials Processing Technology 212*, 1 (2012), 315–322.

[49] Guillemot, N. *Prise en compte de l'intégrité de surface pour la prévision de la tenue en fatigue de pièces usinées en fraisage.* PhD thesis, École Normale Supérieure de Cachan, 2010.

[50] Hamadache, H., Laouar, L., Zeghib, N., and Chaoui, K. Characteristics of Rb40 steel superficial layer under ball and roller burnishing. *Journal of Materials Processing Technology 180*, 1 (2006), 130–136.

[51] Han, W., and Reddy, B. D. *Plasticity: mathematical theory and numerical analysis*, vol. 9. Springer Science & Business Media, 2012.

[52] Hassan, A., Al-Jalil, H., and Ebied, A. Burnishing force and number of ball passes for the optimum surface finish of brass components. *Journal of Materials Processing Technology 83*, 1 (1998), 176–179.

[53] Hassan, A. M. The effects of ball-and roller-burnishing on the surface roughness and hardness of some non-ferrous metals. *Journal of materials processing technology 72*, 3 (1997), 385–391.

[54] Hassan, A. M., and Al-Bsharat, A. S. Improvements in some properties of non-ferrous metals by the application of the ball-burnishing process. *Journal of Materials Processing Technology 59*, 3 (1996), 250–256.

[55] Hassan, A. M., and Al-Bsharat, A. S. Influence of burnishing process on surface roughness, hardness, and microstructure of some non-ferrous metals. *Wear 199*, 1 (1996), 1–8.

[56] Hassan, A. M., and Al-Dhifi, S. Z. Improvement in the wear resistance of brass components by the ball burnishing process. *Journal of Materials Processing Technology 96*, 1 (1999), 73–80.

[57] Hassan, A. M., and Maqableh, A. M. The effects of initial burnishing parameters on non-ferrous components. *Journal of Materials Processing Technology 102*, 1 (2000), 115–121.

[58] Hassan, A. M., and Momani, A. M. Further improvements in some properties of shot peened components using the burnishing process. *International Journal of Machine Tools and Manufacture 40*, 12 (2000), 1775–1786.

[59] Hernot, X., Bartier, O., Bekouche, Y., El Abdi, R., and Mauvoisin, G. Influence of penetration depth and mechanical properties on contact radius determination for spherical indentation. *International Journal of Solids and Structures 43*, 14 (2006), 4136–4153.

[60] Huuki, J., Hornborg, M., and Juntunen, J. Influence of ultrasonic burnishing technique on surface quality and change in the dimensions of metal shafts. *Journal of Engineering* (2014).

[61] Huuki, J., and Laakso, S. V. Integrity of surfaces finished with ultrasonic burnishing. *Proceedings of the Institution of Mechanical Engineers, Part B: Journal of Engineering Manufacture 227*, 1 (2013), 45–53.

[62] Izumi, O., Oyama, K., and Suzuki, Y. Effects of superimposed ultrasonic vibration on compressive deformation of metals. *Transactions of the Japan Institute of Metals 7*, 3 (1966), 162–167.

[63] Izumi, O., Oyama, K., and Suzuki, Y. On the superimposing of ultrasonic vibration during compressive deformation of metals. *Transactions of the Japan Institute of Metals 7*, 3 (1966), 158–161.

[64] Jawahir, I., Brinksmeier, E., M'saoubi, R., Aspinwall, D., Outeiro, J., Meyer, D., Umbrello, D., and Jayal, A. Surface integrity in material removal processes: Recent advances. *CIRP Annals-Manufacturing Technology 60*, 2 (2011), 603–626.

[65] Jayaraman, N., and Prevéy, P. Application of low plasticity burnishing (lpb) to improve the corrosion fatigue performance and fod tolerance of alloy 450 stainless steel. In *Proceedings of the Tri-Service Corrosion Conference* (2003), pp. 17–21.

[66] Jerez-Mesa, R., Travieso-Rodríguez, J., Gómez-Gras, G., and Lluma-Fuentes, J. Ultrasonic vibration-assisted ball burnishing tool. Referencia de patente: P201730385, 2017.

[67] Jiang, X. J., and Whitehouse, D. J. Technological shifts in surface metrology. *CIRP Annals-Manufacturing Technology 61*, 2 (2012), 815–836.

[68] King, T., and Houghton, N. Describing distribution shape: Rk and central moment approaches compared. *The International Journal of Machine Tools and Manufacture 35*, 2 (1995), 247–252.

[69] King, T., and Spedding, T. A. On the relationships between surface profile height parameters. *Wear 83*, 1 (1982), 91–108.

[70] Klocke, F., Bäcker, V., Wegner, H., Feldhaus, B., Baron, H.-U., and Hessert, R. Influence of process and geometry parameters on the surface layer state after roller burnishing of in718. *Production Engineering 3*, 4-5 (2009), 391–399.

[71] Koster, W., and Field, M. Effect of machining variables on the surface and structural integrity of ti. In *Proceedings of the North American Metalworking Research Conference.* (1973), vol. 2.

[72] Kozlov, A., Mordyuk, B., and Chernyashevsky, A. On the additivity of acoustoplastic and electroplastic effects. *Materials Science and Engineering: A 190*, 1 (1995), 75–79.

[73] Kozlov, A., and Selitser, S. Peculiarities in the plastic deformation of crystals subjected to the acoustoplastic effect. *Materials Science and Engineering: A 102*, 2 (1988), 143–149.

[74] Kozlov, A., and Selitser, S. Kinetics of the acoustoplastic effect. *Materials Science and Engineering: A 131*, 1 (1991), 17–25.

[75] Kuznetsov, V., Tarasov, S. Y., and Dmitriev, A. Nanostructuring burnishing and subsurface shear instability. *Journal of Materials Processing Technology 217* (2015), 327–335.

[76] Langenecker, B. Effects of ultrasound on deformation characteristics of metals. *Sonics and Ultrasonics, IEEE Transactions on 13*, 1 (1966), 1–8.

[77] Lee, S., and Loh, N. Computer-integrated ball burnishing of a plastic-injection-mould cavity insert. *Journal of Materials Processing Technology 57*, 1 (1996), 189–194.

[78] Lee, S., Tam, S., and Loh, N. Ball burnishing of 316L stainless steel. *Journal of Materials Processing Technology 37*, 1-4 (1993), 241–251.

[79] Loh, N., and Tam, S. Effects of ball burnishing parameters on surface finish–a literature survey and discussion. *Precision Engineering 10*, 4 (1988), 215–220.

[80] Loh, N., Tam, S., and Miyazawa, S. Optimisation of the surface finish produced by ball burnishing. *Journal of Mechanical Working Technology 19*, 1 (1989), 101–107.

[81] Loh, N., Tam, S., and Miyazawa, S. Statistical analyses of the effects of ball burnishing parameters on surface hardness. *Wear 129*, 2 (1989), 235–243.

[82] Loh, N., Tam, S., and Miyazawa, S. Surface hardening by ball burnishing. *Tribology International 23*, 6 (1990), 413–417.

[83] Loh, N., Tam, S., and Miyazawa, S. Use of response surface methodology to optimize the finish in ball burnishing. *Precision engineering 12*, 2 (1990), 101–105.

[84] Loh, N., Tam, S., and Miyazawa, S. Investigations on the surface roughness produced by ball burnishing. *The International Journal of Machine Tools and Manufacture 31*, 1 (1991), 75–81.

[85] Loh, N., Tam, S., and Miyazawa, S. Application of experimental design in ball burnishing. *The International Journal of Machine Tools and Manufacture 33*, 6 (1993), 841–852.

[86] Loh, N., Tam, S., and Miyazawa, S. Ball burnishing of tool steel. *Precision Engineering 15*, 2 (1993), 100–105.

[87] López de la Calle, L. N., Lamikiz, A., Sánchez, J., and Arana, J. The effect of ball burnishing on heat-treated steel and Inconel 718 milled surfaces. *The International Journal of Advanced Manufacturing Technology 32*, 9-10 (2007), 958–968.

[88] López de la Calle, L. N., Rodriguez, A., Lamikiz, A., Celaya, A., and Alberdi, R. Five-axis machining and burnishing of complex parts for the improvement of surface roughness. *Materials and Manufacturing Processes 26*, 8 (2011), 997–1003.

[89] Luca, L., Neagu-Ventzel, S., and Marinescu, I. Effects of working parameters on surface finish in ball-burnishing of hardened steels. *Precision Engineering 29*, 2 (2005), 253–256.

[90] Luo, H., Liu, J., Wang, L., and Zhong, Q. Investigation of the burnishing process with PCD tool on non-ferrous metals. *The International Journal of Advanced Manufacturing Technology 25*, 5-6 (2005), 454–459.

[91] Lye, S., and Leong, K. Some observations on the use of expert systems for the ball-burnishing operation. *Journal of Materials Processing Technology 22*, 1 (1990), 99–110.

[92] Majzoobi, G., Azadikhah, K., and Nemati, J. The effects of deep rolling and shot peening on fretting fatigue resistance of Aluminum-7075-T6. *Materials Science and Engineering: A 516*, 1 (2009), 235–247.

[93] Malygin, G. Acoustoplastic effect and the stress superimposition mechanism. *Physics of the Solid State 42*, 1 (2000), 72–78.

[94] Marakov, A. Ultrasonic diamond burnishing. *Russian Engineering Journal 53*, 9 (1973), 58–62.

[95] Martinez-Gonzalez, E., Picas, I., Casellas, D., and Romeu, J. Detection of crack nucleation and growth in tool steels using fracture tests and acoustic emission. *Meccanica 50*, 5 (2015), 1155–1166.

[96] Martinez-Gonzalez, E., Picas, I., Romeu, J., and Casellas, D. Filtering of acoustic emission signals for the accurate identification of fracture mechanisms in bending tests. *Materials Transactions 54*, 7 (2013), 1087–1094.

[97] Martinez-Gonzalez, E., Ramirez, G., Romeu, J., and Casellas, D. Damage induced by a spherical indentation test in tool steels detected by using acoustic emission technique. *Experimental Mechanics 55*, 2 (2015), 449–458.

[98] Mason, W. Effect of dislocations on ultrasonic wave attenuation in metals. *Bell System Technical Journal 34*, 5 (1955), 903–942.

[99] Michalski, J., and Pawlus, P. Characterization of the shape of the roughness profile ordinate distribution of honed cylinder surfaces. *Wear 161*, 1-2 (1993), 135–143.

[100] Mordyuk, B., Mordyuk, V., and Buryak, V. Ultrasonic drawing of tungsten wire for incandescent lamps production. *Ultrasonics 42*, 1 (2004), 109–111.

[101] Mordyuk, B. N., and Prokopenko, G. I. Ultrasonic impact peening for the surface properties' management. *Journal of Sound and Vibration 308*, 3 (2007), 855–866.

[102] Morimoto, T., and Tamamura, K. Effect of tool-material on burnishing process. *Bulletin of the Japan Society of Precision Engineering 24*, 3 (1990), 219–220.

[103] Murthy, R., and Kotiveerachari, B. Burnishing of metallic surfaces–a review. *Precision Engineering 3*, 3 (1981), 172–179.

[104] Némat, M., and Lyons, A. An investigation of the surface topography of ball burnished mild steel and aluminium. *The International Journal of Advanced Manufacturing Technology 16*, 7 (2000), 469–473.

[105] Nielsen, H. S. New approaches to surface roughness evaluation of special surfaces. *Precision Engineering 10*, 4 (1988), 209–213.

[106] Novovic, D., Dewes, R., Aspinwall, D., Voice, W., and Bowen, P. The effect of machined topography and integrity on fatigue life. *International Journal of Machine Tools and Manufacture 44*, 2 (2004), 125–134.

[107] Okada, M., Suenobu, S., Watanabe, K., Yamashita, Y., and Asakawa, N. Development and burnishing characteristics of roller burnishing method with rolling and sliding effects. *Mechatronics 29* (2015), 110–118.

[108] Pałka, K., Weroński, A., and Zalewski, K. Mechanical properties and corrosion resistance of burnished X5CrNi18-9 stainless steel. *Journal of Achievements in Materials and Manufacturing Engineering 16*, 1-2 (2006), 57–62.

[109] Pande, S., and Patel, S. Investigations on vibratory burnishing process. *International Journal of Machine Tool Design and Research 24*, 3 (1984), 195–206.

[110] Pervaiz, S., Rashid, A., Deiab, I., and Nicolescu, M. Influence of tool material son machinability of titanium- and nickel-based alloys: a review. *Materials and Manufacturing Processes 29* (2014), 219–252.

[111] Pillet, M. *Les plans d'expériences par la méthode Taguchi.* Editions d'organisation, 1997.

[112] Prevéy, P. S., and Cammett, J. Low cost corrosion damage mitigation and improved fatigue performance of low plasticity burnished 7075-T6. *Journal of Materials Engineering and Performance 10*, 5 (2001), 548–555.

[113] Prevéy, P. S., Hornbach, D., Jacobs, T., and Ravindranath, R. Improved damage tolerance in titanium alloy fan blades with low plasticity burnishing. Tech. rep., DTIC Document, 2002.

[114] Prevéy, P. S., Jayaraman, N., and Ravindranath, R. Low Plasticity Burnishing (LPB) treatment to mitigate FOD and corrosion fatigue damage in 17-4 PH stainless steel. Tech. rep., DTIC Document, 2003.

[115] Rao, D. S., Hebbar, H. S., Komaraiah, M., and Kempaiah, U. Investigations on the effect of ball burnishing parameters on surface hardness and wear resistance of HSLA dual-phase steels. *Materials and Manufacturing Processes 23*, 3 (2008), 295–302.

[116] Reason, R. Progress in the appraisal of surface topography during the first half-century of instrument development. *Wear 57*, 1 (1979), 1–16.

[117] Revankar, G. D., Shetty, R., Rao, S. S., and Gaitonde, V. N. Analysis of surface roughness and hardness in ball burnishing of titanium alloy. *Measurement 58* (2014), 256–268.

[118] Revankar, G. D., Shetty, R., Rao, S. S., and Gaitonde, V. N. Selection of optimal process parameters in ball burnishing of titanium alloy. *Machining Science and Technology 18*, 3 (2014), 464–483.

[119] Rodríguez, A., López de la Calle, L. N., Celaya, A., Lamikiz, A., and Albizuri, J. Surface improvement of shafts by the deep ball-burnishing technique. *Surface and Coatings Technology 206*, 11 (2012), 2817–2824.

[120] Roy, S., Fisher, J. W., and Yen, B. T. Fatigue resistance of welded details enhanced by ultrasonic impact treatment (UIT). *International Journal of Fatigue 25*, 9 (2003), 1239–1247.

[121] Sagbas, A. Analysis and optimization of surface roughness in the ball burnishing process using response surface methodology and desirabilty function. *Advances in Engineering Software 42*, 11 (2011), 992–998.

[122] Sai, W. B., and Saï, K. Finite element modeling of burnishing of aisi 1042 steel. *The International Journal of Advanced Manufacturing Technology 25*, 5-6 (2005), 460–465.

[123] Salahshoor, M., and Guo, Y. Process mechanics in ball burnishing biomedical magnesium–calcium alloy. *The International Journal of Advanced Manufacturing Technology 64*, 1-4 (2013), 133–144.

[124] Sartkulvanich, P., Altan, T., Jasso, F., and Rodriguez, C. Finite element modeling of hard roller burnishing: an analysis on the effects of process parameters upon surface finish and residual stresses. *Journal of Manufacturing Science and Engineering 129*, 4 (2007), 705–716.

[125] Schuh, A., Zeller, C., Holzwarth, U., Kachler, W., Wilcke, G., Zeiler, G., Eigenmann, B., and Bigoney, J. Deep rolling of titanium rods for application in modular total hip arthroplasty. *Journal of Biomedical Materials Research Part B: Applied Biomaterials 81*, 2 (2007), 330–335.

[126] Seemikeri, C., Brahmankar, P., and Mahagaonkar, S. Investigations on surface integrity of AISI 1045 using LPB tool. *Tribology International 41*, 8 (2008), 724–734.

[127] Segawa, T., Sasahara, H., and Tsutsumi, M. Development of a new tool to generate compressive residual stress within a machined surface. *International Journal of Machine Tools and Manufacture 44*, 11 (2004), 1215–1221.

[128] Sequera, A., Fu, C., Guo, Y., and Wei, X. Surface integrity of Inconel 718 by ball burnishing. *Journal of Materials Engineering and Performance 23*, 9 (2014), 3347–3353.

[129] Shepard, M. J., Prevey, P. S., and Jayaraman, N. Effects of surface treatment on fretting fatigue performance of Ti-6Al-4V. Tech. rep., DTIC Document, 2004.

[130] Sherrington, I., and Smith, E. Parameters for characterizing the surface topography of engineering components. *Proceedings of the Institution of Mechanical Engineers, Part C: Journal of Mechanical Engineering Science 201*, 4 (1987), 297–306.

[131] Shiou, F., and Cheng, C. Ultra-precision surface finish of NAK80 mould tool steel using sequential ball burnishing and ball polishing processes. *Journal of Materials Processing Technology 201*, 1 (2008), 554–559.

[132] Shiou, F. J., and Chen, C. H. Freeform surface finish of plastic injection mold by using ball burnishing process. *Journal of Materials Processing Technology 140*, 1 (2003), 248–254.

[133] Shiou, F. J., and Chuang, C. H. Precision surface finish of the mold steel PDS5 using an innovative ball burnishing tool embedded with a load cell. *Precision Engineering 34*, 1 (2010), 76–84.

[134] Shiou, F. J., and Ciou, H. S. Ultra-precision surface finish of the hardened stainless mold steel using vibration-assisted ball polishing process. *The International Journal of Machine Tools and Manufacture 48*, 7 (2008), 721–732.

[135] Siu, K., and Ngan, A. The continuous stiffness measurement technique in nanoindentation intrinsically modifies the strength of the sample. *Philosophical Magazine 93*, 5 (2013), 449–467.

[136] Siu, K., and Ngan, A. Oscillation-induced softening in copper and molybdenum from nano-to micro-length scales. *Materials Science and Engineering: A 572* (2013), 56–64.

[137] Siu, K., Ngan, A., and Jones, I. New insight on acoustoplasticity—ultrasonic irradiation enhances subgrain formation during deformation. *International Journal of Plasticity 27*, 5 (2011), 788–800.

[138] Stout, K., and Davis, E. Surface topography of cylinder bores–the relationship between manufacture, characterization and function. *Wear 95*, 2 (1984), 111–125.

[139] Suh, A. Y., Polycarpou, A. A., and Conry, T. F. Detailed surface roughness characterization of engineering surfaces undergoing tribological testing leading to scuffing. *Wear 255*, 1 (2003), 556–568.

[140] Tadic, B., Randjelovic, S., Todorovic, P., Zivkovic, J., Kocovic, V., Budak, I., and Vukelic, D. Using a high-stiffness burnishing tool for increased dimensional and geometrical accuracies of openings. *Precision Engineering 43* (2016), 335–344.

[141] Tadic, B., Todorovic, P. M., Luzanin, O., Miljanic, D., Jeremic, B. M., Bogdanovic, B., and Vukelic, D. Using specially designed high-stiffness burnishing tool to achieve high-quality surface finish. *The International Journal of Advanced Manufacturing Technology 67*, 1-4 (2013), 601–611.

[142] Taguchi, G., Chowdhury, S., and Wu, Y. *Taguchi's quality engineering handbook.* Wiley, 2005.

[143] Tanibayashi, M. A theory of the blaha effect. *Physica Status Solidi (A) 128*, 1 (1991), 83–94.

[144] Taylor, J. *Introduction to error analysis, the study of uncertainties in physical measurements.* 1997.

[145] Thamizhmanii, S., and Hassan, S. An experimental work on multi-roller burnishing process on difficult to cut material–titanium alloy. *International Journal Of Integrated Engineering 1*, 1 (2009), 1–6.

[146] Thomas, T. Characterization of surface roughness. *Precision Engineering 3*, 2 (1981), 97–104.

[147] Tian, Y., and Shin, Y. C. Laser-assisted burnishing of metals. *The International Journal of Machine Tools and Manufacture 47*, 1 (2007), 14–22.

[148] Travieso-Rodriguez, J. A. *Estudio para la mejora del acabado superficial de superficies complejas aplicando un proceso de deformación plástica (Bruñido con Bola).* PhD thesis, Universitat Politècnica de Catalunya, 2010.

[149] Travieso-Rodríguez, J. A., Dessein, G., and González-Rojas, H. A. Improving the surface finish of concave and convex surfaces using a ball burnishing process. *Materials and Manufacturing Processes 26*, 12 (2011), 1494–1502.

[150] Travieso-Rodríguez, J. A., Gómez-Gras, G., Dessein, G., Carrillo, F., Alexis, J., Jorba-Peiró, J., and Aubazac, N. Effects of a ball-burnishing process assisted by vibrations in g10380 steel specimens. *The International Journal of Advanced Manufacturing Technology 81*, 9-12 (2015), 1757–1765.

[151] Travieso-Rodríguez, J. A., Gómez-Gras, G., Jorba-Peiró, J., Carrillo, F., Dessein, G., Alexis, J., and González-Rojas, H. Experimental study on the mechanical effects of the vibration-assisted ball-burnishing process. *Materials and Manufacturing Processes 30*, 12 (2015), 1490–1497.

[152] Tsuji, N., Tanaka, S., and Takasugi, T. Evaluation of surface-modified Ti-6Al-4V alloy by combination of plasma-carburizing and deep-rolling. *Materials Science and Engineering: A 488*, 1 (2008), 139–145.

[153] Uddin, M., Hall, C., and Murphy, P. Surface treatments for controlling corrosion rate of biodegradable Mg and Mg-based alloy implants. *Science and Technology of Advanced Materials* (2016).

[154] Ugur, E. Use of grey based Taguchi method in ball burnishing process for the optimization of surface roughness and microhardness of AA 7075 aluminum alloy. *Materiali in tehnologije 44*, 3 (2010), 129–135.

[155] Ulutan, D., and Ozel, T. Machining induced surface integrity in titanium and nickel alloys: A review. *International Journal of Machine Tools and Manufacture 51*, 3 (2011), 250–280.

[156] Velásquez, J. P., Tidu, A., Bolle, B., Chevrier, P., and Fundenberger, J. J. Sub-surface and surface analysis of high speed machined Ti-6Al-4V alloy. *Materials Science and Engineering: A 527*, 10 (2010), 2572–2578.

[157] Withers, P., and Bhadeshia, H. Residual stress. Part 1–Measurement techniques. *Materials science and Technology 17*, 4 (2001), 355–365.

[158] Withers, P., and Bhadeshia, H. Residual stress. Part 2–Nature and origins. *Materials science and technology 17*, 4 (2001), 366–375.

[159] Xie, H., Wang, Q., Liu, K., Peng, F., Dong, X., and Wang, J. Investigation of influence of direct-current pulses on springback during V-bending of AZ31B magnesium alloy sheet. *Journal of Materials Processing Technology 219* (2015), 321–327.

[160] Yen, Y., Sartkulvanich, P., and Altan, T. Finite element modeling of roller burnishing process. *CIRP Annals-Manufacturing Technology 54*, 1 (2005), 237–240.

[161] Zhang, T., Bugtai, N., and Marinescu, I. D. Burnishing of aerospace alloy: A theoretical–experimental approach. *Journal of Manufacturing Systems* (2014).

[162] Zipin, R. B. The effect on surface texture of material addition and removal processes. *Surface and Interface Analysis 11*, 6-7 (1988), 291–301.